Photocatalytic and Photoelectrocatalytic Oxidation of Nitrogen Compounds in Wastewater

Adriana Rioja Cabanillas

BEng, MSc

Faculty of Computing and Engineering

Ulster University

Thesis submitted for the degree of Doctor of Philosophy

August 2023

I confirm that the word count of this thesis is less than 100,000 words.

Contents

Acknowledgements

I would like to acknowledge the funding of this PhD to European Union's Horizon 2020 research and innovation programme under the Marie-Curie grant agreement No 812574 under the project REWATERGY.

I would also like to thank the members of REWATERGY, for putting together this project, and providing insightful trainings and meetings.

It is with appreciation that I acknowledge the support and help of my supervisors at Ulster University, Professor Pilar Fernandez-Ibañez and Professor Tony Byrne. Without their guidance and persistent help, this work would not have been possible. I would also like to thank staff, collaborators and colleagues in NIBEC for the help and support provided during this research.

Additionally, I would like to extend my sincere thanks to the team at the industrial partner for this PhD (Delft-IMP) for their supervision, and training in atomic layer deposition.

I would also like to dedicate this work to my friends and family for their constant support and motivation in this journey. Lastly, words cannot express my gratitude towards my partner, without his constant support and encouragement I would not have been here.

Adriana Rioja Cabanillas

Note on access to contents

"I hereby declare that the with the effect from the date on which the thesis is deposited in the Library of the Ulster University, I permit

1. the Librarian of the University to allow the thesis to be copied in the whole or in part without reference to me on the understanding that such authority applies to the provision of single copies made for study purposes or for the inclusion within the stock of another library.
2. the thesis to be made available through the Ulster Institutional Respiratory and/or EThOS under the terms of the Ulster eThesis Deposit Agreement which I have signed.

IT IS A CONDITION OF USE OF THIS THESIS THAT ANYONE WHO CONSULTS IT MUST RECOGNISE THAT THE COPYRIGHT RESTS WITH THE AUTHOR AND THAT NO QUOTATION FROM THE THESIS AND NO INFORMATION DERIVED FROM IT MAY BE PUBLISHED UNLESS THE SOURCE IS PROPERLY ACKNOWLEDGED."

Adriana Rioja Cabanillas

August 2023

Publications and Presentations

Publications

1. **Rioja-Cabanillas, A**., McMichael, S., Tolosana-Moranchel, A., Alkharabsheh, S., Skillen, N., Fernandez-Ibanez, P., Byrne, J. A. (2023). Solar photoelectrocatalytic oxidation of urea in water coupled to green hydrogen production. Journal of Cleaner Production, 138200.
2. Fernandez-Ibanez, P., McMichael, S., **Rioja Cabanillas, A**., Alkharabsheh, S., Tolosana Moranchel, A., Byrne, J. A. (2021). New trends on photoelectrocatalysis (PEC): nanomaterials, wastewater treatment and hydrogen generation. Current Opinion in Chemical Engineering, 34, 100725.
3. **Rioja-Cabanillas, A**., Valdesueiro, D., Fernández-Ibáñez, P., Byrne, J. A. (2020). Hydrogen from wastewater by photocatalytic and photoelectrochemical treatment. Journal of Physics: Energy, 3(1), 12006.

Presentations

1. **Rioja-Cabanillas, A**., McMichael, S., Fernandez-Ibanez, P., Byrne, J. A. Simultaneous oxidation of urea and production of hydrogen using photoelectrocatalysis. *Spring Meeting - European Materials Research Society.* June 2023. Strasbourg, (FR). Oral presentation. Best Oral presentation award at Symposium C: Advanced Materials for Environmental Challenges.
2. **Rioja-Cabanillas, A**., McMichael, S., Fernandez-Ibanez, P., Byrne, J. A. Photoelectrochemical H_2 production from urea in wastewater using WO_3. *RSC Chemical Nanoscience and Nanotechnology Network Annual Symposium.* January 2023, London, (UK). Oral presentation. RSC Travel grant. Best Oral presentation award.
3. **Rioja-Cabanillas, A**., Fernandez-Ibanez, P., Hauser, R., Byrne, J. A. WO_3 photoanode for the removal of urea coupled to H_2 production. *2022 Fall Meeting-European Materials Research Society*. September 2022, Warsaw (PL). Oral presentation.
4. **Rioja-Cabanillas, A**., McMichael, S., Fernandez-Ibanez, P., Hauser, R, Byrne, J. A. WO_3 photoanodes for the oxidation of urea in wastewater and hydrogen

production. *32nd Irish Environmental Researchers Colloquium,* June 2022, Belfast (UK). Oral presentation. Best Chemical Sciences Presentation.

5. **Rioja-Cabanillas, A**., McMichael, S., Fernandez-Ibanez, P., Hauser, R, Byrne, J. A. Photoelectrochemical removal of urea in wastewater using WO_3. *11th European Conference on Solar Chemistry and Photocatalysis: Environmental Applications.* June 2022, Turin (IT). Flash Oral presentation
6. **Rioja-Cabanillas, A**., Fernandez-Ibanez, P., Hauser, R, Byrne, J. A. Photoelectrochemical removal of nitrogen compounds from wastewater. *23rd Netherlands Catalysis and Chemistry Conference.* May 2022, Noordwijkerhout (NL). Poster presentation.
7. **Rioja-Cabanillas, A**., Valdesueiro, D., Fernandez-Ibanez, P., & Byrne, J. A. Photoelectrochemical oxidation of nitrogen compounds in wastewater and hydrogen production. *Catalight Young Scientist Symposium: Light Driven Catalysis 2020.* November 2020, Berlin (DE). Poster presentation.
8. **Rioja-Cabanillas, A**., Valdesueiro, D., Fernandez-Ibanez, P., & Byrne, J. A. Photoelectrochemical oxidation of nitrogen compounds in wastewater and hydrogen production. *30th Irish Environmental Researcher Colloquium 'Ireland's Water, Energy & Environment in a Climate; Biodiversity Emergency' Environ*. October 2020, Dublin (IRL). Poster presentation.

List of Abbreviations

AB	Applied bias
ABPE	Applied bias photon to current conversion efficiency
ALD	Atomic layer deposition
AM	Air mass
BS	British Standards
CE	Counter electrode
CVD	Chemical vapor deposition
DRS	Diffuse reflectance spectroscopy
eV	Electronvolt
FBR	Fluidized bed reactor
FE	Faradaic efficiency
FQE	Formal quantum efficiency
FTO	Fluorine-doped tin oxide
GC	Gas chromatograph
GL	Gaussian-Lorentzian
HER	Hydrogen evolution reaction
HR	High resolution
ID	Internal diameter
IPCE	Incident photon to Faradaic efficiency
IR	Infrared
ISO	International Organization for Standardization
ITO	Indium-doped tin oxide
LSV	Linear swept voltammetry
NP	Nanoparticle
NR	Nanorods
NT	Nanotube
NW	Nanowires
OC	Open circuit
OES	Optical emission spectroscopy
PC	Photocatalysis
PEC	Photoelectrochemistry
PVD	Physical vapor deposition

QE	Quantum efficiency
RE	Reference electrode
SC	Semiconductor
SCE	Saturated calomel electrode
SEM	Scanning electron microscope
SHE	Standard hydrogen electrode
STH	Solar to hydrogen
TCD	Thermal conductivity detector
TEM	Transmission electron microscopy
TiNT	Titanium nanotube
TOC	Total organic carbon
UV	Ultraviolet
UVA	Ultraviolet (315-400 nm)
UVB	Ultraviolet (280-315 nm)
WESS	Wide energy survey scans
XPS	X-ray photoelectron spectroscopy
XRD	X-ray diffraction

List of figures

List of tables

Abstract

In past decades, the intensification of human activities has created an alarming rise in environmental pollution levels. The use of photocatalysis or photoelectrocatalysis present alternatives for the decentralized treatment of domestic wastewater compounds, with the potential coupling to energy recovery. This study aims to explore the use of these technologies for the oxidation of urea and the possible coupling to hydrogen production.

The use of two TiO_2 nanostructured electrodes, P25 and titanium nanotubes (TiNT), was studied for the photoelectrochemical oxidation of urea. The TiNT showed better performance with higher photocurrent, an incident photon-to-current conversion efficiency (IPCE) reaching 55.11 % at 340 nm and an oxidation rate of 0.0037 min^{-1}. The better performance of the TiNT electrode was attributed to the longitudinal pathway provided by the nanotubes, aiding charge transfer.

Subsequently, the enhancement in the TiO_2(P25) performance through the deposition of Cu_xO clusters was explored using atomic layer deposition. The photoelectrocatalytic results showed that the addition of Cu_xO clusters rectified cathodically the TiO_2 generated current. Alternatively, when used in photocatalytic suspension, the Cu_2O clusters with low loadings (<1 wt.%) showed improved urea oxidation achieving up to 1.7 times the rate of unmodified TiO_2(P25).

Additionally, the oxidation of urea coupled to hydrogen production was investigated, using WO_3 as photoanode. The WO_3 electrode exhibited superior performance than P25, with a visible light activity up to 470 nm, 10 times higher photocurrent, an IPCE of 43 % at 360 nm and a urea oxidation rate constant of 1.47×10^{-2} min^{-1}. Hydrogen was simultaneously produced with a Faradaic efficiency of 87.3 % and a solar-to-hydrogen conversion efficiency of 1.1 %.

This thesis showed the potential for the development of technologies based on the photoelectrochemical treatment wastewater pollutants coupled to energy recovery. Further work is needed to address the selective oxidation of urea to dinitrogen and testing under real conditions.

Chapter 1. Introduction

In the last decades, the intensification of anthropogenic activities and the rapid growth of the global population have resulted in alarming, ever increasing, levels of environmental pollution. Pollutants from different sources as industrial discharge, agricultural runoff, sewage and improper waste disposal end up in different water bodies as groundwater, river, lakes and oceans. This causes toxicity and harm to aquatic organism, as well as challenges to the drinking water system and economic impact [1].

1.1 Nitrogen pollution in wastewater

Nutrient pollution is one of the most widespread types of water pollution worldwide, causing adverse environmental effects. Eutrophication is a direct consequence of excessive nutrients in water, with a depletion of the oxygen in water bodies, causing an unbalance in the ecosystems. This harmful outcome can also entail the bloom of harmful algae, and in extreme cases the creation of dead zones [2,3] (Figure 1-1). This type of pollution occurs when an excess loss of nutrients gets released uncontrollably to soil, air and water. On of the major contributors to the nutrient pollution in water bodies is the excess of nitrogen compounds. Most of the nitrogen in wastewater derives from diverse human activities, like intensive farming, excessive use of fertilizers and wastes from some industries [2,4].

Figure 1-1. Pictures of some Dutch urban waters that annually suffer from cyanobacterial blooms. Figure reproduced from [5]**.**

Additionally, there is an elevated nitrogen concentration coming from domestic and municipal sewage [2,3]. Urine contributes to 80% of all the nitrogen waste found in domestic wastewater, with urea ($(NH_2)_2CO$) as a major constituent [6].

Nitrogen excess is often treated in wastewater treatment plants based on biological processes. These methods require several steps using nitrogen transformations [7]. Firstly, in the ammonification step, the nitrogen bacteria convert the organic nitrogen to ammonia. Secondly, during the nitrification step, the ammonia is biologically oxidized to nitrates; using a two steps process. In the first step, bacteria as *Nitrosomona* convert the ammonia to nitrite, and in the second step, bacteria as *Nitrobacter* transform the nitrite into nitrate [7]. These steps (i.e., the biological oxidation of ammonia to nitrates) require high quantities of dissolved oxygen and alkaline additives to keep the pH in the bacteria working range [7,8]. Finally, during the de-nitrification step, the nitrates are converted to dinitrogen (N_2) gas; for this process a low oxygen environment is required. Even though these biological processes are a quite mature technology, they also have several drawbacks: multistep process, oxygen and pH control, use of alkaline additives and low nitrification rate. These biological reactors are thus characterized by high energy demand, large space requirement and elevated operational costs [9].

Recently, with the purpose of addressing the drawbacks from the current water treatment technology, alternative biological processes are being studied. These include simultaneous nitrification and denitrification (anammox), aerobic deammonification, partial nitrification and denitrification, complete autotrophic nitrogen removal over nitrite (CANON), and oxygen-limited nitrification and denitrification (OLAND) [9]. Moreover, in order to increase the removal rates, reduce the size of reactors and the operational costs, the use of non-biological technologies are also being researched, e.g., air stripping, membranes, electrochemistry and photocatalysis [10,11].

1.2 Greenhouse emission and the necessity of fossil-free fuels

At present, the average surface temperature of the earth is reported to be $1 \pm 0.2\,^{o}C$ higher than at pre-industrial times [12] (Figure 1-2). The emission of GHG from human activities, mostly from burning fossil fuels in the energy, agricultural and industrial sector, is considered to be the leading reason for this increase in temperature [13].

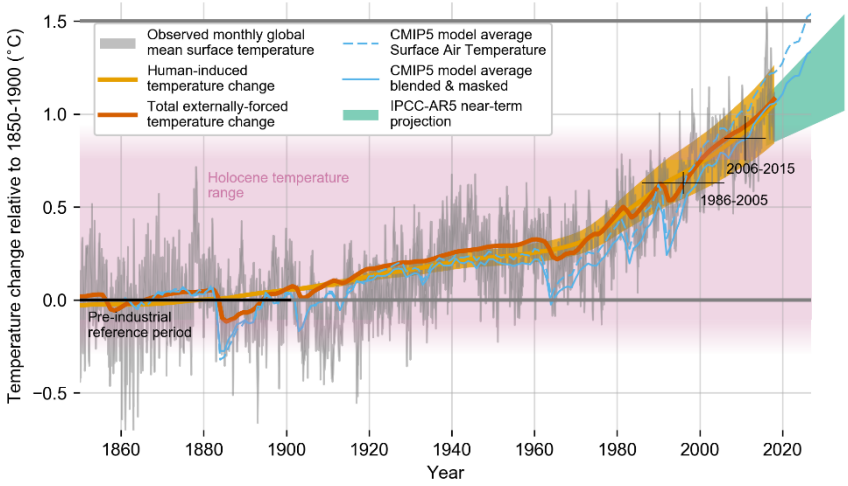

Figure 1-2. Evolution of global mean surface temperature (GMST) over the period of instrumental observations. Figure reproduced from [14].

The Intergovernmental Panel on Climate Change (IPCC) stated that increase in temperature should not exceed 1.5° C above pre-industrial level [15]. Beyond this threshold irreversible and catastrophic events would be unavoidable, posing a threat to the existence of life as we know it today [15]. According to the IPCC report, if we keep the current emission level, we will reach 1.5°C in 2040 (Figure 1-3), therefore an urgent decrease on GHG emission is required to accomplish this target [12].

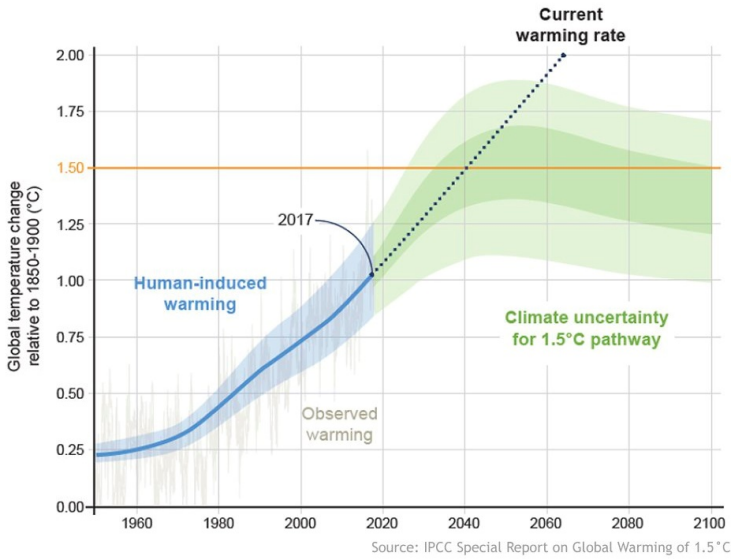

Figure 1-3. How close are we to 1.5°C?. Figure reproduced from [14].

In order to fulfil this goal, it is necessary to decarbonize the energy, agriculture and industrial sectors, by the use of renewable energy and sustainable fuels. Hydrogen, when produced from a sustainable technology, is considered crucial clean energy carrier that can enable a decarbonized society fuelled by renewable energy. The use of hydrogen in fuel cells or combustion engines produces only water, resulting in zero carbon emissions. Moreover, H_2 has a high gravimetric value, making it an attractive green energy carrier. The International Renewable Energy Agency (IRENA) reported in 2019 that more than 95 % hydrogen is produced using fossil fuel based technologies, as oil and coal gasification or steam-methane reforming [16]. This data highlights the critical necessity to develop alternative and sustainable H_2 production processes.

1.3 Energy recovery from wastewater

The current society is constructed on the basis of a linear production route, the extraction of raw matter is followed by its industrial transformation into products, and its disposal as waste. This linear approach originates long-term issues, threatening the limited available natural resources and highlighting its inefficient use. This linear practice contributes to the climate crisis and water pollution. Consequently, it is vital to embrace alternative approaches following the circular economy concept, where materials and products are in the economy for as long as it is possible. Wastewater has a notable potential to be used for resource recovery, since it contains nutrients, like phosphorus and nitrogen, but also precious metals [17]. In addition, wastewater also represents a potential source of energy [17]. The operation of conventional wastewater treatment plants requires a high energy use [18]. However, the energy required to run these processes may be produced from wastewater itself in distinct forms, including electricity, heat or fuels, as methane or hydrogen. A clear example of energy recovery from wastewater is the production of biogas by anaerobic digestion. This process is currently being employed in some wastewater treatment facilities around the world [17]. The anaerobic digestion is based on the degradation of organic waste employing bacteria, which in the absence of oxygen produce biogas, i.e., a mixture of methane and carbon dioxide. Yet, the methane is a carbon-based fuel, and its use leads to the emission of GHG. Therefore, it would be more interesting to extract carbon-free fuels, such as H_2.

Hydrogen can be produced from wastewater, for instance, using biological processes. Due to its high content of organic matter, wastewater is a good candidate for the

generation of hydrogen via fermentation. Biological hydrogen production methods include photo-fermentation and dark fermentation [19]. In photo-fermentation, photosynthetic bacteria driven by sunlight convert organic compounds into CO_2 and H_2. In dark fermentation, diverse bacteria groups take part in a sequence of biochemical reactions to transform organic substrates into biohydrogen. Usually, these two processes are coupled, since the organic acids, i.e., the by-products of dark fermentation, can be converted to hydrogen during photo-fermentation by the photosynthetic bacteria [20]. An alternative pathway to recover energy from wastewater consist in using microbial fuel cells (MFC). In MFC, organic matter is oxidized by the bacteria in the anode while injecting electrons. The latter can be used to produce electricity or hydrogen at the cathode, depending on the application. MCF are regarded as a promising candidate for energy recovery from wastewater; however, challenges for the rapid scale-up of this technology include low power generation, sluggish electron transfer, membrane fouling and low growth rate of microbes [21,22].

Between alternative non-biological processes, an attractive approach is the utilization of photocatalysis to yield hydrogen from wastewater. With this technology, the excitation of a semiconductor with photons with energy equal or greater than the band gap energy, results in the formation of electron-hole pairs. These charge carriers can recombination in the bulk of the semiconductor with the energy emitted as heat or light, or they can migrate to the surface of the semiconductor. If the charges reach the surface, they can drive redox reactions with the adsorbed chemical species on the surface. The redox reactions that take place are dependent on the band edge potentials. If at appropriate potentials, the photogenerated hole can be used to oxidize wastewater compounds and the photogenerated electron to produce hydrogen.

An interesting step forward from photocatalysis is the use of electrochemically assisted photocatalysis, also commonly referred as photoelectrochemistry or photoelectrocatalysis. This approach commonly utilizes a semiconductor photoanode which when irradiated, is able to oxidize organic or inorganic waste compounds. This (photo)anode is connected to a counter electrode through an external circuit. Through this circuit, the photogenerated electrons passe to the counter electrode where reduction of protons (H^+) to H_2 can occur. The counter electrode can be formed by a metallic or carbon conducting electrode, or a semiconductor photocathode (with or without a photoanode).

A detailed description of the photocatalytic and photoelectrochemical fundamentals, materials and their use on hydrogen production from wastewater is given in Chapter 2.

1.4 Aim and Objectives of the thesis

1.4.1 Aim

The overall aim of this research is to investigate the use of semiconductor materials in photocatalytic or photoelectrochemical configuration applied to the oxidation of N pollutants in wastewater, with the simultaneous recovery of energy as hydrogen gas.

1.4.2 Objectives

i. Conduct a detailed literature review on the use of photocatalytic and photoelectrochemical processes for the treatment of wastewater coupled to the production of hydrogen.
ii. Fabrication of nanostructured titanium dioxide (TiO_2) and tungsten trioxide (WO_3) photoanodes.
iii. Modification of the semiconductor surface using atmospheric-pressure Atomic Layer Deposition.
iv. Use of material characterization techniques to study morphology, chemical composition, crystalline phase, and optical properties (SEM, XPS, XRD, UV-Vis DRS).
v. Use photoelectrochemical analysis to study material performance and determine the incident photon to electron conversion efficiency (IPCE).
vi. Design and fabrication of customized photoelectrochemical cells for the lab-scale prototype for the simultaneous degradation of urea and production of hydrogen
vii. Determination of the materials activity for urea oxidation.
viii. Identification and quantification of urea oxidation products.
ix. Quantification of hydrogen production and assessment of system performance through faradaic and solar-to-hydrogen conversion efficiency.

1.5 Thesis structure

Chapter 2 contains an overview of the fundamentals, materials and the parameters used to evaluate the performance of photocatalytic and photoelectrochemical processes. It focuses on reviewing the removal of wastewater pollutants and the possible coupling to

hydrogen production using photocatalysis and photoelectrochemistry. This chapter also includes the materials used, possible mechanisms and performance of these processes. Finally, the chapter concludes with a critical evaluation of the current limitations and future opportunities.

Chapter 3 includes the materials and methodology used in this research project, describing the synthesis methods, material characterisation, (photo)electrochemical characterization and analytical techniques that were utilized.

Chapter 4 reports the use of two different nanostructured TiO_2 electrodes (P25 and TiNT) for the oxidation of urea. It included a comparison of their material properties and photoelectrochemical performance. Moreover, the behaviour of these electrodes in the presence of common nitrogen wastewater compounds (urea and ammonia) was also studied, including the influence of the pH on the photocurrent. Finally, the urea oxidation rate for both materials was compared with the use of a photoelectrochemical custom-made cell.

Chapter 5 reports the use of ALD for the controlled deposition of Cu_xO clusters on the surface of TiO_2 and the study their performance for photocatalytic and photoelectrochemistry. This study included the material characterization of the modified samples for the different loadings with a special focus in the copper clusters oxidation state and particle size. The photoelectrochemical properties of the modified samples were also assessed together with the photocatalytic performance for the oxidation of urea.

Chapter 6 reports on the use WO_3 as photoanode material for the oxidation of urea. The photoelectrochemical behaviour of the WO_3 electrodes was studied and compared to TiO_2 (as benchmark). Urea oxidation kinetics and product distribution were investigated comparing the use of 1 or 2 compartment custom-made photoelectrochemical cells. Moreover, the simultaneous production of hydrogen was detected and quantified, calculating faradaic and solar-to-hydrogen efficiencies. The findings presented in this chapter demonstrate the proof of concept of oxidizing common pollutants present wastewater as urea, coupled to the simultaneous generation of hydrogen in a photoelectrochemical cell.

Chapter 7 presents the overall conclusion of this thesis, ending with recommendations for future work.

References

[1] S. Madhav, A. Ahamad, A.K. Singh, J. Kushawaha, J.S. Chauhan, S. Sharma, P. Singh, Water Pollutants: Sources and Impact on the Environment and Human Health BT - Sensors in Water Pollutants Monitoring: Role of Material, in: D. Pooja, P. Kumar, P. Singh, S. Patil (Eds.), Springer Singapore, Singapore, 2020: pp. 43–62. https://doi.org/10.1007/978-981-15-0671-0_4.

[2] European Environment Agency, Publications 13. Eutrophication, 2008.

[3] EPA, Nutrient Pollution, United States Environ. Prot. Agency. https://www.epa.gov/nutrientpollution, Accessed January 2023.

[4] WHO, Ammonia in Drinking-water, Background document for the development of WHO Guidelines for Driking-water Quality. World Health Organization, Geneva, 2003.

[5] M. Lürling, M. Mucci, Mitigating eutrophication nuisance: in-lake measures are becoming inevitable in eutrophic waters in the Netherlands, Hydrobiologia. 847 (2020) 4447–4467. https://doi.org/10.1007/s10750-020-04297-9.

[6] L. Egle, H. Rechberger, M. Zessner, Resources, Conservation and Recycling Overview and description of technologies for recovering phosphorus from municipal wastewater, "Resources, Conserv. Recycl. 105 (2015) 325–346. https://doi.org/10.1016/j.resconrec.2015.09.016.

[7] M. Gerardi, Nitrification and Denitrification in the Activated Sludge Process (Wastewater Microbiology), Wiley, 2002. https://doi.org/10.1002/0471216682.

[8] D. Paredes, P. Kuschk, T.S.A. Mbwette, F. Stange, R.A. Müller, H. Köser, New aspects of microbial nitrogen transformations in the context of wastewater treatment, Eng. Life Sci. 7 (2007) 13–25. https://doi.org/10.1002/elsc.200620170.

[9] S. Rahimi, O. Modin, I. Mijakovic, Technologies for biological removal and recovery of nitrogen from wastewater, Biotechnol. Adv. 43 (2020) 107570. https://doi.org/10.1016/j.biotechadv.2020.107570.

[10] Y. Feng, L. Yang, J. Liu, B.E. Logan, Electrochemical technologies for wastewater treatment and resource reclamation, Environ. Sci. Water Res. Technol. 2 (2016) 800–831. https://doi.org/10.1039/c5ew00289c.

[11] R.R. Karri, J.N. Sahu, V. Chimmiri, Critical review of abatement of ammonia from wastewater, J. Mol. Liq. 261 (2018) 21–31. https://doi.org/10.1016/j.molliq.2018.03.120.

[12] J.R. Arias, P.A., N. Bellouin, E. Coppola, R.G. Jones, G. Krinner, J. Marotzke, V. Naik, M.D. Palmer, G.-K. Plattner, G.B. M. Rojas, J. Sillmann, T. Storelvmo, P.W. Thorne, B. Trewin, K. Achuta Rao, B. Adhikary, R.P. Allan, K. Armour, F.C. R. Barimalala, S. Berger, J.G. Canadell, C. Cassou, A. Cherchi, W. Collins, W.D. Collins, S.L. Connors, S. Corti, F.E. F.J. Dentener, C. Dereczynski, A. Di Luca, A. Diongue Niang, F.J. Doblas-Reyes, A. Dosio, H. Douville, I.G. V. Eyring, E. Fischer, P. Forster, B. Fox-Kemper, J.S. Fuglestvedt, J.C. Fyfe, N.P. Gillett, L. Goldfarb, Y.K. J.M. Gutierrez, R. Hamdi, E. Hawkins, H.T. Hewitt, P. Hope, A.S. Islam, C. Jones, D.S. Kaufman, R.E. Kopp, P.M.S.M. J. Kossin, S. Krakovska, J.-Y. Lee, J. Li, T. Mauritsen, T.K. Maycock, M. Meinshausen, S.-K. Min, B.H.S. T. Ngo-Duc, F. Otto, I. Pinto, A. Pirani, K. Raghavan, R. Ranasinghe, A.C. Ruane, L. Ruiz, J.-B. Sallée, R.V. S. Sathyendranath, S.I. Seneviratne, A.A. Sörensson, S. Szopa, I. Takayabu, A.-M. Tréguier, B. van den Hurk, and K.Z. K. von Schuckmann, S. Zaehle, X. Zhang, Technical Summary. In Climate Change 2021: The Physical Science Basis. Contribution of Working Group I to the Sixth Assessment Report of the Intergovernmental Panel on Climate Change, 2021. https://doi.org/10.1017/9781009157896.002.

[13] B. Friedlingstein, P., O'Sullivan, M., Jones, M. W., Andrew, R. M., Gregor, L., Hauck, J., Le Quéré, C., Luijkx, I. T., Olsen, A., Peters, G. P., Peters, W., Pongratz, J., Schwingshackl, C., Sitch, S., Canadell, J. G., Ciais, P., Jackson, R. B., Alin, S. R., Global Carbon Budget 2022, 2022. https://doi.org/doi.org/10.5194/essd-14-4811-2022.

[14] N.M. Allen, M.R., O.P. Dube, W. Solecki, F. Aragón-Durand, W. Cramer, S. Humphreys, M. Kainuma, J. Kala, J. Y. Mulugetta, R. Perez, M.Wairiu, and K. Zickfeld [Masson-Delmotte, V., P. Zhai, H.-O. Pörtner, D. Roberts, X.Z. Skea, P.R. Shukla, A. Pirani, W. Moufouma-Okia, C. Péan, R. Pidcock, S. Connors, J.B.R. Matthews, Y. Chen, and T.W. (eds.). M.I. Gomis, E. Lonnoy, T. Maycock, M. Tignor, Framing and Context. In: Global Warming of 1.5°C. An IPCC Special Report on the impacts of global warming

of 1.5°C above pre-industrial levels and related global greenhouse gas emission pathways, in the context of strengthening the global response to the, Cambridge, UK and New York, NY, USA, n.d. https://doi.org/10.1017/9781009157940.003.

[15] R. Masson-Delmonte,V; Zhai,P; Portner, H; Roberts,D; Skea, J; Shukla,P;Pirani,A; Moufouma-Okia,w; Pean,C; Picok, Global warming of 1.5 C. An IPCC special report on the impacts of global warming, 2018.

[16] IRENA, Hydrogen: A renewable energy perspective, International Renewable Energy Agency, Abu Dhabi, 2019.

[17] J.S. Guest, S.J. Skerlos, J.L. Barnard, M.B. Beck, G.T. Daigger, H. Hilger, S.J. Jackson, K. Karvazy, L. Kelly, L. Macpherson, J.R. Mihelcic, A. Pramanik, L. Raskin, M.C.M. Van Loosdrecht, D. Yeh, N.G. Love, A new planning and design paradigm to achieve sustainable resource recovery from wastewater, Environ. Sci. Technol. 43 (2009) 6126–6130. https://doi.org/10.1021/es9010515.

[18] M. Molinos-Senante, A. Maziotis, Evaluation of energy efficiency of wastewater treatment plants: The influence of the technology and aging factors, Appl. Energy. 310 (2022) 118535. https://doi.org/10.1016/j.apenergy.2022.118535.

[19] C.Y. Lin, C.H. Lay, B. Sen, C.Y. Chu, G. Kumar, C.C. Chen, J.S. Chang, Fermentative hydrogen production from wastewaters: A review and prognosis, Int. J. Hydrogen Energy. 37 (2012) 15632–15642. https://doi.org/10.1016/j.ijhydene.2012.02.072.

[20] M.Y. Azwar, M.A. Hussain, A.K. Abdul-Wahab, Development of biohydrogen production by photobiological, fermentation and electrochemical processes: A review, Renew. Sustain. Energy Rev. 31 (2014) 158–173. https://doi.org/10.1016/j.rser.2013.11.022.

[21] A. ElMekawy, H.M. Hegab, X. Dominguez-Benetton, D. Pant, Internal resistance of microfluidic microbial fuel cell: Challenges and potential opportunities, Bioresour. Technol. 142 (2013) 672–682. https://doi.org/10.1016/j.biortech.2013.05.061.

[22] M.H. Do, H.H. Ngo, W.S. Guo, Y. Liu, S.W. Chang, D.D. Nguyen, L.D. Nghiem, B.J. Ni, Challenges in the application of microbial fuel cells to wastewater treatment and

energy production: A mini review, Sci. Total Environ. 639 (2018) 910–920. https://doi.org/10.1016/j.scitotenv.2018.05.136.

Chapter 2. Literature Review

The contents of this chapter have been published in part in "Rioja-Cabanillas A., Valdesueiro D., Fernández-Ibáñez P., Byrne J.A., Hydrogen from wastewater by photocatalytic and photoelectrochemical treatment, J. Phys. Energy. 3 (2021) 012006. https://doi.org/ 10.1088/2515-7655/abceab"

2.1 Introduction

The present chapter contains an overview of the fundamentals, materials and the parameters used to evaluate the performance of photocatalytic (section 2.2) and photoelectrochemical processes (section 2.3). The main section reviews the treatment of several wastewater coupled to hydrogen production using both photocatalysis and photoelectrochemistry, the different waste compounds are categorized in groups with a special emphasis put on nitrogen compounds, specifically on urea and ammonia (section 2.4). This section also includes a discussion of materials used, possible mechanisms and performance of these processes. Finally, this review chapter concludes with an evaluation of the current limitations on this field and future opportunities.

2.2 Photocatalysis

In photocatalysis, a semiconductor is irradiated with photons with energy equal to or greater than the band gap energy, resulting in the excitation of electrons from the valence band (VB) to the conduction band (CB). The photo-excited electron leaves a positively charged hole in the VB. These charge carriers are referred to as an electron-hole pair. The charge carriers can recombine in the semiconductor bulk dissipating energy as heat or light or they can migrate to the surface of the semiconductor. At the surface, they can undergo charge transfer processes driving redox reactions with chemical species which are adsorbed at the surface of the photocatalyst.

2.2.1 Fundamentals

Photocatalysis has been widely studied for the degradation of organic pollutants, extensive information can be found in previous reviews [1–4]. The organic pollutants can either undergo direct oxidation by holes, indirect oxidation by reactive oxygen species including hydroxyl radicals, or they may be transformed by a reductive route involving CB electrons. The most employed electron acceptor in photocatalytic oxidation reactions

is molecular oxygen since it is abundant in the air and is reasonably soluble in aqueous solutions. The oxygen is reduced by the CB electrons to form the superoxide radical anion ($O_2^{\bullet -}$). Subsequent reduction reactions lead to H_2O_2, •OH, and eventually H_2O. A representation of this process is shown in Figure 2-1.

Photocatalysis has also been investigated for hydrogen production through water splitting, as detailed described in several reviews [5–8]. In this application, the photogenerated holes are used to oxidize the water molecules to evolve oxygen, while the photo-generated electrons in the CB reduce protons and evolve hydrogen, as shown in Figure 2-1 (b). However, photocatalytic hydrogen production from water splitting is a challenging reaction because it is thermodynamically unfavourable (2-1) requiring a high energy input and the transfer of four electrons. It should be recognised that technically, uphill thermodynamic processes are photosynthetic, however, to avoid confusion, in this review both endothermic and exothermic reactions will be referred as photocatalytic. Hydrogen production from the oxidation of other compounds with reactions requiring less energy or being thermodynamically favourable ($\Delta G° < 0$) have also been investigated. This is schematically represented in Figure 2-2. These compounds can donate electrons and scavenge the VB holes while also acting as a source of protons. There are many compounds present in wastewater that could act as a hydrogen source, as ammonia and urea.

$$H_2O = H_2 + \frac{1}{2}\,O_2 \quad (\Delta G° = +237\ \mathrm{kJ.mol^{-1}}) \tag{2-1}$$

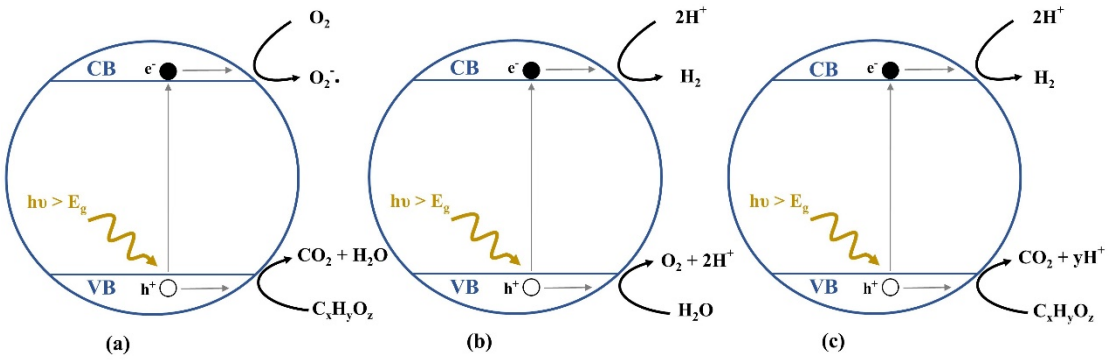

Figure 2-1. Schematic representation of photocatalytic process. (a) Photocatalytic degradation of organic pollutants with oxygen as the electron acceptor. (b) Photocatalytic water splitting. (c) Photocatalytic oxidation of pollutant with H_2 evolution as the reduction reaction.

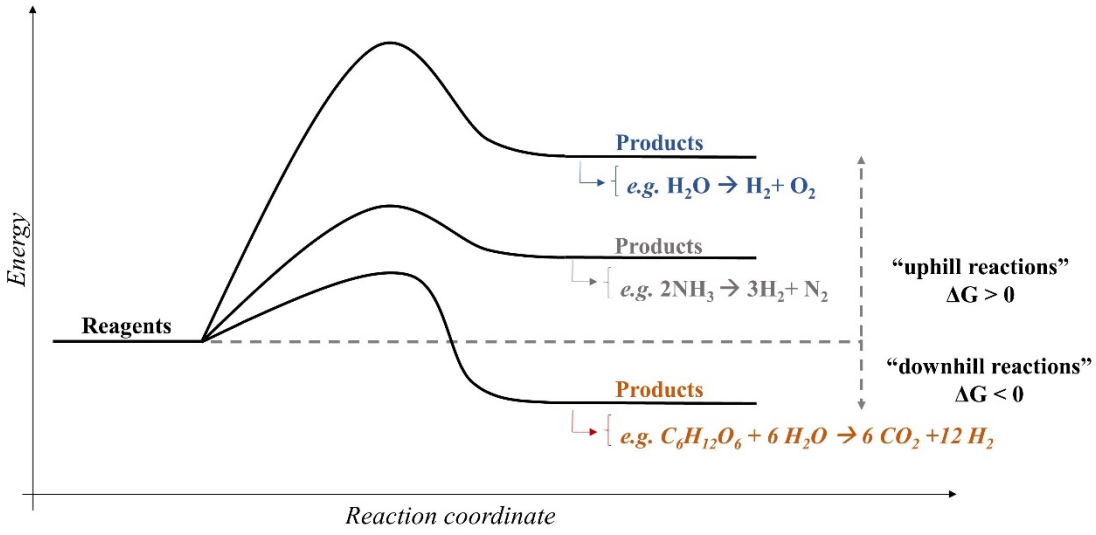

Figure 2-2. Thermodynamic energy diagram with examples for hydrogen production from water, ammonia, and glucose. Values obtained from [9–11].

Most studied compounds have been organics, but this is also possible with inorganic compounds as e.g., ammonia. In this application, the photo-generated holes are used to oxidize the unwanted compounds, which can take place through direct oxidation or indirect oxidation via hydroxyl radicals (•OH). The photo-generated electrons reduce the protons to form hydrogen. A schematic representation of this process is shown in Figure 2-1(c), with the oxidation of a generic organic compound. The photocatalytic oxidation of organic substances to form hydrogen is also referred as photoreforming and it follows the general equation given in (2-2).

$$C_xH_yO_z + (2x\text{-}z)\ H_2O \rightarrow x\ CO_2 + (2x + \frac{1}{2}y - z)\ H_2 \qquad (2\text{-}2)$$

The ability of a semiconductor to perform the desired redox reactions depends on the band gap energy and the band edge potentials for the VB and the CB. For the reactions to be thermodynamically possible, the CB edge potential should be more negative than the desired reaction reduction potential and the VB edge potential should be more positive than the desired reaction oxidation potential. In the water splitting reaction, the CB should be more negative than the hydrogen evolution reaction (HER) potential (0 V vs. NHE at pH 0), and the VB should be more positive than the oxygen evolution potential (+1.23 V vs NHE at pH 0). While in the reactions with oxidation of wastewater compounds, the conduction band needs to be more positive than the oxidation potential of the waste

compounds and pollutants. These potentials are more negative than the potential for water oxidation, requiring less energy for the overall reaction. The CB and VB of several semiconductor materials, together with the oxidation and reduction potential of these reactions are given in Figure 2-3.

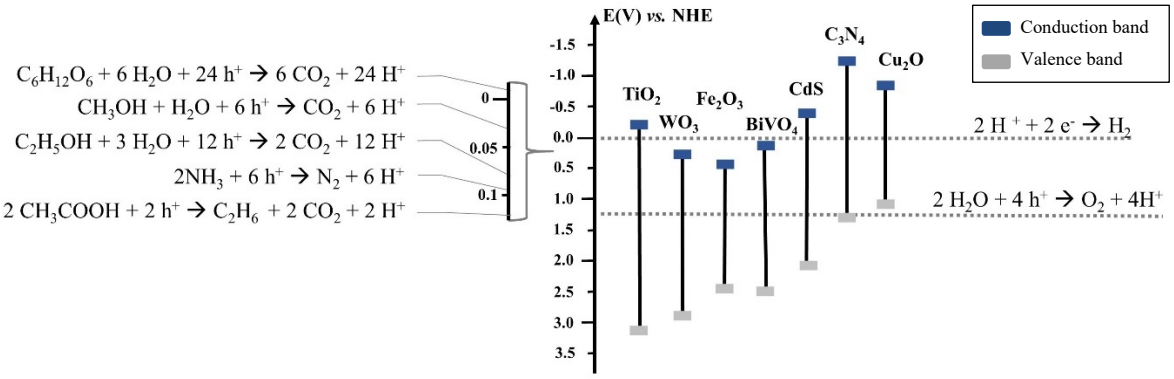

Figure 2-3. Band gap position of semiconductors in relation to oxidation and reduction reactions from wastewater compounds. Energy levels were previously reported in [12–18].

The ideal semiconductor material for photocatalytic hydrogen production from wastewater compounds would have the following general requirements:

- suitable band edges position,
- good light absorption,
- efficient charge transport,
- chemical and photochemical stability,
- low overpotentials for the desired reduction and oxidation reactions,
- low cost and being abundant.

It is important to consider that almost half of the incident solar energy on the earth's surface is in the visible region (400 nm < λ < 800 nm), and therefore, for solar applications the photocatalyst should be able to utilise both the UV and visible photons.

2.2.2 Materials

While a wide range of materials have been investigated for photocatalytic hydrogen production [5–8], the present review will focus on the materials reported for H_2 production coupled to the oxidation of pollutants found in wastewater. Titanium dioxide

is the most reported photocatalyst to investigate the coupling of H_2 production to the degradation of compounds found in wastewater [19–26]. Other materials as cadmium sulphide [27,28] and graphitic carbon nitride [29,30] have also been reported for H_2 production from wastewater compounds.

Titanium dioxide (TiO_2) is employed in a wide variety of fields, ranging from energy applications such as hydrogen production and CO_2 reduction, to environmental applications as water treatment, air purification and water disinfection [31]. TiO_2 exists as three different polymorphs: anatase, rutile and brookite (Figure 2-4). Its properties include high photo-activity, low cost, low toxicity and good chemical and thermal stability. Nevertheless, it suffers from having a high electron-hole recombination and a large band gap. TiO_2 band gap is 3.2 eV for anatase, 3.0 eV for rutile, and ~3.2 eV for brookite [31]. This wide band gap limits the light absorption to the ultraviolet range, which just accounts for 4-5 % of the solar spectrum, consequently, limiting its practical application.

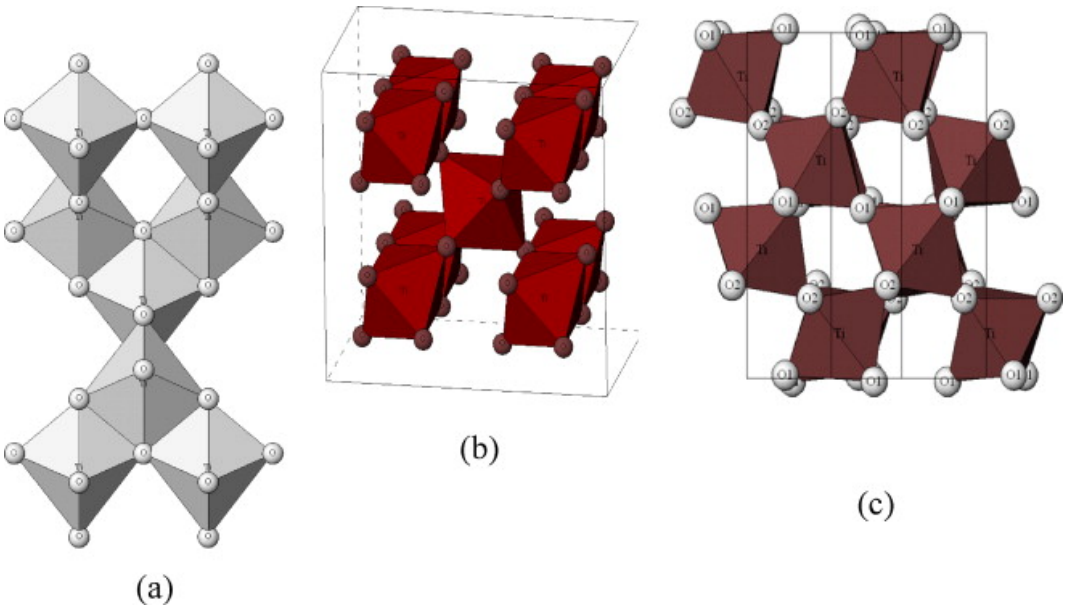

Figure 2-4. Titanium dioxide crystalline structures: a) anatase, b) rutile and c) brookite. Image reproduced from reference [12].

Developments to improve light absorption of TiO_2 include doping, metal deposition, dye sensitization and coupled semiconductors [12]. Non-metal doping has been extensively researched, with some reports claiming some non-metal dopants to give visible light absorption [32]. Nitrogen is easily inserted in the TiO_2 structure since it has a high stability, small ionization and its atomic size is similar to oxygen [33]. Other promising

non-metal dopants are carbon and sulphur [34,35]. Alternatively, the generation of oxygen rich TiO_2 has been reported to produce an increase in the Ti-O-Ti bond strength and an upward shift in the VB, achieving visible light absorption [36]. Doping with metals as chromium, cobalt, vanadium and iron has also been reported to improve the light absorption [12]. Dye sensitization has been considered as one of the most effective strategies to extend the spectral response into the visible region, benefiting from the knowledge of dye sensitized solar cells. Moreover, coupling TiO_2 with other semiconductors has also resulted in an improvement of the light absorption and a reduction of the recombination losses [37].

A commercially available TiO_2 product, Degussa (Evonik Aeroxide) P25, has been often used as a benchmark in research. It contains a combination of two phases, anatase and rutile, with proportions of around 80 % anatase and 20 % rutile. This configuration enhances the photoactivity since the rutile phase, it is reported to have, a less negative position of the conduction band, being able to act as electron sink for the photogenerated electrons of the anatase phase [12]. Alternatively, it is also reported the better photoactivity to be due to rutile extending light absorption into the visible region, charge separation and rutile small size crystallites which facilitates the electrons transfer between the anatase/rutile interface [38].

The overpotential for HER on TiO_2 is large so usually metal co-catalysts are added. Since the work function of noble metals is typically larger than TiO_2, the photogenerated electrons transfer from the semiconductor CB to the metal [31]. Pt is one of the most used co-catalysts for HER because of its work function being the largest among the noble metals. This results in a stronger electron trapping ability and a low activation energy for proton reduction [12,31]. Pt co-catalyst ability strongly depends in its particle size and loading [31]. Alternatively, the heterojunction of TiO_2 with NiO or Cu_2O have also been reported to improve the photocatalytic performance of TiO_2. Cu_2O is a p-type semiconductor with a narrow bandgap of 2.2 eV. Its junction with TiO_2 have been reported to form a p-n heterojunction, which helps the charge separation [39]. Moreover, the presence of Cu_2O is known to induce a narrowing of the band gap of TiO_2, thereby enhancing its light absorption [40]. NiO is also a p-type heterojunction that can form a p-n heterojunction with TiO_2, improving charge separation [41].

Cadmium sulphide (CdS) is a widely researched visible light photocatalyst. It has been investigated in diverse applications, such as hydrogen production, carbon dioxide reduction to hydrocarbons or pollutants degradation [16]. CdS is characterized by a narrow bandgap of 2.4 eV, which enables the absorption of light until 516 nm [16]. It exhibits good photochemical properties and quantum efficiency [42,43]. However, it suffers from photo-corrosion, since the photogenerated holes react with the sulphur ions oxidizing them to sulfur [44]. CdS low stability makes difficult its application in industry. Some of the strategies to improve CdS stability and inhibit photo-oxidation include the addition of surface protective layers, constructing heterojunctions and combining them with microporous and mesoporous materials [27,45].

Graphitic carbon nitride (g-C_3N_4) has received lot of attention as visible light photocatalyst, and it has been reported to be a promising photocatalyst for a diverse number of applications including H_2 production [46]. g-C_3N_4 is usually produced by thermal condensation of nitrogen-rich precursors. Its polymeric nature allows the modification of properties such as morphology, conductivity and electronic structure which modifies the bandgap energy and bandgap edges potential position [17]. However, some studies have found g-C_3N_4 to have a poor photocatalytic activity [47] or even to self-oxidize [48]. g-C_3N_4 photocatalytic activity and efficiency have been improved using several strategies. Heteroatom doping and copolymerization have been employed to modify the electronic band structure to enhance light absorption [49]. Moreover, the heterojunction with other semiconductors as CdS [50] or TiO_2 [51] have been reported to achieve an improved separation of the photogenerated charges [17].

2.2.3 Photocatalyst fabrication methods

The most used methods for the synthesis of photocatalyst are as follows:

- Hydrothermal method. This method is widely employed for the fabrication of semiconductor particles [52,53]. This technique involves the use of chemical precursors dissolved in aqueous or organic solvents placed into a sealed reactor and exposed to heat and pressure. As for example, the synthesis of WO_3 using Na_2WO_4 as precursor. The size, shape and crystal phase of the semiconductors can then be controlled by varying the synthesis conditions (i.e. temperature, pressure, type and concentration of the solution and duration of the treatment).

- Calcination method. In this procedure the precursors are subject to a thermal process, which bring a chemical or physical transformation, such as removal of volatile component, decomposition of compounds, phases transitions or crystallization [54].

- Chemical precipitation. This method consists in the formation of a solid insoluble compound from the reaction of soluble precursors. The synthesis is normally controlled through pH, temperature and concentration of reactants, an example is the synthesis of TiO_2 from $TiCl_3$ using NaOH and NH_4OH as precipitants[55].

- Sol-gel method. This procedure involves the transformation of a "sol" (colloidal suspension of solid particles in a liquid), into a gel-like material through a series of chemical reactions. This process entails four main reactions: hydrolysis, polycondensation, drying, and thermal decomposition [55]. An example of this method is the fabrication of TiO_2 from tertbutyl titanate.

Developments to improve photocatalysts performance include doping, metal deposition, dye sensitization and coupled semiconductors. Common techniques that have been widely employed for the deposition of metal or metal oxide nanoparticles are as follows:

- Impregnation consists in the exposure of the semiconductor photocatalyst in a solution containing the modifier catalyst and then dried [41].

- Photo-deposition is a method in which the semiconductor particles are placed in a solution containing the catalyst precursor, and subsequently illuminated. The light induces redox reactions that allow the deposition of particles on the semiconductor. For this deposition to happen, the oxidation/reduction potential of the metals to be deposited needs to be at favourable positions of the band gap of the semiconductor [56]. An example of this method is the photo-deposition of NiO using Ni_2SO_4 as electrolyte.

In recent years, alternative techniques have been reported for photocatalyst surface modification which could achieve high precision [57]. Some of these techniques are:

- Chemical vapour deposition (CVD) is a gas-phase method in which the semiconductor is placed in a reactor. Two precursors are then fed simultaneously, forming a coating through chemical reactions on the substrate. In this technique,

the variation of temperature, pressure, precursor concentration, gas flow rate, reaction time offer a control over thickness, composition, morphology and crystallinity [58].

- Atomic layer deposition (ALD) is a gas-phase method consisting in the consecutive exposure of the semiconductor to two gas precursors, alternated by a purge step with an inert gas. In this technique, one precursor at a time is introduced in the reactor chamber and reacts with the surface of the semiconductor, forming a monolayer (self-limiting process). The unreacted excess of the precursor is then removed with the purging step. The second precursor reacts with the previously deposited monolayer, leaving on the surface of the substrate the desired material. This technique is based on the self-limiting nature of the chemical reactions, which only react at the available active sites on the substrate surface. Once all the active sites are occupied, the reaction cease, independently of the excess on precursor dosing, enabling precise control over the coating size and uniformity. To ensure the self-limitation of the reactions, temperature, pressure, pulsing frequency of the reactants, and purging steps must be adjusted accordingly [57,59]. For the application of ALD to semiconductor particles, several types of reactors have been investigated: rotary reactors [60], vibration reactor [61], pulse-bed reactor [62], and the most used one being the fluidized bed reactor [57]. In the latter case, the fluidization of semiconductors when the particle size is smaller than 30 μm, including nanoparticles, has been reported to be challenging. In most cases there is increased cohesion due to van der Waals forces which provoke the agglomeration of the nanoparticles [57]. If agglomeration is excessive, it can have a detrimental effect in the fluidization, therefore, fluidization tools are usually needed as stirring, vibration or microjets [57].

2.2.4 Efficiency

The photocatalytic performance can be evaluated using quantum efficiency. The quantum efficiency or yield is defined as the useful photo-conversion events per absorbed photons at a determined wavelength. The useful events are usually calculated by the reaction rate. This is given in (2-3) where r is the reaction rate given in number of molecules converted per second, and Φ_{pa} is the flux of absorbed photons expressed as number of photons per second. However, it is challenging to determine the absorbed photons in the

semiconductor. Therefore, the external or apparent quantum efficiency, which is also referred as photonic yield, is usually used instead [63]. It can be defined as the useful events per incident photons in the system at a determined wavelength. This expression is given in (**2-4**), where r is the reaction rate given in number of molecules converted per second and Φ_{pi} is the flux of incident photons expressed as number of photons per second. The incident photons can be measured using radiometric or actinometric procedures. Moreover, the external quantum efficiency takes into account the efficiency of the overall process including the efficiency of the material absorbing photons as well as catalysing the reaction and the efficiency of the reactor design [63].

$$QE(\lambda) = \frac{r}{\Phi_{pa}} \tag{2-3}$$

$$EQE(\lambda) = \frac{r}{\Phi_{pi}} \tag{2-4}$$

If one is using a polychromatic irradiation source then the Formal Quantum Efficiency (FQE) should be reported, normally integrating the number of photons which can be utilised by the semiconductor in question. Of course, for many semiconductors the true solar efficiency will be very low due to only a small proportion of the solar spectrum being utilised.

Additionally, the performance of a photocatalytic hydrogen production process can also be evaluated using the solar-to-hydrogen conversion efficiency (η_{STH}), which relates chemical hydrogen energy produced to the solar energy. This expression is shown in (2-5), where Φ_{H_2} is the hydrogen rate in mol s^{-1} m^{-2}, $G^{\circ}_{H_2}$ the Gibbs free energy of hydrogen formation and P is the photon flux in mW cm^{-2} measured for a light source with a spectra equal to air mass global (AM) 1.5 [64].

$$\eta_{STH} = \left[\frac{\Phi_{H_2} \cdot G^{\circ}_{H_2}}{P}\right]_{AM\ 1.5G} \tag{2-5}$$

However, it is still challenging to compare between different photocatalytic efficiencies reported in literature due to the wide range of equipment and experimental conditions in the studies. Therefore, it is also helpful to include the comparison to a benchmark as e.g., P25.

2.3 Photoelectrochemical cells

2.3.1 Fundamentals

An approach to enhance the efficiency of photocatalysis is the use of electrochemically assisted photocatalysts in a photoelectrochemical (PEC) cell. In this configuration, the oxidation and reduction reactions are performed by two different electrode materials that are connected through an external circuit. The oxidation is driven by the holes in the (photo)anode, while the electrons travel from the photoanode through the external circuit to the (photo)cathode, where the reduction reaction takes place. This configuration helps to separate the photogenerated electron-hole pairs, reducing recombination. This process is schematically represented in Figure 2-4. When a photoelectrochemical cell is utilized to produce a fuel (e.g. hydrogen) from solar energy it can be referred as photosynthetic cell. Similarly, when the photoelectrochemical cell is employed to produce electricity from the photodegradation of substances, it can be defined as a photo-galvanic cell or photo fuel cell [65]. In systems where wastewater compounds are being oxidized in a PEC cell to generate H_2, depending on the thermodynamics of reaction, the system can also produce electricity and therefore being a combination of both cells; not clearly defined as one or the other. Moreover, a system without applied bias, where hydrogen is produced by a flow of current, could also be considered a photo-galvanic cell or photo-fuel cell.

Photoelectrochemical cells can be used with different configurations, i.e., semiconductor photoanode with metallic cathode, semiconductor photocathode with metallic anode, or photoanode with photocathode. These cells are driven by the potential difference between the Fermi levels of the two electrodes. For a typical n-type semiconductor photoanode, the Fermi level is close to the CB while for a typical p-type semiconductor photocathode the Fermi level is close to the VB [66]. If the photoelectrochemical cell uses a dark anode or cathode, these potentials are ideally dependent on the reaction oxidation and reduction reaction potentials, respectively. If the reaction oxidation and reduction potentials have the right positions with respect to the CB and VB, the cell produces electric power in open

circuit voltage as in a photo fuel cell. When this is not the case, an external voltage can be applied to drive the reactions.

With electrochemically assisted photocatalysis, an external electrical bias can be applied to assist the reactions. This may allow the use of semiconductors photoanodes with more positive CB potentials than the H^+/H_2 reaction and which would not drive HER purely photocatalytically.

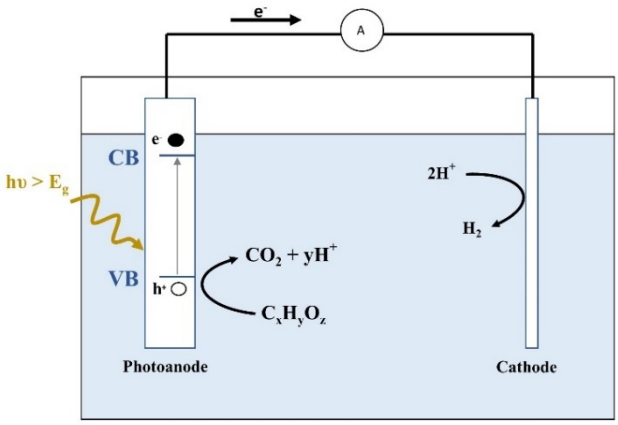

Figure 2-5. Schematic representation of a photoelectrochemical cell, containing a photoanode and a dark cathode, for the oxidation of a generic organic and H_2 production.

2. 3.2 Materials

Titanium dioxide is the most used photoanode material for H_2 production from wastewater compounds [67–70]. Other photoanode materials that have also been used for H_2 production are tungsten trioxide, bismuth vanadate and hematite [71–73]. Concerning the cathode material, platinum is widely used [67,68,74,75], while cuprous oxide is a common choice for photocathode [70].

2.3.2.1 Photoanodes

Titanium dioxide (TiO_2)

TiO_2, is the most used semiconductor material for photoanodes. Its properties and applications have been described in the previous section. When compared with other photoanodes semiconductor materials as tungsten trioxide, bismuth vanadate or hematite, titanium dioxide shows good charge transport properties and a very high hole diffusion length, which is in the order of 10^4 nm [71]. However, TiO_2 has one of the lowest

theoretical solar-to-hydrogen (STH) conversion efficiency just accounting for around 2.2 %, due to its excitation being limited to the UV region [72]. One of the strategies studied to improve activity and reduce recombination losses, is to synthesize one- or two-dimensional nanostructures which increases the specific surface area and decreases internal resistance. A very popular approach is the nano-engineering of TiO_2 to form either dispersed or aligned self-organised Titania nanotubes (TiNT) [76].

In 1999, Zwilling *et al*. reported the production of self-organized nanotube layers on Ti substrate by electrochemical anodization using chromic acid electrolytes containing fluorine ions. Since then, this method has been one of the most popular, due to its simplicity and operability. Through the adjustment of operation parameters, as applied potential, time, temperature, pH, and the composition of the electrolyte, it is possible to control the nanostructure size, shape and degree of order [77]. Several studies have made significant advancements in improving this method, and these developments are typically categorized into generations [77]. Currently, the most widely employed method falls under the third generation. In this process, polar organic electrolytes, primarily ethylene glycol, are combined with water and a fluoride ion source such as NH_4F.

Other used strategies to improve activity of TiO_2 include non-metal doping, co-catalyst deposition, dye sensitization and coupled semiconductors as explained previously [12].

Tungsten trioxide (WO_3)

WO_3 is a popular metal oxide semiconductor used as photoanodes, extensively researched applied to water splitting. WO_3 can form five different crystalline phases: monoclinic I (γ-WO_3), monoclinic II (ε-WO_3), triclinic (δ-WO_3), orthorhombic (β-WO_3) and tetragonal (α-WO_3). Monoclinic I (γ-WO_3) is the most used crystalline phase as photoanode, due to its higher stability and performance [71,78]. WO_3 has a bandgap of 2.5-2.8 eV, absorbing light in the visible range up to 500 nm which accounts for 12 % of the solar radiation on earth surface [73]. Its theoretical STH conversion efficiency is around 4.8% [71], and it has a modest hole diffusion length of around 150 nm [71]. Moreover, its conduction band is positioned at positive potentials of around +0.4 V vs. NHE [13], therefore a bias is necessary to drive the HER. A common strategy to enhance the performance of WO_3 is the engineering of the morphology to produce nanostructures. These nanostructures can provide higher surface area, providing more active sites for the reaction to take place, and shorter paths for the holes to diffuse compared to bulk structures, reducing electron-hole

recombination. Different WO_3 nanostructure fabrication methods have been reported, including the electrochemical anodization of tungsten foil, sol-gel, pulsed laser deposition, chemical vapour deposition and hydrothermal synthesis [71]. Among all the different methods, hydrothermal synthesis has been one of the most established, producing 1-D nanostructures, e.g., nanoneedles, nanowires, nanorods and nanotubes. The hydrothermally obtained WO_3 nanostructures have less grain boundaries and defects when compared to bulk structures, reducing recombination of electron-hole pairs [79]. Other hydrothermally synthesized WO_3 structures are, 2-D nanostructures, e.g., nanoplates, nanosheets and nanoflakes. Similarly, to the 1-D nanostructures, the 2-D have been reported to have more efficient and directional transfer of charges compared to the bulk material, but a higher surface/volume ration when compared to 1-D nanostructures, resulting in a further improved performance [80].

Other approaches to improve the activity of WO_3 include the enhancement of light absorption with anion doping as C [81] or N [82], defect engineering based on oxygen vacancies [83] or forming heterojunctions with other semiconductors as $WO_3/BiVO_4$ or WO_3/TiO_2 [83,84].

Bismuth vanadate ($BiVO_4$)

$BiVO_4$ is the most popular visible light absorption semiconductor used as photoanode, it attracted interest for water-splitting applications. $BiVO_4$ occurs in three polymorphs, from which monoclinic scheelite is the one being used as photoanode. It has a bandgap of 2.4 eV, a high theoretical STH conversion efficiency of 9.1% [72] and its conduction band potential is located slightly under than the HER potential [85]. However, it suffers from an extensive electron-hole recombination and a low charge mobility, consequently a bias is always necessary to obtain significant photocurrents [72]. In order to increase $BiVO_4$ carrier concentration doping with elements as Mo or W have been studied [86,87]. Other strategies to improve $BiVO_4$ activity include the loading of co-catalysts as Co-Pi [88] to decrease the bias potential and help the oxidation reaction or the heterojunction with other semiconductors as SnO_3 or WO_3 to have a more efficient electron-hole separation [89,90].

Hematite (α-Fe_2O_3)

α-Fe_2O_3 is considered a very promising metal oxide photoanode since it has a narrow bandgap of around 2 eV, allowing to absorb light beyond 600 nm [72]. Therefore, its maximum theoretical STH conversion efficiency is around 15% [15]. Moreover, α-Fe_2O_3 presents a good chemical stability, and it is inexpensive and abundant. Its conduction band is situated at positive potentials of around 0.4 V vs NHE [15], therefore, it is necessary to apply a bias to drive hydrogen production. Nevertheless, it has a very low hole diffusion length of around 2-4 nm and a low electron mobility both factors limit its performance [73]. Strategies to improve α-Fe_2O_3 conductivity and activity include, doping with elements as W, Mo and Nb [91–93], loading of co-catalysts as Co-Pi or $Ni(OH)_2$ [68,94] or surface passivation with Al_2O_3 [95].

2.3.2.2 Photocathodes

Contrary to the case of photoanodes, the choice of p-type materials for photocathodes is limited due to their low stability in contact with the electrolyte [96]. Some strategies to improve the performance of the photocathode include the use of protective layers that improve stability and the deposition of co-catalysts to enhance the reduction ability [97–99].

Cuprous oxide (Cu_2O), is a popular photocathode choice, it has a band gap of 2 eV and a theoretical STH conversion efficiency of 18% [98]. Its conduction band is well positioned for water reduction, around 0.7 V vs NHE more negative than hydrogen evolution potential [18]. However, Cu_2O reduction potentials are within its band gap, making it possible for Cu_2O to reduce to Cu, reducing its stability [100]. There are several research studies that had improved its stability adding protective layers as ZnO [97]. Moreover, co-catalysts as Pt had been added to enhance the reduction activity [98].

Copper based chalcogenide semiconductors have also been proposed as promising photocathodes for hydrogen production [101]. One of them is $CuIn_xGa_{1-x}Se_2$ (CIGS) which has a tuneable composition, with a band gap ranging from 1 eV to 1.7 eV and a large absorption coefficient [99]. Their activity has been enhanced adding protective layers and co-catalysts such as Pt [102]. However, CIGS include In and Ga which are scarce and expensive elements. Another type of chalcogenide photocathode is Cu_2ZnSnS_4 (CZTS), which has earth abundant elemental constituents, high absorption coefficient and

small band gap, however; it suffers from low long-term stability [103]. The research to improve its activity has also focused into surface modification, adding protecting layers as TiO_2 and co-catalysts as Pt [99].

2.3.2.3 Dark cathode electrocatalysts

The selection of a cathode for hydrogen evolution reaction benefits from extensive research in the electrochemistry field. HER involves the adsorption of a proton on the electrocatalyst surface and the desorption of hydrogen. For this reason, following Sabatier principle, the optimal catalytic activity will be achieved with a catalyst that achieves intermediate binding energy between the substrate and the catalyst [104]. The catalyst activity is as well dependent on the pH of the electrolyte, and in general, HER activities in alkaline electrolyte are lower than in acid. Consequently, the majority of the research is done in acid environment. For HER, the catalyst closer to the optimum intermediate binding energy is Pt. Platinum has generally the best performance as hydrogen production catalyst, it has a low overpotential and high reaction rates in acidic environment [74]. Pt foil and wires, together with Pt supported carbon are the most common cathodes used in the studies for H_2 production from driven photoelectrochemical oxidation of substances in wastewater.

Other catalysts with a good performance are Ru, Rh, Ir and Pd. However, all these noble metal catalysts, together with Pt, have a high cost and they are scarce, which makes challenging their large-scale application. Different approaches have been widely researched to find electrocatalysts with low cost and good performance. Two strategies that have been used to improve activity and reduce the cost of using noble metal catalysts are nanostructuring the catalyst to achieve a large surface to volume ratio, and forming alloys which reduce the catalyst loading [105,106].

Non-noble metal alloys have also been used for HER, Ni-based electrodes are preferred cathodes for hydrogen production in basic environment as Ni-Mo [106]. Transition metals chalcogenides as carbides and phosphides have also showed HER activity. Chalcogenides as MoS_2 showed activity for HER due to their sulphided Mo-edges with and overpotential close to Pt [107]. Similarly, WS_2 also demonstrates HER activity [108] as well as their seleneids forms $MoSe_2$ and WSe_2 [109]. Tungsten carbides such as WC and W_2C, exhibit promising potential as HER catalysts [110]. Phosphides as CoP and Ni_2P are among the most HER active non-noble electrocatalysts [111,112]. Alternatively, non-metals

electrocatalysts options have also been explored as heteroatom doped graphene nanosheets [112] or carbon nitride [113].

2.3.2.4 Photoelectrode fabrication methods

Photoelectrodes can be fabricated in a single-step method, in which both synthesis and immobilization on the conductive substrate occurs simultaneously. Alternatively, a two-step method can be employed, where the material is first synthesized and subsequently adhered to conductive substrate using an immobilization technique. In addition, after either of these methods, the electrodes are usually annealed to improve substrate adhesion or modify semiconductor properties.

Among the single-step fabrication methods, the most commonly reported are as follows:

- In situ hydrothermal synthesis. This method (previously explained in section 2.2.3 Photocatalyst fabrication methods) can also be used with the substrate being placed in the reactor, resulting on the semiconductor being directly formed onto the surface of the substrate [114].

- Electrochemical anodization. In this method the conductive substrate is used as anode, being immersed into a specific electrolyte together with a cathode. When a potential is applied oxide structures are produced on the surface of the conductive substrate [115].

- Physical vapour deposition (PVD). In this method, the semiconductor material is vaporized or sputtered in a vacuum chamber, with the vapor or particle being transported and condensed in a substrate [116].

- Methods as CVD and ALD (previously described in section 2.2.3 Photocatalyst fabrication methods), can be also employed to directly synthesize semiconductors onto the flat conductive substrate [117].

Some of the most used synthesis methods for particulate semiconductors include calcination, chemical precipitation, sol-gel, and hydrothermal, which have been described in section 2. These loose nanoparticles can then be immobilized in the conductive substrate, commonly used immobilization methods are as follows:

- Dip coating. In this method the substrate is immersed in a solution containing the semiconductor material at a controlled speed. As the substrate is withdrawn, a film of material has adhered to its surface forming a coating [118].

- Spin coating. In this technique the substrate is placed onto a spinning platform which rotates at high speeds. A liquid solution containing the semiconductor material, is dropped at the centre of the substrate, with the centrifugal force causing the liquid to spread outward, forming a thin and uniform layer [119].

- Doctor blading. In this process, a liquid solution containing the semiconductor material is applied onto a substrate using a flat-edge blade. The thickness of the obtained film is controlled by adjusting the gap between the blade and the substrate [120].

- Spray coating. In this technique, a liquid solution containing the semiconductor material is sprayed in the form of aerosol or fine mist using a nozzle or spray gun. The small droplets land in the substrate where they adhere forming a coating [40].

- Electrophoretic deposition. In this method, the semiconductor particles are placed in a liquid medium, referred to as electrolyte. The conductive substrate is also immersed into the electrolyte and used as working electrode, together with a counter electrode and reference electrode. When an electric field is applied, the charged particles migrate towards the conductive substrate and deposit on the surface [121].

2.3.3 Photoelectrochemical cell design

There are several design factors that influence the overall performance of photoelectrochemical cells. Among others, to produce hydrogen wastewater it is necessary to consider the irradiation configuration, and the use of separated compartments to avoid the need for gas separation following treatment.

Regarding the irradiation configuration of the photoelectrode, two main different orientations can be used: back-face irradiation or front-face irradiation. In front-face configuration, the light reaches semiconductor first, while for back-face irradiation, the light hits the conductive substrate before reaching the semiconductor, therefore the conductive substrate must be transparent. Most common substrates used are F-doped SnO_2 (FTO) and In-doped SnO_2 (ITO). These substrates have a relatively high conductivity when compared to the semiconductor and large spectral transmission. In addition to the consideration of the transparency of the conductive substrate, in the case of front-face irradiation, the light absorption will happen close to surface of the semiconductor. Since this process would occur near the semiconductor-liquid junction, the hole diffusion length does not need to be very long, however, the electrons created at the surface need to need to diffuse and reach the conductive substrate. In the case of back-face irradiation, the opposite would be required, short diffusion length for electrons to arrive to conductive substrate while holes need to diffuse through semiconductor, arriving to the surface to and participate in oxidation reactions. For wastewater application, back-face irradiation is preferred, avoiding optical interferences between the light and the wastewater components [122].

To produce high purity hydrogen (as required by chemical standards) coupled to the oxidation of wastewater compounds, the electrodes can be separated in two different compartments. Thus, separating the H_2 produced from other possible gases derived from the oxidation of wastewater compounds. The anolyte and catholyte compartments are often separated by ion-exchange membranes but other separators as glass frits have also been explored [123]. Most studies are performed using small volume (i.e. <100 mL) and one compartment reactors. Alternatively, in other studies, an H-type reactor is employed, where the anolyte and catholyte compartments are separated by a membrane [124,125]. In addition, it has also been proven the possibility of using a filter-press reactor operated in batch recirculation mode [126].

2.3.4 Efficiency

When evaluating the performance of photoelectrochemical cells, the external quantum efficiency is also referred as Incident Photon to Current Efficiency (IPCE), and the number of successful events can be evaluated by the photo-electrical current generated. This expression is given in (2-6), where λ is the wavelength of irradiation in nm, J is the photocurrent density given in mA cm^{-2}, P is the photon flux in mW cm^{-2} at a particular λ, h is Plank's constant and c is the speed of light in vacuum [66].

$$EQE(\lambda) = \text{IPCE}(\lambda) = \frac{\Phi_e}{\Phi_{pi}} = \frac{J \cdot hc}{\lambda \cdot P_\lambda} \tag{2-6}$$

Moreover, when evaluating the performance of photoelectrochemical cells, η_{STH} can also be determined from the photocurrent density generated. This expression is shown in (**2-7**) where J is the photocurrent density given in mA cm^{-2}, V is the required potential in V derived from Gibbs free energy, η_f is the HER faradaic efficiency and P is the light power in mW cm^{-2} measured with a light source with a spectrum equal to air mass global (AM) 1.5 [64]. It is important to note that J needs to be measured between the working and counter electrode in a 2 electrode PEC cell configuration. No bias potential should be applied in the evaluation of η_{STH}. Whenever a bias potential is applied between working and counter electrode to drive the reaction, the Applied Bias Photon to Current Conversion Efficiency (ABPE) can be derived, as shown in (**2-8**) [64]. In this expression V_{bias} is the applied voltage in V, which is subtracted from the required potential derived from Gibbs energy.

$$\eta_{STH} = \left[\frac{J \cdot V \cdot \eta_f}{P}\right]_{AM\ 1.5G} \tag{2-7}$$

$$ABPE = \left[\frac{J \cdot (V - V_{bias}) \cdot \eta_f}{P}\right]_{AM\ 1.5G} \tag{2-8}$$

For wastewater treatment applications, an UV source is commonly used as opposed to solar irradiation; therefore, the power coming from the sun should be replaced by the power of the UV source.

2.4 Wastewater treatment coupled to hydrogen production

Wastewater includes every water stream that has been polluted by human utilization, therefore, its chemical composition varies greatly depending on its origin. Domestic wastewater, which derives from urban areas, is generally rich in microorganism, organic materials, metals, and nutrients as phosphorous or nitrogen [127]. These effluents are usually treated at municipal wastewater treatment plants. On the contrary, industrial effluents are diverse, being originated by very different processes. Some industrial wastewaters have a similar chemical composition than domestic wastewater and can be treated in urban wastewater treatment plants, while other industrial effluents contain substances that need a specific and complex treatment process, as persistent organics, antibiotics or metals [128]. Finally, agricultural activities generate wastewater with a high content of nitrogen compounds, due to excessive use of fertilizers and intensive farming [129], although agricultural wastewater normally cannot be collected and treated.

These wastewaters, originated by human activities, need to be treated to avoid pollution and protect the ecosystems. Therefore, coupling the production of hydrogen with the removal of pollutants represents a promising option to recover energy from wastewater and at the same time managing the water pollution issue. This section describes the studies that produced hydrogen coupled to the degradation of wastewater compounds, including the materials used and the possible mechanisms.

Compounds are categorized into three groups. The first group comprises nitrogen compounds, which are the main of focus in this thesis. The second group, labelled as organic compounds, encompasses commonly studied compounds that have been linked to hydrogen production. These compounds include saccharides, phenolic compounds, alcohols, organic acids, and aldehydes. Lastly, the third category covers the generation of hydrogen from wastewater mixtures, as oil mill wastewater, juice production wastewater and sludge from wastewater treatment plants.

2.4.1 Nitrogen compounds

Ammonia and urea, along with nitrates and nitrites, contribute to nitrogen pollution. Nitrogen pollution of water has deleterious effects including eutrophication and toxicity to the organisms living in the water body. The hazardous concentration of nitrogen in wastewater originates from diverse sources, as intensive farming and excessive fertilizer

use [129]. Additionally, high nitrogen concentrations can also be found in either domestic and municipal sewage sludge and in wastewater from some industries [130]. Among the nitrogen compounds, both ammonia and urea exhibit significant hydrogen weight content (wt%). Ammonia contains 17.6% of hydrogen, while urea contains 6.7%. This substantial hydrogen content makes their oxidation and subsequent H_2 production an appealing process.

2.4.1.1 Ammonia

In water, un-ionized ammonia (NH_3) exists in pH dependent equilibrium with ionized ammonium (NH_4^+), having a pKa of 9.25, when the pH is lower than the pKa, NH_4^+ is the major form and when the pH is higher than the pKa is NH_3 the major form. Therefore, one of the research focuses has been to determine which of the forms would have a higher photocatalytic oxidation rate.

Several studies have revealed that ammonia in neutral form presents better oxidation rates compared to ionized ammonium [19,131,132]. Nemoto *et al*. investigated the pH effect in the photocatalytic ammonia oxidation, testing a pH range from 0.68 to 13.7 [19]. The study reports that the evolution of gaseous products (N_2 and H_2) increased between the pH 9 and 10 and peaked at pH around 11, due to higher oxidation rates with neutral ammonia. Zhu *et al*. reported how the oxidation rates obtained were proportional to the initial concentration of NH_3 and not the total content of NH_3 and NH_4^+ [131]. From this study, it was concluded that high oxidation rates are obtained when ammonia is in neutral form, even if better photocatalytic activity could be expected with positively ionized NH_4^+ and a negative photocatalyst surface charge, which occurs when the pH is higher than the photocatalyst point of zero charge and lower than the ammonium pKa. Wang *et al*. compared the photocatalytic activity in acidic, basic and neutral environment using g-C_3N_4 as photocatalyst and reported higher rate of photocatalytic ammonia oxidation in basic solutions [132].

Feng *et al*. studied the photocatalytic oxidation of ammonia using Cu loaded into TiO_2 [133]. The research reported N_2, NO_2^- and NO_3^- as products from the oxidation of NH_3, with hydroxyl radicals identified as the main oxidizing species. Additionally, the study proposed $O_2^{\bullet -}$ as the major oxidant influencing N_2 production, while h^+ was suggested to be responsible for the conversion of NH_3 to NO_3^-.

The most studied photocatalyst for ammonia oxidation has been TiO_2 [19,134–136], covering how the co-catalyst material affects the activity and product selectivity [19,134–136] and determining the possible reaction mechanism on H_2 production from ammonia decomposition [135]. Nemoto *et al*. compared the activity of TiO_2 loaded with RuO_2, Pt and both RuO_2 and Pt as co-catalysts for photocatalytic ammonia oxidation and hydrogen production [19]. The results showed that the N_2 gas produced was similar for all the co-catalysts; however, the H_2 production varied significantly. The photocatalyst loaded with Pt achieved the highest H_2 production and an external quantum yield of 5.1 % at 340 nm, while the system with both co-catalysts produced a small amount of H_2. The system loaded with RuO_2 did not produce any H_2, showing that RuO_2 cannot reduce protons to form hydrogen.

Altomare and Selli studied how the conversion and selectivity of ammonia oxidation to N_2 would be affected by the deposition of noble metals (Pt, Pd, Au and Ag) on the TiO_2 photocatalyst [134]. The experiments showed that all the metal-modified photocatalysts had better catalytic performance that the bare TiO_2, with the exception of Au/TiO_2. The loaded photocatalyst that showed higher ammonia removal was Ag/TiO_2 and the one that showed better selectivity towards N_2 was Pd/TiO_2. This latter study did not link the oxidation of ammonia to H_2 production.

Yuzawa *et al*. studied the mechanism of decomposition of ammonia to produce dinitrogen and hydrogen using TiO_2 photocatalyst loaded with Pt, Rh, Pd, Au, Ni and Cu [135]. Pt presented the best activity with high production rate of H_2 and N_2 and Cu the worse. The study concluded that the metal with larger work function would easily accept the photo-excited electrons to produce hydrogen. The mechanism proposed consisted in the predominant adsorption of ammonia to the Lewis acid site and some to the hydroxyl groups in TiO_2. The TiO_2 is irradiated generating holes and electrons, where the holes migrate to the surface and the electrons to the Pt site. The photogenerated holes oxidize the adsorbed NH_3 to form amide radicals and protons, while the amide radicals can produce hydrazine. The hydrazine could produce diazene that would be decomposed to form N_2 and H_2. The photogenerated electrons reduce the protons to form hydrogen in Pt [135]. This mechanism is represented in Figure 2-6.

Shiraishi *et al.* investigated the photocatalytic hydrogen production from ammonia using TiO_2 loaded with Au and Pt [136]. Pt-Au/TiO_2 showed a growth in hydrogen production

rate compared to Pt/TiO_2, suggesting that alloying Au to Pt resulted in a decrease of the Schottky barrier height at the interface between metal and TiO_2. The catalyst with the highest H_2 production rates consisted in a homogeneous mixture of 10 % mol of Au and 90 % mol of Pt loaded on TiO_2.

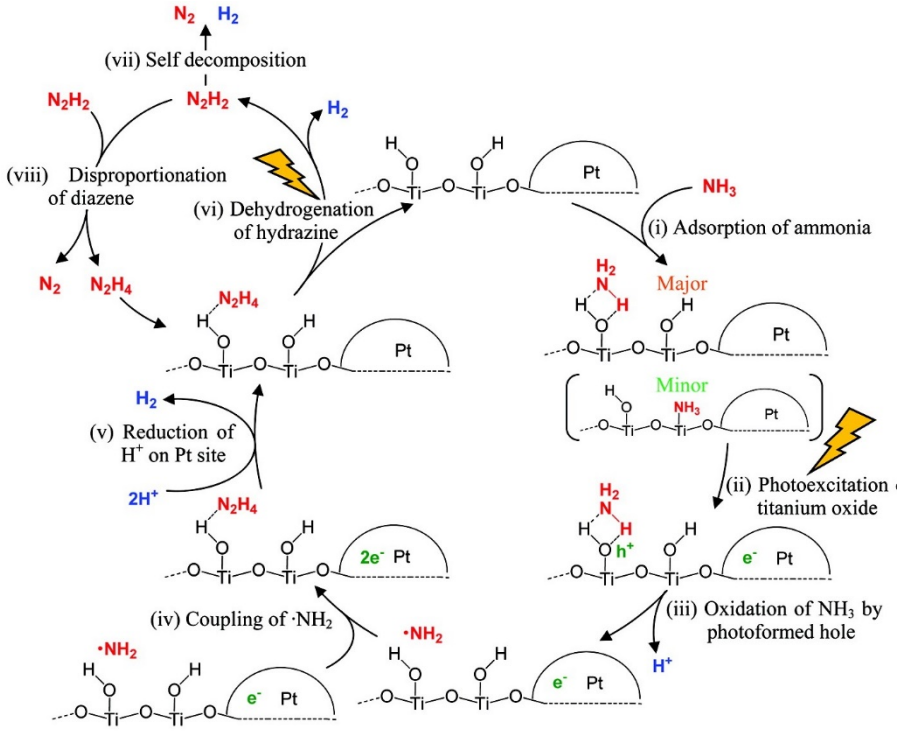

Figure 2-6. Suggested mechanism for photocatalytic ammonia degradation using Pt loaded on TiO_2. Figure reproduced from [135].

Photocatalytic ammonia oxidation has also been reported using metal free photocatalyst. Wang *et al*. used an atomic single layer g-C_3N_4 as photocatalyst, achieving an ammonia removal of 80% of the initial concentration [132]. Both hydroxyl radicals and photogenerated holes were suggested to be responsible for the ammonia oxidation; in this study ammonia oxidation was not coupled to H_2 production.

The number of research articles reported on ammonia oxidation using photoelectrochemical cells is much less than compared to photocatalysis [67,137]. Wang *et al*. used highly ordered TiO_2 nanotube arrays as a photoanode and Pt foil as cathode [137], reporting an ammonia removal of 99.9% under an applied bias of 1.0 V (not coupled to H_2 production). Kaneko *et al*. used nanoporous TiO_2 film as photoanode, formed by P25 deposited on FTO glass and a Pt foil as a cathode [67]. The experiments

showed a 150 μA cm^{-2} photocurrent and a production of 194 ml of H_2 and 63 ml of N_2 after 2 hours with no bias applied under a pH of 14.1.

2.4.1.2 Urea

Some studies have investigated the photocatalytic oxidation of urea using TiO_2 [138–140]. Pelizzetti *et al.* proposed a mechanism for the photocatalytic oxidation of urea using TiO_2, where one of the amino groups of urea undergoes an initial conversion to a nitroso group, followed by a transformation into a nitro group mediated by •OH radicals [138]. Afterwards, the nitroformamide undergoes hydrolysis, liberating NO_2^- ions, which are rapidly converted into NO_3^- by •OH [141]. The residual carbamic acid, existing as a zwitterion, can undergo two distinct oxidation pathways. One of the possible pathways involves the oxidation to CO_2 and NH_2OH by •OH radicals, subsequently, NH_2OH undergoes further oxidation by •OH to form NO_2^- and NO_3^-. The alternative pathway entails the simultaneous •OH and e^- attacks, decomposing the carbamic acid into HCO_3^- and NH_3. The molar ratio of NO_3^- to NH_4^+ serves as an indicator of the favoured reactions. This mechanism is shown in Figure 2-7. Previous studies on the photocatalytic degradation of urea using TiO_2 have reported NO_3^-/NH_4^+ ratios of 2 [139] and 1.9 [140].

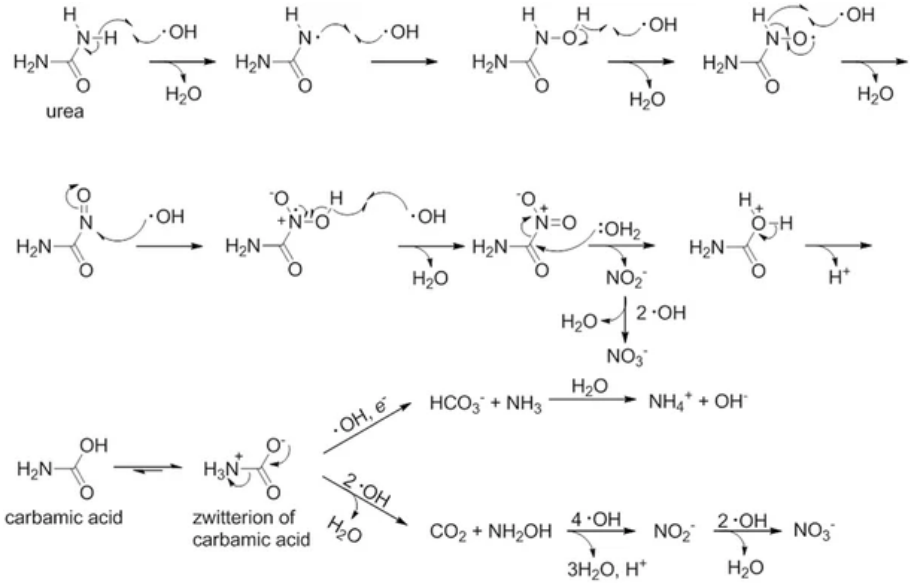

Figure 2-7. Proposed mechanism for photocatalytic oxidation of urea using TiO_2. Figure reproduced from [140].

Bahmani *et al*. reported the synthesis of a photocatalyst formed by UiO-66(Zr/Ti)–NF decorated with Fe_3O_4/WO_3 core-shell for the oxidation of urea [142]. The product analysis confirmed the production of NO_3^- and NH_4^+.

Kim *et al.* investigated the effect of dual surface photocatalyst modification in the production of hydrogen and oxidation of urea [20]. TiO_2 modified with both a noble metal, Pt, and an anion adsorbate [20]. The results showed that F-TiO_2/Pt achieved higher H_2 production rates than Pt/TiO_2, besides, F-TiO_2 did now show any H_2 production, highlighting the combined effect of surface anions and metal deposits to reduce charge recombination and improve electron transfer. Moreover, the effect of other anions as Cl^-, ClO^- and Br^- was studied, resulting in only F^- to have an enhancement effect, Cl^- and ClO^- had no effect and Br^- inhibited the hydrogen production. These results were explained by the surface complexation among acidic Ti(IV) sites and basic anions, which is dependent on the hardness of the anions, being only F^- the one that has higher hardness than OH^-. Furthermore, experiments with deuterated urea were performed, showing than H_2 production comes mainly from water molecules while urea acts as an electron donor.

Luo *et al*. reported the production of hydrogen coupled to oxidation of urea using CdS_xO NPs conjugated with sulphurous groups [143]. The study achieved an EQE of 2.4 % at 420 nm.

Wang *et al*. studied the feasibility of hydrogen production driven by urea or urine oxidation in a photoelectrochemical cell [68]. In this work, the suitability of two photoanodes was studied, TiO_2 nanowires and α-Fe_2O_3 nanowires, both loaded with $Ni(OH)_2$ as urea oxidation co-catalyst. Pt was used as counter electrode. The viability of solar driven urea oxidation with Ni/TiO_2 as photoanode was reported using an unbiased cell, producing a current density of 0.35 mA cm^{-2}. Moreover, the feasibility of using directly urine was also studied, resulting in comparable results to urea, highlighting the possibility of driving the production of hydrogen with the oxidation of urine. The effect of loading α-Fe_2O_3 with $Ni(OH)_2$ was studied, showing a negative shift in the onset potential of 400 mV, suggesting that $Ni(OH)_2$ is an efficient catalyst for urea oxidation. However, the use of α-Fe_2O_3 as photoanode required an external bias due to the low position of its conduction band. Xu *et al*. investigated as well the role of $Ni(OH)_2$ as a co-catalyst in the photoelectrochemical oxidation of urea, not coupled to the production of hydrogen [144], by using a photoanode formed by Ti-doped α-Fe_2O_3 and loaded with

$Ni(OH)_2$. The addition of $Ni(OH)_2$ reduced the onset potential by 100 mV and increased the photocurrent density by 4 times, showing the enhanced effect of the use of $Ni(OH)_2$ as urea oxidation co-catalyst.

Pop *et al*. focused their study on the comparison of the hydrogen production rates driven by oxidation of three nitrogen compounds found in wastewater: ammonia, urea and formamide [69]. The cell configuration combined a nanoparticulate TiO_2 photoanode and a mixture of carbon paste dispersing platinum nanoparticles as cathode in the same electrode. This configuration was unbiased and used under UV illumination. The detected hydrogen production after 4 hours was about 30, 140 and 240 μmol in presence of ammonia, formamide and urea, respectively. From these results, urea proved to be the best choice for photoelectrochemical hydrogen production. Additionally, a cell configuration with a separated photoanode and cathode, applying 0.5 V bias was also tested. The results from the two configurations were compared after 50 min, in which the biased configuration reported a H_2 production rate of 2.7 μmol min^{-1} while the unbiased configuration reported a rate of 1.4 μmol min^{-1}, highlighting the improved charge separation induced by the use of a bias.

Recently, some studies have reported the use of novel materials for the production of hydrogen in the presence of urea [145–147]. Bezboruah *et al*. reported the production of H_2 with urea present in the electrolyte [145], using Ni–TiO_2/p-NDIHBT photoanode and a Pt cathode. For this study, one compartment cell was used achieving a STH of 0.34 % with a 0.5 M KOH electrolyte. Tao *et al*. investigated the oxidation of urea coupled to H_2 production using La-Ni-based perovskites photoanode and a Pt cathode [146]. This study reported the use of a H-cell reactor and an electrolyte with 1 M KOH, generating 120 μmol cm^{-2} h^{-1}. In a different study, Tao *et al.* reported the production of hydrogen with a rate of 200 μmol h^{-1} using a Ni_2P clusters sensitized TiO_2 nanotube arrays photoanode and a Pt cathode [147]. This study identified NO_3^- and N_2 as products using an electrolyte containing 1 M KOH. However, in these studies, the performance of these materials was studied at alkaline pH (13-14) [145–147], which if applied to wastewater, it would involve an additional treatment step to modify the wastewater pH.

Table 2-1. Summary of the materials used in the photocatalytic oxidation of ammonia or urea and H_2 production.

Waste	Photocatalyst	Co-Catalyst	Maximum Efficiency (%)	pH	H_2 production	Reference
Ammonia	TiO_2	Cu	-	10	No	[133]
	TiO_2	-	-	2-10	No	[131]
	TiO_2	Pt or RuO_2	$EQE_{(340nm)}$ = 5.1	2-14	Yes	[19]
	TiO_2	Pt, Rh, Pd, Au, Ni or Cu	-	14	Yes	[135]
	TiO_2	Pt-Au	-	11	Yes	[136]
	g-C_3N_4	-	-	11	No	[132]
Urea	F-TiO_2	Pt	-	4-10	Yes	[20]
	CdS	-	$EQE_{(420nm)}$=2.4	7	Yes	[143]
	TiO_2	-	-	5	No	[138]
	TiO_2	-	-	6	No	[140]
	UiO-66(Zr)-NFs/Fe3O4@WO3	-	-	7	No	[142]

Table 2-2. Summary of the materials used in the H_2 production from degradation of ammonia or urea compounds using photoelectrochemical cells.

Waste	Photoanode	(Photo) Cathode	Maximum Efficiency (%)	pH	H_2 production	Reference
Ammonia	TiO_2	Pt	-	1-12	Yes	[67]
	TiO_2	Pt/C	-	13	Yes	[69]
Urea	$Ni(OH)_2$ loaded on TiO_2 or α-Fe_2O_3	Pt	-	14	Yes	[68]
	TiO_2	Pt/C	-	13	Yes	[69]
	Ni–TiO_2/p-NDIHBT NHs	Pt	STH= 0.34	14	Yes	[145]
	La-Ni-based perovskites	Pt	-	14	Yes	[146]
	Ni_2P/TiNT	Pt	-	14	Yes	[147]

2.4.2 Organic compounds

2.4.2.1 Saccharides

Different saccharides compounds can be found wastewater; among them, cellulose is commonly found in domestic wastewater and effluents from industries as the paper industry [148].

Kawai and Sakata demonstrated the feasibility of producing hydrogen from Saccharides $(C_6H_{12}O_6)_n$, as saccharose (n=2), starch (n ≈ 100) and cellulose (n ≈ 1000 to 5000), using a photocatalyst formed by $RuO_2/TiO_2/Pt$. A quantum yield of 1 % at 380 nm was reported for cellulose in 6 M NaOH [149]. Moreover, Kondarides *et al*. studied the hydrogen production from the photocatalytic reforming of several compounds including cellulose using an Pt/TiO_2 photocatalyst, proving the potential of cellulose for H_2 production [21]. Speltini *et al*. investigated the photocatalytic hydrogen production from cellulose using a Pt/TiO_2 photocatalyst [150]. The study showed higher H_2 production rates with neutral pH and reported a H_2 production of 54 μmol under UV-A irradiation. A degradation mechanism was also reported suggesting that cellulose depolymerizes and converts into glucose and other water-soluble products. Caravaca *et al*. researched the photocatalytic H_2 production from cellulose using different metals as co-catalysts loaded in TiO_2. The H_2 production was reported highest with Pd and lowest with Ni and Au, following the trend Pd > Pt > Ni ~ Au [151]. Even the H_2 production using Ni as co-catalyst was lower compared to the noble metals Pd and Pt, it was in the same magnitude, highlighting the possibility of using a no noble metal as co-catalyst. Moreover, the study suggested the possibility of the hydrolysis of cellulose taking place during photo-irradiation to produce glucose, which could follow different pathways to produce hydrogen.

The photoreforming of glucose, which is proposed to be an intermediate in the cellulose photoreforming process has been reported in several studies [21,22,152–154]. Kondarides *et al*. studied the hydrogen production from the photocatalytic reforming glucose using an Pt/TiO_2 photocatalyst, reporting an external quantum efficiency of 63 % at 365 nm [21]. Fu *et al.* studied the effect of different parameters as pH and co-catalyst material and proposed a mechanism for the hydrogen production from photocatalytic reforming of glucose using a metal loaded photocatalyst [22]. The study reported the effect of different co-catalysts loaded in TiO_2, showing all of them a better activity than the bare TiO_2; the best activity was obtained using Pd and Pt and the worse with Ru and Au, following the

trend Pd > Pt > Au ≈ Rh > Ag ≈ Ru. Moreover, the variation of pH over a wide range resulted in an increasing H_2 production rate with increasing pH, with a plateau region from pH 5 to 9 and maximum peak at pH 11. The p*K*a of glucose is around 12.3; therefore, higher rates of glucose oxidation are produced with glucose in its neutralform. In the proposed mechanism, the glucose is adsorbed preferentially in the uncoordinated Ti atoms through its hydroxyl group; it dissociates and then it is oxidized by a photogenerated hole. The radicals generated attack other glucose molecules, forming R-CHOH, which are deprotonated and further oxidized to $[R\text{-}COOH]^-$ by the radical •OH. Lastly, $[R\text{-}COOH]^-$ species are photo-oxidized by a hole to generate CO_2 via a photo-Kolbe reaction [22]. This mechanism is presented in Figure 2-8. Chong *et al.* investigated the glucose photoreforming mechanism using Rh/TiO_2 photocatalyst, reporting the production of arabinose, erythrose, glyceraldehyde, gluconic acid and formic acid (together with CO and CO_2 gas) [152]. In the suggested mechanism, glucose is oxidised into arabinose, then further oxidised into erythrose and ultimately into glyceraldehyde. These oxidation reactions take place through •OH radicals, which leads to the generation of formic acid and hydrogen. Subsequently, formic acid is converted into CO or CO_2. Imizcoz and Puga studied photocatalytic hydrogen production from glucose using TiO_2 loaded with different metals as Au, Ag, Pt and Cu [153]. The study reported a catalyst efficiency following the trend Pt>Au>Cu>Ag, without significative differences between Cu and Au, proposing Cu as an inexpensive co-catalyst for hydrogen production. Bahadori *et al.* researched the hydrogen production from glucose photoreforming using CuO or NiO loaded TiO_2 as photocatalyst [154]. The highest hydrogen production yield reported was 9.7 mol g_{cat}^{-1} h^{-1} using 1 wt% CuO on P25.

Other semiconductor materials as WO_3 and $\alpha\text{-}Fe_2O_3$ have also been studied using a photoelectrochemical cell for hydrogen production from photoreforming of glucose. Esposito *et al.* reported how a thin film WO_3 photoanode presented a good photocatalytic activity for H_2 production from glucose photoreforming using a tandem cell device [155]. Wang *et al.* investigated the possibility of using $Ni(OH)_2$ as co-catalyst for glucose oxidation (not coupled to H_2 production) in a photoelectrochemical cell, reporting an increased activity for $Ni(OH)_2$ loaded in $\alpha\text{-}Fe_2O_3$ [75].

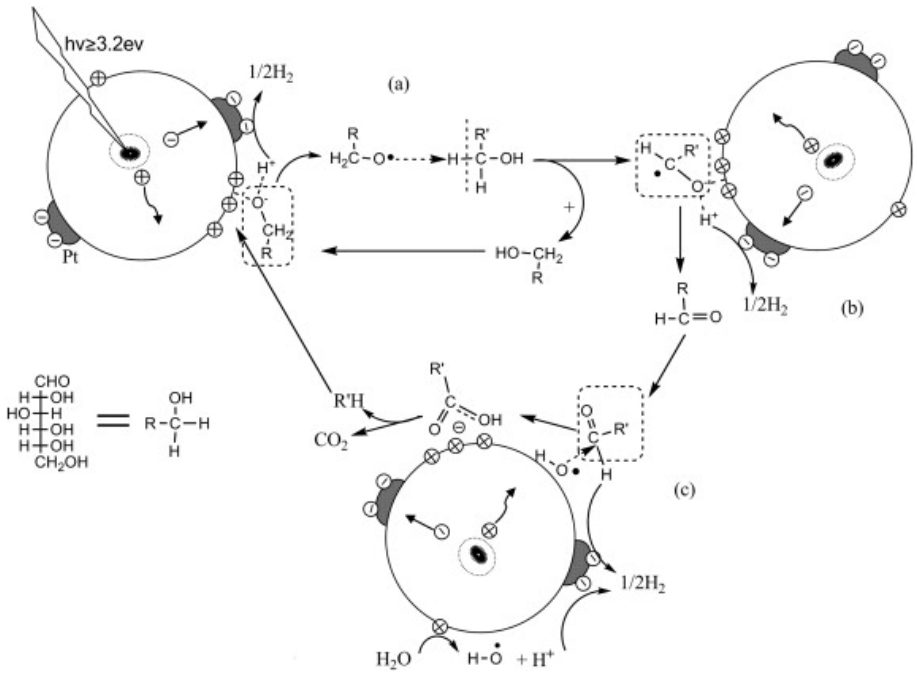

Figure 2-8. Proposed mechanism for photoreforming of glucose on Pt loaded TiO_2. Figure reproduced from [22].

2.4.2.2 Phenolic compounds

Phenolic compounds are found in significant quantities in wastewater from effluents of several industries as oil refining, petrochemicals, resin manufacturing and pulp, but also in agricultural and domestic wastewaters [128,156]. Phenolic compounds are considered toxic and its discharge without treatment produces harmful effects in the aquatic systems [157]. The photocatalytic degradation of phenolic compounds has been widely studied [158]. However, only few cases coupled the photocatalytic oxidation of phenolic compound to H_2 production [20,23,29,70,159–161], demonstrating the feasibility of this process.

Hashimoto *et al*. investigated the photocatalytic H_2 production in presence of different aliphatic and aromatic compounds with suspended Pt/TiO_2 [23], demonstrating the production of hydrogen in presence of phenol. Moreover, the study showed an increased rate of H_2 production in presence of phenol in alkaline conditions over acidic conditions. Languer *et al*. reported that the photocatalytic phenol degradation over TiO_2 nanotubes produced hydrogen at a rate of about 0.06 $\mu mol\ h^{-1}\ cm^{-2}$ [160]. Kim *et al*. demonstrated the feasibility of hydrogen production coupled to photocatalytic degradation of 4-chlorophenol [20]. The study involved the activity comparison of the following

photocatalysts: TiO_2/Pt, F-TiO_2/Pt and P-TiO_2/Pt. The highest H_2 production rate was obtained with F-TiO_2/Pt and the lowest with TiO_2/Pt. However, the good activity of F-TiO_2/Pt was limited to acidic region since the fluorides desorb at the alkaline region. P-TiO_2/Pt had higher H_2 production range than TiO_2 for all the pH range. Lv *et al*. used S doped two-dimensional g-C_3N_4 for the photocatalytic hydrogen production from phenol, achieving a H_2 production rate of 127.4 μmol/h and an external quantum efficiency of 8.35 % at 400 nm [29].

In photoelectrochemical cells, several photoanodes materials have been tested. Wu *et al*. studied the effect of the photoanode and photocathode materials on the voltage and current generated in the phenol degradation and hydrogen production [70]. Different photoanode and photocathode nanostructures, as nanorods (NRs), nanoparticles (NPs) and nanowires (NWAs) were tested from TiO_2, CdS, CdSe and Cu_2O. It was demonstrated that the open circuit voltage depends not only on the Fermi level between the photoelectrodes, but also on crystal facet for the same semiconductor materials with different microstructures. The best phenol removal efficiency was achieved with the combination of the photoanode TiO_2 NRs/FTO-C/Cu_2O and the photocathode C/Cu_2O NWAs/Cu. This combination reached a phenol removal rate of 84.2 % and an overall hydrogen production rate of 86.8 μmol cm^{-2} in 8 hours. Park *et al*. demonstrated the feasibility of hydrogen production driven by the photoelectrochemical degradation of phenol using improved multi-layered BiO_χ-TiO_2/Ti electrodes [159]. The electrodes were formed by an under layer of TaO_χ–IrO_χ, a middle layer of BiO_χ–SnO_2, and an upper layer of BiO_χ–TiO_2 which covered on both sides of Ti foil. The study showed that bismuth doping, even at high concentration, increased TiO_2 conductivity, while preserving the original photoelectrochemical properties. Li *et al.* studied the photoelectrocatalytic hydrogen production in presence of phenol using Bi/$BiVO_4$ as photoanode [161]. The study reported a hydrogen production rate of 27.8 μmol cm^{-2} h^{-1}.

2.4.2.3 Alcohols

Although alcohols are not expected to be abundant and common substances in municipal wastewater, they may be present in some industrial wastewater [162]. The production of H_2 from photocatalytic oxidation of alcohols has been extensively studied, mainly methanol, ethanol, and glycerol oxidation.

Kawai and Sakata demonstrated the feasibility of producing hydrogen by photoreforming of methanol [163]. The study reports the highest H_2 production rate Pt and an apparent quantum yield of 44 % at 380 nm with a photocatalyst formed by $RuO_2/TiO_2/Pt$. In the proposed reaction mechanism, methanol forms an intermediate, formaldehyde, which further oxidises to formic acid and finally decomposes to CO_2 and H_2. Chiarello *et al*. studied the effect of loading different noble metal co-catalysts to a TiO_2 photocatalyst in the photoreforming of methanol [164]. Among the investigated co-catalysts (Ag, Au and Pt), Pt showed the highest hydrogen production rate. Moreover, Naldoni *et al*. studied the difference between loading TiO_2 photocatalyst with Au or Pt, concluding that photogenerated electrons are more easily transferred to the Pt nanoparticles to reduce protons, than to Au [165]. Chen *et al*. studied the mechanism of the photocatalytic reaction of methanol for hydrogen production on Pt/TiO_2 [166]. The proposed mechanism (Figure 2-9) involves the formation of H_2 on Pt sites, in which the proton transfer to the Pt sites is mediated by the adsorbed water and methanol molecules. Most of the protons that form H_2 in the Pt sites come from water and not methanol. The study demonstrates that the surface species of CH_2O, CH_2OO and HCOO were formed. Moreover, an increase in Pt loading generated a decrease on methanol adsorption, which suggest that Pt atoms occupy sites for methanol adsorption [166]. Ismael studied the use of a Ru doped TiO_2 photocatalyst for the hydrogen production from methanol, reporting an enhancement on the activity due to the decrease in the band gap and a larger surface area. The highest activity was reported doping with of 0.1 % mol of Ru. In another study, Chen *et al.* reported the possibility of using a low cost photocatalyst formed by carbon coated Cu/TiO_2 ($C/Cu/TiO_2$) for hydrogen production from methanol [167]. This photocatalyst produced a H_2 yield of 269.1 μmol h^{-1} which is comparable to 290.8 μmol h^{-1}, the yield produced with Pt/TiO_2.

Liu *et al.* investigated the interaction between CuO_x-TiO_2 and its effect on the photocatalytic production of hydrogen from methanol [168]. The highest H_2 production was reported with CuO_x/TiO_2-{0 0 1}which has the highest Cu_2O dispersion and strongest interaction. Jiménez-Rangel *et al.* study the performance of g-C_3N_4/NiOOH/Ag as photocatalyst for the photoreforming of methanol, obtaining a maximum H_2 yield of 350.6 μmol/h. The hydrogen yield of the combined g-C_3N_4/NiOOH/Ag photocatalyst resulted significantly higher compared to the yield of g-C_3N_4, g-C_3N_4/NiOOH or g-C_3N_4/Ag alone [30]. Hojamberdiev *et al.* studied the use of a photocatalyst composed of

g-C_3N_4 $Ni(OH)_2$ and halloysite nanotubes for the production of hydrogen from methanol [169]. This photocatalyst presented a higher H_2 production rate (18.42 μmol h^{-1}) than g-C_3N_4/$Ni(OH)_2$ (9.12 μmol h^{-1}) or g-C_3N_4 (0.43 μmol h^{-1}). This enhancement was attributed to charge separation being the holes trapped by the halloysite nanotubes and the electrons transferred to $Ni(OH)_2$.

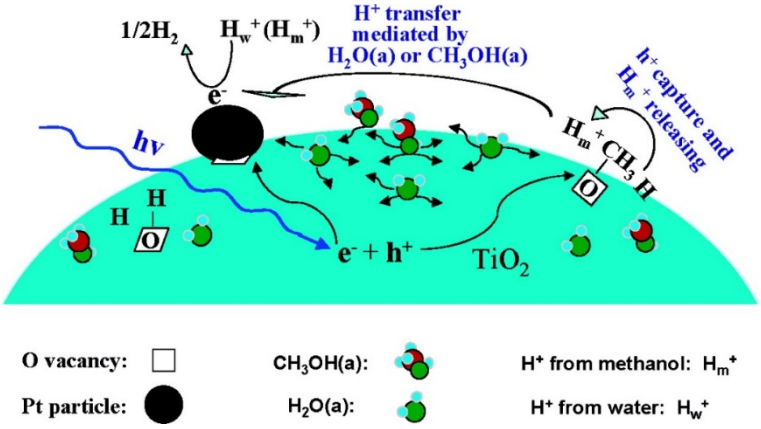

Figure 2-9. Proposed mechanism for the photoreforming of methanol on Pt loaded TiO_2. Figure reproduced from [166].

Ethanol has been extensively studied as a sacrificial agent for H_2 production [21,27,28,170–176]. Kawai and Sakata studied the photocatalytic production of hydrogen from ethanol [170]. The study reports the production of hydrogen, methane, and acetaldehyde. Moreover, different co-catalyst loaded in TiO_2 were studied as Ni, Pd, Pt and Rh, being Pt the one with the highest H_2 production rate and with a reported external quantum yield of 38 % at 380 nm. Kondarides *et al.* studied the hydrogen production from the photocatalytic reforming of ethanol with an Pt/TiO_2 photocatalyst, reporting an external quantum efficiency of 50 % at 365 nm [21]. Yang *et al.* researched the photocatalytic production of hydrogen from ethanol using metal loaded TiO_2 as photocatalyst and compared it to the H_2 production from other alcohols [171]. Pt and Pd presented higher H_2 production rates than Rh. Moreover, it was suggested that the hydrogen production over Pt/TiO_2 is governed by the solvation of the alcohol, following the H_2 production the following trend: methanol ≈ ethanol > propanol ≈ Isopropanol > n-butanol. Sola *et al.* investigated the effect of the morphology and structure of Pt/TiO_2 photocatalysts on the hydrogen production from ethanol [172]. The study showed an improved performance for the Pt/TiO_2 photocatalysts with higher surface area and lower pore size. The best performing photocatalyst was found to be Pt/TiO_2 with an average

pore size of 29.1 nm and a surface area of 51 m^2 g^{-1}, reporting an apparent quantum yield of 5.14%. Acetic acid, 2-3 butanediol and acetaldehyde were the main products in the liquid phase, finding a higher concentration of 2-3 butanediol with lower pore size. Puga *et al*. studied the hydrogen production from photocatalytic ethanol oxidation over Au/TiO_2, obtaining as main products acetaldehyde in the liquid phase and H_2 in the gas phase with a volumetric proportion of 99%, while the other gaseous product detected were CH_4, C_2H_4, C_2H_6, CO and CO_2 [173].

Deas *et al.* used Au loaded on TiO_2 nanoflowers as photocatalyst for hydrogen production from ethanol, reporting a hydrogen production rate of 24.3 mmol g^{-1} h^{-1}, compared to only 12.1 mmol g^{-1} h^{-1} obtained with Au/P25 [174]. This enhancement was ascribed to the thin and crystalline anatase sheets of the nanoflower petals which reduce the bulk recombination. Pajares *et al*. investigated the use of WC as TiO_2 co-catalyst for the photocatalytic hydrogen production from ethanol, reporting an enhancement of 40% the H_2 yield compared to P25 [175]. Zhang *et al.* investigated the effect of Ti^{3+} defects of Au/TiO_2 on the hydrogen production from ethanol [176]. The study reported an increased activity with higher defects, concluding that oxygen vacancies on TiO_2 rich in defects, facilitates the adsorption of ethanol and hole transfer. Ryu *et al*. studied the photoreforming of ethanol using CdS attached on microporous and mesoporous silicas as photocatalyst. The study suggests that the photoactivity was dependent on the silica cavity size, which partially controls the CdS particle size [27]. Cebada *et al.* studied the use of Ni/CdS as photocatalyst for the hydrogen production from ethanol, proving that higher Ni content resulted in increased hydrogen production [28].

Antoniadou *et al*. studied the hydrogen production from ethanol using a photoelectrochemical cell chemically biased [177]. The cell had two compartments, with a TiO_2 photoanode in an acidic electrolyte compartment and a Pt cathode in alkaline electrolyte compartment. The study reported an IPCE of 96 % at 360 nm and proved that the photoreforming of ethanol is more efficient than photocatalytic water splitting. Adamopoulos *et al*. investigated the effect of adding a top layer of TiO_2 to a WO_3 photoanode in the hydrogen production from ethanol using a biased photoelectrochemical cell [178]. Carbon black loaded on carbon paper was used as cathode. Increased current density and hydrogen production were reported when using the TiO_2/WO_3 bilayer photoanode; this improvement was ascribed to the lower number of recombination sites.

H_2 production from photoreforming of glycerol has also been widely studied [21,179–184]. Kondarides *et al*. studied the hydrogen production from the photocatalytic reforming of glycerol, reporting an external quantum efficiency higher than 70 % at 365 nm with a Pt/TiO_2 photocatalyst and 1 M of glycerol [21]. Fu *et al*. studied the mechanism of photoreforming polyols as glycerol using a Pt/TiO_2 photocatalyst, proposing that just the H atoms connected to hydroxyl C atoms can form H_2 while the C atoms are oxidized to CO_2 [179]. For non-OH bonded C atoms, the bond H and C atoms form products in the form of alkanes as CH_4 or C_2H_6. Bowker *et al*. investigated the photocatalytic reforming of glycerol using Pd and Au modified TiO_2 and proposed a possible mechanism [180]. Hydrogen production rate from Pd was four times larger than the one of Au. The mechanism suggests that H_2 is produced through the dissociation of adsorbed glycerol molecules with the associated production of CO, when using Pd/TiO_2. Subsequently, the CO reacts with oxygen radical at the metal surface to produce CO_2 freeing sites. Montini *et al*. studied the hydrogen production from glycerol using Cu/TiO_2 photocatalyst [181]. Hydrogen and carbon dioxide were the main products in gas phase, and 1,3-dihydroxypropanone and hydroxyacetaldehyde in liquid phase. Moreover, Chen *et al.* reported a quantum efficiency of 24.9% at 365 nm and hydrogen production rate of 17.6 mmol g^{-1} h^{-1} from glycerol using Cu/TiO_2 as photocatalyst [182]. Daskalaki and Kondarides studied the hydrogen production from photoreforming of glycerol over Pt/TiO_2, reporting H_2 and CO_2 as the only products in gas phase and methanol and acetic acid as intermediates in liquid phase [183]. Naffati *et al.* reported a hydrogen production rate of 2091 μmol g^{-1} from glycerol using a photocatalyst consisting of TiO_2 loaded with Pt and carbon nanotubes (CNT) [184].

Hydrogen production from glycerol has been also demonstrated using photoelectrochemical cells using a TiO_2 photoanode [185], or a TiO_2 photoanode functionalized with CdS [186].

2.4.2.4 Organic acids and aldehydes

Other compounds that can be part of the organic waste contained in wastewater are organic acids and aldehydes [187,188]. Patsoura *et al*. studied the hydrogen production and simultaneous degradation of formic acid, acetic acid and acetaldehyde over a Pt/TiO_2 photocatalyst [189]. The study reported a hydrogen production after 20 hours of 183.2 μmol from acetic acid and 72.5 μmol from acetaldehyde.

Li *et al*. researched the photocatalytic hydrogen production in presence of oxalic acid, formic acid and formaldehyde using a Pt/TiO_2 photocatalyst [24]. The study reported that the photocatalytic activity of these electron donors follows the trend of oxalic acid > formic acid > formaldehyde which agrees with the order of adsorption affinity of these electron donors on TiO_2.

Imizcoz and Puga investigated the photoreforming of acetic acid using Cu/TiO_2 as photocatalyst [190]. Hydrogen production from acetic acid was enhanced by including a photoreduction step to control the oxidation stage of Cu. On the contrary, when Cu was used directly, its passivation resulted in a high decarboxylation, producing mainly CH_4 instead of H_2.

All the materials used in the reviewed works for H_2 production by photocatalytic and photoelectrochemical oxidation of organic compounds are summarize in 2-3 and Table 2-4.

Table 2-3. Summary of the materials used in the H_2 production from photocatalytic degradation of organic compounds, with the reported external quantum efficiency (EQE) or formal quantum efficiency (FQE).

Waste	Photocatalyst	Co-Catalyst	Maximum Efficiency (%)	Reference
Cellulose	RuO_2/TiO_2	Pt	$EQE_{(380\ nm)} = 1$	[149]
	TiO_2	Pt	-	[21]
	TiO_2	Pt	-	[150]
	TiO_2	Pd, Pt, Ni or Au	-	[151]
Glucose	TiO_2	Pt	$EQE_{(365\ nm)} = 63$	[21]
	TiO_2	Pd, Pt, Au, Rh, Ag or Ru	-	[22]
	TiO_2	Rh	-	[152]
	TiO_2	Pt, Au, Ag or Cu	-	[153]
	TiO_2	CuO	-	[154]
Phenol	TiO_2	Pt	-	[23]
	TiO_2	-	-	[160]
	S-g-C_3N_4	-	$EQE_{(400\ nm)}$= 8.35	[29]
4-chlorophenol	F-TiO_2 or P-TiO_2	Pt	-	[20]

Methanol	TiO_2/RuO_2	Pt or Pd	$EQE_{(380\ nm)} = 44$	[163]
	TiO_2	Ag, Au or Pt	-	[164]
	TiO_2	Au or Pt	FQE = 14	[165]
	Ru- TiO_2	Pt	-	[168]
	TiO_2	Pt	$EQE_{(355\ nm)} = 2.9$	[166]
	TiO_2/C	Cu/C	-	[167]
	g-C_3N_4	NiOOH/Ag	-	[30]
	g-C_3N_4	Ni(OH)2/ $Al_2Si_2O_5(OH)_4$	-	[169]
Ethanol	TiO_2	Pt	$EQE_{(365\ nm)} = 50$	[21]
	TiO_2	Ni, Pd, Pt or Rh	$EQE_{(380\ nm)} = 38$	[170]
	TiO_2	Pt, Pd or Rh	FQE = 10	[171]
	TiO_2	Pt	EQE= 5.14	[172]
	TiO_2	Au	-	[174]
	TiO_2	Au	-	[176]
	TiO_2	WC	-	[175]
	CdS	-	-	[27]
	CdS	Ni	-	[28]
Glycerol	TiO_2	Pt	$EQE_{(365\ nm)} = 70$	[21]
	TiO_2	Pt	-	[179]
	TiO_2	Pd or Au	-	[180]
	TiO_2	Cu	-	[181]
	TiO_2	Cu	$EQE_{(365nm)}$=24.9	[182]
	TiO_2	Pt	-	[183]
	TiO_2	CNT-Pt	-	[184]
Formic acid	TiO_2	Pt	-	[189]
	TiO_2	Pt	-	[24]
Acetic acid	TiO_2	Pt	-	[189]
	TiO_2	Cu	-	[190]
Oxalic acid	TiO_2	Pt	-	[24]
Acetaldehyde	TiO_2	Pt	-	[189]
Formaldehyde	TiO_2	Pt	-	[24]

Table 2-4. Summary of the materials used in the H_2 production from degradation of organic compounds using photoelectrochemical cells with the reported external quantum efficiency (EQE) or incident photon-to-current efficiency (IPCE).

Waste	Photoanode	(Photo)Cathode	Maximum Efficiency (%)	Reference
Formamide	TiO_2	Pt/C	-	[69]
Glucose	WO_3	WC	$EQE_{(600\ nm)}$ = *80*	[155]
	$Ni(OH)_2$ loaded on α-Fe_2O_3	Pt	-	[75]
Phenol	TiO_2 NRs, TiO_2 NTs/Ti, CdS and CdSe	C/Cu_2O/Cu and Cu_2O	$IPCE_{(380\ nm)}$ = 68	[70]
	BiO_χ-TiO_2/Ti	SS	-	[159]
	Bi/$BiVO_4$	Pt	-	[161]
Ethanol	TiO_2	Pt	$IPCE_{(360nm)}$ = 96	[177]
	TiO_2/WO_3	Carbon black	-	[178]
Glycerol	TiO_2	Pt	-	[185]
	TiO_2/ CdS	Pt	-	[186]

2.4.3 Wastewater mixtures

The feasibility of photocatalytic H_2 production from wastewater mixtures such as olive mill wastewater, juice production wastewater and waste activated sludge has been demonstrated [25,26,153,191].

Olive mill wastewater (OMW) contains a high load of organics varying from 40 to 220 g L^{-1} [192]. The main components found on this wastewater are oil, grease, polyphenols and sugars [191]. Badawy *et al*. studied the photocatalytic degradation of OMW with simultaneous hydrogen production using nanostructured mesoporous TiO_2 as photocatalyst [25]. TiO_2 loading and pH were the main factors affecting the photocatalytic degradation and H_2 production in this study. The maximum hydrogen production was 38 mmol after 2 hours at a pH of 3 and a photocatalyst concentration of 2 g L^{-1}. The organic pollutants contained in OMW enhanced the H_2 production, by scavenging holes and decreasing the electron hole recombination. Speltini *et al*. investigated the effects of factors as photocatalyst concentration, pH and OMW concentration in H_2 production, using Pt/TiO_2 as photocatalyst and UV-A irradiation [191]. The study reports an apparent quantum yield of 5.5 10^{-3} at 366 nm and the production of 44 µmol of H_2 after 4 hours of UV-A irradiation, using a photocatalyst concentration of 2 g L^{-1}, OMW concentration of

3.35 v/v, and a pH of 3. Moreover, the H_2 yield produced by OMW was compared to glucose, which have been considered a good sacrificial donor for H_2 production, and similar production rates were obtained.

Imizcoz and Puga demonstrated the feasibility of photocatalytic hydrogen production using wastewater from a juice production industry, which contains high amounts of saccharides [153]. The study reported a H_2 yield of 115 mol g_{cat}^{-1} h^{-1} using Au/TiO_2 as photocatalyst.

The simultaneous H_2 production and degradation of waste activated sludge from wastewater treatment processes was investigated by Liu *et al.*, using Ag/TiO_2 as photocatalyst, proving the possibility of this process [26]. The review articles for the photocatalytic production of H_2 from wastewater mixtures are summarized in Table 2-5.

Table 2-5. Summary of the materials used in the H_2 production from wastewater mixtures.

Waste	Photocatalyst	Co-Catalyst	Maximum Efficiency (%)	Reference
OMW	TiO_2	-	-	[25]
		Pt	$EQE_{(366\ nm)}$ = 0.5	[191]
Juice industry wastewater	TiO_2	Au	-	[153]
Sludge	TiO_2	Ag	-	[26]

2.5 Photocatalysis and Photoelectrocatalysis Research at Ulster

The research presented in this thesis also builds up on the knowledge and expertise developed over many years at Ulster University concerning photocatalysis and photoelectrocatalysis, particularly applied to water and wastewater treatment.

In 1995, one of the first works on the photocatalytic treatment of drinking water was presented at the World Environmental Congress and Second International Conference on Advanced Oxidation Technologies for Water and Air Treatment, London, Ontario, Canada. Some of the early works by Byrne *et al.* included the use of P25 for the

degradation of humic acid [193], the use of immobilized TiO_2 powder for water treatment [121], and the use of a photoelectrochemical cell to couple the oxidation of organic pollutants to the recovery of metals from wastewater [194]. Coleman *et al.* studied the use of TiO_2 for the photocatalytic degradation of 17-β-oestradiol [195], steroid estrogens [196] and 17α-ethynyloestradiol with TiO_2 [197]. Dunlop *et al.* investigated the use of TiO_2 photoanodes for the inactivation of *Clostridium perfringens* spores [198] and *E. coli* K12 [199], as well as the use of different commercial immobilized TiO_2 powders for the degradation of phenol and formic acid [200]. McMurray *et al.* examined the use of immobilized TiO_2 for the photocatalytic oxidation for oxalic and formic acid [201] and atrazine [202], as well as the oxidation of formic acid using photoelectrochemistry [203].

Alrousan *et al.* studied the use of immobilised TiO_2 on the inactivation of *E. coli* in surface water [204]. Sunnotel *et al.* investigated the photocatalytic inactivation of *Cryptosporidium parvum* using TiO_2 film deposited by electrophoresis on to ITO glass [205]. Wadhwa *et al*. studied the effect of post-annealing titania nanotubes that were hydrothermally synthesized [206]. Dale *et al.* studied the use of titania nanotubes in photoelectrocatalysis [207] and the effect of surface roughness and applied potential [208]. More recent works continued expanding the knowledge on the use of titania nanotubes for photoelectrocatalytic water treatment and disinfection. Studies include the application of titania nanotubes for rainwater disinfection [209], the investigation of the radicals produced [210] and the performance of nitrogen doped nanotubes [32].

Alternatively, other works have also explored the performance of other materials as WO_3, g-C_3N_4 and $BiVO_4$ for photocatalytic water disinfection [47,211]. In addition, the modification of P25 and titania nanotubes with Cu_2O was also explored applied to the photocatalytic and photoelectrocatalytic reduction of CO_2 [40,212].

The expertise over the years in photocatalysis and photoelectrocatalysis applied to water treatment has also occasioned the publication of highly cited reviews by Byrne and collaborators [12,213–215] and book chapters [216–218].

2.6 Conclusions

This literature review has described the potential of treating wastewater using photocatalysis and photoelectrochemistry, as well, as the possibility to couple it with energy recovery as hydrogen production. The production of hydrogen from pollutants and

wastes can be energetically more favourable than the production of hydrogen from water splitting.

Using suspensions of photocatalytic particles has been the most common approach to date, while only a limited number of works have adopted the use of photoelectrochemical cells represent a promising option since this configuration reduces the recombination losses within the system. Most studies for hydrogen production coupled to the oxidation of wastewater has been performed using organic compounds as saccharides, phenolic compounds, alcohols, or organic acids, with the higher number reported being alcohols, however they are not a major component in most wastewater. Therefore, more studies with common wastewater compounds are needed.

Additionally, nitrogen compounds which are common constituents of domestic and municipal sewage sludge, are one of the interesting targets to couple to hydrogen production. Specially, urea and ammonia since they exhibit significant hydrogen weight content, with more investigation needed using PEC cells, visible light materials and analysis of the by-products formed.

Comparing the performance from the different published works is extremely challenging. Hydrogen production rates, when given, are measured under very different operating conditions and the quantum efficiencies are usually not reported. Therefore, following a systematic procedure in reporting photocatalytic performance would be beneficial for the evaluation of the different compounds. Nevertheless, hydrogen production linked to the treatment of pollutants in wastewater is an exciting area for research and may have true potential for scale up in niche applications.

References

[1] J.-M. Herrmann, C. Guillard, P. Pichat, Heterogeneous photocatalysis: an emerging technology for water treatment, Catal. Today. 17 (1993) 7–20. https://doi.org/10.1016/0920-5861(93)80003-J.

[2] D. Bahnemann, Photocatalytic water treatment: Solar energy applications, Sol. Energy. 77 (2004) 445–459. https://doi.org/10.1016/j.solener.2004.03.031.

[3] U.I. Gaya, A.H. Abdullah, Heterogeneous photocatalytic degradation of organic contaminants over titanium dioxide: A review of fundamentals, progress and problems, J. Photochem. Photobiol. C Photochem. Rev. 9 (2008) 1–12. https://doi.org/10.1016/j.jphotochemrev.2007.12.003.

[4] S. Malato, P. Fernández-Ibáñez, M.I. Maldonado, J. Blanco, W. Gernjak, Decontamination and disinfection of water by solar photocatalysis: Recent overview and trends, Catal. Today. 147 (2009) 1–59. https://doi.org/10.1016/j.cattod.2009.06.018.

[5] M. Ni, M.K.H. Leung, D.Y.C. Leung, K. Sumathy, A review and recent developments in photocatalytic water-splitting using TiO_2 for hydrogen production, Renew. Sustain. Energy Rev. 11 (2007) 401–425. https://doi.org/10.1016/j.rser.2005.01.009.

[6] S.J.A. Moniz, S.A. Shevlin, D.J. Martin, Z.-X. Guo, J. Tang, Visible-light driven heterojunction photocatalysts for water splitting – a critical review, Energy Environ. Sci. 8 (2015) 731–759. https://doi.org/10.1039/C4EE03271C.

[7] A.A. Ismail, D.W. Bahnemann, Photochemical splitting of water for hydrogen production by photocatalysis: A review, Sol. Energy Mater. Sol. Cells. 128 (2014) 85–101. https://doi.org/10.1016/j.solmat.2014.04.037.

[8] K. Maeda, Photocatalytic water splitting using semiconductor particles: History and recent developments, J. Photochem. Photobiol. C Photochem. Rev. 12 (2011) 237–268. https://doi.org/10.1016/j.jphotochemrev.2011.07.001.

[9] E.S. Domalski, E.D. Hearing, Heat Capacities and Entropies of Organic Compounds in the Condensed Phase Volume II, J. Phys. Chem. Ref. Data. 19 (1990) 881–1047. https://doi.org/10.1063/1.555876.

[10] R. Overstreet, W.F. Giauque, Ammonia. The Heat Capacity and Vapor Pressure of Solid and Liquid. Heat of Vaporization. The Entropy Values from Thermal and Spectroscopic Data, J. Am. Chem. Soc. 59 (1937) 254–259. https://doi.org/10.1021/ja01281a008.

[11] R. Li, C. Li, Chapter One - Photocatalytic Water Splitting on Semiconductor-Based Photocatalysts, in: C.B.T.-A. in C. Song (Ed.), Academic Press, 2017: pp. 1–57. https://doi.org/10.1016/bs.acat.2017.09.001.

[12] M. Pelaez, N.T. Nolan, S.C. Pillai, M.K. Seery, P. Falaras, A.G. Kontos, P.S.M. Dunlop, J.W.J. Hamilton, J.A. Byrne, K. O'Shea, M.H. Entezari, D.D. Dionysiou, A review on the visible light active titanium dioxide photocatalysts for environmental applications, Appl. Catal. B Environ. 125 (2012) 331–349. https://doi.org/10.1016/j.apcatb.2012.05.036.

[13] G.R. Bamwenda, H. Arakawa, The visible light induced photocatalytic activity of tungsten trioxide powders, Appl. Catal. A Gen. 210 (2001) 181–191. https://doi.org/10.1016/S0926-860X(00)00796-1.

[14] J.K. Cooper, S. Gul, F.M. Toma, L. Chen, P.A. Glans, J. Guo, J.W. Ager, J. Yano, I.D. Sharp, Electronic structure of monoclinic $BiVO_4$, Chem. Mater. 26 (2014) 5365–5373. https://doi.org/10.1021/cm5025074.

[15] A.G. Tamirat, J. Rick, A.A. Dubale, W.-N. Su, B.-J. Hwang, Using hematite for photoelectrochemical water splitting: a review of current progress and challenges, Nanoscale Horizons. 1 (2016) 243–267. https://doi.org/10.1039/C5NH00098J.

[16] L. Cheng, Q. Xiang, Y. Liao, H. Zhang, CdS-Based photocatalysts, Energy Environ. Sci. 11 (2018) 1362–1391. https://doi.org/10.1039/c7ee03640j.

[17] W.-J. Ong, L.-L. Tan, Y.H. Ng, S.-T. Yong, S.-P. Chai, Graphitic Carbon Nitride ($g\text{-}C_3N_4$)-Based Photocatalysts for Artificial Photosynthesis and Environmental Remediation: Are We a Step Closer To Achieving Sustainability?, Chem. Rev. 116 (2016) 7159–7329. https://doi.org/10.1021/acs.chemrev.6b00075.

[18] P.E. de Jongh, D. Vanmaekelbergh, J.J. Kelly, Photoelectrochemistry of Electrodeposited Cu2O, 147 (2000) 486–489.

[19] J. Nemoto, N. Gokan, H. Ueno, M. Kaneko, Photodecomposition of ammonia to dinitrogen and dihydrogen on platinized TiO_2 nanoparticules in an aqueous solution, J. Photochem. Photobiol. A Chem. 185 (2007) 295–300. https://doi.org/10.1016/j.jphotochem.2006.06.024.

[20] J. Kim, D. Monllor-Satoca, W. Choi, Simultaneous production of hydrogen with the degradation of organic pollutants using TiO_2 photocatalyst modified with dual surface components, Energy Environ. Sci. 5 (2012) 7647–7656. https://doi.org/10.1039/c2ee21310a.

[21] D.I. Kondarides, V.M. Daskalaki, A. Patsoura, X.E. Verykios, Hydrogen production by photo-induced reforming of biomass components and derivatives at ambient conditions, Catal. Letters. 122 (2008) 26–32. https://doi.org/10.1007/s10562-007-9330-3.

[22] X. Fu, J. Long, X. Wang, D.Y.C. Leung, Z. Ding, L. Wu, Z. Zhang, Z. Li, X. Fu, Photocatalytic reforming of biomass: A systematic study of hydrogen evolution from glucose solution, Int. J. Hydrogen Energy. 33 (2008) 6484–6491. https://doi.org/10.1016/j.ijhydene.2008.07.068.

[23] K. Hashimoto, T. Kawai, T. Sakata, Photocatalytic reactions of hydrocarbons and fossil fuels with water. Hydrogen production and oxidation, J. Phys. Chem. 88 (1984) 4083–4088. https://doi.org/10.1021/j150662a046.

[24] Y. Li, G. Lu, S. Li, Photocatalytic production of hydrogen in single component and mixture systems of electron donors and monitoring adsorption of donors by in situ infrared spectroscopy, Chemosphere. 52 (2003) 843–850. https://doi.org/10.1016/S0045-6535(03)00297-2.

[25] M.I. Badawy, M.Y. Ghaly, M.E.M. Ali, Photocatalytic hydrogen production over nanostructured mesoporous titania from olive mill wastewater, Desalination. 267 (2011) 250–255. https://doi.org/10.1016/j.desal.2010.09.035.

[26] C. Liu, Z. Lei, Y. Yang, Z. Zhang, Preliminary trial on degradation of waste activated sludge and simultaneous hydrogen production in a newly-developed solar photocatalytic reactor with Ag_X/TiO_2-coated glass tubes, Water Res. 47 (2013) 4986–4992. https://doi.org/10.1016/j.watres.2013.05.040.

[27] S.Y. Ryu, W. Balcerski, T.K. Lee, M.R. Hoffmann, Photocatalytic Production of Hydrogen from Water with Visible Light Using Hybrid Catalysts of CdS Attached to Microporous and Mesoporous Silicas, J. Phys. Chem. C. 111 (2007) 18195–18203. https://doi.org/10.1021/jp074860e.

[28] S. Cebada, E. Soto, N. Mota, J.L. Garcı, R.M. Navarro, ScienceDirect Effect of photodeposition conditions on Ni e CdS photocatalysts and its role in the photoactivity for H_2 production from ethanolic solutions, (2020). https://doi.org/10.1016/j.ijhydene.2020.01.169.

[29] H. Lv, Y. Huang, R.T. Koodali, G. Liu, Y. Zeng, Q. Meng, M. Yuan, Synthesis of Sulfur-Doped 2D Graphitic Carbon Nitride Nanosheets for Efficient Photocatalytic Degradation of Phenol and Hydrogen Evolution, ACS Appl. Mater. Interfaces. 12 (2020) 12656–12667. https://doi.org/10.1021/acsami.9b19057.

[30] K. Jiménez-rangel, J.E. Samaniego-benítez, L. Lartundo-rojas, H.A. Calderón, A. Mantilla, Ternary g-C_3N_4/NiOOH/Ag nanocomposite photocatalyst with efficient charges separation and high activity for H_2 production, Fuel. 280 (2020) 118672. https://doi.org/10.1016/j.fuel.2020.118672.

[31] Y. Ma, X. Wang, Y. Jia, X. Chen, H. Han, C. Li, Titanium dioxide-based nanomaterials for photocatalytic fuel generations, Chem. Rev. 114 (2014) 9987–10043. https://doi.org/10.1021/cr500008u.

[32] T. Morikawa, R. Asahi, T. Ohwaki, K. Aoki, Y. Taga, Band-Gap Narrowing of Titanium Dioxide by Nitrogen Doping, Jpn. J. Appl. Phys. 40 (2001) L561–L563. https://doi.org/10.1143/jjap.40.l561.

[33] L.G. Devi, R. Kavitha, A review on non metal ion doped titania for the photocatalytic degradation of organic pollutants under UV/solar light: Role of photogenerated charge carrier dynamics in enhancing the activity, Appl. Catal. B Environ. 140–141 (2013) 559–587. https://doi.org/10.1016/j.apcatb.2013.04.035.

[34] S. Sakthivel, H. Kisch, Daylight Photocatalysis by Carbon-Modified Titanium Dioxide, Angew. Chemie - Int. Ed. 42 (2003) 4908–4911. https://doi.org/10.1002/anie.200351577.

[35] T. Umebayashi, T. Yamaki, H. Itoh, K. Asai, Band gap narrowing of titanium dioxide by sulfur doping, Appl. Phys. Lett. 81 (2002) 454–456. https://doi.org/10.1063/1.1493647.

[36] V. Etacheri, M.K. Seery, S.J. Hinder, S.C. Pillai, Oxygen rich titania: A dopant free, high temperature stable, and visible-light active anatase photocatalyst, Adv. Funct. Mater. 21 (2011) 3744–3752. https://doi.org/10.1002/adfm.201100301.

[37] J. Zhu, M. Zäch, Nanostructured materials for photocatalytic hydrogen production, Curr. Opin. Colloid Interface Sci. 14 (2009) 260–269. https://doi.org/10.1016/j.cocis.2009.05.003.

[38] D.C. Hurum, A.G. Agrios, K.A. Gray, T. Rajh, M.C. Thurnauer, Explaining the Enhanced Photocatalytic Activity of Degussa P25 Mixed-Phase TiO2 Using EPR, J. Phys. Chem. B. 107 (2003) 4545–4549. https://doi.org/10.1021/jp0273934.

[39] S. Lettieri, M. Pavone, A. Fioravanti, L. Santamaria Amato, P. Maddalena, Charge Carrier Processes and Optical Properties in TiO_2 and TiO_2-Based Heterojunction Photocatalysts: A Review, Materials (Basel). 14 (2021). https://doi.org/10.3390/ma14071645.

[40] P.K. Sharma, M.A.L.R.M. Cortes, J.W.J. Hamilton, Y. Han, J.A. Byrne, M. Nolan, Surface modification of TiO_2 with copper clusters for band gap narrowing, Catal. Today. 321–322 (2019) 9–17. https://doi.org/10.1016/j.cattod.2017.12.002.

[41] C.-J. Chen, C.-H. Liao, K.-C. Hsu, Y.-T. Wu, J.C.S. Wu, P–N junction mechanism on improved NiO/TiO_2 photocatalyst, Catal. Commun. 12 (2011) 1307–1310. https://doi.org/10.1016/j.catcom.2011.05.009.

[42] X. Li, T. Xia, C. Xu, J. Murowchick, X. Chen, Synthesis and photoactivity of nanostructured CdS–TiO_2 composite catalysts, Catal. Today. 225 (2014) 64–73. https://doi.org/10.1016/j.cattod.2013.10.086.

[43] J. Yang, H. Yan, X. Wang, F. Wen, Z. Wang, D. Fan, J. Shi, C. Li, Roles of cocatalysts in Pt–PdS/CdS with exceptionally high quantum efficiency for photocatalytic hydrogen production, J. Catal. 290 (2012) 151–157. https://doi.org/10.1016/j.jcat.2012.03.008.

[44] Y. Tang, X. Hu, C. Liu, Perfect inhibition of CdS photocorrosion by graphene sheltering engineering on TiO_2 nanotube array for highly stable photocatalytic activity, Phys. Chem. Chem. Phys. 16 (2014) 25321–25329. https://doi.org/10.1039/C4CP04057K.

[45] A. Wu, C. Tian, Y. Jiao, Q. Yan, G. Yang, H. Fu, Sequential two-step hydrothermal growth of MoS_2/CdS core-shell heterojunctions for efficient visible light-driven photocatalytic H_2 evolution, Appl. Catal. B Environ. 203 (2017) 955–963. https://doi.org/10.1016/j.apcatb.2016.11.009.

[46] G. Dong, Y. Zhang, Q. Pan, J. Qiu, A fantastic graphitic carbon nitride (g-C_3N_4) material: Electronic structure, photocatalytic and photoelectronic properties, J. Photochem. Photobiol. C Photochem. Rev. 20 (2014) 33–50. https://doi.org/10.1016/j.jphotochemrev.2014.04.002.

[47] A.K. Singhal, An Evaluation of g-C_3N_4 and $BiVO_4$ for Photocatalytic Water Treatment and Disinfection, 2021.

[48] F.R. Pomilla, M.A.L.R.M. Cortes, J.W.J. Hamilton, R. Molinari, G. Barbieri, G. Marcì, L. Palmisano, P.K. Sharma, A. Brown, J.A. Byrne, An Investigation into the Stability of Graphitic C_3N_4 as a Photocatalyst for CO2 Reduction, J. Phys. Chem. C. 122 (2018) 28727–28738. https://doi.org/10.1021/acs.jpcc.8b09237.

[49] S. Cao, J. Yu, G-C_3N_4-based photocatalysts for hydrogen generation, J. Phys. Chem. Lett. 5 (2014) 2101–2107. https://doi.org/10.1021/jz500546b.

[50] L. Ge, F. Zuo, J. Liu, Q. Ma, C. Wang, D. Sun, L. Bartels, P. Feng, Synthesis and efficient visible light photocatalytic hydrogen evolution of Polymeric g-C_3N_4 coupled with CdS quantum dots, J. Phys. Chem. C. 116 (2012) 13708–13714. https://doi.org/10.1021/jp3041692.

[51] J. Wang, J. Huang, H. Xie, A. Qu, Synthesis of g-C_3N_4/TiO_2 with enhanced photocatalytic activity for H2 evolution by a simple method, Int. J. Hydrogen Energy. 39 (2014) 6354–6363. https://doi.org/10.1016/j.ijhydene.2014.02.020.

[52] A. Mishra, A. Mehta, S. Basu, N.P. Shetti, K.R. Reddy, T.M. Aminabhavi, Graphitic carbon nitride (g–C_3N_4)–based metal-free photocatalysts for water splitting: A review, Carbon N. Y. 149 (2019) 693–721. https://doi.org/10.1016/j.carbon.2019.04.104.

[53] M.C. Hidalgo, M. Aguilar, M. Maicu, J.A. Navío, G. Colón, Hydrothermal preparation of highly photoactive TiO_2 nanoparticles, Catal. Today. 129 (2007) 50–58. https://doi.org/10.1016/j.cattod.2007.06.053.

[54] Y. Meng, G. Xin, D. Chen, A facile pyrolysis method for g–C_3N_4 synthesizing: photocatalytic degradation of methylene blue under visible light, Optoelectron. Adv. Mater. Commun. 5 (2011) 648–650.

[55] C. Burda, X. Chen, R. Narayanan, M.A. El-Sayed, Chemistry and Properties of Nanocrystals of Different Shapes, Chem. Rev. 105 (2005) 1025–1102. https://doi.org/10.1021/cr030063a.

[56] K. Wenderich, G. Mul, Methods, Mechanism, and Applications of Photodeposition in Photocatalysis: A Review, Chem. Rev. 116 (2016) 14587–14619. https://doi.org/10.1021/acs.chemrev.6b00327.

[57] J.R. van Ommen, A. Goulas, Atomic layer deposition on particulate materials, Mater. Today Chem. 14 (2019) 100183. https://doi.org/10.1016/j.mtchem.2019.08.002.

[58] X. Zhao, C. Wei, Z. Gai, S. Yu, X. Ren, Chemical vapor deposition and its application in surface modification of nanoparticles, Chem. Pap. 74 (2020) 767–778. https://doi.org/10.1007/s11696-019-00963-y.

[59] J. Guo, D. Benz, T.-T.D. Nguyen, P.-H. Nguyen, T.-L.T. Le, H.-H. Nguyen, D. La Zara, B. Liang, H.T.B. Hintzen, J.R. van Ommen, Tuning the photocatalytic activity of TiO_2 nanoparticles by ultrathin SiO_2 films grown by low-temperature atmospheric pressure atomic layer deposition, Appl. Surf. Sci. 530 (2020) 147244.

[60] J.A. McCormick, B.L. Cloutier, A.W. Weimer, S.M. George, Rotary reactor for atomic layer deposition on large quantities of nanoparticles, J. Vac. Sci. Technol. A. 25 (2007) 67–74. https://doi.org/10.1116/1.2393299.

[61] S.W. Park, J. Woo Kim, H. Jong Choi, J. Hyung Shim, Vibration atomic layer deposition for conformal nanoparticle coating, J. Vac. Sci. Technol. A. 32 (2013) 01A115. https://doi.org/10.1116/1.4845735.

[62] X. Liang, L.F. Hakim, G.-D. Zhan, J.A. McCormick, S.M. George, A.W. Weimer, J.A. Spencer II, K.J. Buechler, J. Blackson, C.J. Wood, J.R. Dorgan, Novel Processing to

Produce Polymer/Ceramic Nanocomposites by Atomic Layer Deposition, J. Am. Ceram. Soc. 90 (2007) 57–63. https://doi.org/10.1111/j.1551-2916.2006.01359.x.

[63] J. Marugán, R. van Grieken, A.E. Cassano, O.M. Alfano, Photocatalytic Reactor Design, in: Photocatal. Fundam. Perspect., The Royal Society of Chemistry, 2016: pp. 367–387. https://doi.org/10.1039/9781782622338-00367.

[64] S. Giménez, J. Bisquert, Photoelectrochemical solar fuel production, Springer, Switzerland, 2016. https://doi.org/10.1007/978-3-319-29641-8.

[65] P. Lianos, Review of recent trends in photoelectrocatalytic conversion of solar energy to electricity and hydrogen, Appl. Catal. B Environ. 210 (2017) 235–254. https://doi.org/10.1016/j.apcatb.2017.03.067.

[66] R. van de Krol, M. Grätzel, Photoelectrochemical Hydrogen Production, Vol. 90, Springer, New York, 2012. https://doi.org/10.1007/978-1-4614-1380-6.

[67] M. Kaneko, N. Gokan, N. Katakura, Y. Takei, M. Hoshino, Artificial photochemical nitrogen cycle to produce nitrogen and hydrogen from ammonia by platinized TiO_2 and its application to a photofuel cell, Chem. Commun. (2005) 1625–1627. https://doi.org/10.1039/b418580c.

[68] G. Wang, Y. Ling, X. Lu, H. Wang, F. Qian, Y. Tong, Y. Li, Solar driven hydrogen releasing from urea and human urine, Energy Environ. Sci. 5 (2012) 8215–8219. https://doi.org/10.1039/c2ee22087c.

[69] L.C. Pop, I. Tantis, P. Lianos, Photoelectrocatalytic hydrogen production using nitrogen containing water soluble wastes, Int. J. Hydrogen Energy. 40 (2015) 8304–8310. https://doi.org/10.1016/j.ijhydene.2015.04.116.

[70] Z. Wu, G. Zhao, Y. Zhang, J. Liu, Y.N. Zhang, H. Shi, A solar-driven photocatalytic fuel cell with dual photoelectrode for simultaneous wastewater treatment and hydrogen production, J. Mater. Chem. A. 3 (2015) 3416–3424. https://doi.org/10.1039/c4ta06604a.

[71] X. Liu, F. Wang, Q. Wang, Nanostructure-based WO_3 photoanodes for photoelectrochemical water splitting, Phys. Chem. Chem. Phys. 14 (2012) 7894–7911. https://doi.org/10.1039/c2cp40976c.

[72] Z. Li, W. Luo, M. Zhang, J. Feng, Z. Zou, Photoelectrochemical cells for solar hydrogen production: current state of promising photoelectrodes, methods to improve their properties, and outlook, Energy Environ. Sci. 6 (2013) 347–370. https://doi.org/10.1039/c2ee22618a.

[73] J. Gan, X. Lu, Y. Tong, Towards highly efficient photoanodes: Boosting sunlight-driven semiconductor nanomaterials for water oxidation, Nanoscale. 6 (2014) 7142–7164. https://doi.org/10.1039/c4nr01181c.

[74] P.C.K. Vesborg, B. Seger, I. Chorkendorff, Recent development in hydrogen evolution reaction catalysts and their practical implementation, J. Phys. Chem. Lett. 6 (2015) 951–957. https://doi.org/10.1021/acs.jpclett.5b00306.

[75] G. Wang, Y. Ling, X. Lu, T. Zhai, F. Qian, Y. Tong, Y. Li, A mechanistic study into the catalytic effect of $Ni(OH)_2$ on hematite for photoelectrochemical water oxidation, Nanoscale. 5 (2013) 4129–4133. https://doi.org/10.1039/c3nr00569k.

[76] I. Paramasivam, H. Jha, N. Liu, P. Schmuki, A review of photocatalysis using self-organized TiO_2 nanotubes and other ordered oxide nanostructures, Small. 8 (2012) 3073–3103. https://doi.org/10.1002/smll.201200564.

[77] Y. Fu, A. Mo, A Review on the Electrochemically Self-organized Titania Nanotube Arrays: Synthesis, Modifications, and Biomedical Applications, Nanoscale Res. Lett. 13 (2018) 187. https://doi.org/10.1186/s11671-018-2597-z.

[78] S. Pokhrel, J. Birkenstock, A. Dianat, J. Zimmermann, M. Schowalter, A. Rosenauer, L.C. Ciacchi, L. Mädler, In situ high temperature X-ray diffraction, transmission electron microscopy and theoretical modeling for the formation of WO_3 crystallites, CrystEngComm. 17 (2015) 6985–6998. https://doi.org/10.1039/C5CE00526D.

[79] G. Zheng, J. Wang, H. Liu, V. Murugadoss, G. Zu, H. Che, C. Lai, H. Li, T. Ding, G. Qiang, Guo Zhanhu, Tungsten oxide nanostructures and nanocomposites for photoelectrochemical water splitting, Nanoscalenoscale. 18968 (2019) 18968–18994. https://doi.org/10.1039/c9nr03474a.

[80] X. Liu, F. Wang, Q. Wang, Nanostructure-based WO_3 photoanodes for photoelectrochemical water splitting, Phys. Chem. Chem. Phys. 14 (2012) 7894–7911. https://doi.org/10.1039/C2CP40976C.

[81] Y. Sun, C.J. Murphy, K.R. Reyes-Gil, E.A. Reyes-Garcia, J.M. Thornton, N.A. Morris, D. Raftery, Photoelectrochemical and structural characterization of carbon-doped WO_3 films prepared via spray pyrolysis, Int. J. Hydrogen Energy. 34 (2009) 8476–8484. https://doi.org/10.1016/j.ijhydene.2009.08.015.

[82] B. Cole, B. Marsen, E. Miller, Y. Yan, B. To, K. Jones, M. Al-Jassim, Evaluation of Nitrogen Doping of Tungsten Oxide for Photoelectrochemical Water Splitting, J. Phys. Chem. C. 112 (2008) 5213–5220. https://doi.org/10.1021/jp077624c.

[83] M.G. Peleyeju, E.L. Viljoen, WO_3-based catalysts for photocatalytic and photoelectrocatalytic removal of organic pollutants from water – A review, J. Water Process Eng. 40 (2021) 101930. https://doi.org/10.1016/j.jwpe.2021.101930.

[84] J. Su, L. Guo, N. Bao, C.A. Grimes, Nanostructured WO_3/$BiVO_4$ Heterojunction Films for Efficient Photoelectrochemical Water Splitting, Nano Lett. 11 (2011) 1928–1933. https://doi.org/10.1021/nl2000743.

[85] A. Walsh, Y. Yan, M.N. Huda, M.M. Al-Jassim, S.H. Wei, Band edge electronic structure of $BiVO_4$: Elucidating the role of the Bi s and V d orbitals, Chem. Mater. 21 (2009) 547–551. https://doi.org/10.1021/cm802894z.

[86] W. Luo, Z. Yang, Z. Li, J. Zhang, J. Liu, Z. Zhao, Z. Wang, S. Yan, T. Yu, Z. Zou, Solar hydrogen generation from seawater with a modified $BiVO_4$ photoanode, Energy Environ. Sci. 4 (2011) 4046–4051. https://doi.org/10.1039/C1EE01812D.

[87] M. Li, L. Zhao, L. Guo, Preparation and photoelectrochemical study of $BiVO_4$ thin films deposited by ultrasonic spray pyrolysis, Int. J. Hydrogen Energy. 35 (2010) 7127–7133. https://doi.org/10.1016/j.ijhydene.2010.02.026.

[88] F.F. Abdi, R. van de Krol, Nature and Light Dependence of Bulk Recombination in Co-Pi-Catalyzed $BiVO_4$ Photoanodes, J. Phys. Chem. C. 116 (2012) 9398–9404. https://doi.org/10.1021/jp3007552.

[89] P. Chatchai, Y. Murakami, S. Kishioka, A.Y. Nosaka, Y. Nosaka, Efficient photocatalytic activity of water oxidation over $WO_3/BiVO_4$ composite under visible light irradiation, Electrochim. Acta. 54 (2009) 1147–1152. https://doi.org/10.1016/j.electacta.2008.08.058.

[90] P. Chatchai, Y. Murakami, S. -y. Kishioka, A.Y. Nosaka, Y. Nosaka, $FTO/SnO_2/BiVO_4$ Composite Photoelectrode for Water Oxidation under Visible Light Irradiation, Electrochem. Solid-State Lett. 11 (2008) H160. https://doi.org/10.1149/1.2906109.

[91] R. Shinar, J.H. Kennedy, Photoactivity of doped α-Fe_2O_3 electrodes, Sol. Energy Mater. 6 (1982) 323–335. https://doi.org/10.1016/0165-1633(82)90038-7.

[92] A. Kleiman-Shwarsctein, Y.-S. Hu, A.J. Forman, G.D. Stucky, E.W. McFarland, Electrodeposition of α-Fe_2O_3 Doped with Mo or Cr as Photoanodes for Photocatalytic Water Splitting, J. Phys. Chem. C. 112 (2008) 15900–15907. https://doi.org/10.1021/jp803775j.

[93] C. Sanchez, K.D. Sieber, G.A. Somorjai, The photoelectrochemistry of niobium doped α-Fe_2O_3, J. Electroanal. Chem. Interfacial Electrochem. 252 (1988) 269–290. https://doi.org/10.1016/0022-0728(88)80216-X.

[94] D.K. Zhong, M. Cornuz, K. Sivula, M. Grätzel, D.R. Gamelin, Photo-assisted electrodeposition of cobalt–phosphate (Co–Pi) catalyst on hematite photoanodes for solar water oxidation, Energy Environ. Sci. 4 (2011) 1759–1764. https://doi.org/10.1039/C1EE01034D.

[95] F. Le Formal, N. Tétreault, M. Cornuz, T. Moehl, M. Grätzel, K. Sivula, Passivating surface states on water splitting hematite photoanodes with alumina overlayers, Chem. Sci. 2 (2011) 737–743. https://doi.org/10.1039/C0SC00578A.

[96] Q. Huang, Z. Ye, X. Xiao, Recent progress in photocathodes for hydrogen evolution, J. Mater. Chem. A. 3 (2015) 15824–15837. https://doi.org/10.1039/C5TA03594E.

[97] A. Paracchino, V. Laporte, K. Sivula, M. Grätzel, E. Thimsen, Highly active oxide photocathode for photoelectrochemical water reduction, Nat. Mater. 10 (2011) 456–461. https://doi.org/10.1038/nmat3017.

[98] C. Li, T. Hisatomi, O. Watanabe, M. Nakabayashi, N. Shibata, K. Domen, J.J. Delaunay, Simultaneous enhancement of photovoltage and charge transfer in Cu_2O-based photocathode using buffer and protective layers, Appl. Phys. Lett. 109 (2016). https://doi.org/10.1063/1.4959098.

[99] Y. Chen, X. Feng, M. Liu, J. Su, S. Shen, Towards efficient solar-to-hydrogen conversion: Fundamentals and recent progress in copper-based chalcogenide photocathodes, Nanophotonics. 5 (2016) 468–491. https://doi.org/10.1515/nanoph-2016-0027.

[100] C. Yang, P.D. Tran, P.P. Boix, P.S. Bassi, N. Yantara, L.H. Wong, J. Barber, Engineering a $Cu_2O/NiO/Cu_2MoS_4$ hybrid photocathode for H_2 generation in water, Nanoscale. 6 (2014) 6506–6510. https://doi.org/10.1039/c4nr00386a.

[101] Y. Chen, X. Feng, M. Liu, J. Su, S. Shen, Towards efficient solar-to-hydrogen conversion: Fundamentals and recent progress in copper-based chalcogenide photocathodes, Nanophotonics. 5 (2016) 524–547. https://doi.org/10.1515/nanoph-2016-0027.

[102] D. Yokoyama, T. Minegishi, K. Maeda, M. Katayama, J. Kubota, A. Yamada, M. Konagai, K. Domen, Photoelectrochemical water splitting using a $Cu(In,Ga)Se_2$ thin film, Electrochem. Commun. 12 (2010) 851–853. https://doi.org/10.1016/j.elecom.2010.04.004.

[103] J. Wang, N. Yu, Y. Zhang, Y. Zhu, L. Fu, P. Zhang, L. Gao, Y. Wu, Synthesis and performance of Cu_2ZnSnS_4 semiconductor as photocathode for solar water splitting, J. Alloys Compd. 688 (2016) 923–932. https://doi.org/10.1016/j.jallcom.2016.07.012.

[104] P. Sabatier, Hydrogénations et déshydrogénations par catalyse, Berichte Der Dtsch. Chem. Gesellschaft. 44 (1911) 1984–2001. https://doi.org/10.1002/cber.19110440303.

[105] J. Greeley, T.F. Jaramillo, J. Bonde, I. Chorkendorff, J.K. Nørskov, Computational high-throughput screening of electrocatalytic materials for hydrogen evolution, Nat. Mater. 5 (2006) 909–913. https://doi.org/10.1038/nmat1752.

[106] K.I. Raj, I.A., Vasu, Transition metal-based hydrogen electrodes in alkaline solution — electrocatalysis on nickel based binary alloy coatings, J Appl Electrochem. 20 (1990) 32–38. https://doi.org/10.1007/BF01012468.

[107] B. Hinnemann, P.G. Moses, J. Bonde, K.P. Jørgensen, J.H. Nielsen, S. Horch, I. Chorkendorff, J.K. Nørskov, Biomimetic hydrogen evolution: MoS_2 nanoparticles as catalyst for hydrogen evolution, J. Am. Chem. Soc. 127 (2005) 5308–5309. https://doi.org/10.1021/ja0504690.

[108] D. Voiry, H. Yamaguchi, J. Li, R. Silva, D.C.B. Alves, T. Fujita, M. Chen, T. Asefa, V.B. Shenoy, G. Eda, M. Chhowalla, Enhanced catalytic activity in strained chemically exfoliated WS_2 nanosheets for hydrogen evolution, Nat. Mater. 12 (2013) 850–855. https://doi.org/10.1038/nmat3700.

[109] C. Tsai, K. Chan, F. Abild-Pedersen, J.K. Nørskov, Active edge sites in $MoSe_2$ and WSe_2 catalysts for the hydrogen evolution reaction: a density functional study, Phys. Chem. Chem. Phys. 16 (2014) 13156–13164. https://doi.org/10.1039/C4CP01237B.

[110] S. Trasatti, Work function, electronegativity, and electrochemical behaviour of metals: III. Electrolytic hydrogen evolution in acid solutions, J. Electroanal. Chem. Interfacial Electrochem. 39 (1972) 163–184. https://doi.org/10.1016/S0022-0728(72)80485-6.

[111] E.J. Popczun, J.R. McKone, C.G. Read, A.J. Biacchi, A.M. Wiltrout, N.S. Lewis, R.E. Schaak, Nanostructured nickel phosphide as an electrocatalyst for the hydrogen evolution reaction, J. Am. Chem. Soc. 135 (2013) 9267–9270. https://doi.org/10.1021/ja403440e.

[112] Y. Zheng, Y. Jiao, L.H. Li, T. Xing, Y. Chen, M. Jaroniec, S.Z. Qiao, Toward design of synergistically active carbon-based catalysts for electrocatalytic hydrogen evolution, ACS Nano. 8 (2014) 5290–5296. https://doi.org/10.1021/nn501434a.

[113] M. Shalom, S. Gimenez, F. Schipper, I. Herraiz-Cardona, J. Bisquert, M. Antonietti, Controlled carbon nitride growth on surfaces for hydrogen evolution electrodes, Angew. Chemie - Int. Ed. 53 (2014) 3654–3658. https://doi.org/10.1002/anie.201309415.

[114] J. Yang, W. Li, J. Li, D. Sun, Q. Chen, Hydrothermal synthesis and photoelectrochemical properties of vertically aligned tungsten trioxide (hydrate) plate-like arrays fabricated directly on FTO substrates, J. Mater. Chem. 22 (2012) 17744–17752. https://doi.org/10.1039/C2JM33199C.

[115] V. Zwilling, E. Darque-Ceretti, A. Boutry-Forveille, D. David, M.Y. Perrin, M. Aucouturier, Structure and physicochemistry of anodic oxide films on titanium and TA6V alloy, Surf. Interface Anal. 27 (1999) 629–637. https://doi.org/10.1002/(SICI)1096-9918(199907)27:7<629::AID-SIA551>3.0.CO;2-0.

[116] M. Salado, M. Oliva-Ramirez, S. Kazim, A.R. González-Elipe, S. Ahmad, 1-dimensional TiO_2 nano-forests as photoanodes for efficient and stable perovskite solar cells fabrication, Nano Energy. 35 (2017) 215–222. https://doi.org/10.1016/j.nanoen.2017.03.034.

[117] A. Kafizas, L. Francàs, C. Sotelo-Vazquez, M. Ling, Y. Li, E. Glover, L. McCafferty, C. Blackman, J. Darr, I. Parkin, Optimizing the activity of nanoneedle structured WO_3 photoanodes for solar water splitting: direct synthesis via chemical vapor deposition, J. Phys. Chem. C. 121 (2017) 5983–5993.

[118] S. Matsuzawa, C. Maneerat, Y. Hayata, T. Hirakawa, N. Negishi, T. Sano, Immobilization of TiO_2 nanoparticles on polymeric substrates by using electrostatic interaction in the aqueous phase, Appl. Catal. B Environ. 83 (2008) 39–45. https://doi.org/10.1016/j.apcatb.2008.01.036.

[119] C. Kim, J.T. Kim, K.S. Kim, S. Jeong, H.Y. Kim, Y.S. Han, Immobilization of TiO_2 on an ITO substrate to facilitate the photoelectrochemical degradation of an organic dye pollutant, Electrochim. Acta. 54 (2009) 5715–5720.

[120] A.I. Kontos, I.M. Arabatzis, D.S. Tsoukleris, A.G. Kontos, M.C. Bernard, D.E. Petrakis, P. Falaras, Efficient photocatalysts by hydrothermal treatment of TiO_2, Catal. Today. 101 (2005) 275–281. https://doi.org/10.1016/j.cattod.2005.03.003.

[121] J.A. Byrne, B.R. Eggins, N.M.D. Brown, B. McKinney, M. Rouse, Immobilisation of TiO_2 powder for the treatment of polluted water, Appl. Catal. B Environ. 17 (1998) 25–36.

[122] P. Fernandez-Ibanez, S. McMichael, A. Rioja Cabanillas, S. Alkharabsheh, A. Tolosana Moranchel, J.A. Byrne, New trends on photoelectrocatalysis (PEC): nanomaterials, wastewater treatment and hydrogen generation, Curr. Opin. Chem. Eng. 34 (2021) 100725. https://doi.org/10.1016/j.coche.2021.100725.

[123] Z. Xing, X. Zong, J. Pan, L. Wang, On the engineering part of solar hydrogen production from water splitting: Photoreactor design, Chem. Eng. Sci. 104 (2013) 125–146. https://doi.org/10.1016/j.ces.2013.08.039.

[124] G. Iervolino, I. Tantis, L. Sygellou, V. Vaiano, D. Sannino, P. Lianos, Photocurrent increase by metal modification of Fe_2O_3 photoanodes and its effect on photoelectrocatalytic hydrogen production by degradation of organic substances, Appl. Surf. Sci. 400 (2017) 176–183. https://doi.org/10.1016/j.apsusc.2016.12.173.

[125] T.T. Guaraldo, V.R. Gonçales, B.F. Silva, S.I.C. de Torresi, M.V.B. Zanoni, Hydrogen production and simultaneous photoelectrocatalytic pollutant oxidation using a TiO_2/WO_3 nanostructured photoanode under visible light irradiation, J. Electroanal. Chem. 765 (2016) 188–196. https://doi.org/10.1016/j.jelechem.2015.07.034.

[126] M.I. Jaramillo-Gutiérrez, E.P. Rivero, M.R. Cruz-Díaz, M.E. Niño-Gómez, J.A. Pedraza-Avella, Photoelectrocatalytic hydrogen production from oilfield-produced wastewater in a filter-press reactor using TiO_2-based photoanodes, Catal. Today. 266 (2016) 17–26. https://doi.org/10.1016/j.cattod.2015.12.008.

[127] M. Henze, M.C.M. van Loosdrecht, G.A. Ekama, D. Brdjanovic, Biological Wastewater Treatment: Pinciples, Modelling and Design, IWA Publishing, London, 2008.

[128] European Environment Agency, Industrial waste water treatment - pressures on Europe's environment doi:10.2800/496223, (2018). https://doi.org/10.2800/496223.

[129] F.J.. ed Cervantes, ed., Environmental technologies to treat nitrogen pollution., IWA Publishing, 2009.

[130] J.A. Camargo, Á. Alonso, Ecological and toxicological effects of inorganic nitrogen pollution in aquatic ecosystems: A global assessment, Environ. Int. 32 (2006) 831–849. https://doi.org/10.1016/j.envint.2006.05.002.

[131] X. Zhu, S.R. Castleberry, M.A. Nanny, E.C. Butler, Effects of pH and catalyst concentration on photocatalytic oxidation of aqueous ammonia and nitrite in titanium dioxide suspensions, Environ. Sci. Technol. 39 (2005) 3784–3791. https://doi.org/10.1021/es0485715.

[132] H. Wang, Y. Su, H. Zhao, H. Yu, S. Chen, Y. Zhang, X. Quan, Photocatalytic oxidation of aqueous ammonia using atomic single layer graphitic-C_3N_4, Environ. Sci. Technol. 48 (2014) 11984–11990. https://doi.org/10.1021/es503073z.

[133] J. Feng, X. Zhang, G. Zhang, J. Li, W. Song, Z. Xu, Improved photocatalytic conversion of high−concentration ammonia in water by low−cost Cu/TiO_2 and its mechanism study, Chemosphere. 274 (2021) 129689. https://doi.org/10.1016/j.chemosphere.2021.129689.

[134] M. Altomare, E. Selli, Effects of metal nanoparticles deposition on the photocatalytic oxidation of ammonia in TiO_2 aqueous suspensions, Catal. Today. 209 (2013) 127–133. https://doi.org/10.1016/j.cattod.2012.12.001.

[135] H. Yuzawa, T. Mori, H. Itoh, H. Yoshida, Reaction mechanism of ammonia decomposition to nitrogen and hydrogen over metal loaded titanium oxide photocatalyst, J. Phys. Chem. C. 116 (2012) 4126–4136. https://doi.org/10.1021/jp209795t.

[136] Y. Shiraishi, S. Toi, S. Ichikawa, T. Hirai, Photocatalytic NH_3 Splitting on TiO_2 Particles Decorated with Pt-Au Bimetallic Alloy Nanoparticles, ACS Appl. Nano Mater. 3 (2020) 1612–1620. https://doi.org/10.1021/acsanm.9b02380.

[137] H. Wang, X. Zhang, Y. Su, H. Yu, S. Chen, X. Quan, F. Yang, Photoelectrocatalytic oxidation of aqueous ammonia using TiO_2 nanotube arrays, Appl. Surf. Sci. 311 (2014) 851–857. https://doi.org/10.1016/j.apsusc.2014.05.195.

[138] E. Pelizzetti, P. Calza, G. Mariella, V. Maurino, C. Minero, H. Hidaka, Different photocatalytic fate of amido nitrogen in formamide and urea, Chem. Commun. 4 (2004) 1504–1505. https://doi.org/10.1039/b404574b.

[139] P. Calza, E. Pelizzetti, C. Minero, The fate of organic nitrogen in photocatalysis: An overview, J. Appl. Electrochem. 35 (2005) 665–673. https://doi.org/10.1007/s10800-005-1626-7.

[140] S. Park, J.T. Lee, J. Kim, Photocatalytic oxidation of urea on TiO_2 in water and urine: mechanism, product distribution, and effect of surface platinization, Environ. Sci. Pollut. Res. 26 (2019) 1044–1053. https://doi.org/10.1007/s11356-017-8380-3.

[141] A. Zafra, J. Garcia, A. Milis, X. Domènech, Kinetics of the catalytic oxidation of nitrite over illuminated aqueous suspensions of TiO_2, J. Mol. Catal. 70 (1991) 343–349. https://doi.org/10.1016/0304-5102(91)80129-Q.

[142] M. Bahmani, K. Dashtian, D. Mowla, F. Esmaeilzadeh, M. Ghaedi, Robust charge carrier by Fe_3O_4 in Fe_3O_4/WO_3 core-shell photocatalyst loaded on UiO-66(Ti) for urea photo-oxidation, Chemosphere. 267 (2021) 129206. https://doi.org/10.1016/j.chemosphere.2020.129206.

[143] F. Luo, W. Qiao, H. He, X. Xu, J. Hu, Y. Zhou, D. Wang, Hole dynamic acceleration over CdSO nanoparticles for high-efficiency solar hydrogen production with urea photolysis, J. Mater. Chem. A. 7 (2019) 25650–25656. https://doi.org/10.1039/C9TA08357J.

[144] D. Xu, Z. Fu, D. Wang, Y. Lin, Y. Sun, D. Meng, T. Feng Xie, A $Ni(OH)_2$-modified Ti-doped α-Fe_2O_3 photoanode for improved photoelectrochemical oxidation of urea: The role of $Ni(OH)_2$ as a cocatalyst, Phys. Chem. Chem. Phys. 17 (2015) 23924–23930. https://doi.org/10.1039/c5cp03310a.

[145] J. Bezboruah, D.M. Sanke, A.V. Munde, S. Das, H.S. Karmakar, S.S. Zade, Nickel-doped TiO_2 and thiophene-naphthalenediimide copolymer based inorganic/organic nano-heterostructure for the enhanced photoelectrochemical urea oxidation reaction, Int. J. Hydrogen Energy. 48 (2023) 7361–7373. https://doi.org/10.1016/j.ijhydene.2022.11.098.

[146] Y. Tao, L. Chen, Z. Ma, C. Zhang, Y. Zhang, D. Zhang, D. Pan, J. Wu, G. Li, Near-infrared-driven photoelectrocatalytic oxidation of urea on La-Ni-based perovskites, Chem. Eng. J. 446 (2022) 137240. https://doi.org/10.1016/j.cej.2022.137240.

[147] Y. Tao, Z. Ma, W. Wang, C. Zhang, L. Fu, Q. Zhu, Y. Li, G. Li, D. Zhang, Nickel Phosphide Clusters Sensitized TiO_2 Nanotube Arrays as Highly Efficient Photoanode for Photoelectrocatalytic Urea Oxidation, Adv. Funct. Mater. 33 (2023) 2211169. https://doi.org/10.1002/adfm.202211169.

[148] M. Gupta, D. Ho, D. Santoro, E. Torfs, J. Doucet, P.A. Vanrolleghem, G. Nakhla, Experimental assessment and validation of quantification methods for cellulose content in municipal wastewater and sludge, Environ. Sci. Pollut. Res. 25 (2018) 16743–16753. https://doi.org/10.1007/s11356-018-1807-7.

[149] T. Kawai, T. Sakata, Conversion of carbohydrate into hydrogen fuel by a photocatalytic process, Nature. 286 (1980) 474–476. https://doi.org/10.1038/286474a0.

[150] A. Speltini, M. Sturini, D. Dondi, E. Annovazzi, F. Maraschi, V. Caratto, A. Profumo, A. Buttafava, Sunlight-promoted photocatalytic hydrogen gas evolution from water-suspended cellulose: A systematic study, Photochem. Photobiol. Sci. 13 (2014) 1410–1419. https://doi.org/10.1039/c4pp00128a.

[151] A. Caravaca, W. Jones, C. Hardacre, M. Bowker, H_2 production by the photocatalytic reforming of cellulose and raw biomass using Ni, Pd, Pt and Au on titania, Proc. R. Soc. A Math. Phys. Eng. Sci. 472 (2016). https://doi.org/10.1098/rspa.2016.0054.

[152] R. Chong, J. Li, Y. Ma, B. Zhang, H. Han, C. Li, Selective conversion of aqueous glucose to value-added sugar aldose on TiO_2-based photocatalysts, J. Catal. 314 (2014) 101–108. https://doi.org/10.1016/j.jcat.2014.03.009.

[153] M. Imizcoz, A. V. Puga, Assessment of photocatalytic hydrogen production from biomass or wastewaters depending on the metal co-catalyst and its deposition method on TiO_2, Catalysts. 9 (2019). https://doi.org/10.3390/catal9070584.

[154] E. Bahadori, G. Ramis, D. Zanardo, F. Menegazzo, M. Signoretto, D. Gazzoli, D. Pietrogiacomi, A. Di Michele, I. Rossetti, Photoreforming of glucose over CuO/TiO_2, Catalysts. 10 (2020). https://doi.org/10.3390/catal10050477.

[155] D. V. Esposito, R. V. Forest, Y. Chang, N. Gaillard, B.E. McCandless, S. Hou, K.H. Lee, R.W. Birkmire, J.G. Chen, Photoelectrochemical reforming of glucose for hydrogen production using a WO_3-based tandem cell device, Energy Environ. Sci. 5 (2012) 9091–9099. https://doi.org/10.1039/c2ee22560c.

[156] L.G.C. Villegas, N. Mashhadi, M. Chen, D. Mukherjee, K.E. Taylor, N. Biswas, A Short Review of Techniques for Phenol Removal from Wastewater, Curr. Pollut. Reports. 2 (2016) 157–167. https://doi.org/10.1007/s40726-016-0035-3.

[157] W. Duan, F. Meng, H. Cui, Y. Lin, G. Wang, J. Wu, Ecotoxicity of phenol and cresols to aquatic organisms: A review, Ecotoxicol. Environ. Saf. 157 (2018) 441–456. https://doi.org/10.1016/j.ecoenv.2018.03.089.

[158] S. Ahmed, M.G. Rasul, W.N. Martens, R. Brown, M.A. Hashib, Heterogeneous photocatalytic degradation of phenols in wastewater: A review on current status and developments, Desalination. 261 (2010) 3–18. https://doi.org/10.1016/j.desal.2010.04.062.

[159] H. Park, A. Bak, Y.Y. Ahn, J. Choi, M.R. Hoffmannn, Photoelectrochemical performance of multi-layered BiO_x-TiO_2/Ti electrodes for degradation of phenol and production of molecular hydrogen in water, J. Hazard. Mater. 211–212 (2012) 47–54. https://doi.org/10.1016/j.jhazmat.2011.05.009.

[160] M.P. Languer, F.R. Scheffer, A.F. Feil, D.L. Baptista, P. Migowski, G.J. Machado, D.P. De Moraes, J. Dupont, S.R. Teixeira, D.E. Weibel, Photo-induced reforming of alcohols with improved hydrogen apparent quantum yield on TiO_2 nanotubes loaded with ultra-small Pt nanoparticles, Int. J. Hydrogen Energy. 38 (2013) 14440–14450. https://doi.org/10.1016/j.ijhydene.2013.09.018.

[161] F. Li, W. Zhao, D.Y.C. Leung, Enhanced photoelectrocatalytic hydrogen production via Bi/$BiVO_4$ photoanode under visible light irradiation, Appl. Catal. B Environ. 258 (2019) 117954. https://doi.org/10.1016/j.apcatb.2019.117954.

[162] N.M. Daud, S.R. Sheikh Abdullah, H. Abu Hasan, Z. Yaakob, Production of biodiesel and its wastewater treatment technologies: A review, Process Saf. Environ. Prot. 94 (2015) 487–508. https://doi.org/10.1016/j.psep.2014.10.009.

[163] T. Kawai, T. Sakata, Photocatalytic hydrogen production from liquid methanol and water, J. Chem. Soc. Chem Commun. (1980) 694–695.

[164] G.L. Chiarello, M.H. Aguirre, E. Selli, Hydrogen production by photocatalytic steam reforming of methanol on noble metal-modified TiO_2, J. Catal. 273 (2010) 182–190. https://doi.org/10.1016/j.jcat.2010.05.012.

[165] A. Naldoni, M. D'Arienzo, M. Altomare, M. Marelli, R. Scotti, F. Morazzoni, E. Selli, V. Dal Santo, Pt and Au/TiO_2 photocatalysts for methanol reforming: Role of metal

nanoparticles in tuning charge trapping properties and photoefficiency, Appl. Catal. B Environ. 130–131 (2013) 239–248. https://doi.org/10.1016/j.apcatb.2012.11.006.

[166] T. Chen, Z. Feng, G. Wu, J. Shi, G. Ma, P. Ying, C. Li, Mechanistic studies of photocatalytic reaction of methanol for hydrogen production on Pt/TiO_2 by in situ fourier transform IR and time-resolved IR spectroscopy, J. Phys. Chem. C. 111 (2007) 8005‑8014. https://doi.org/10.1021/jp071022b.

[167] S. Chen, X. Li, W. Zhou, S. Zhang, Y. Fang, Carbon-coated Cu-TiO 2 nanocomposite with enhanced photostability and photocatalytic activity, Appl. Surf. Sci. 466 (2019) 254–261. https://doi.org/10.1016/j.apsusc.2018.10.036.

[168] M. Ismael, Highly effective ruthenium-doped TiO_2 nanoparticles photocatalyst for visible-light-driven photocatalytic hydrogen production, New J. Chem. 43 (2019) 9596–9605. https://doi.org/10.1039/c9nj02226k.

[169] M. Hojamberdiev, M.M. Khan, Z. Kadirova, K. Kawashima, K. Yubuta, K. Teshima, R. Riedel, M. Hasegawa, Synergistic effect of g-C_3N_4, $Ni(OH)_2$ and halloysite in nanocomposite photocatalyst on efficient photocatalytic hydrogen generation, Renew. Energy. 138 (2019) 434–444. https://doi.org/10.1016/j.renene.2019.01.103.

[170] T. Sakata, T. Kawai, Heterogeneous photocatalytic production of hydrogen and methane from ethanol and water, Chem. Phys. Lett. 80 (1981) 341–344. https://doi.org/10.1016/0009-2614(81)80121-2.

[171] Y.Z. Yang, C.H. Chang, H. Idriss, Photo-catalytic production of hydrogen form ethanol over M/TiO_2 catalysts (M = Pd, Pt or Rh), Appl. Catal. B Environ. 67 (2006) 217–222. https://doi.org/10.1016/j.apcatb.2006.05.007.

[172] A.C. Sola, P. Ramírez de la Piscina, N. Homs, Behaviour of Pt/TiO_2 catalysts with different morphological and structural characteristics in the photocatalytic conversion of ethanol aqueous solutions, Catal. Today. 341 (2020) 13–20. https://doi.org/10.1016/j.cattod.2018.06.017.

[173] A. V. Puga, A. Forneli, H. García, A. Corma, Production of H_2 by ethanol photoreforming on Au/TiO_2, Adv. Funct. Mater. 24 (2014) 241–248. https://doi.org/10.1002/adfm.201301907.

[174] R. Deas, S. Pearce, K. Goss, Q. Wang, W.T. Chen, G.I.N. Waterhouse, Hierarchical Au/TiO_2 nanoflower photocatalysts with outstanding performance for alcohol photoreforming under UV irradiation, Appl. Catal. A Gen. 602 (2020) 39–41. https://doi.org/10.1016/j.apcata.2020.117706.

[175] A. Pajares, Y. Wang, M.J. Kronenberg, N. Homs, ScienceDirect Photocatalytic H 2 production from ethanol aqueous solution using TiO_2 with tungsten carbide nanoparticles as co-catalyst, 5 (2020) 2–11. https://doi.org/10.1016/j.ijhydene.2020.04.010.

[176] X. Zhang, L. Luo, R. Yun, M. Pu, B. Zhang, X. Xiang, Increasing the Activity and Selectivity of TiO_2-Supported Au Catalysts for Renewable Hydrogen Generation from Ethanol Photoreforming by Engineering Ti^{3+} Defects, ACS Sustain. Chem. Eng. 7 (2019) 13856–13864. https://doi.org/10.1021/acssuschemeng.9b02008.

[177] M. Antoniadou, P. Bouras, N. Strataki, P. Lianos, Hydrogen and electricity generation by photoelectrochemical decomposition of ethanol over nanocrystalline titania, Int. J. Hydrogen Energy. 33 (2008) 5045–5051. https://doi.org/10.1016/j.ijhydene.2008.07.005.

[178] P. Marios Adamopoulos, I. Papagiannis, D. Raptis, P. Lianos, Photoelectrocatalytic hydrogen production using a TiO_2/WO_3 bilayer photocatalyst in the presence of ethanol as a fuel, Catalysts. 9 (2019) 1–12. https://doi.org/10.3390/catal9120976.

[179] X. Fu, X. Wang, D.Y.C. Leung, Q. Gu, S. Chen, H. Huang, Photocatalytic reforming of C_3-polyols for H_2 production. Part (I). Role of their OH groups, Appl. Catal. B Environ. 106 (2011) 681–688. https://doi.org/10.1016/j.apcatb.2011.05.045.

[180] M. Bowker, P.R. Davies, L.S. Al-Mazroai, Photocatalytic reforming of glycerol over gold and palladium as an alternative fuel source, Catal. Letters. 128 (2009) 253–255. https://doi.org/10.1007/s10562-008-9781-1.

[181] T. Montini, V. Gombac, L. Sordelli, J.J. Delgado, X. Chen, G. Adami, P. Fornasiero, Nanostructured Cu/TiO_2 photocatalysts for H_2 production from ethanol and glycerol aqueous solutions, ChemCatChem. 3 (2011) 574–577. https://doi.org/10.1002/cctc.201000289.

[182] W.T. Chen, Y. Dong, P. Yadav, R.D. Aughterson, D. Sun-Waterhouse, G.I.N. Waterhouse, Effect of alcohol sacrificial agent on the performance of Cu/TiO_2 photocatalysts for UV-driven hydrogen production, Appl. Catal. A Gen. 602 (2020) 117703. https://doi.org/10.1016/j.apcata.2020.117703.

[183] V.M. Daskalaki, D.I. Kondarides, Efficient production of hydrogen by photo-induced reforming of glycerol at ambient conditions, Catal. Today. 144 (2009) 75–80. https://doi.org/10.1016/j.cattod.2008.11.009.

[184] N. Naffati, M.J. Sampaio, E.S. Da Silva, M.F. Nsib, Y. Arfaoui, A. Houas, J.L. Faria, C.G. Silva, Carbon-nanotube/TiO_2 materials synthesized by a one-pot oxidation/hydrothermal route for the photocatalytic production of hydrogen from biomass derivatives, Mater. Sci. Semicond. Process. 115 (2020). https://doi.org/10.1016/j.mssp.2020.105098.

[185] S.K. Mohapatra, K.S. Raja, V.K. Mahajan, M. Misra, Efficient photoelectrolysis of water using TiO_2 nanotube arrays by minimizing recombination losses with organic additives, J. Phys. Chem. C. 112 (2008) 11007–11012. https://doi.org/10.1021/jp7100539.

[186] M. Antoniadou, P. Lianos, Near Ultraviolet and Visible light photoelectrochemical degradation of organic substances producing electricity and hydrogen, J. Photochem. Photobiol. A Chem. 204 (2009) 69–74. https://doi.org/10.1016/j.jphotochem.2009.02.001.

[187] N. Narkis, S. Henefeld-Fourrier, M. Rebhun, Volatile organic acids in raw wastewater and in physico-chemical treatment, Water Res. 14 (1980) 1215–1223. https://doi.org/10.1016/0043-1354(80)90179-7.

[188] J.M. Garrido, R. Méndez, J.M. Lema, Treatment of wastewaters from a formaldehyde-urea adhesives factory, Water Sci. Technol. 42 (2000) 293–300. https://doi.org/10.2166/wst.2000.0527.

[189] A. Patsoura, D.I. Kondarides, X.E. Verykios, Photocatalytic degradation of organic pollutants with simultaneous production of hydrogen, Catal. Today. 124 (2007) 94–102. https://doi.org/10.1016/j.cattod.2007.03.028.

[190] M. Imizcoz, A. V. Puga, Optimising hydrogen production: Via solar acetic acid photoreforming on Cu/TiO_2, Catal. Sci. Technol. 9 (2019) 1098–1102. https://doi.org/10.1039/c8cy02349b.

[191] A. Speltini, M. Sturini, F. Maraschi, D. Dondi, G. Fisogni, E. Annovazzi, A. Profumo, A. Buttafava, Evaluation of UV-A and solar light photocatalytic hydrogen gas evolution from olive mill wastewater, Int. J. Hydrogen Energy. 40 (2015) 4303–4310. https://doi.org/10.1016/j.ijhydene.2015.01.182.

[192] I. Ntaikou, C. Kourmentza, E.C. Koutrouli, K. Stamatelatou, A. Zampraka, M. Kornaros, G. Lyberatos, Exploitation of olive oil mill wastewater for combined biohydrogen and biopolymers production, Bioresour. Technol. 100 (2009) 3724–3730. https://doi.org/10.1016/j.biortech.2008.12.001.

[193] B.R. Eggins, F.L. Palmer, J.A. Byrne, Photocatalytic treatment of humic substances in drinking water, Water Res. 31 (1997) 1223–1226. https://doi.org/10.1016/S0043-1354(96)00341-7.

[194] J.A. Byrne, B.R. Eggins, W. Byers, N.M.D. Brown, Photoelectrochemical cell for the combined photocatalytic oxidation of organic pollutants and the recovery of metals from waste waters, Appl. Catal. B Environ. 20 (1999) L85–L89. https://doi.org/10.1016/S0926-3373(98)00103-9.

[195] H.M. Coleman, B.R. Eggins, J.A. Byrne, F.L. Palmer, E. King, Photocatalytic degradation of 17-β-oestradiol on immobilised TiO_2, Appl. Catal. B Environ. 24 (2000) L1–L5. https://doi.org/10.1016/S0926-3373(99)00091-0.

[196] H.M. Coleman, E.J. Routledge, J.P. Sumpter, B.R. Eggins, J.A. Byrne, Rapid loss of estrogenicity of steroid estrogens by UVA photolysis and photocatalysis over an immobilised titanium dioxide catalyst, Water Res. 38 (2004) 3233–3240. https://doi.org/10.1016/j.watres.2004.04.021.

[197] H.M. Coleman, M.I. Abdullah, B.R. Eggins, F.L. Palmer, Photocatalytic degradation of 17β-oestradiol, oestriol and 17α-ethynyloestradiol in water monitored using fluorescence spectroscopy, Appl. Catal. B Environ. 55 (2005) 23–30. https://doi.org/10.1016/j.apcatb.2004.07.004.

[198] P.S.M. Dunlop, T.A. McMurray, J.W.J. Hamilton, J.A. Byrne, Photocatalytic inactivation of Clostridium perfringens spores on TiO_2 electrodes, J. Photochem. Photobiol. A Chem. 196 (2008) 113–119. https://doi.org/10.1016/j.jphotochem.2007.11.024.

[199] P.S.M. Dunlop, J.A. Byrne, N. Manga, B.R. Eggins, The photocatalytic removal of bacterial pollutants from drinking water, J. Photochem. Photobiol. A Chem. 148 (2002) 355–363. https://doi.org/10.1016/S1010-6030(02)00063-1.

[200] P.S.M. Dunlop, A. Galdi, T.A. McMurray, J.W.J. Hamilton, L. Rizzo, J.A. Byrne, Comparison of Photocatalytic Activities of Commercial Titanium Dioxide Powders Immobilised on Glass Substrates, 13 (2010) 99–106. https://doi.org/doi:10.1515/jaots-2010-0113.

[201] T.A. McMurray, J.A. Byrne, P.S.M. Dunlop, J.G.M. Winkelman, B.R. Eggins, E.T. McAdams, Intrinsic kinetics of photocatalytic oxidation of formic and oxalic acid on immobilised TiO_2 films, Appl. Catal. A Gen. 262 (2004) 105–110. https://doi.org/10.1016/j.apcata.2003.11.013.

[202] T.A. McMurray, P.S.M. Dunlop, J.A. Byrne, The photocatalytic degradation of atrazine on nanoparticulate TiO_2 films, J. Photochem. Photobiol. A Chem. 182 (2006) 43–51. https://doi.org/10.1016/j.jphotochem.2006.01.010.

[203] T.A. McMurray, J.A. Byrne, P.S.M. Dunlop, E.T. McAdams, Photocatalytic and electrochemically assisted photocatalytic oxidation of formic acid on TiO_2 films under UVA and UVB irradiation, J. Appl. Electrochem. 35 (2005) 723–731. https://doi.org/10.1007/s10800-005-1397-1.

[204] D.M.A. Alrousan, P.S.M. Dunlop, T.A. McMurray, J.A. Byrne, Photocatalytic inactivation of E. coli in surface water using immobilised nanoparticle TiO_2 films, Water Res. 43 (2009) 47–54. https://doi.org/10.1016/j.watres.2008.10.015.

[205] O. Sunnotel, R. Verdoold, P.S.M. Dunlop, W.J. Snelling, C.J. Lowery, J.S.G. Dooley, J.E. Moore, J.A. Byrne, Photocatalytic inactivation of Cryptosporidium parvum on nanostructured titanium dioxide films, J. Water Health. 8 (2009) 83–91. https://doi.org/10.2166/wh.2009.204.

[206] S. Wadhwa, J.W.J. Hamilton, P.S.M. Dunlop, C. Dickinson, J.A. Byrne, Effect of Post-annealing on the Photocatalytic Activity of Hydrothermally Synthesised Titania Nanotubes, 14 (2011) 147–157. https://doi.org/doi:10.1515/jaots-2011-0118.

[207] G.R. Dale, J.W.J. Hamilton, P.S.M. Dunlop, J.A. Byrne, Electrochemically assisted photocatalysis on anodic titania nanotubes, Curr. Top. Electrochem. 14 (2009) 89–97.

[208] G.R. Dale, J.W.J. Hamilton, P.S.M. Dunlop, P. Lemoine, J.A. Byrne, Electrochemical growth of titanium oxide nanotubes: the effect of surface roughness and applied potential, J. Nanosci. Nanotechnol. 9 (2009) 4215–4219.

[209] S. McMichael, M. Waso, B. Reyneke, W. Khan, J.A. Byrne, P. Fernandez-Ibanez, Electrochemically assisted photocatalysis for the disinfection of rainwater under solar irradiation, Appl. Catal. B Environ. 281 (2021) 119485. https://doi.org/https://doi.org/10.1016/j.apcatb.2020.119485.

[210] S. McMichael, A. Tolosana-Moranchel, M.A.L.R.M. Cortes, J.W.J. Hamilton, P. Fernandez-Ibanez, J.A. Byrne, An investigation of photoelectrocatalytic disinfection of water using titania nanotube photoanodes with carbon cathodes and determination of the radicals produced, Appl. Catal. B Environ. 311 (2022) 121339. https://doi.org/https://doi.org/10.1016/j.apcatb.2022.121339.

[211] A. Singh, 2D Heterostructured Photocatalytic Materials for Water Treatment and Disinfection. Ulster University, 2020.

[212] M.A.L.R.M. Cortes, J.W.J. Hamilton, P.K. Sharma, A. Brown, M. Nolan, K.A. Gray, J.A. Byrne, Formal quantum efficiencies for the photocatalytic reduction of CO2 in a gas phase batch reactor, Catal. Today. 326 (2019) 75–81. https://doi.org/https://doi.org/10.1016/j.cattod.2018.10.047.

[213] D.A. Keane, K.G. McGuigan, P.F. Ibáñez, M.I. Polo-López, J.A. Byrne, P.S.M. Dunlop, K. O'Shea, D.D. Dionysiou, S.C. Pillai, Solar photocatalysis for water disinfection: materials and reactor design, Catal. Sci. Technol. 4 (2014) 1211–1226. https://doi.org/10.1039/C4CY00006D.

[214] J.A. Byrne, P.S.M. Dunlop, J.W.J. Hamilton, P. Fernández-Ibáñez, I. Polo-López, P.K. Sharma, A.S.M. Vennard, A review of heterogeneous photocatalysis for water and

surface disinfection, Molecules. 20 (2015) 5574–5615. https://doi.org/10.3390/molecules20045574.

[215] J.A. Byrne, P.A. Fernandez-Ibañez, P.S.M. Dunlop, D.M.A. Alrousan, J.W.J. Hamilton, Photocatalytic Enhancement for Solar Disinfection of Water: A Review, Int. J. Photoenergy. 2011 (2011) 798051. https://doi.org/10.1155/2011/798051.

[216] C. Han, B. Ren, M.N. Nadagouda, G.E.M. Romanos, P. Falaras, T.T. Lim, V.K. Sharma, N. Johnson, P. Fernández-Ibáñez, J.A. Byrne, Nanotechnology applications, in: Sustain. Water Technol., CRC Press, 2016: pp. 105–143.

[217] J.A. Byrne, P. Fernández-Ibáñez, P.K. Sharma, Water scarcity in developing regions, Sustain. Water Manag. 227 (9AD).

[218] J.A. Byrne, P. Fernandez-Ibañez, Solar photocatalytic drinking water treatment for developing countries, in: Nanotechnol. Sustain. Manuf., CRC Press, 2014: pp. 199–226.

Chapter 3. Materials and methods

3.1 Introduction

This chapter presents the materials, methods and equipment used throughout the research of this thesis. The majority of the experiments were carried out at Ulster university except for the Atomic Layer Deposition experiments and related characterization, performed at the company Delft-IMP, the detection of hydrogen gas experiments, performed at Queens University of Belfast and the Inductively Coupled Plasma tests, performed by the external company Laboratorium voor Multi-element Analysis.

3.2 Materials

The reagents utilized in this research were of analytical grade and no further purification was performed. A list of reagents and materials is shown in Table 3-1, including the corresponding supplier and the purity.

Table 3-1 – List of reagents used, including chemical formula, supplier and purity.

Name	Chemical formula	Supplier	Purity
Ammonium fluoride	NH_4F	Sigma-Aldrich	≥ 99.99 %
Ammonium sulphate	$(NH_4)_2SO_4$	Sigma-Aldrich	≥ 99.99 %
Brij-35	-	Sigma Aldrich	-
Conductive Epoxy CW 2400	-	Circuit works	-
Copper hexafluoroacetylacetonate trimethylvinylsilane	$C_{10}H_{13}CuF_6O_2Si$	Gelest	-
Copper sheet	Cu	RS Components	99.9 %
Copper sulphate pentahydrate	$CuSO_4 \cdot 5H_2O$	Sigma-Aldrich	≥ 99 %
Copper wire	Cu	RS Components	Garde II
Distilled water	H_2O	In-House	-
Decon 90	-	Decon Laboratories	-

Fluorine-doped tin oxide glass	SnO_2:F	Sigma-Aldrich	-
Ethylenediamine	$C_2H_8N_2$	Sigma-Aldrich	≥ 98 %
Ethylene glycol	$(CH_2OH)_2$	Sigma-Aldrich	≥ 99.8 %
Hydrazine sulphate	$N_2H_6SO_4$	Sigma-Aldrich	≥ 99 %
Ultrapure water	Millipore H_2O	ELGA Pure Lab	15 $M\Omega cm^{-1}$
Nafion 117	$(C_7HF_{13}O_5S \cdot C_2F_4)_x$	Sigma Aldrich	-
Nitric acid	HNO_3	Sigma Aldrich	≥ 65 %
Nitrogen (oxygen-free)	N_2	BOC	≥ 99.99 %
N-(1-naphtyl) ethylenediamine Dihydrochloride (NED)	$C_{10}H_7NHCH_2CH_2NH_2 \cdot 2HCl$		≥ 98 %
Platium wire	Pt	Birmingham metal special products	-
Platinized titanium mesh	Pt	Umicore	-
Phthalaldehyde	$C_6H_4(CHO)_2$	Sigma-Aldrich	≥ 99 %
Potassium perchlorate	$KClO_4$	Sigma-Aldrich	≥ 99 %
Potassium nitrite	KNO_2	Sigma-Aldrich	≥ 99 %
Primaquine bisphosphate	$C_{15}H_{21}N_3O \cdot 2H_3PO_4$	Sigma-Aldrich	≥ 98 %
Silver epoxy	-	MG Chemicals	-
Trisodium citrate	$Na_3C_6H_5O_7$	Alfa Aesar	≥ 99 %
Sodium chloride	NaCl	Sigma-Aldrich	≥ 99.8 %
Sodium dichloroisocyanurate	$C_3Cl_2N_3NaO_3$	Sigma-Aldrich	≥ 98 %
Sodium hydroxide	NaOH	Sigma-Aldrich	≥ 98 %
Sodium nitrate	$NaNO_3$	Sigma-Aldrich	≥ 99 %
Sodium nitroprusside	$Na_2(Fe(CN)_5NO) \cdot 2H2O$	Sigma-Aldrich	≥ 99 %
Sodium salicylate	$C_7H_5NaO_3$	Sigma-Aldrich	≥ 99.5 %
Sodium tungstate dehydrate	Na_2WO_4	Sigma-Aldrich	≥ 99 %
Sodium oxalate	$Na_2C_2O_4$	Sigma-Aldrich	> 99.5 %
Sodium Sulphate	Na_2SO_4	Fluka Analytical	≥99 %

Sulphanilamide	$C_6H_8N_2O_2S$	Sigma-Aldrich	> 99 %
SU8 photoresist	-	MicroChem	-
Sulfuric acid	H_2SO_4	Sigma Aldrich	95-97 %
Titanium foil	Ti	Sigma-Aldrich	99.8 %
Titanium mesh	Ti	Ti-Shop	Grade I
Zinc sulphate heptahydrate	$ZnSO_4 \cdot 7H_2O$	Sigma-Aldrich	≥ 99 %

3.3 Methods

3.3.1 Surface modification by Atomic Layer deposition (ALD)

3.3.1.1 ALD setup

The ALD experiments were carried out in a fluidized bed reactor (FBR) operated at atmospheric pressure. This system consisted of a borosilicate glass column placed on a vertical vibration table to assist the fluidization of the nanoparticles. The FBR was heated using an infrared (IR) lamp. The inlet lines, valves and bubblers were brought to the desired temperature using heating tape. The temperature was measured with a type-K thermocouple and regulated with a PID controller. All the lines, valves and bubblers were uniformly covered externally with two layer of glass fibre tape for a better temperature isolation. The gas was introduced from the bottom of the FBR through a stainless-steel distributor plate, formed by sintered particles to achieve a homogenous flow of gas through the full cross-section of the column. An identical distributor plate was placed on top of the column to prevent nanoparticles from leaving the column.

3.3.1.2 Fluidization test

Prior to the ALD deposition experiments, the optimal fluidization conditions for the substrate were determined by a fluidization test. The fluidization test was performed in the FBR reactor at atmospheric pressure and room temperature. Nitrogen was utilized as fluidizing tool together with the vertical vibration table. The nitrogen gas was introduced from the bottom of the column at different flow rates, ranging from 0.5 to 1.5 mL min^{-1}. The quality of fluidization was assessed visually. The optimal nitrogen flow rate was chosen when the substrate packed bed expanded, changing into a fluidized bed, and the particles were in suspension in an upward gas stream with no preferential paths.

3.3.1.3 Cu_xO deposition

Cu_xO was deposited onto the commercial TiO_2 (P25) substrate using Copper hexafluoroacetylacetonate trimethylvinylsilane, Cu(I)(hfac)(TMVS), as precursor and H_2O as oxidizer. The bubbler containing the Cu precursor was maintained at 60 °C, whereas the H_2O bubbler was kept at room temperature. The deposition temperature was 150 °C. For each ALD deposition batch, 1 g of TiO_2 was used, fluidized using inert N_2 with a flow of 0.5 L min^{-1}. An ALD cycle consisted of four sequential steps: (1) the exposure of the TiO_2 powder to the precursor, Cu(I)(hfac)(tmvs) vapor, (2) a purge with N_2, (3) the exposure to deionized H_2O vapor and (4) a purge with N_2. An additional purge of 5 min N_2 was used in between cycles to ensure the removal of possible by-products and precursor residues.

3.3.2 Electrode preparation

3.3.2.1 Immobilization of P25(TiO_2) on FTO glass by spray coating

The P25(TiO_2) electrode was fabricated by immobilizing commercial P25 on a fluorine doped tin oxide (FTO) coated glass using spray coating procedure. Prior to immobilization, the FTO glasses were ultrasonically cleaned in a solution of 5 % Decon 90 detergent, followed by ultrasonic wash in distilled water and finally dried in air. In this method, the P25 was suspended in methanol with a density of 25 g L^{-1} and sonicated for 10 min to improve mixing. Later, the glass was placed on a hot plate at a temperature of 80 °C. The suspension was then coated onto the FTO glass using a spray gun. Several cycles of spraying and weighing were performed until the desired loading of 1 mg cm^{-2} was achieved. This loading was chosen based on previous studies that described the optimal loading for the degradation of formic acid and atrazine [1,2]. The coated FTO was then annealed in a Lenton furnace at 450 °C in air for 1 h using a ramp rate of 2 °C min^{-1}.

3.3.2.2 Hydrothermal synthesis of WO_3 onto FTO glass

The WO_3 electrode was synthesized directly on the FTO glass using a hydrothermal method adapted from previously published work by Yang *et al.* [3]. Prior to being utilized in the synthesis, the FTO glasses were cleaned in a sonicator, using a solution of 5 % Decon 90 detergent followed by ultrasonic wash in distilled water and finally dried in air. In this procedure, 0.18 g of $Na_2WO_4 \cdot H_2O$ was dissolved in 24 mL of distilled water, after

that 8 mL of HCl 33% was added dropwise. 1.32 g of $Na_2C_2O_4$ was then added and left stirring for 10 min. Subsequently, 24 mL of distilled water was added and stirred for 30 min, accounting for a total solution volume 56 mL. For the synthesis of the 1.5 cm x 2 cm FTO glasses, the solution was then transferred to a Teflon liner of 80 mL. The FTO glass slides were placed at an angle with the conductive side facing down, for a controlled growth. For the FTO glasses with a dimension of 7 cm x 7 cm, 380 mL of solution was prepared and placed in a Teflon liner of 1 L.

In both cases, the liner was then placed in a Parr reactor in which the hydrothermal synthesis was performed at a temperature of 120 °C for 12 h. Once ready, the FTO coated glasses were extracted, rinsed with distilled water and dried in ambient air. The WO_3 coated FTO coupons were annealed in a Lenton furnace at 450 °C in air for 1 h using a ramp up rate of 2 °C min^{-1} and a ramp down rate of 2 °C min^{-1}.

3.3.2.3 Anodization of titanium

The titanium nanotube electrodes were fabricated using electrochemical driven anodization. Prior to this process, all titanium (Ti) metal sheets/meshes were ultrasonically cleaned in a solution of 5 % Decon 90 detergent, followed by ultrasonic wash in distilled water and finally dried in air. The anodization procedure followed was previously reported by Yeonmi et al [4]. In this process, a working electrode and two counter electrodes were used, with the Ti sample being used as the working electrode and two platinized titanium meshes as the cathodes. The distance between the working electrode and each cathode was 2.5 cm. The electrodes were submerged in the electrolyte containing NH_4F (0.3 wt%) in distilled water (3 vol%) and ethylene glycol (97 vol%). Due to the corrosive nature F^- towards glass, a polypropylene beaker was employed. An anodising potential of +30.0 V was applied for 3 h using a power supply (PLH120 DC Aim-TTi). The electrode was cleaned by rinsing multiple times in distilled water and then annealed in lenton furnace at a temperature of 450 ^oC in air for 1 h ramp 2 ^oC min^{-1} up and 2 ^oC min^{-1} down.

3.3.2.4 Electrical contact

The electrical contact for all small size photoanodes (size 2 cm by 1.5 cm) was done using a copper wire with a thickness of 1.5 mm. The end of the copper wire that was attached to the electrode was sanded with grit paper to remove the wire protective layer. For the

electrodes fabricated with FTO as conducting substrate, the copper wire was attached directly to the semiconductor uncoated area of the FTO. For the electrodes using Ti as the conducting substrate, the oxide layer on the annealed titanium was removed with abrasive grit paper. In order to attach the copper wire with the conductive substrates, silver epoxy (CircuitWorks CW2400) was used. The epoxy was applied and then cured in an oven at 120 ºC for 30 min. A negative photoresist (SU8 MicroChem) was used to insulate the contact and any area of the conductive substrate not covered with nanostructures. The photoresist was applied and left to dry at room temperature, after that, it was exposed to UVA light (PL-S 9W/10/2P (UVA)) for 10 min on both sides to enable the cross-linking of the epoxy groups, followed by curing in an oven at a temperature of 160 °C for 30 min.

3.3.3 Material characterisation

This section describes the techniques employed to study the physical and chemical properties of the materials used. In order to determine the morphology of the electrodes transmission electron microscopy (TEM) and scanning electron microscopy (SEM) were used. The crystal structure of the materials was studied using X-ray diffraction (XRD). For the elemental and chemical composition of the semiconductors, X-ray photoelectron spectroscopy (XPS) was utilized. The metal content of the materials was determined using inductively coupled plasma optical emission spectrometry (ICP-OES). And the optical properties of the materials were investigated using ultraviolet-visible diffuse reflectance spectroscopy (UV-Vis DRS).

3.3.3.1 Scanning electron microscopy

The surface morphology of the electrodes was studied using scanning electron microscope (Hitachi SU500 FE-SEM). The accelerating voltage used varied from 10 kV to 15 kV, the working distance was between 5 and 15 mm and the high vacuum pressure used was 10^{-8} bar. The images were recorded using the secondary electron detector. The electrodes were studied as prepared, with no additional coating being applied. The size of the nanoparticles was determined from the obtained SEM images, using the software ImageJ [5].

3.3.3.2 Transmission electron microscopy

The high-resolution images of materials were acquired using transmission electron microscopy (JEOLJEM1400). These measurements were recorded with an operating voltage of 120 kV. For the TEM analysis, the samples were dispersed in ethanol and

directly drop-casted onto carbon-coated Cu grids (Agar Scientific, 400 mesh). The TEM images were analysed using the software ImageJ [5].

3.3.3.3 X-ray Photoelectron Spectroscopy

X-ray photoelectron spectroscopy was utilized to determine the elemental composition and oxidation state of the samples surface. A Kratos Axis Ultra instrument having Al Kα as X-ray source with photon energy hν = 1486.7 eV was employed for all XPS measurements. The wide energy survey scans (WESS) were measured for all samples in the binding energy range of 0-1250 eV and a pass energy of 160 eV. High resolution (HR) scans of each target element (copper 2p; titanium 2p; carbon 1s; oxygen 1s and tungsten 4f) were investigated at slow scan speeds and 14.2 eV pass energy. The XPS peak fitting was performed using CasaXPS software. All the XPS spectra were calibrated with respect to the reference to C-C adventitious carbon (C 1s) with peak position of 284.8 eV. The high-resolution scan peaks were fitted using Gaussian-Lorentzian (GL) function and a Shirley background correction was done before quantification.

3.3.3.4 X-ray diffraction

The crystalline phase of the electrodes was studied using X-ray diffraction (Malvern Panalytical) with Cu Kα (λ= 1.560 Å) radiation and using a scanning angle between 20° and 70°. For these measurements, the divergence slit was fixed to 0.5, scan ranged from 20° to 89° with a scan step size of 0.0065° and a time per step of 2.9 s. The revolution time was set to 8 s.

3.3.3.5 Inductively Coupled Plasma -Optical Emission Spectroscopy

Inductively coupled plasma optical emission spectroscopy was employed to quantify the metal content in ALD materials. For the quantification of Cu_xO deposited on TiO_2, 0.1 g of sample was placed in an alumina crucible with sodium peroxide and melted in the furnace using a temperature of 750 °C. The melt was let to cool down, and after it was leached with a diluted hydrochloric acid solution.

3.3.3.6 Ultraviolet-visible diffuse reflectance spectroscopy

The optical properties of the semiconductors were studied using a UV-Vis spectrophotometer equipped with an integrating sphere (LAMBDA 365 UV-Vis, PerkinElmer). The diffuse reflectance spectra were collected with the semiconductor samples already immobilized in the FTO glass.

To estimate the band gap of the semiconductors using the optical spectra, the Tauc plot was used [6]. This method is based on the hypothesis that the absorption coefficient (α) can be expressed following equation (**3-1**), where h is Planck's constant, v is photon frequency, E_g is the band gap, B is a constant and γ a factor which represents the electron transition. For γ, a value of 0.5 for direct and 2 for indirect transition band gaps is used.

$$(\alpha \,.\, h\nu)^{\frac{1}{\gamma}} = B\left(h\nu - E_g\right) \tag{3-1}$$

To transform the diffuse reflectance absorption collected spectra it into absorption spectra, the method proposed by Kubelka-Munk is used [6]. According to this theory, spectra can be transformed using (3-2), as F(R). In this equation, K represents the absorption coefficient while S the scattering coefficient R the reflectance. Therefore, α in the Tauc equation (3-1) can be substituted with F(R), which results in equation (3-3).

$$F(R) = \frac{K}{S} = \frac{(1-R)^2}{2R} \tag{3-2}$$

$$\boldsymbol{(F(R).h\nu)^{\,1/n} = B(h\nu - E_g)} \tag{3-3}$$

For the Tauc plot, $(F(R).h\nu)^{\,1/n}$ is plotted against the photon energy ($h\nu$), with the intersection point between the x-axis and the linear fit providing and approximate bandgap for bare semiconductors [7].

This method is effectively used to estimate bang gap from semiconductors that have a negligible light absorbance in the sub-band gap energy. However, for doped, defected or surface modified semiconductors, which show some absorbance at energies below Eg (due to the intraband gap states), a direct application (intersection with x-axis) of the Tauc method might create inaccurate and underestimated values. This estimation can be improved by the use of a baseline in the sub-bandgap region of the Tauc plot as proposed by Makula *et al*. [7].

3.3.4 Photoelectrochemistry and Photocatalysis

3.3.4.1 Light source

For all the presented photoelectrochemical and photocatalytic experiments, two different lamps were used a 450 W and a 1000 W Xe lamps. The 450 W Xe lamp (Horiba Jobin Yvon FL-1039/40) was equipped with a monochromator (Horiba Jobin Yvon MicroHR), an optical shutter (Uniblitz, WMM-T1 by Vincent associates, Rochester, NY, USA) and an IR filter. The 1000 W Xe lamp (Quantum Design LSE641) was equipped with an IR filter.

The intensity of both lamps was measured using a spectral radiometer with an integrating sphere (FLAME-S-UV-VIS-ES, Ocean Optics B.V, Netherlands), shown in Figure 3-1. The cells were positioned at a distance from the lamps to match the intensities in the absorption range of the materials with the AM 1.5 and each other, as much as possible. The total measured irradiance for the 1000 W lamp was 954 W m^{-2}, which was used for the STH efficiency calculation. The measured irradiance from both lamps is given in Table 3-2.

Table 3-2. Measured irradiance from 450 W and 1000 W Xe lamps.

Wavelength range	**450 W Xe lamp (W m^{-2})**	**1000 W Xe lamp (W m^{-2})**
280 nm to 400 nm	47	46
280 nm to 500 nm	177	173
Total (200 nm to 1100 nm)	1090	954

The monochromatic intensity from the 450 Xe lamp was measured from 270 nm to 500 nm with 10 nm intervals as shown in Figure 3-2. At each wavelength, the irradiance follows a normal distribution pattern varying ±10 nm from the peak value.

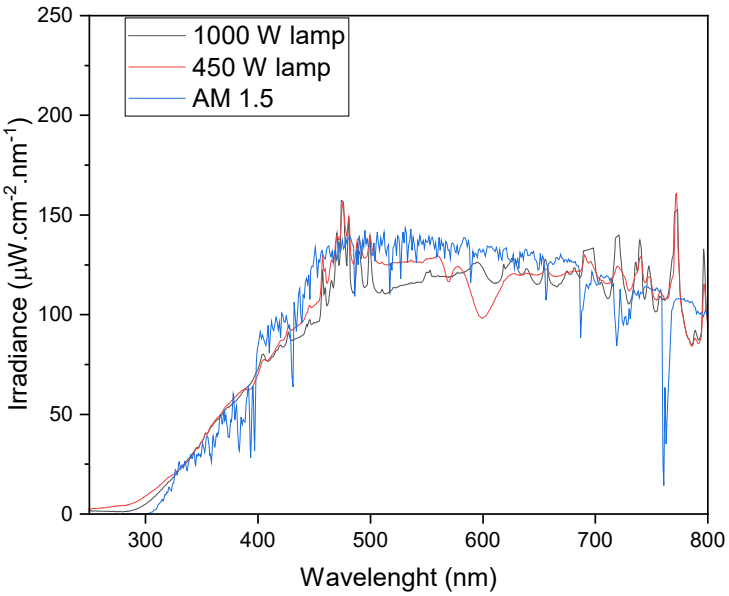

Figure 3-1. Spectra from the 1000 W(black), 450 W(red) Xe lamps and AM 1.5 (blue).

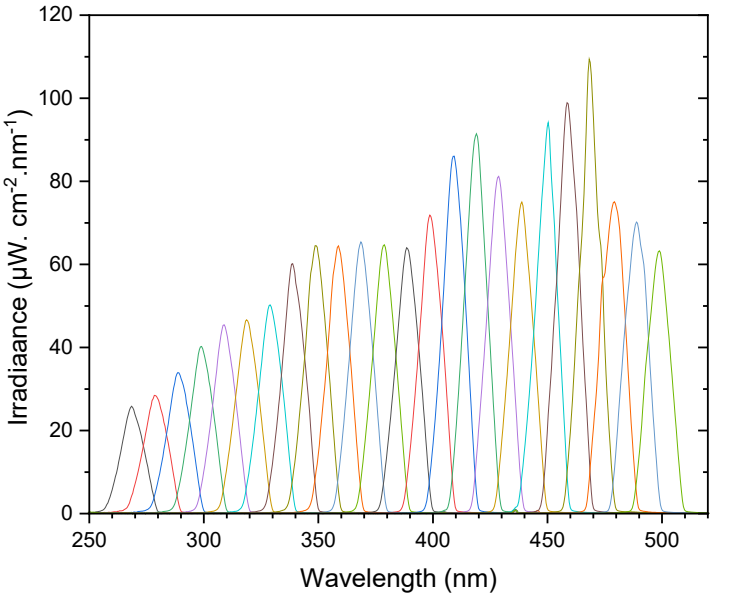

Figure 3-2. Spectral emission of the 450 W Xe lamp with a monochromator (10 nm peak-to-peak intervals from 270 nm to 500 nm).

3.3.4.2 Photoelectrochemical characterization

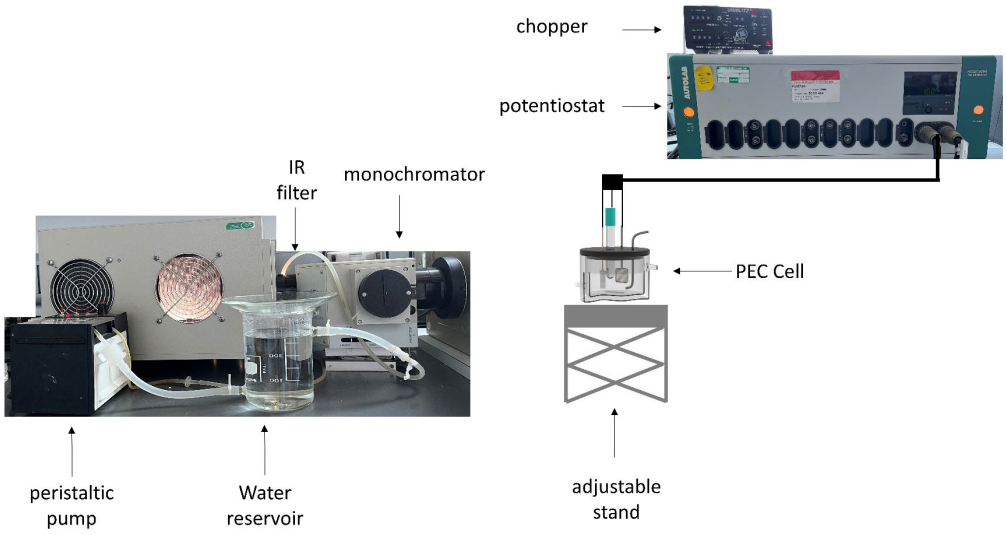

Figure 3-3. Schematic representation of photoelectrochemical characterization laboratory setup.

The electrochemical characterization was carried out using an AUTOLAB potentiostat with the general purpose electrochemical software (GPES). The The 450 W Xe lamp was used with the monochromator, optical shutter and IR filter. A schematic representation of this setup is shown in Figure 3-3. These experiments were performed in a cylindrical quartz cell of 20 mL, using a three-electrode configuration, with the working electrode being the photoanode, the counter electrode, being the cathode and a reference electrode. As counter electrode a platinum gauze was used. A schematic representation of this cell setup is shown in Figure 3-4. All potentials were referred against the saturated calomel electrode (SCE) unless otherwise stated.

The photoelectrochemical behaviour of the semiconductor electrodes was assessed using linear sweep voltammetry, amperometry, spectral photocurrent and open circuit photopotential. The photoelectrochemical tests were performed at least three times with different electrodes to ensure reproducibility.

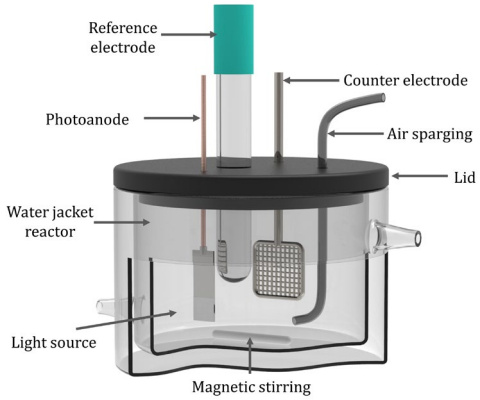

Figure 3-4. Cylindrical quartz cell. This figure was adapted from [8].

Linear sweep voltammetry

In this method, the potential was swept between two values at a constant scan rate, while the current response was recorded. Typically, LSV measurements were performed from -1 V to +1 V or 0 V to 1.5 V using a sweep rate of 5 mVs^{-1}. The measurements were performed with chopped irradiation, with intervals of 10 s. LSV was used to measure the photocurrent density (j) which is the difference between current density under illumination and in the dark. The photocurrent represents the efficiency of the photoinduced process at a potential value. The LSV measurement was also used to find the anodic onset potential.

Amperometry

In this method, a potential vs the reference electrode was applied, and the current response was recorded in time. Amperometry was carried out both in dark and under irradiation to determine photocurrent. Different fixed potentials were used to measure photocurrent without being altered by the changing potential.

Spectral photocurrent

The spectral photocurrent response was utilized to study the performance of the photoanodes at different wavelengths. For this method, amperometry was employed, a fixed potential vs reference electrode was applied in time while varying the monochromatic irradiation in 10 nm intervals from 280 nm to 420 nm or 500 nm. The used applied potential was 1 V vs SCE (unless otherwise stated).

Incident photon-to current conversion

The incident photon-to-current conversion efficiency (IPCE), also referred as external quantum efficiency, was used to evaluate the generation of charge carrier per incident photons in the system at a determined wavelength. It was calculated using the spectral photocurrent, and the photon flux at each wavelength, integrated from the lamp irradiance data (Figure 3-2), according to equation (3-4). In this expression h is Plank's constant, c is the speed of light in vacuum, λ is the irradiation in wavelength in nm, J is the photocurrent density in mA cm^{-2} and P_λ is the photon flux in mW cm^{-2} at a particular λ.

$$IPCE = \frac{number\ of\ generated\ charger\ carrier}{number\ of\ incident\ photons} = \frac{j\ hc}{\lambda\ P_\lambda} \qquad (3\text{-}4)$$

Open-circuit potential and Open circuit Photopotential

For the determination of the open-circuit potential (E_{ocp}) and open-circuit Photopotential (E_{pho}), the open circuit potential was recorded in time using potentiometry. First, the E_{ocp}, also referred as equilibrium potential, was recorded in the dark. Once the E_{ocp} was reached, the semiconductor electrode was irradiated, producing a change in potential due to the generation of electron hole pairs. Subsequent, a new equilibrium was reached which is referred as quasi-Fermi level. The E_{pho} was calculated as the difference between the Fermi level (E_{ocp}) in the dark and the and the quasi-Fermi level under irradiation.

3.3.4.3 Photoelectrochemical experiments

For these experiments, the irradiation source used was the 1000 W Xe lamp, equipped with the IR filter. A power supply (PHL120 DC Aim-TTi) was used to provide the external electrical bias. A schematic representation of the setup is shown in Figure 3-5.

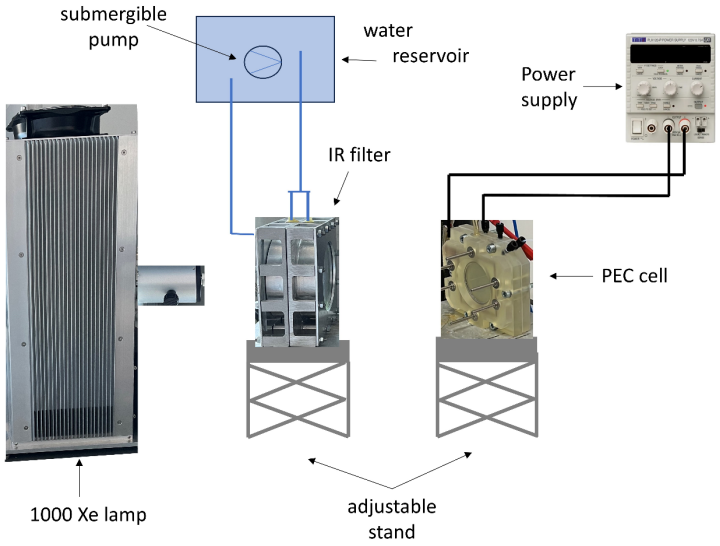

Figure 3-5. Schematic representation of photoelectrochemical laboratory setup.

Two different custom-made cells were designed using the software Inventor from Autodesk. They were fabricated using a high resolution stereolithography 3D printer (Formlabs Form 2) and a chemical resistant clear resin (Formlabs RS-F2-GPCL-04). After printing, the cell parts were rinsed with isopropanol and then cured at 60 °C for 40 min. Finally, they were cleaned with MilliQ water. Both cells were designed with an irradiation area of 19.6 cm^2. The window glass is placed between two O-rings to avoid leaking of the electrolyte.

When used in back-face irradiation configuration, an uncoated area of FTO is in contact to a copper plate which makes the electrical contact. As cathode, a commercial platinized titanium mesh (2.5 ± 0.3 μm) was used, the electrical contact to the cathode was done using Pt wire. Both cells were equipped with septum ports to extract liquids samples using syringes. A 3D exploded view of the one compartment is shown in Figure 3-6, this cell had a total volume of 33 mL and a separation between anode and cathode of 1 cm. The exploded view of the two-compartments cell is shown in Figure 3-7. The cell compartments were separated by a Nafion membrane, placed between two silicon gaskets, to seal the cell and avoid liquid and gas leaks. In order achieve sufficient gas tightening of the cell by compression of the gaskets without compromising the structural integrity of the glass, the cell was designed with two sets of bolts. One set of bolts had the purpose of closing the anode and cathode compartments, with enough pressure so the Nafion and gasket seal that part of the cell, to exert same force in each bolt a torque tool

was used. A different set of bolts closed the cell with the front holder with the glass in between, using O-rings. In this cell, each compartment had a volume of 33 mL and the distance between electrodes was 15 mm.

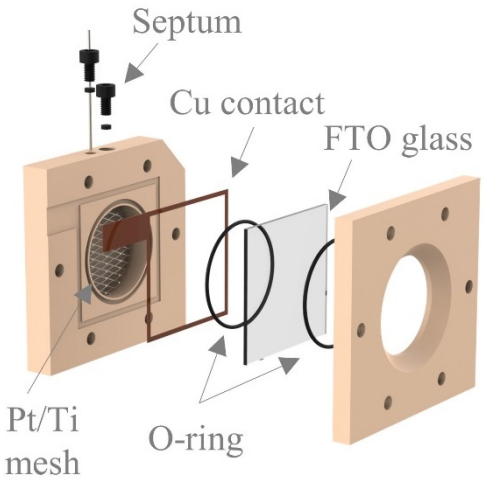

Figure 3-6. 3D exploded view of the custom-made one compartment cell.

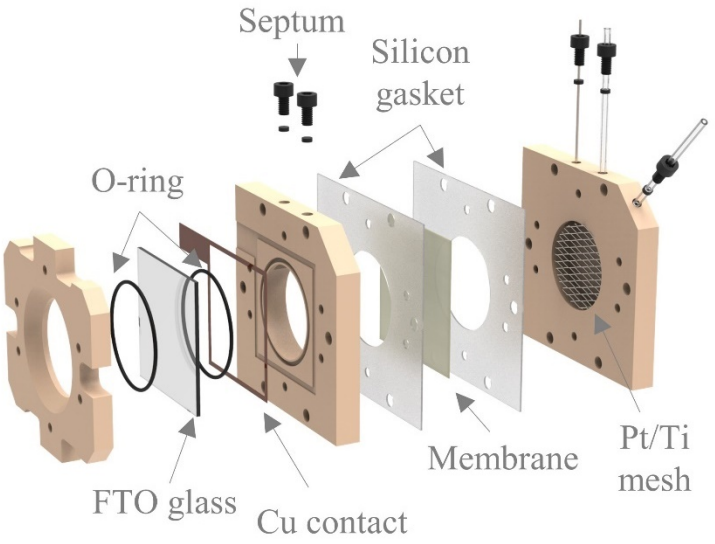

.

Figure 3-7. 3D exploded view of the custom-made two compartments cell.

Faradaic Efficiency

The performance to electrochemically generate a product was determined using the Faradaic Efficiency (FE), which relates the number of electrons in the system with the number of moles produced for a determined product. This expression is given in equation (3-5), where n is the mol of chemical produced, Z is the number of electrons exchanged, F the Faraday's constant and Q the charge transferred through electrode in C.

$$FE = \frac{n_{produced}}{n_{theoretical}} = \frac{n_{produced}}{\frac{Q}{ZF}} \quad (3\text{-}5)$$

Solar-to-hydrogen conversion efficiency

The performance of the photoelectrochemical production of hydrogen was assessed using solar-to-hydrogen (STH) conversion efficiency, which relates the solar energy to the chemical hydrogen energy. The expression is given in equation (3-6), where Φ_{H_2} is the hydrogen rate given in mol s^{-1} m^{-2}, $G^{\circ}_{H_2}$ the Gibbs free energy of hydrogen formation and P is the photon flux given in mW cm^{-2}, measured for a light source with a spectra equal to air mass global (AM) 1.5.

$$STH = \frac{\Phi_{H_2} \cdot G^{\circ}_{H_2}}{P} \quad (3\text{-}6)$$

3.3.4.2 Photocatalytic experiments

The photocatalytic experiments were performed using a borosilicate glass water jacket reactor with a total volume of 22 mL and the 1000 W Xe lamp (Figure 3-8). The IR filter was placed between the lamp and the reactor. Air was bubbled into the solution during the experiment to maintain the level of dissolved oxygen. The experiment was performed under constant stirring to provide efficient mixing and mass transfer. Before starting the experiments, the lamp was shielded and the solution was stirred under air sparging in the dark for 20 min, to allow the system to stabilize. Samples of 0.7 mL were collected in time with a pipette and analysed following the UV-vis methods detailed in the following section.

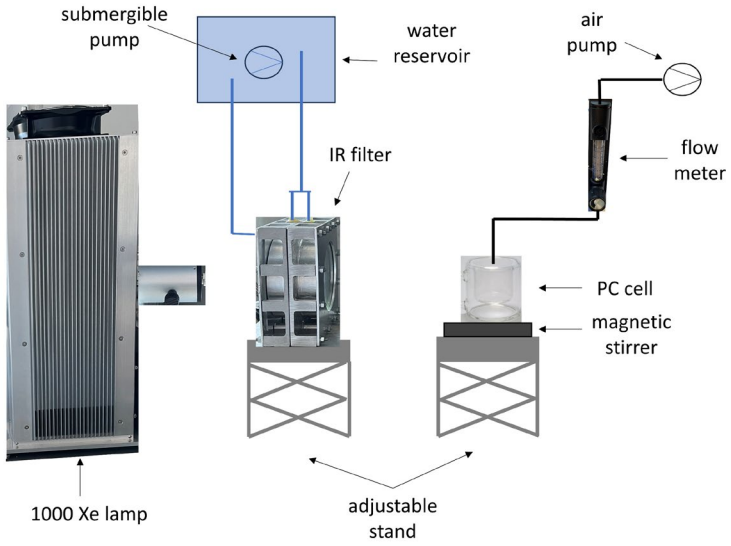

Figure 3-8. Schematic representation of photocatalytic laboratory setup.

3.3.5 Quantification of reactants and products

The quantification of reactants and products was performed at least three times with different electrodes-photocatalysts to assure reproducibility. The results include the standard error between measurements represented with error bars.

3.3.5.1 Urea

For the quantification of urea, a spectrophotometric method previously reported by Zawada et al was used [9,10]. This method is based on the reaction of urea with phthalaldehyde to form 1,3-dihydroxyisoindoline or 1-ureido-3-hydroxyphthalan. Afterwards, the reaction with primaquine bisphosphate allow the occurrence of characteristic colours [9,10]. Brij-35 is a surfactant, and it is used in this method to enhance the fluorescence of the dye [10].

The reagents for this method were prepared as follows:

- Reagent A. In a 100 mL volumetric flask with 50 mL of water, 7.4 mL of sulfuric acid 95-97 % (H_2SO_4) was added and allowed to cool down to room temperature. When this solution cooled down, 20 mg of phthalaldehyde ($C_6H_4(CHO)_2$) was added to the solution and dissolved. Subsequently, 100 µL of Brij-35 was added to the volumetric flask and filled with ultrapure water. To reduce its viscosity, the Brij-35 was slightly warmed up to 40°C using a water bath before use.

- Reagent B. 0.5 g of boric acid (H_3BO_3) was dissolved in 50 mL of water in a 100 mL volumetric flask. Later, 22 mL of sulfuric acid (H_2SO_4) was added and allowed to cool down to room temperature. Then, 51.3 mg of primaquine bisphosphate ($C_{15}H_{21}N_3O \cdot 2H_3PO_4$) was added and dissolved. Finally, 100 µL of Brij-35 was added to the volumetric flask and filled with ultrapure water.

The colorimetric solutions were prepared adding 2 parts by volume of reagent A, with 2 parts of reagent B and 1 part of sample and left to incubate for 1 hour at room temperature. After that, the absorbance was measured at 430 nm in the UV-vis, using a 1 mL quartz cuvette. Calibration curves were performed weekly to assess quality of reagents, an example of calibration curve is shown in Figure 3-9.

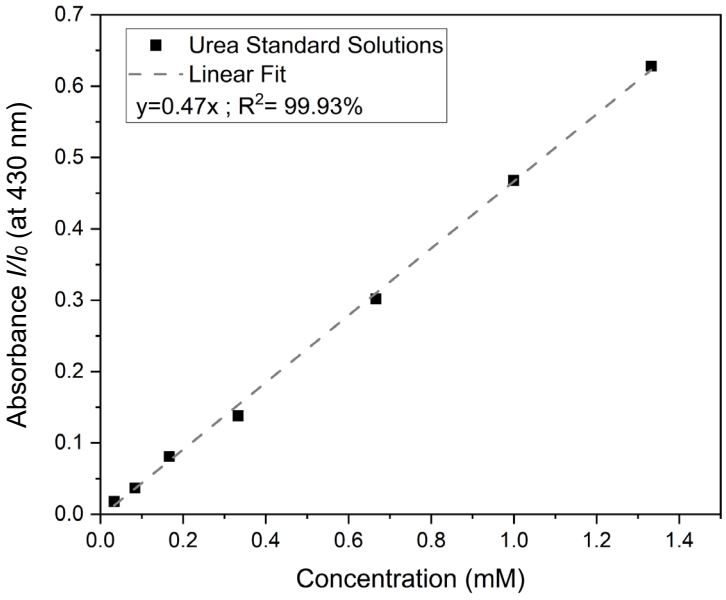

Figure 3-9. Example of calibration curve for UV-vis colorimetric determination of urea concentration.

3.3.5.2 Ammonium

The quantification of ammonium was performed following the method described in the BS ISO 15923-1:2013 [12].

For the preparation of the colorimetric solutions, 1 part per volume of sample mixed with 2 parts per volume of ultrapure water and 10 part per volume of reagent A. Subsequently, 10 parts per volume of reagent B were added, followed by 5 parts per volume reagent C. Finally, 2 part per volume of reagent D were inserted and the solutions were incubated at 35 ^{o} C for 30 min. After incubation, the colorimetric solutions were analysed at a wavelength of 660 nm, using a 1 mL quartz cuvette. Calibration curves for this method were performed daily, an example of this curve is shown in Figure 3-10.

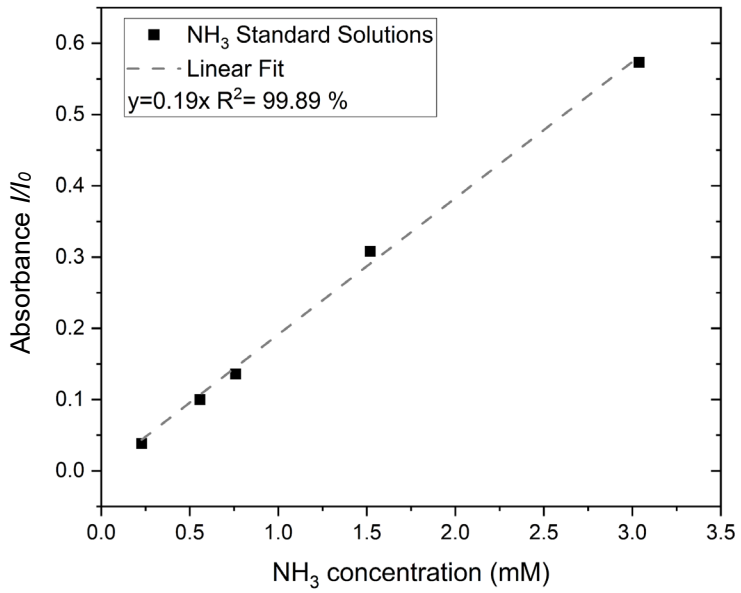

Figure 3-10. Example of calibration curve for UV-vis colorimetric determination of ammonium concentration.

3.3.5.3 Nitrite

The quantification of NO_2^- was performed following the method specified in the BS ISO 15923-1:2013 [12]. An example of calibration curve for this method is shown in Figure 3-11.

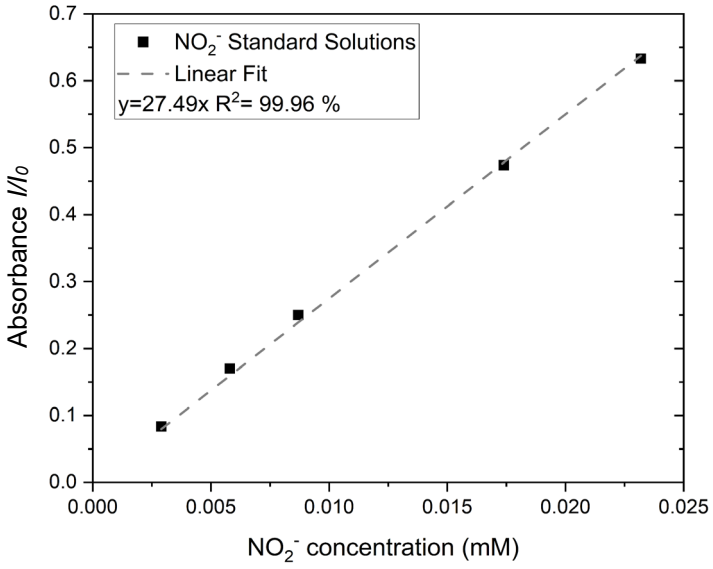

Figure 3-11. Example of calibration curve for UV-vis colorimetric determination of nitrite concentration.

3.3.5.4 Nitrate

For the quantification of NO_3^-, the method specified in the BS ISO 15923-1:2013 [12]. Calibration curves for this method were performed weekly, an example of this curve is shown in Figure 3-12.

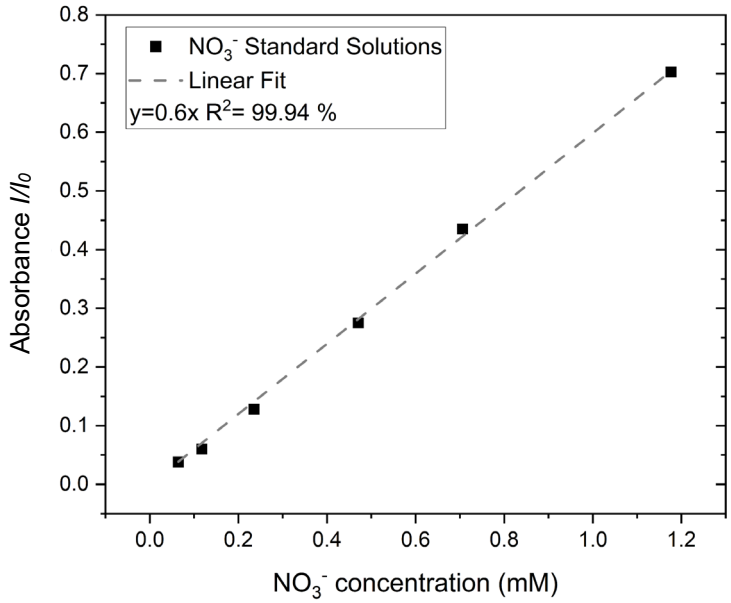

Figure 3-**12**. Example of calibration curve for UV-vis colorimetric determination of nitrate concentration.

3.3.5.5 Hydrogen detection

The detection of hydrogen gas was done using a gas chromatograph (GC - Agilent Technologies 7280 A). The GC was equipped with thermal conductivity detector (TCD) and a packed stainless-steel column (MoleSieve 5A, Mesh 80/100, 6 ft length and 2 mm ID, RESTEK). A pressure of 26.1 psi, a temperature of 150 °C and a flow rate of 22.9 mL min^{-1} were employed to drive the injector. The column was operated with a flow rate of 20 mL min^{-1}, and an oven temperature of 50 °C. The detector was kept at 200 °C using a flow rate of 5 mL min^{-1}. The exact retention time of hydrogen was established by injecting pure H_2, while the quantification was carried out constructing a calibration curve (shown in Figure 3-13). The latter was obtained by areal integration of the H_2 peak corresponding to multiple samples with known concentrations. Gas samples with of 0.1 mL were injected into the GC using a gas tight syringe.

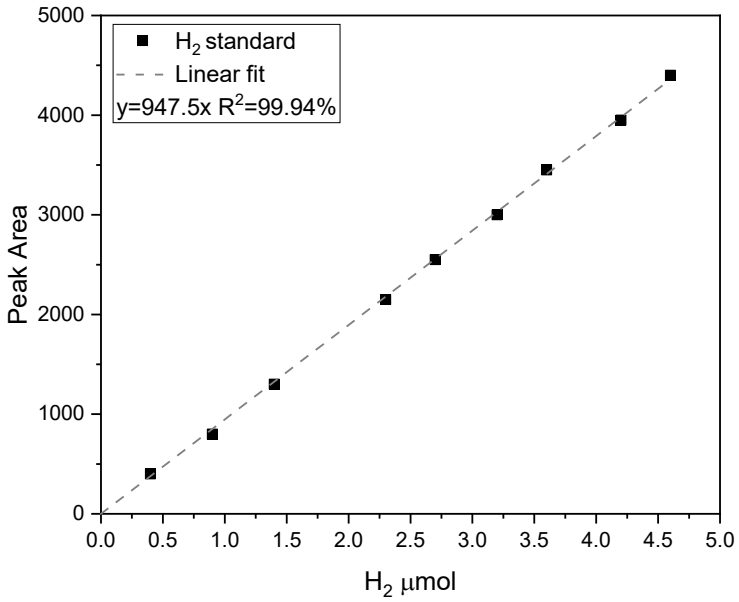

Figure 3-13. Calibration curve for H_2 quantification.

The quantification of the total volume of H_2 gas produced during photoelectrochemical experiments was carried out using water displacement through a gas tight connection of the headspace to an inverted graduated cylinder. The gas produced in the cathode compartment was collected in a Tedlar sampling bag (Restek). Before the experiments, the electrolyte was bubbled with N_2 gas to remove the O_2.

References

[1] T.A. McMurray, J.A. Byrne, P.S.M. Dunlop, J.G.M. Winkelman, B.R. Eggins, E.T. McAdams, Intrinsic kinetics of photocatalytic oxidation of formic and oxalic acid on immobilised TiO2 films, Appl. Catal. A Gen. 262 (2004) 105–110. https://doi.org/10.1016/j.apcata.2003.11.013.

[2] T.A. McMurray, P.S.M. Dunlop, J.A. Byrne, The photocatalytic degradation of atrazine on nanoparticulate TiO_2 films, J. Photochem. Photobiol. A Chem. 182 (2006) 43–51. https://doi.org/10.1016/j.jphotochem.2006.01.010.

[3] J. Yang, W. Li, J. Li, D. Sun, Q. Chen, Hydrothermal synthesis and photoelectrochemical properties of vertically aligned tungsten trioxide (hydrate) plate-like arrays fabricated directly on FTO substrates, J. Mater. Chem. 22 (2012) 17744–17752. https://doi.org/10.1039/C2JM33199C.

[4] Y. Shin, S. Lee, Self-organized regular arrays of anodic TiO_2 nanotubes., Nano Lett. 8 (2008) 3171–3173. https://doi.org/10.1021/nl801422w.

[5] C.A. Schneider, W.S. Rasband, K.W. Eliceiri, NIH Image to ImageJ: 25 years of image analysis, Nat. Methods. 9 (2012) 671–675. https://doi.org/10.1038/nmeth.2089.

[6] J. Tauc, R. Grigorovici, A. Vancu, Optical Properties and Electronic Structure of Amorphous Germanium, Phys. Status Solidi. 15 (1966) 627–637. https://doi.org/10.1002/pssb.19660150224.

[7] P. Makuła, M. Pacia, W. Macyk, How To Correctly Determine the Band Gap Energy of Modified Semiconductor Photocatalysts Based on UV–Vis Spectra, J. Phys. Chem. Lett. 9 (2018) 6814–6817. https://doi.org/10.1021/acs.jpclett.8b02892.

[8] S. McMichael, P. Fernández-Ibáñez, J.A. Byrne, A Review of Photoelectrocatalytic Reactors for Water and Wastewater Treatment, Water. 13 (2021). https://doi.org/10.3390/w13091198.

[9] R.J.X. Zawada, P. Kwan, K.L. Olszewski, M. Llinas, S.G. Huang, Quantitative determination of urea concentrations in cell culture medium, Biochem. Cell Biol. 87 (2009) 541–544. https://doi.org/10.1139/O09-011.

[10] D. Jung, H. Biggs, J. Erikson, P.U. Ledyard, New colorimetric reaction for end point, continuous flow, and kinetic measurement of urea, Clin. Chem. 21 (1975) 1136–1140. https://doi.org/10.1093/clinchem/21.8.1136.

[11] D. Scheiner, Determination of ammonia and Kjeldahl nitrogen by indophenol method, Water Res. 10 (1976) 31–36. https://doi.org/10.1016/0043-1354(76)90154-8.

[12] B.S. Publication, Water quality-Determination of selected parameters by discrete analysis systems BS ISO 15923-1:2013, 2013. 978 0 580 70683 7

Chapter 4. Nanostructured Titanium dioxide electrodes and their performance as photoanodes for the oxidation of ammonia and urea

4.1 Aim and Objectives

4.1.1 Aim

The overall objective of this work is to fabricate different Titanium dioxide (TiO_2) nanostructured photoanodes, compare their photoelectrochemical performance and study their implementation for the oxidation of common nitrogen wastewater pollutants.

4.1.2 Objectives

The specific objectives of this research are the following:

- Fabrication nanostructured TiO_2 electrodes, P25 and TiNT.
- Analysis of material properties of electrodes e.g. morphology.
- Evaluation of photoelectrochemical response of the electrodes.
- Study of the photoelectrochemical performance of the electrodes in the presence of common domestic nitrogen wastewater pollutants (urea and ammonia).
- Determination of pH effect on the photoelectrochemical behaviour.
- Determination of IPCE efficiencies of both photoanodes in presence of urea or ammonia.
- Investigation of the use of this electrode for the oxidation nitrogen wastewater pollutants a scaled-up custom-made photoelectrochemical cell.
- Comparison of photocatalytic and photoelectrochemical performance for urea degradation.
- Study of urea oxidation kinetics.
- Identification of main products from urea oxidation.

4.2 Introduction

TiO_2 is one of the most widely used semiconductor materials for photocatalytic applications. It has high photo-activity, low cost and good chemical and thermal stability [1]. In 1972, Fujishima and Honda reported a photoelectrolytic system for water splitting using a crystalline TiO_2 electrode under UV irradiation [2]. Since then, research in the field of photocatalysis for energy and environmental application gained attention producing a substantial number of studies [3,4]. TiO_2 has been extensively researched as a photocatalyst in suspension as free particles. The photogenerated holes are used for the degradation of organic pollutants either by direct oxidation or indirect oxidation by reactive oxygen species, and oxygen is commonly used as electron acceptor. The use of immobilized TiO_2 has also been explored for water treatment using supporting substrates include glass, glass beads, glass fibre etc. If the TiO_2 is immobilised on an electrically conducting support, then these electrodes may be used with external applied bias in a photoelectrochemical configuration [5]. Electrochemically assisted photocatalysis (photoelectrocatalysis) results in an improvement in charge separation, reduction in recombination and enhancement in reaction rates [6].

In order to improve light absorption, reduce recombination of the photogenerated charge carriers and promote chemical reactions, TiO_2 electrodes are often engineered to form nanostructures. A popular TiO_2 commercial product is Evonik Aeroxide P25 (formerly known as Degussa P25), which has been widely adopted as a benchmark in research. P25 is formed by combination of the polymorphs anatase and rutile in proportions of around 80 % anatase and 20 % rutile. This composition has been reported to enhance the photoactivity because the rutile phase, which has a more positive CB potential, might act as electron sink for the photogenerated electrons of the anatase phase [7]. Several immobilisation techniques with different complexity have been reported for P25 electrodes, including spray coating, dip coating, spin coating, doctor blading, drop casting and electrophoretic deposition [8–11].

Titanium nanotubes (TiNT) have also been reported to be used in photoanodes and are reported to have high mechanical strength, shorter diffusion lengths and large specific surface area [12]. Methods for the fabrication of TiNT include hydrothermal, template assisted and electrochemical oxidation [13]. Zwilling *et al*. reported in 1999, the production of the first self-organized nanotube layers on Ti substrate by electrochemical

anodization in chromic acid electrolytes containing fluorine ions [14]. Since then, this method has been one of the most utilized due to its low cost, simplicity and facile tunability of the nanostructures size, shape and order. These parameters can be varied by adjusting the applied potential, anodization time, temperature, pH and composition of the electrolyte. The formation mechanism of the TiNT is reported to proceed by the electrochemical oxidation from Ti to TiO_2, followed by the fluorine chemical induced dissolution of TiO_2 [13]. Numerous studies have optimized the fabrication method further, and all the developments are generally classified in generations [13]. The most popular procedure nowadays belongs to the third generation. This procedure uses polar organic electrolytes, often ethylene glycol, which is mixed with water and a source of fluoride ions such as NH_4F. The reported diameters of the tubes range from 40 to 160 nm, with lengths ranging from 0.5 μm up to 1000 μm (216 h) [15]. However, lengths varying from 2 μm to 5 μm are usually used for the oxidation of pollutants [16]. Most commonly reported applied potential for the formation of TiNT ranges from 20 V to 60 V, and time from 1 to 6 h in which 3 h has been reported as the most effective for photocatalytic degradation of organic pollutants [17,18]. Moreover, the post annealing time and temperature of the TiNT electrodes, have been reported to determine the phase, conductivity and charge carrier lifetime [13]. Temperatures between 350°C and 450 °C have shown smaller resistances when compared to other annealing temperatures, this could be due to the prepared amorphous phase nanotubes converting into anatase at temperatures between 350°C and 450 °C [19].

Some studies have reported the photocatalytic oxidation of urea [20–22] or ammonia [23–25] using TiO_2, focusing on the kinetics and mechanism. Limited studies have studied the use photoelectrochemical cells containing urea, using P25 [26,27], or TiNT [28,29] as photoanodes, highlighting material improvements. However, these studies lack a solid proof of the occurring oxidation of urea, as well as the determination of reaction kinetics and products.

This work aimed to compare the performance of two different nanostructured TiO_2 photoanodes (P25 and TiNT) and study their photoelectrochemical behaviour in the presence of urea and ammonia, quantifying the effect of this substances in the IPCE of these materials. The influence of pH on the photocurrent for these processes was assessed. A scaled-up custom-made photoelectrochemical cell was used to study the oxidation of

urea with both materials, comparing oxidation kinetics and reaction products. This study highlights the use of PEC for the treatment and oxidation of urea in domestic wastewater.

4.3 Experimental Methodology

4.3.1 Electrode fabrication

The P25 electrode was fabricated by the immobilization of commercial Evonik Aeroxide P25 on FTO glass using spray coating. The TiNT electrode was fabricated using electrochemical driven anodization of a titanium metal sheet. (For detailed fabrication procedures see Chapter 3. Materials and methods).

For the photoelectrochemical characterization experiments, FTO glasses and Ti sheets with size 2 x 1.5 cm were used (see Chapter 3. Materials and methods).

4.3.2 Material Characterization

The surface morphology of the electrodes was analysed using scanning electron microscope (Hitachi SU500 FE-SEM) with an accelerating voltage of 10 kV and a high vacuum pressure of 10^{-8} bar. The size of the nanoparticles was determined using the software ImageJ averaging more than 100 measurements from several images.

The UV-vis diffuse reflectance spectra were measured using a LAMBDA 365 UV/Vis spectrometer (PerkinElmer) which was equipped with an integrating sphere. The optical band gap was estimated following the Kubelka-Munk method.

4.3.3 Photoelectrochemical Characterization

The photoelectrochemical characterization was performed using a potentiostat (AUTOLAB PGSTAT 30) and a 450 W Xe lamp (Horiba Jobin Yvon FL-1039/40) equipped with a monochromator (Horiba Jobin Yvon microHR), a chopper (Uniblitz) and an infra-red (IR) filter. The experiments were performed in a cylindrical water jacketed quartz cell with a total volume of 30 mL. A three-electrode configuration was employed with the TiO_2 electrodes used as working electrodes, a Saturated Calomel Electrode (SCE) as reference and a platinum gauze as counter electrode (Chapter 3.Materials and methods). A LSV from 0 to 1.2 (V) was performed at each pH, the photocurrent density value was selected from the saturated photocurrent region.

Linear sweep voltammetry (LSV) with chopped irradiation was used to determine the photocurrent density, onset potential and critical band bending. The potential was swept from -1.0 to +1.0 V using a scan rate of 5 mV s^{-1}. The open circuit potential and open circuit photo-potential were measured using potentiometry. The spectral photocurrent response measurements were performed from a wavelength ranging from 280 nm to 500 nm in steps of 10 nm with chopped irradiation intervals of 20 s and a fixed potential of +1.0 V vs SCE. The urea concentration effect in photocurrent was recorded using amperometry. For this measurement, the cell was kept under constant stirring and 250 µL of a urea solution were added every 200 s with a pipette through the cell orifice.

The electrolyte consisted of 0.05 M of $KClO_4$ (referred as blank electrolyte), to which 0.05 M of urea or 0.025 M ammonium sulphate were added, unless otherwise stated. For the ammonia experiments the pH was adjusted to 10.5 using potassium hydroxide. The pH was adjusted using nitric acid or potassium hydroxide.

4.3.4 Oxidation experiments

The oxidation experiments were performed in a custom-made 3D printed PEC cell. The cell consisted of one compartment, and an irradiation window of 19.6 cm^2 (see Chapter 3. Materials and methods). A two electrode configuration was used with platinized titanium mesh as the cathode. The connection to this electrode was done with a platinum wire. For the photoanode, the P25 electrode, was deposited on a FTO of 7cm by 7 cm, the contact was done by pressing to a copper sheet which was integrated in the cell. For the TiNT electrode, 3 layers of titanium mesh were anodized and annealed following the same procedure as the foil (Chapter 3. Materials and methods). The contact for the TiNT electrode was done using platinum wire. The irradiation source used for these experiments was a 1000 W Xe lamp (Quantum Design, see Chapter 3. Materials and methods). The electrical bias was provided by a power supply (PHL120 DC Aim-TTi) and multimeters were used to record the potential and current (1351 Data precision).

To quantify the urea concentration over time, 1 mL was extracted every hour through the extraction port of the cell. A colorimetric method was used previously reported by Zawada *et al*. [30,31]. The products quantification (NH_4^+, NO_2^-, NO_3^-) was done following the protocols defined in ISO 15923-1. For these methods UV/Vis spectrometer (PerkinElmer) was used.

4.4 Results and discussion

4.4.1 Electrode morphology

The surface morphology of the immobilized P25 and TiNT electrodes was analysed using SEM (Figure 4-1 and 4-2). The images at low and high magnification of the P25 photoanode (Figure 4-1) showed agglomerates of small spherical P25 nanoparticles uniformly covering the FTO surface. Figure 4-2 displays the surface of the titanium foil covered with highly ordered TiNT at low and high magnification. An average size of the nanotube diameter of 99.89 nm ±14 nm was obtained from the particle size distribution resulted from more than 100 measurements, as shown in Figure 4-2. Length of the nanotubes varied between 3.3 μm and 3.5 μm, (Figure 4-2). The measured dimensions of the synthesized TiNT are comparable to other works that have employed similar anodization conditions (30V, 3 hours and 2 cm separation) [32–34].

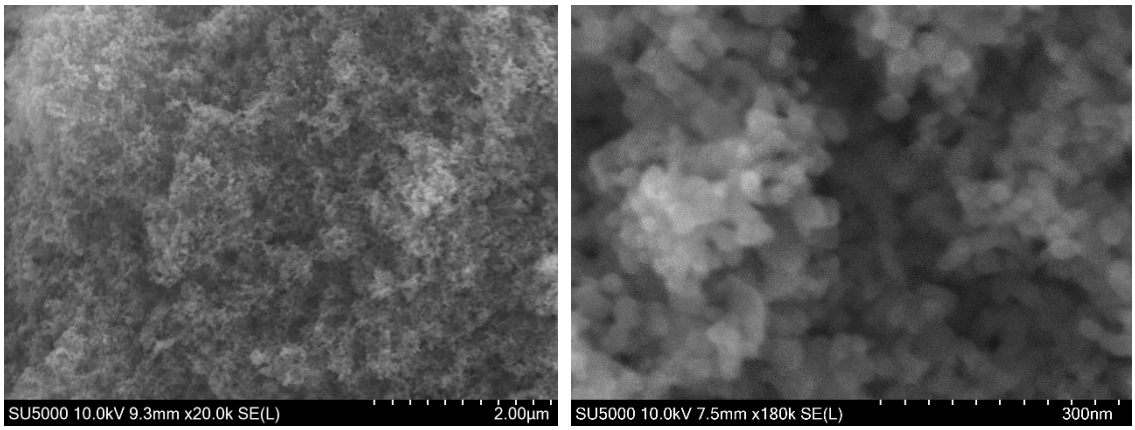

Figure 4-1- SEM images for the P25 photoanode at 20 k magnification (left) and 180k magnification (right).

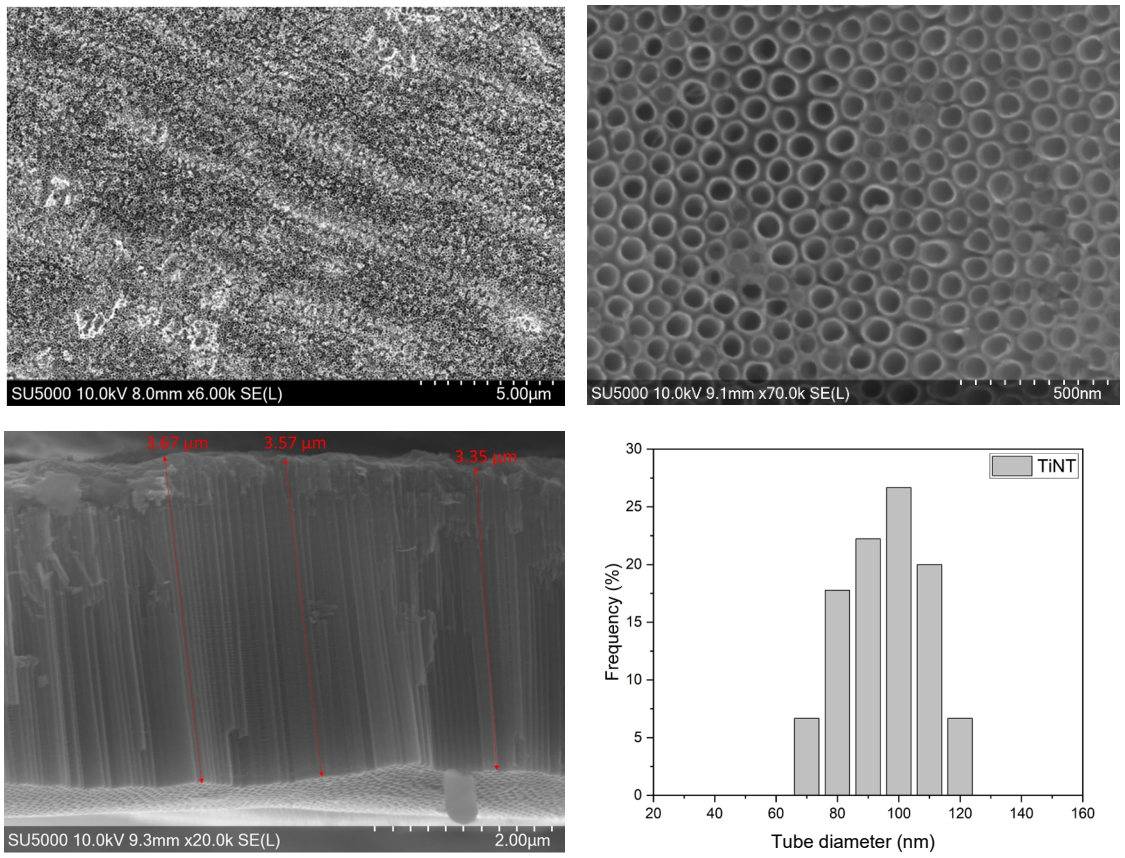

Figure 4-2 - SEM images of the TiNT photoanode at 10k magnification (top left), 100k magnification (top right), cross section for the inspection of the longitudinal dimension of the nanotubes (bottom left) and tube diameter size distribution (bottom right).

4.4.2 Diffuse reflectance spectroscopy

Diffuse reflectance measurements were performed to estimate the band gap energy of the TiO_2 nanostructured electrodes and a Tauc plot is shown in Figure 4-3. Due to the absorption of sub-band gap energy photons, a baseline was introduced to intercept the linear fitting, obtaining an optical band gap of 3.18 eV for the electrode formed by P25 deposited on FTO by spray coating [35]. This value is in agreement with reported values of 3.2 eV for anatase and 3.0 eV for rutile, with P25 being formed by a mixture of 80% anatase and 20% rutile [1]. TiNT electrodes synthesized by comparable conditions and annealing temperature to the ones used in this study have been reported to mainly be in anatase phase [13]. For the TiNT electrode, an estimated band gap of 3.24 eV was obtained (Figure 4-3), which is consistent with the anatase value of 3.2 eV reported in literature.

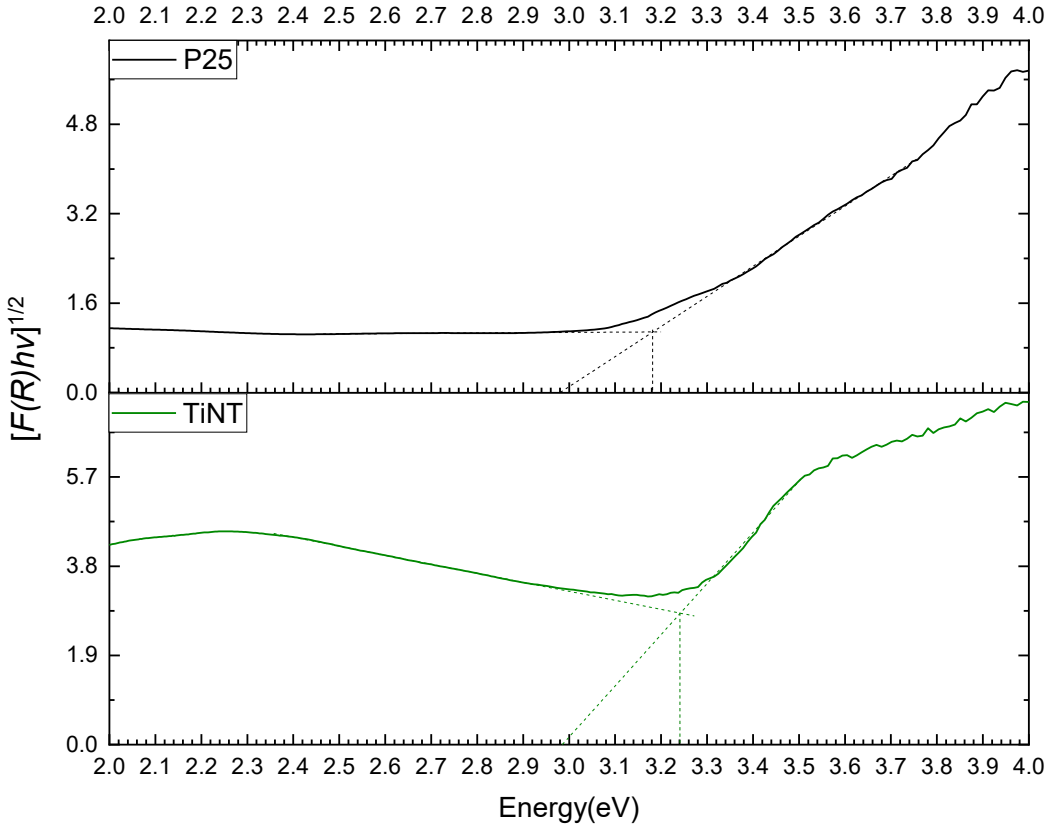

Figure 4-3. Tauc plots for the TiO_2 electrodes, P25 (black) and TiNT (green).

4.4.3 Photoelectrochemical characterization

4.4.3.1 Photoelectrochemical response of P25 and TiNT electrodes

To study the behaviour of the photoanodes at different potentials, LSV was performed from -1.0 to +1.0 V vs SCE. The LSV are shown in Figure 4-4. When a semiconductor is in contact with an electrolyte, a flow of charge between both phases occurs to achieve equilibrium. This forms the bending of the electronic band structure of the semiconductor, which is termed band bending. After this equilibrium is achieved, the region in the semiconductor that has been depleted from the majority carrier, is referred as space charge region or depletion layer. Band bending can be induced by metal or electrolyte contact, surface states, the absorption of molecule and applied bias. In the case of TiO_2 (n-type semiconductor), a positive applied bias increases the depletion layer, resulting in upwards band bending.

The results obtained (Figure 4-4) can be used to obtain the critical band bending ($\varnothing_s$) of each nanostructured TiO_2 electrode, $\varnothing_s$ is calculated by making the difference between the onset potential (close to flat band E_{fb}) and the potential required to obtain the maximum or saturated photocurrent (i.e., where all charge carriers are separated). The P25 photoanode showed an onset potential for anodic current of -0.65 V vs SCE while the saturated photocurrent is reached at a potential of -0.4 V, giving a $\varnothing_s$ of 0.15 V (Figure 4-4). On the other hand, for the TiNT electrode the anodic onset potential was -0.55 V vs SCE and the photocurrent increased with increasing potential up to 0.5 V, which results in a $\varnothing_s \sim 1.05$ V. In general, in bulk electrodes the separation photogenerated charges can be driven by the space charge layer, however, in the case of P25, being a porous particulate electrode, the electron hole pair separation is mainly driven by the reactivity of holes towards species in the solid electrolyte interface i.e. hole transfer kinetics. This explains why the P25 electrode has a smaller $\varnothing_s$. Conversely, in the case of the TiNT electrode, the ordered nanostructured tubes have a dimension larger than the space charge layer. Therefore, the potential induced band bending aids the charge separation and transport, showing the larger $\varnothing_s$.

Comparing the saturated photocurrent density obtained in each electrode, the P25 achieved 50 $\mu A.cm^{-2}$, and the TiNT 270 $\mu A.cm^{-2}$, which is 5 times higher than the P25 electrode. The photocurrent is a measurement of the CB electrons that are able to reach the conductive substrate and transfer to the counter electrode via an external circuit. There are various causes that impede the photogenerated electrons to reach supporting electrode, these include surface and bulk recombination, and electron scavenging by oxidants in the electrolyte, such as dissolved O_2. For the immobilised P25, the nanoparticles are isolated from each other, limiting the interparticle transfer of photogenerated electrons to the current collector. This charge transfer increases the probability of recombination at the interparticle boundary. In the case of the TiNT, the nanotubes provide a pathway along the longitudinal direction for charge transfer. This reduces the possibility of interparticle recombination, achieving higher photocurrent when, compared to P25.

The LSV of the TiNT (Figure 4-4) showed spikes upon illumination at potentials slightly higher than the onset (-0.5 V to -0.1 V). These spikes arise from the surface recombination with either surface-trapped holes or intermediates of the photooxidation [36]. At

potentials significatively higher (0.0 V to +1.0 V), the spikes are not present due to lower recombination.

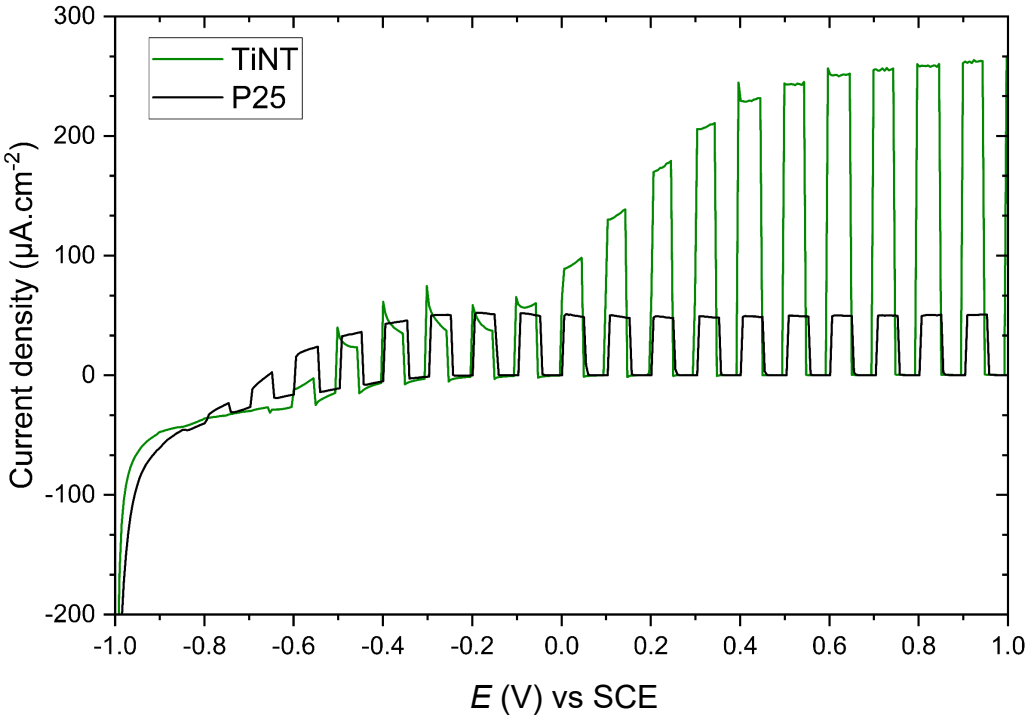

Figure 4-4. Linear sweep voltammetry from -1.0 V to +1.0 V for P25 (black) and TiNT (green), scan rate 5 mV/s, chopped irradiation (10s), Electrolyte = 0.05 M KClO4, I_0 (280-400 nm) = 44 W m^{-2}.

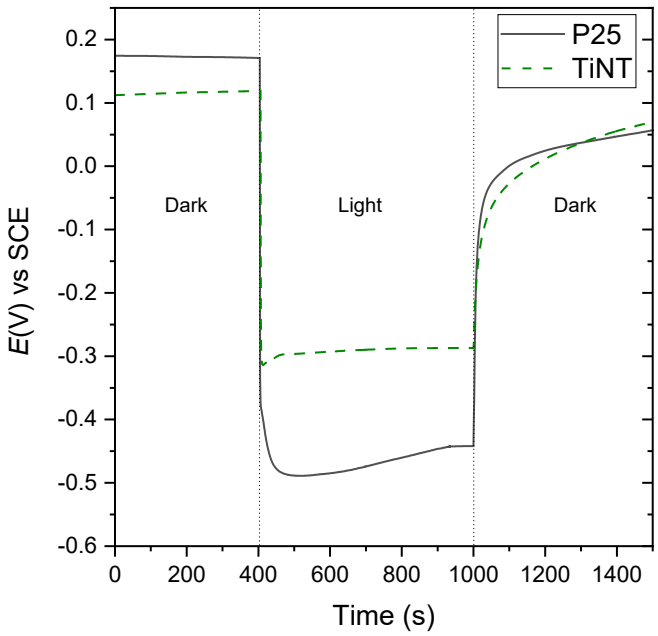

Figure 4-5. Open circuit potential for P25 (black) and TiNT (green) under dark and irradiation. I_0 (280-400 nm) = 44 W m^{-2}. Electrolyte = 0.05 M $KClO_4$.

The results from the OCP measurement are shown in Figure 4-5. When the semiconductor electrode is irradiated, the potential changes due to the generation of electron-hole pairs, when the rates of electron and hole transfer become equal a new equilibrium is achieved which is denoted as quasi-Fermi level. The difference between the dark Fermi level and the quasi-Fermi level is referred as open circuit photo-potential (E_{pho}). In the open circuit potential measurement, as there is no applied bias the conducting substrate (in this case FTO/Ti sheet) does not behave as electron sink as in photocurrent measurements. The potential measured corresponds to the potential of the conducting substrate equilibrated with the deposited TiO_2 layer. The counter electrode in these measurements is a Pt gauze.

In the obtained open circuit potential graph, four different regions can be differentiated (Figure 4-5). In the first one, the electrode is in steady-state in the dark, and the measured potential is dependent on the electrolyte. In this region, potentials +0.17 V (vs SCE) for P25 and + 0.12 V (vs SCE) for TiNT can observed. In the second region, one can observe a decrease in the open circuit potential (E_{ocp}). This indicates that the semiconductor film generates an excess of electrons under irradiation in non-steady conditions. After some time, in the third region, the steady state condition is reached under irradiation. The steady state potentials for the P25 and TiNT electrodes are -0.44 V (vs SCE) and -0.28 V (vs SCE), respectively; giving corresponding E_{pho} values of 0.61 and 0.40 V. In the last region, after turning off the irradiation, the electrode eventually reaches the steady state in the dark. The time required for that will vary depending on the redox processes occurring at the solid electrolyte interface, as interaction with water molecules. The measured E_{ocp} depends on the recombination and charge transfer rate to the interface. The results showed the P25 electrode reaching a more negative potential than TiNT, suggesting a higher hole transfer rate to the interface in P25. In addition, P25 contains a mixture of anatase and rutile, while the TiNT synthesized in similar conditions than this study is reported to be in anatase phase [13]. The mixture present in P25 might be responsible for electron trapping, shifting the photopotential to negative values.

The spectral photocurrent response of both P25 and TiNT photoanodes is shown in Figure 4-6. The P25 electrode showed a maximum photocurrent density of 27 $\mu A.cm^{-2}$ at a wavelength of 340 nm with 1.62 $\mu A.cm^{-2}$ at 390 nm. The TiNT electrode reached a maximum photocurrent of 103 $\mu A.cm^{-2}$ at 350 nm, which is 4 times higher than the one achieved with P25. For the TiNT electrode, a photocurrent of 5.12 $\mu A.cm^{-2}$ was recorded at 390 nm and 1.62 $\mu A.cm^{-2}$ at 400nm.

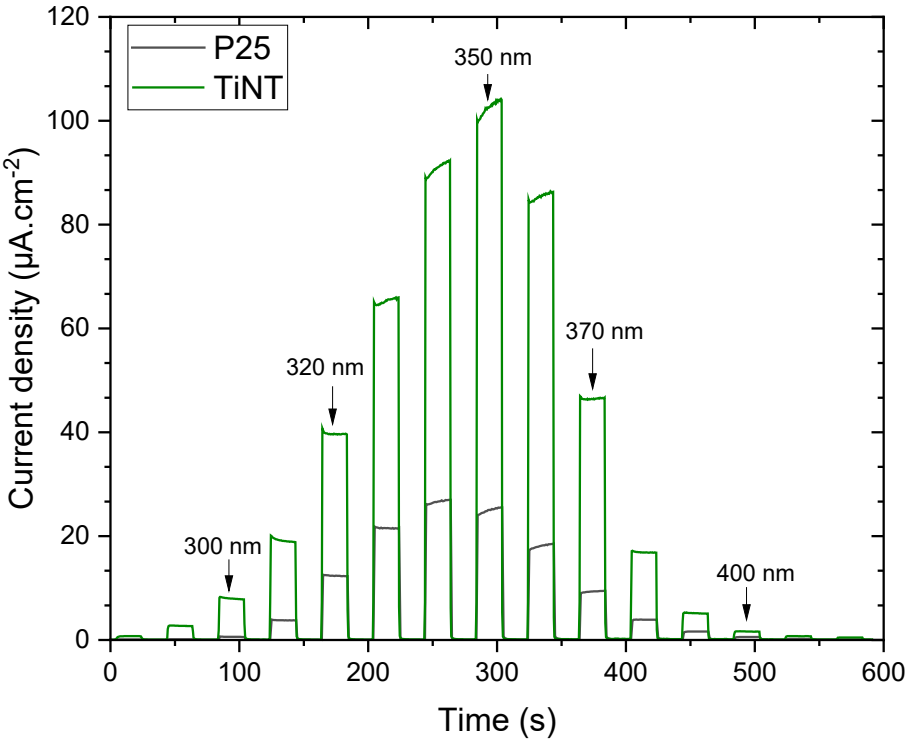

Figure 4-6. Spectral photocurrent density with monochromatic irradiation from 280 nm to 420 nm at a fixed potential of +1.0 V for P25 (black) and TiNT (green). Electrolyte = 0.05 M $KClO_4$. I_0 (280-400 nm) = 44 W m^{-2}.

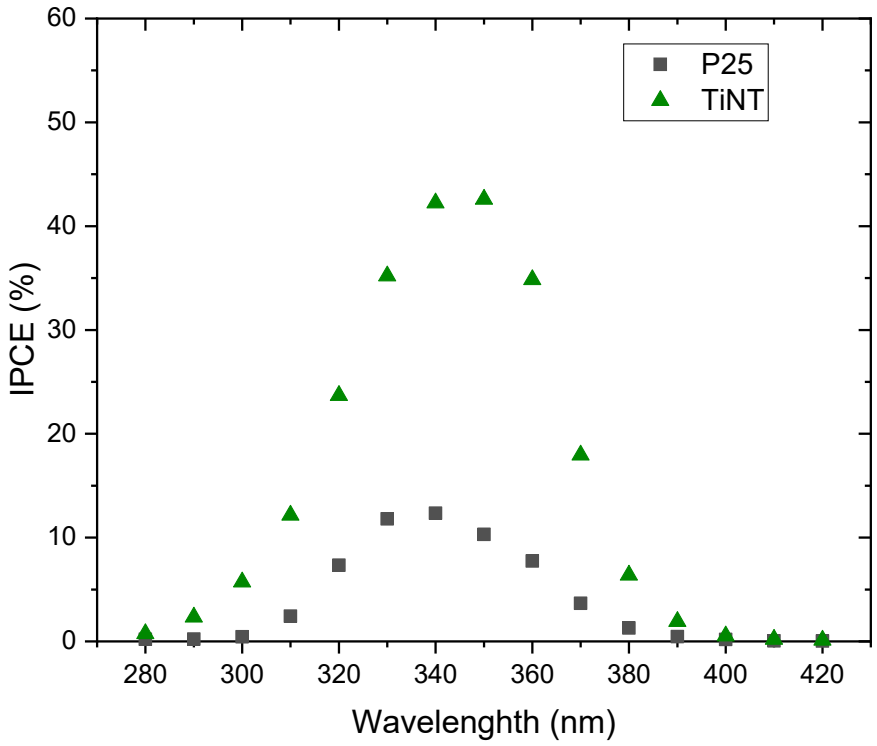

Figure 4-7. Incident photon-to-current efficiency (IPCE) for P25 and TiNT. I_0 (280-400 nm) = 44 W m^{-2}. Electrolyte = 0.05 M $KClO_4$.

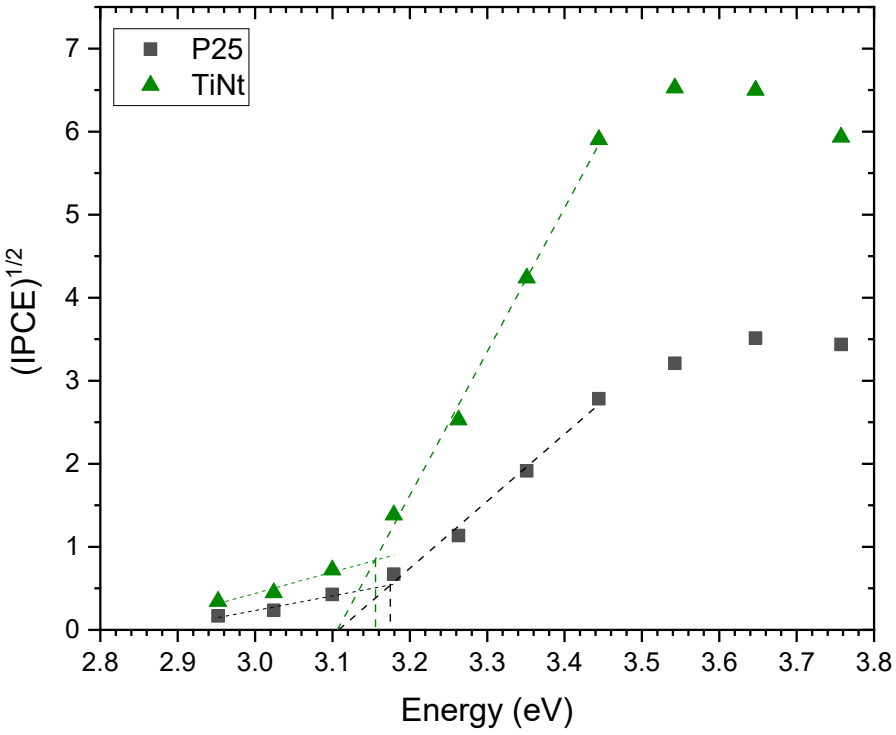

Figure 4-8. $(IPCE)^{1/2}$ vs *hv* plots for the P25 and TiNT electrodes.

The spectral photocurrent was used to calculate the IPCE for both photoanodes (Figure 4-7). The TiNT electrode reached an efficiency of 43 % at 350 nm, which is more than 3 times the one achieved by P25 (12 % at 340 nm). The IPCE values obtained for TiNT in this work are within the range of previously reported in works (35 % - 45 %) for similar fabrication and testing conditions [33,37,38]. The IPCE values reported in literature for P25 photoanodes vary in the range 10 - 25% [39–42], due to the different experimental conditions, including the electrode thickness, immobilization process and electrolyte; nevertheless, the value obtained in this study is within the range reported in comparable studies.

The IPCE values were used to estimate the effective indirect bandgap energy of the TiO_2 photoanodes, plotting the $(IPCE)^{1/2}$ vs wavelength in Figure 4-8 [43]. The P25 electrode presented an estimated bandgap of 3.18 eV which matches the value obtained in the Tauc plot using DRS (3.18 eV). The value obtained for the TiNT corresponds to a bandgap of 3.16 eV which, is a bit lower than the value that was obtained from the Tauc plot (3.24 eV) but in the same range. Therefore, it is possible to conclude that the band gap estimation performed from the measured optical absorption (calculated from the Tauc plot), is quite close to the experimental value that was obtained from the photocurrent

recorded from the excitation of the semiconductor under monochromatic irradiation (estimated using IPCE). That is, the optical gap is similar to the effective band gap.

This work shows that the main factor affecting the performance of the TiO_2 photoanodes is the morphology of their nanostructure. This nanostructure determines charge transfer, recombination rates and the possibility of inducing band bending through applied potential.

4.4.3.2 Photoelectrochemistry in presence of urea

The photocurrent measured in the presence of urea as function of electrolyte pH is shown in Figure 4-9. In these results, the recorded photocurrent is higher in presence of urea, compared to the blank electrolyte. The photocurrent value does not vary with different pH in the range (3-11); however, a decrease can be observed at pH 13. In general, the pH of domestic wastewater has been reported to be close to neutral, with values varying from 6 to 8 [44]. Therefore, since the results showed that the pH does not significatively affect photocurrent, a neutral pH will be used for the following sections of the study in presence of urea.

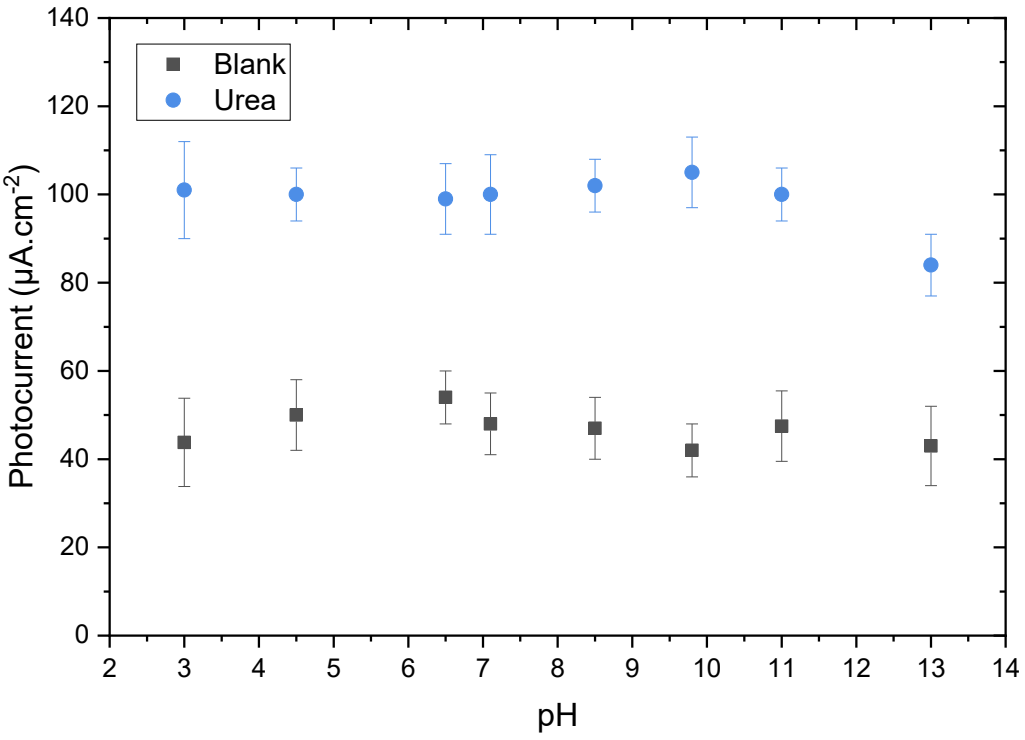

Figure 4-9. Photocurrent vs pH plot for urea. P25 electrode. I_0 (280-400 nm) = 44 W m^{-2}. Electrolyte = 0.05 M $KClO_4$ and 0.05 M Urea.

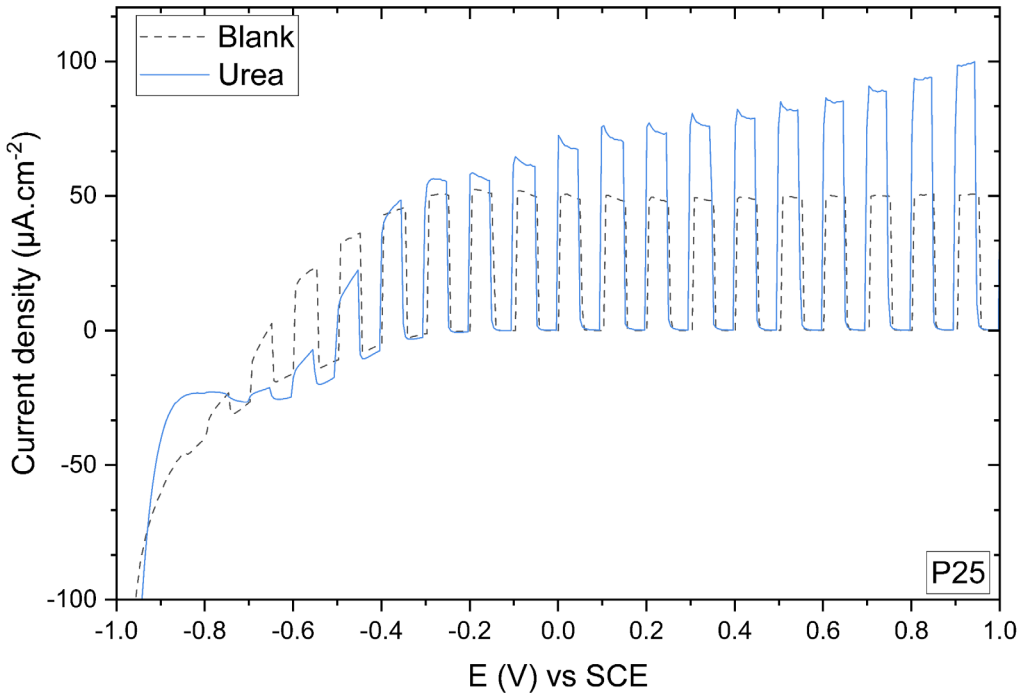

Figure 4-10. Linear sweep voltammetry for blank electrolyte (black), and added urea (blue), with P25 photoanode, scan rate 5 mV/s, chopped irradiation (10s), I_0 (280-400 nm) = 44 W m^{-2}. Electrolyte = 0.05 M $KClO_4$ and 0.05 M Urea.

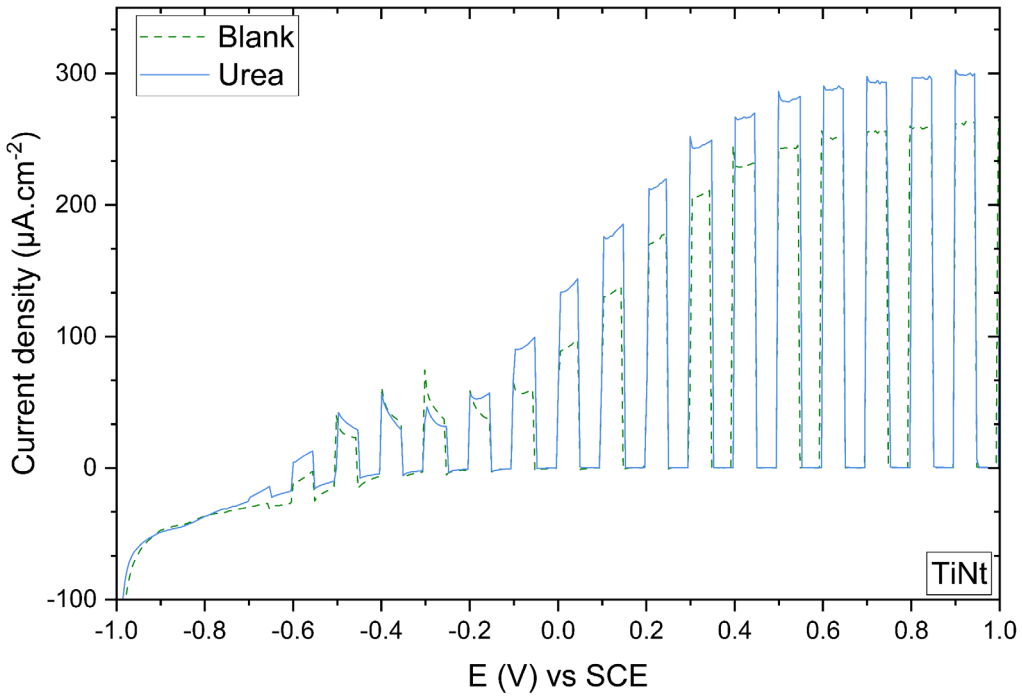

Figure 4-11. Linear sweep voltammetry for blank electrolyte (black), and with the addition of urea (blue), with TiNT photoanode, scan rate 5 mV/s, chopped irradiation (10s), I_0 (280-400 nm) = 44 W m^{-2}. Electrolyte = 0.05 M $KClO_4$ and 0.05 M Urea.

The photoelectrochemical response of the TiO_2 electrodes (P25 and TiNT) in the presence of urea was studied performing linear sweep voltammetry, comparing the measurements with the blank electrolyte (Figure 4-10 and Figure 4-11). For the P25 electrode the addition of urea, resulted in lower photocurrent densities, up to - 0.3 V vs SCE. However, at higher potentials, the photocurrent density increased with increasing potential, reaching 100 $\mu A.cm^{-2}$ at +1.0 V, which is double when compared to the blank electrolyte. The addition of urea did not produce any effects with TiNT electrode, until ca. -0.1 V. For more positive potentials, the photocurrent density in presence of urea resulted was 1.15 times higher, compared to the blank. The increase in photocurrent density upon addition of urea, observed for both electrodes, may be attributed to the holes being scavenged by the urea either via direct hole transfer or via hydroxyl radical mediated hole transfer. This scavenging action, results in lower recombination rates, with more photogenerated electrons reaching the conductive substrate and being transferred to the cathode. An increase in photocurrent with the addition of urea was reported in two studies using P25 [27,45]. Kim *et al*. reported a 3 times photocurrent rise when using a concentration of 0.33 M urea [45]. Lucian-Cristian *et al*. showed an increment varying from 15% to 35% with urea concentrations ranging from 0.1 to 1 M [27]. In the present study, using a urea concentration of 0.05 M, a 2-fold increase in photocurrent is observed with P25 and photoanode.

In order to study the effect of urea concentration in the photocurrent produced with the P25 photoanode and compare it with previously reported literature, an experiment was performed measuring the photocurrent under additions of urea every 200 s (Figure 4-12). The results showed that the photocurrent increased with rising urea concentration until a concentration of 0.017 M, where current saturation is achieved. Therefore, for the urea concentration used in this study, 0.05 M, it is possible to assume that current saturation is reached, corresponding to the highest possible enhancement cause by urea addition.

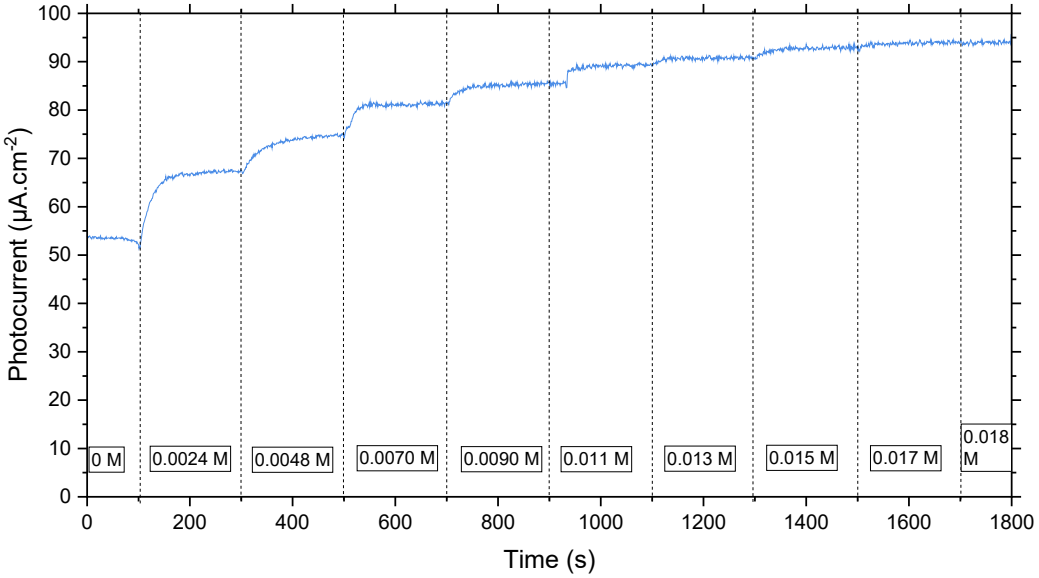

Figure 4-12. Photocurrent change with addition of urea concentration. From 0 to 0.0185 M of urea in 0.05 M $KClO_4$. I_0 (280-400 nm) = 44 W m^{-2}. E=+1.0 V. P25 photoanode. Under stirring.

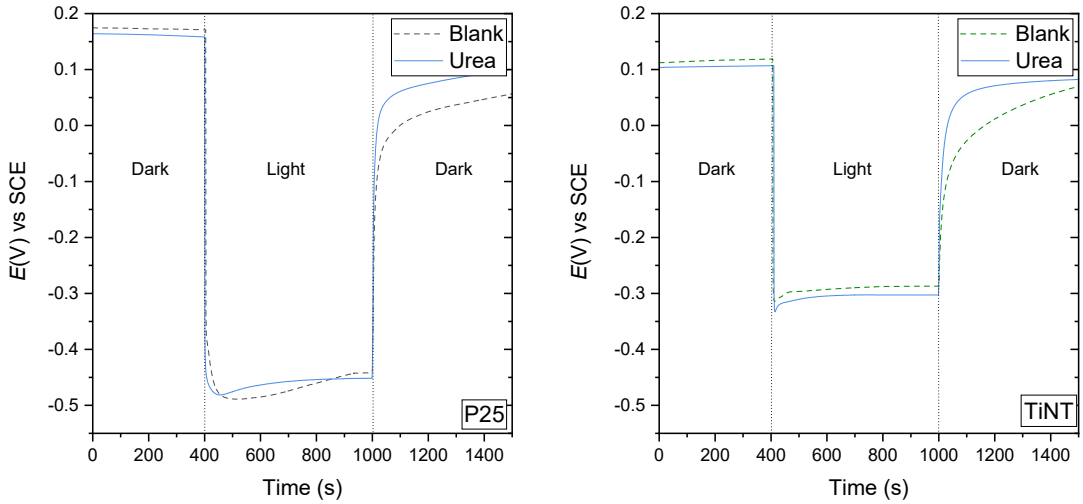

Figure 4-13. Open circuit potential for P25 (left) and TiNT (right) in presence (solid) and absence (dash) of urea under dark and irradiation. I_0 (280-400 nm) = 44 W m^{-2}. Electrolyte = 0.05 M $KClO_4$ and 0.05 M Urea.

The effect of the addition of urea in the open-circuit potential (E_{ocp}) and open-circuit photopotential (E_{pho}) is shown in Figure 4-13. These results showed no significant variation in presence of urea when compared to the blank electrolyte, suggesting no significative change in hole transfer rate to the interface, which generates a similar excess of electrons, showing a comparable negative potential.

The spectral photocurrent response was recorded under wavelengths varying from 280 nm to 420 nm, using intervals of 20 s. For the P25 electrode, the addition of urea resulted in an increase in the maximum photocurrent density from 25 $\mu A.cm^{-2}$ to 45 $\mu A.cm^{-2}$ at 340 nm (Figure 4-14). For the TiNT electrode, the photocurrent increased from 100 $\mu A.cm^{-2}$ to 120 $\mu A.cm^{-2}$ at 350 nm (Figure 4-15). Using the spectral photocurrent, the increase in IPCE in the presence of urea for both photoanodes was calculated (Figure 4-16). The highest efficiency was recorded with the TiNT nanotube electrode, reaching 55.11 % at 340 nm, which is 13 % more than the efficiency that is obtained with the TiNT without urea. For the P25 electrode, a maximum efficiency of 21.22 % was achieved at 330 nm with urea, resulting in 10 % increased efficiency when compared to the P25 in the absence of urea. Comparing both electrodes, TiNT gave more than double the IPCE of P25.

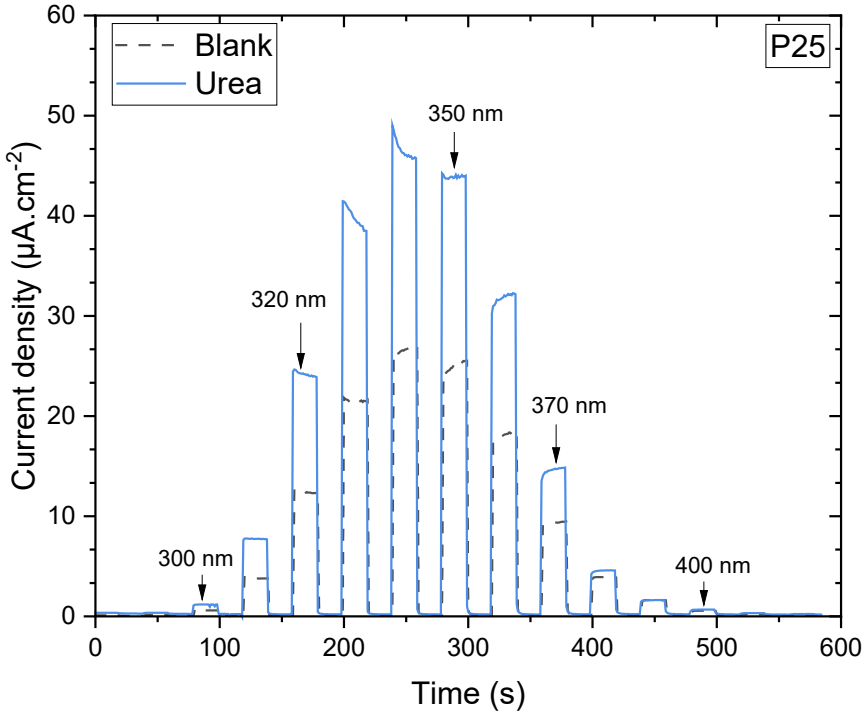

Figure 4-14. Spectral photocurrent density with monochromatic irradiation from 280 nm to 420 nm at +1.0 V for blank electrolyte (black) and added urea (blue). P25 electrode. I_0 (280-400 nm) = 44 W m^{-2}. Electrolyte = 0.05 M $KClO_4$ and 0.05 M Urea.

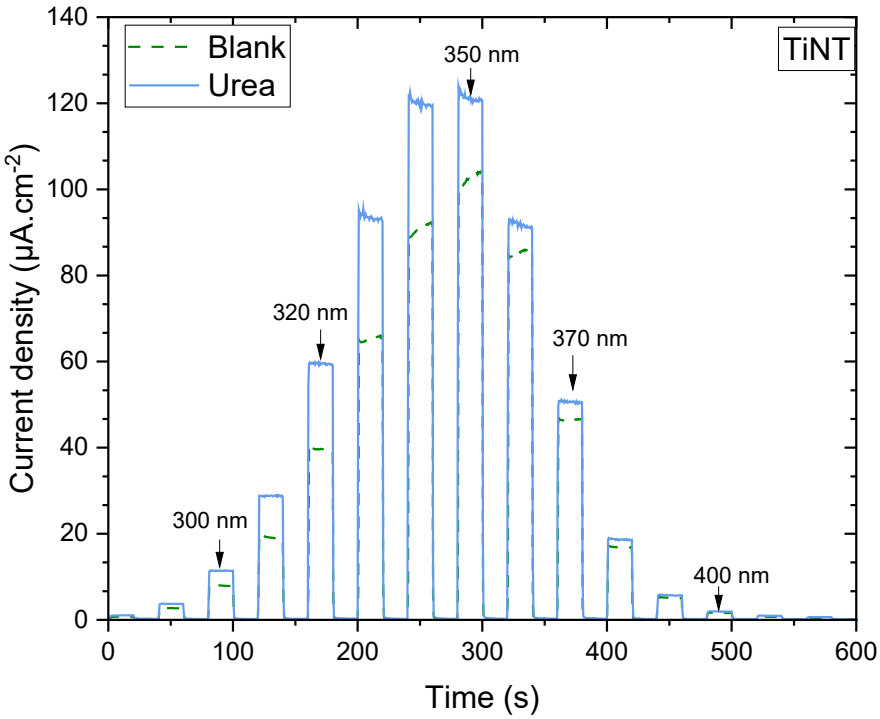

Figure 4-15. Spectral photocurrent density with monochromatic irradiation from 280 nm to 420 nm at + 1.0 V for blank electrolyte (black) and added urea (blue). TiNT electrode. I_0 (280-400 nm) = 44 W m^{-2}. Electrolyte = 0.05 M $KClO_4$ and 0.05 M Urea.

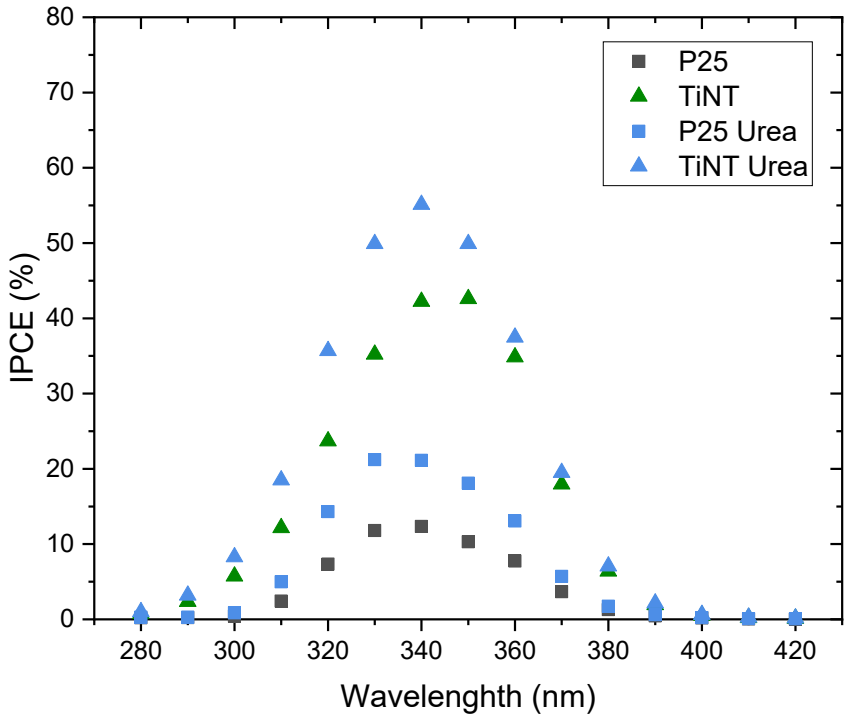

Figure 4-16. Incident photon-to-current efficiency (IPCE) for P25 and TiNT in presence and absence of urea. I_0 (280-400 nm) = 44 W m^{-2}. Electrolyte = 0.05 M $KClO_4$ and 0.05 M Urea.

4.4.3.3 Photoelectrochemistry in the presence of ammonia

In water, un-ionized ammonia (NH_3) exists in equilibrium with ionized ammonium (NH_4^+). This equilibrium is pH dependent and has a pKa of 9.25. When the pH is lower than 9.25, NH_4^+ is the majority form, while at higher pH than the pKa, NH_3 is the dominant form. To study the effect of the pH on the photocurrent, several linear sweep voltammetries were taken at different pH. The photocurrent as a function of the solution pH in presence of ammonia is shown in Figure 4-17. The results showed an increase in photocurrent when the solution pH is higher than 8, which peaks at a pH around 10.5. This observation, clearly proves a higher photocurrent when ammonia is in un-ionized form (NH_3), showing more efficient hole scavenging at these conditions. The obtained result is consistent with previous TiO_2 photocatalytic studies using suspension, which report the highest oxidation with molecular ammonia at pH between 10 to 11 [24,25].

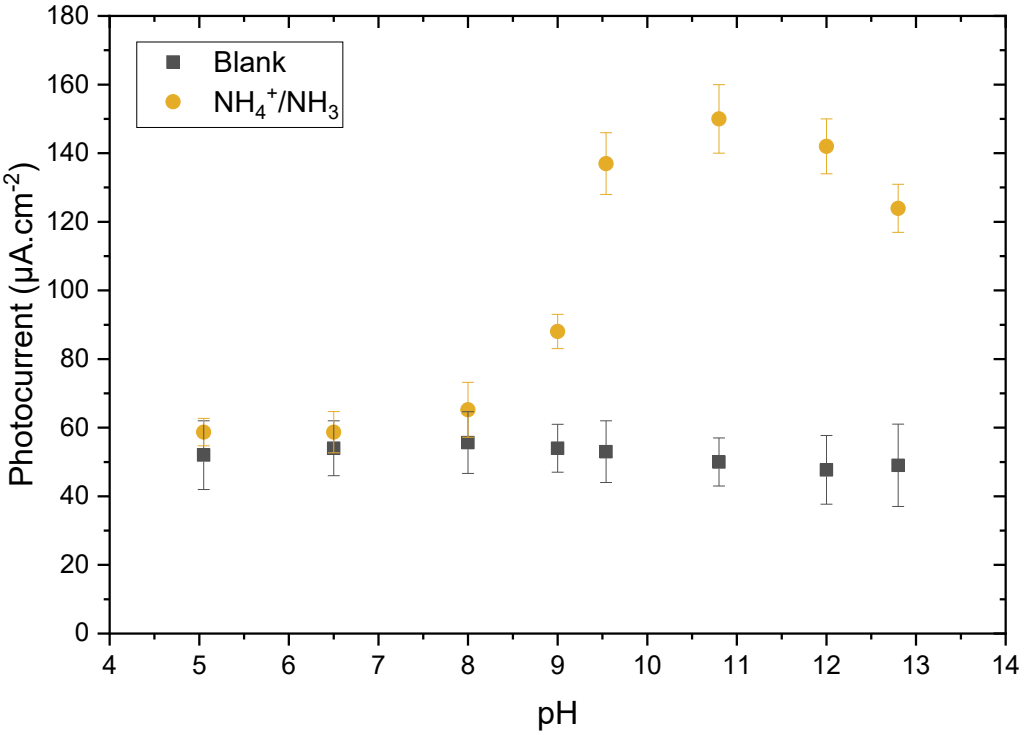

Figure 4-17. Photocurrent vs pH plot for NH_4^+/NH_3. P25 electrode. I_0 (280-400 nm) = 44 W m^{-2}. NH_4^+/NH_3 pKa= 9.25. Electrolyte = 0.05 M $KClO_4$ and 0.05 M NH_3/NH_4^+.

Taking into account the possible preferential adsorption of NH_4^+ or NH_3 into the surface of the nanoparticulated P25 anode. An indication on the reactants adsorption based on the catalyst surface charge, can be obtained from the point of zero charge (pzc). The pzc indicates the pH at which the net charge of the particle surface is equal to zero. For P25, it has been reported to be around pH of 6.5. This means that at pH lower than 6.5, the TiO_2 surface should be positively charged, while at higher pH the surface is negatively charged. Therefore, at pH lower than 6.5 both the semiconductor and the NH_4^+ are positively charged, exercising a repelling force, thus hindering adsorption. For pH values between 6.5 and 9.25, the TiO_2 surface is negatively charged, and the equilibrium sifted to NH_4^+. Therefore, in this range, one can expect favoured attraction and adsorption. However, the highest photocurrent is observed at pH higher than 9.25, corresponding to mainly NH_3 neutral form and negatively charged P25 surface. Nevertheless, it is also necessary to consider that the P25 photoelectrode is under potentiostatic conditions and irradiation, which also have additional influence on the surface charge. In particular, the

applied anodic potential might result in the FTO to be positively charged, with the P25 charge depending in the electron transfer rate to the FTO, resulting in a more complex process.

With the purpose of studying the photoelectrochemical behaviour of the TiO_2 electrodes in the presence of ammonia, linear sweep voltammetry and open circuit voltage measurements were performed adding ammonia to the electrolyte. For these experiments, a pH of 10.5 was chosen, corresponding to the highest photocurrent observed from the pH study of Figure 4-17.

For the P25 electrode, the LSV in the presence of ammonia showed an increase in photocurrent density for the whole potential range, when compared to the blank. This corresponds to a 3 times enhancement in photocurrent, reaching values of about 160 μA cm^{-2}. For TiNT electrode, the presence of NH_3 also showed a higher photocurrent density, reaching maximum value of 361 $\mu A.cm^{-2}$, as compared to the 262 $\mu A.cm^{-2}$ reached with the blank. Other studies also reported more than 2-fold increase in photocurrent in the presence of some inorganic and organic substances [46–48]. The remarkable enhancement in the photocurrent can be attributed to a more efficient scavenging of the photogenerated hole by the compounds. Moreover, in some particular cases some of these substances have been referred as current doublers, showing how the number of electrons produced by these substances is higher than the number of absorbed photons (sometimes showing IPCE values even higher than 100 %) [49]. This current doubling process is explained by the formation of unstable radicals that inject additional electrons in the CB. In this way, a hole can generate two conduction electrons, one photogenerated and one injected, resulting in the observed doubling of the current. However, the current doubling process is not easily differentiable from other processes, as semiconductors also have extensive electron-hole recombination. In the present study, even if ammonia resulted in 3 times an increase in photocurrent using the P25 photoanode, the increase observed with TiNT was less than double (1.4 times). Therefore, the 3-fold increase in the P25 is likely produced by increased rate of hole scavenging reducing the rate of surface recombination reactions.

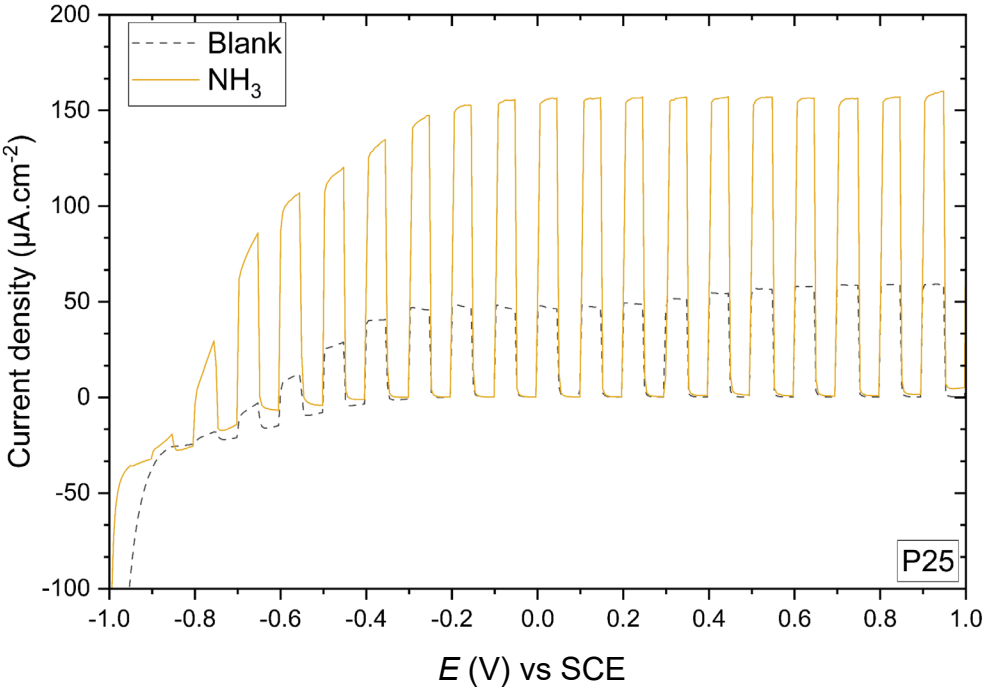

Figure 4-18. Linear sweep voltammetry for blank electrolyte (black), and added ammonia (orange) with P25 photoanode, scan rate 5 mVs^{-1}, chopped irradiation (10s), I_0 (280-400 nm) = 44 W m^{-2}. Electrolyte = 0.05 M $KClO_4$ and 0.05 M NH_3.

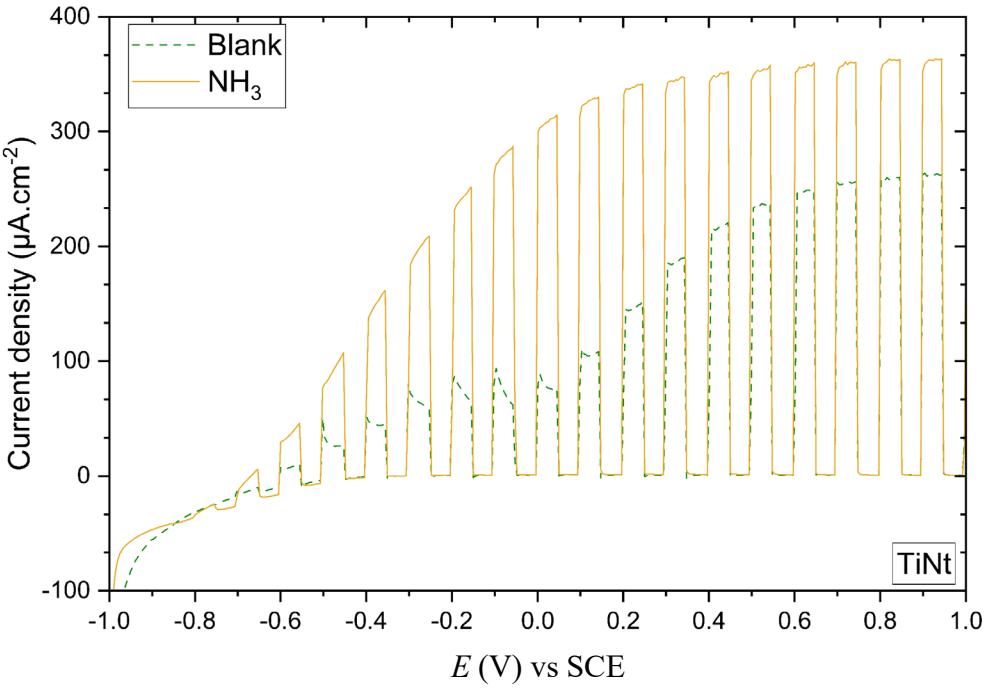

Figure 4-19. Linear sweep voltammetry for blank electrolyte (black), and added ammonia (orange), with TiNT photoanode, scan rate 5 mVs^{-1}, chopped irradiation (10s), I_0 (280-400 nm) = 44 W m^{-2}. Electrolyte = 0.05 M $KClO_4$ and 0.05 M NH_3.

The NH_3 present in the electrolyte resulted in a higher rate of hole transfer to the interface, generating a higher excess of conduction band electrons, as suggested from the results of the open circuit measurements presented in Figure 4-20. A larger difference is observed for the P25 electrode, which could be due its high porosity, with higher number of holes being transferred to the interface in comparison with TiNT. P25 particulate films have a very high specific surface area estimated to be in the region of 1000 times larger than the geometric area [50].

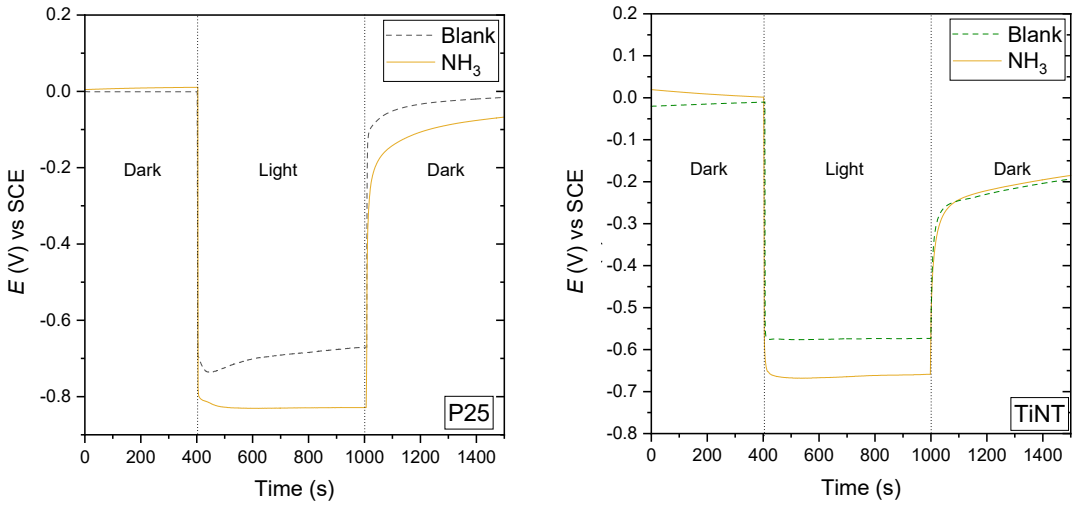

Figure 4-20. Open circuit potential for P25 (left) and TiNT (right) in presence (solid) and absence (dash) of ammonia under dark and irradiation. I_0 (280-400 nm) = 44 W m^{-2}. Electrolyte = 0.05 M $KClO_4$ and 0.05 M NH_3.

In order to study the effect of the presence of NH_3 in the photocurrent at each wavelength, the spectral photocurrent was measured and IPCE efficiency calculated. For the P25 electrode, the addition of ammonia results in an increase in the maximum photocurrent density from 27 µA cm^{-2} to 68 µA cm^{-2} at 340 nm. For the TiNT electrode at 350 nm the photocurrent increased from 150 µA cm^{-2} to 100 µA cm^{-2} at 350 nm. The highest efficiency was achieved with the TiNT nanotube electrode, reaching 65 % at 340 nm, which is 23 % higher than in the absence of ammonia. For the P25 electrode, a maximum efficiency of 30 % was achieved at 330 nm with NH_3, corresponding to 18 % increased efficiency compared to the blank electrolyte. Thus, TiNT can achieve more than 5 times the IPCE when compared to P25 in the presence of ammonia.

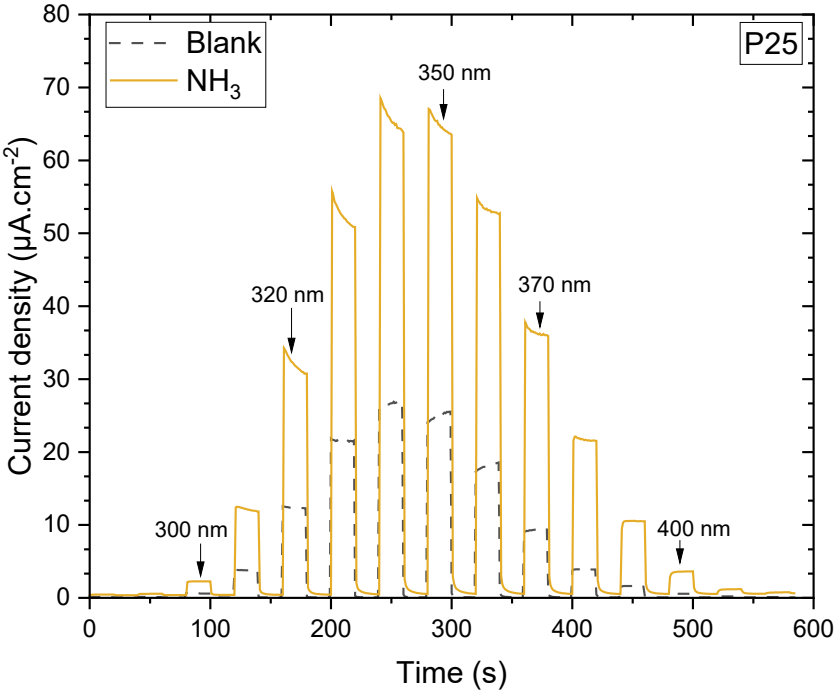

Figure 4-21. Spectral photocurrent density with monochromatic irradiation from 280 nm to 420 nm +1.0 V for blank electrolyte (black) and added ammonia (orange). P25 electrode. I_0 (280-400 nm) = 44 W m^{-2}. Electrolyte = 0.05 M $KClO_4$ and 0.05 M NH_3.

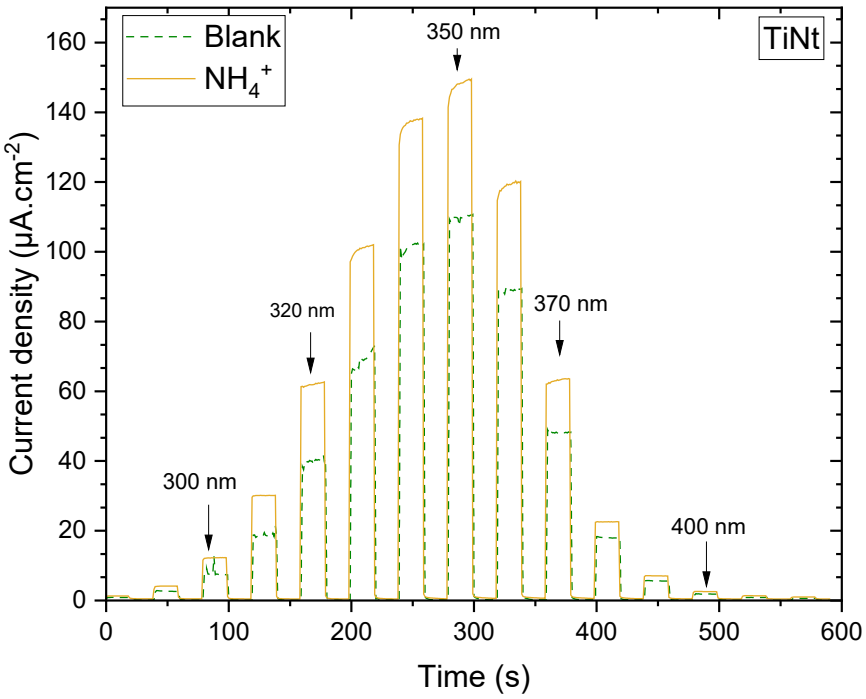

Figure 4-22. Spectral photocurrent density with monochromatic irradiation from 280 nm to 420 nm +1.0 V for blank electrolyte (black) and added ammonia (orange). TiNT electrode. I_0 (280-400 nm) = 44 W m^{-2}. Electrolyte = 0.05 M $KClO_4$ and 0.05 M NH_3.

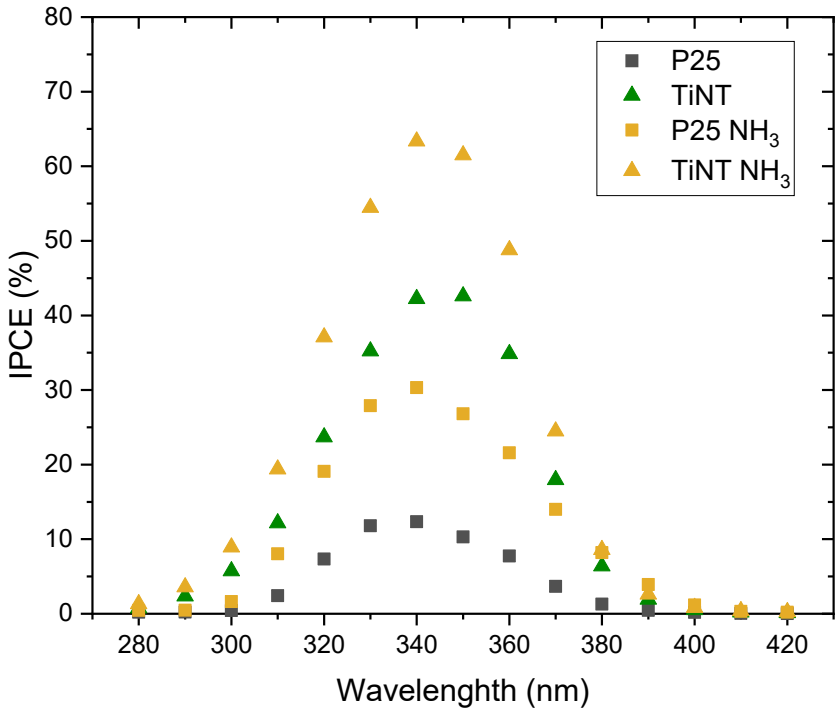

Figure 4-23. Incident photon-to-current efficiency (IPCE) for P25 and TiNT in absence and presence of NH_3. I_0 (280-400 nm) = 44 W m^{-2}. Electrolyte = 0.05 M $KClO_4$ and 0.05 M NH_3.

The present study has demonstrated an enhancement of the PEC process in the presence of ammonia and urea, showing a considerable increment in photocurrent for both TiO_2 photoanodes (P25 and TiNT). This increase in photocurrent was explained by more efficient scavenging of the photogenerated hole by the added substances either directly or mediated by hydroxyl radicals. The variation in pH had no effect on the photocurrent achieved in presence of urea, however, in the presence of ammonia the photocurrent was pH dependent, with the highest achieved at 10.5, which correspond to NH_3 in neutral form. From both electrodes, the highest efficiency was obtained with the TiNT in presence of urea, with a 55 % efficiency achieved with urea and a 65 % with ammonia. However, it is necessary to take into account that the 65 % efficiency was obtained with NH_3 at pH of 10.5. If this approach was to be used to treat wastewater, then a pH correction would be necessary. Consequently, the following section of this chapter will study the oxidation of urea, as its application would not involve the pH adjustment of the wastewater.

4.4.4 Photoelectrocatalytic oxidation of urea

In order to study the oxidation of urea, its reaction kinetics and the resulting products, a custom-made scale-up photoelectrochemical cell was built with an irradiation area of 19.6 cm^2 (Chapter 2. Materials and methods, Figure 3-6).

A larger P25 electrode was fabricated using same immobilization method previously adopted in this study, but on a larger FTO glass of 7 cm x 7 cm (details in experimental section). However, since the TiNT electrode was fabricated by growing the nanotubes on a foil and used in a front irradiation configuration. Thus, the scale up of this electrode to a size that would cover all the window area, using front irradiation, would create mass transfer problems between the anode and the cathode. For this reason, a titanium mesh was chosen instead of a titanium foil, allowing a better mass transfer of reactants and products. Since the mesh has an open area, limiting the area for photon absorption, several meshes were layered on top of one another. Previous studies have utilized titanium meshes in scaled-up reactors, concluding that the use of 3 layers resulted in the higher performance [33]. Consequently, the TiNT photoanode for this study was formed by 3 layers of mesh. A schematic representation of the layered meshes is shown in Figure 4-24. One mesh with 0.2 mm diameter has an open area of 53 %, with three layers it is reduced to 2% (assuming a 100 % alignment) [33].

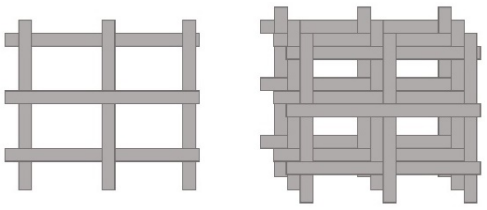

Figure 4-24. Schematic representation of the layered mesh with 100% alignment for 1 mesh (left) and 3 meshes (right).

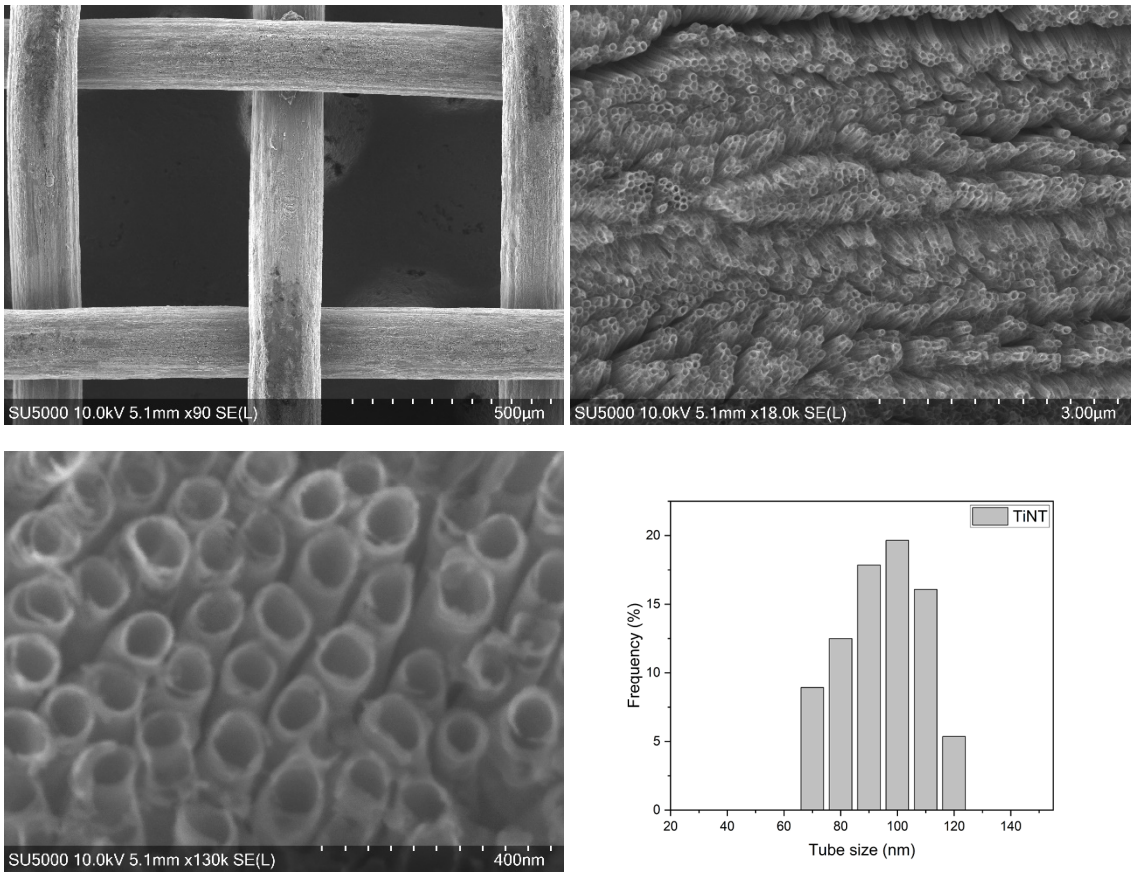

Figure 4-25. SEM images of TiNT mesh at magnifications of 90 (top left), 18k (top rigth) and 130k (bottom left) and the size distribution of the tube diameter (bottom rigth).

SEM images of the TiNT mesh at different magnifications (90, 18k and 130k) are shown in Figure 4-25. The mesh electrode had a mean tube diameter of 94.31 nm with a standard deviation of 19.26 nm (Figure 4-25). For the TiNT foil (section 4.4.1), an average diameter of 99.89 nm and a standard deviation of 14 nm were obtained (Figure 4-2). Therefore, it can be concluded that both titanium substrates produce comparable nanotubes.

The performance of P25 and TiNT electrodes in the custom-made PEC cell was studied varying the applied cell potential between the photoanode and the platinized titanium mesh cathode. For the P25 electrode, the current increased with the increasing cell potential, under dark, current breakdown was observed at a potential around + 1.2 V (Figure 4-26). Therefore, this potential was chosen to operate the system with this electrode, reaching a current of 1 mA. For the TiNT electrode, current increases with

increasing applied potential, obtaining a saturated current after potential of + 1.4 V, which was chosen as the operational cell potential for this electrode. The photocurrent achieved at this potential was 4.3 mA (Figure 4-27).

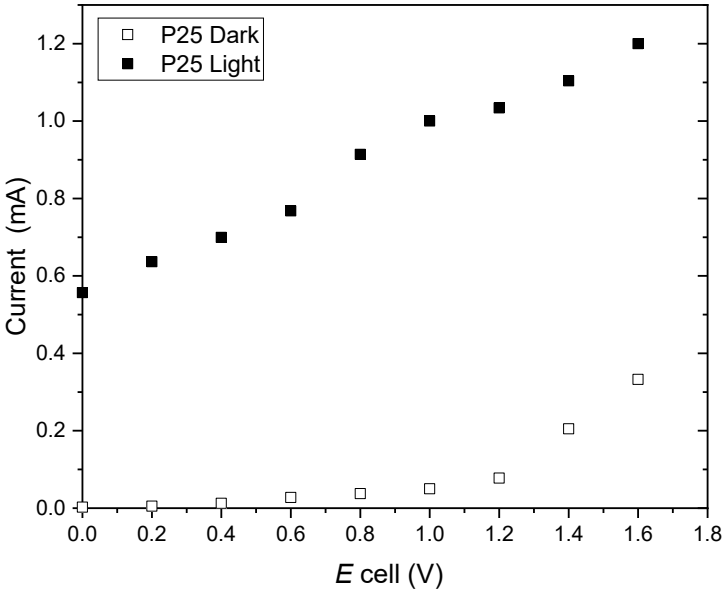

Figure 4-26. Current for P25 electrode at different cell potentials for light and dark. Measured carried in the 1-compartmet customized PEC cell. I_0 (280-400 nm) = 47 W m^{-2}. Anode geometrical area = 19.6 cm^{-2}. Electrolyte = 50mM $KClO_4$ and 0.33 mM Urea.

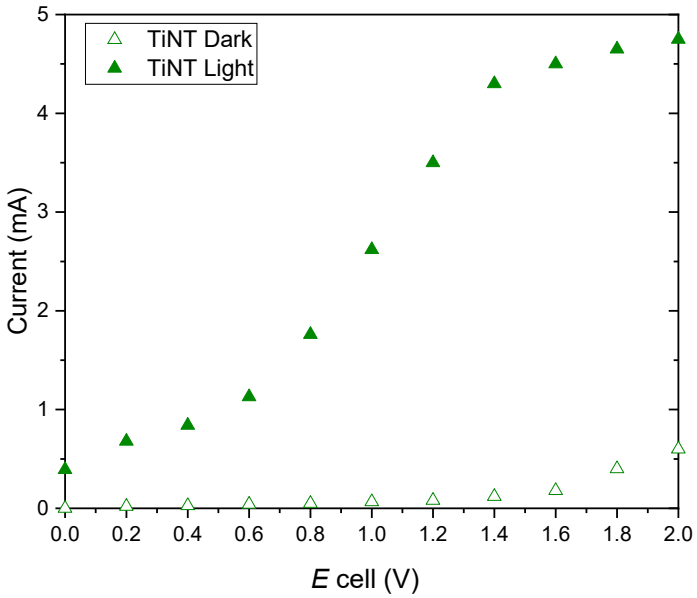

Figure 4-27. Measured current for TiNT electrode at different cell potentials for light and dark. Measured carried in the 1-compartmet customized PEC cell. I_0 (280-400 nm) = 47 W m^{-2}. Anode geometrical area = 19.6 cm^{-2}. Electrolyte = 50mM $KClO_4$ and 0.33 mM Urea.

The activity of both electrodes for the oxidation of urea was studied over a period of 4 h (Figure 4-28). The experimental urea oxidation data was fitted to a pseudo-first-order kinetic model (Figure 4-29) where C_0 is the initial concentration and Ct the concentration that was measured at time t. For the TiNT electrode a rate constant (k_1) of 0.0037 min^{-1} was obtained, which is almost 2 times the rate obtained for P25 (0.0021 min^{-1}).

Moreover, to further study the enhancement produced by the applied potential working in PEC configuration, additional experiments were performed in photocatalytic (PC) configuration with the cell at open circuit (Figure 4-28). For the TiNT PC, only a 0.0002 min^{-1} urea oxidation rate constant, which is a considerable difference when compared to the 0.0037 min^{-1} obtained in PEC with applied bias. This increase in oxidation highlights the benefit of using an applied bias, which drives electrons to the cathode, reducing recombination and leaving an increased number of holes available for the oxidation of urea. For the P25 electrode, the difference between PC (0.0012 min^{-1}) and PEC (0.0021 min^{-1}) was smaller. In this case the use of applied bias produced a much lower improvement on the urea oxidation rate constant (1.8 times), when compared to the TiNT electrode. This limited enhancement might be due to the P25 having a morphology that hinders electron transfer, favouring surface interparticle recombination, as discussed in section 4.4.3 Photoelectrochemical characterization. One should also note that the P25 electrode in PC configuration obtained more than 3-fold the degradation rate of TiNT. This can be explained, as in P25 the high porosity the holes are easily scavenged by the urea. Besides, the rutile anatase mixture present in P25 might help to separate the photogenerated charges, reducing recombination.

From the obtained results, a correlation between photocurrent (1 mA for P25 and 4.3 mA for TiNT) and urea oxidation rate (0.0021 min^{-1} for P25 and 0.0037 min^{-1} for TiNT) could not be extrapolated. As such, TiNT, showed 4.3 times higher photocurrent but only 1.8 times higher oxidation rate. This could be explained by the fact that the P25 nanoparticles have a high urea oxidation rate without the applied bias, in comparison to TiNT.

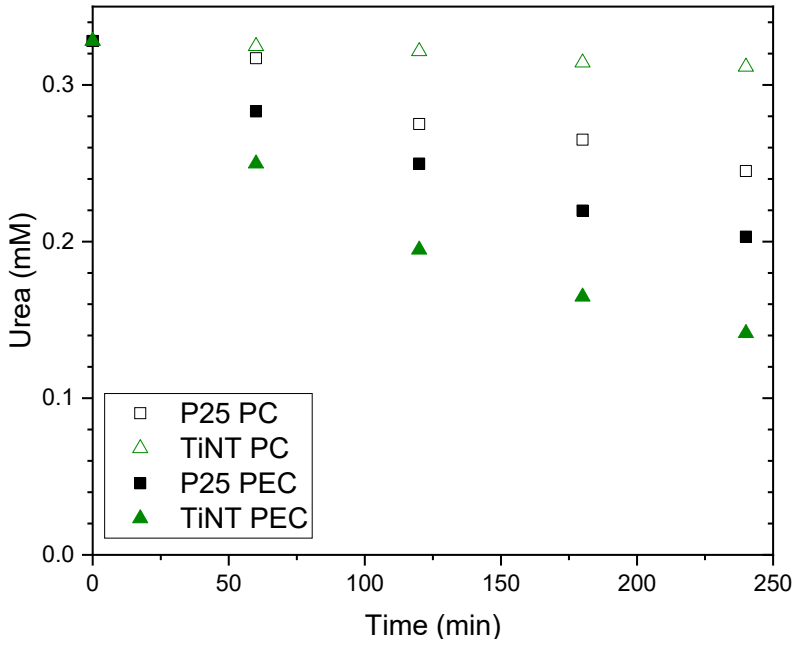

Figure 4-28. Concentration vs time for P25 and TiNt in both PEC and PC configurations. Measurement carried in the 1-compartmet customized PEC cell. I_0 (280-400 nm) = 47 W m^{-2}. Anode geometrical area = 19.6 cm^{-2}. Electrolyte = 50mM $KClO_4$ and 0.33 mM Urea.

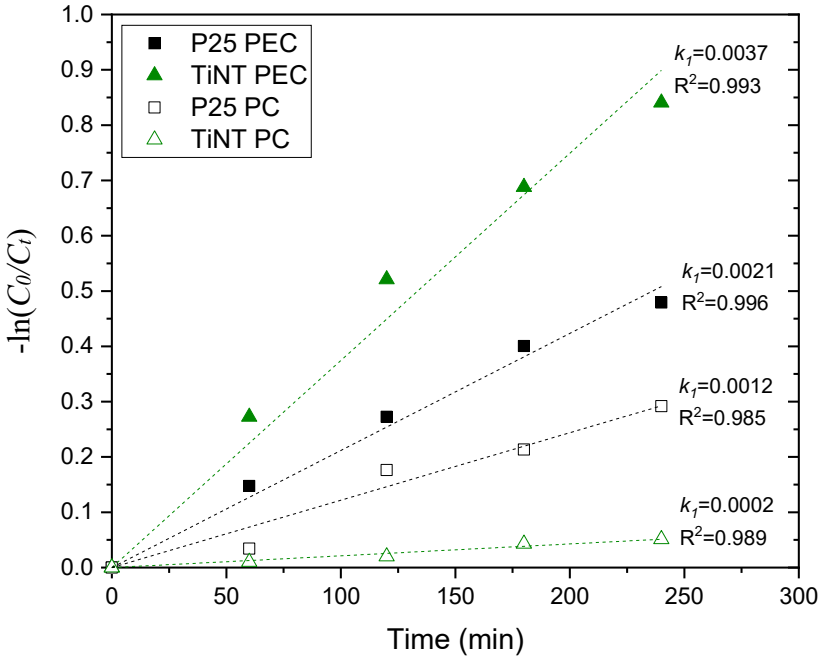

Figure 4-29. Negative natural log of normalized concentration vs time for P25 and TiNT in both PEC and PC configurations. Measurement carried in the 1-compartmet customized PEC cell. I_0 (280-400 nm) = 47 W m^{-2}. Anode geometrical area = 19.6 cm^{-2}. Electrolyte = 50mM $KClO_4$ and 0.33 mM Urea.

The analysis of the products from the photoelectrochemical urea oxidation indicated that NO_3^- and NH_4^+ were the major products, with low concentrations of NO_2^- ($5.1x10^{-3}$ mM) for P25 below the detection limit(LOD_{NO2^-} =$1x10^{-4}$ mM) for TiNT (Figure 4-30, Figure 4-31).

Previous reports have identified NO_3^- and NH_4^+ as main products in the oxidation of urea, with hydroxyl radicals (•OH) having a key role in this reaction [20–22]. A mechanism for the photocatalytic oxidation of urea by suspended TiO_2, was reported by Pelizzetti *et al.* [20]. In this mechanism, •OH radicals attack the ammino group of urea to convert the nitroso group into a nitro group, following a release of NO_2^- ions, which get oxidize to NO_3^-. The carbamic acid can experience two different reactions. One option, consider the production of NO_2^- and NO_3^- after several oxidations with •OH radicals. The second proposed option, results into the formation of HCO_3^- and NH_4^+ by simultaneous attack of •OH and e^- (more information of this mechanism can be found in section 2.4.1.2 Urea and Figure 2-7). The molar ration between NO_3^-/NH_4^+ can reveal the favoured reaction. Some studies have reported the use of suspended TiO_2 for the photocatalytic oxidation of urea to result in NO_3^-/NH_4^+ molar ratios of 2 [21] and 1.9 [22],

In the present study, the molar ratio NO_3^-/NH_4^+ from the photoelectrochemical oxidation of urea was different for each nanostructured TiO_2 electrode. The molar ratio measured using P25 was 1.1, while with TiNT it was 0.5. This observation suggests that different reaction pathways occur with these photoanodes. It is important to consider that beside the proposed urea oxidation mechanism, NO_3^- can be reduced to form NH_4^+, either from the photogenerated electrons in the anode or the electrons transferred to the cathode through the external circuit.

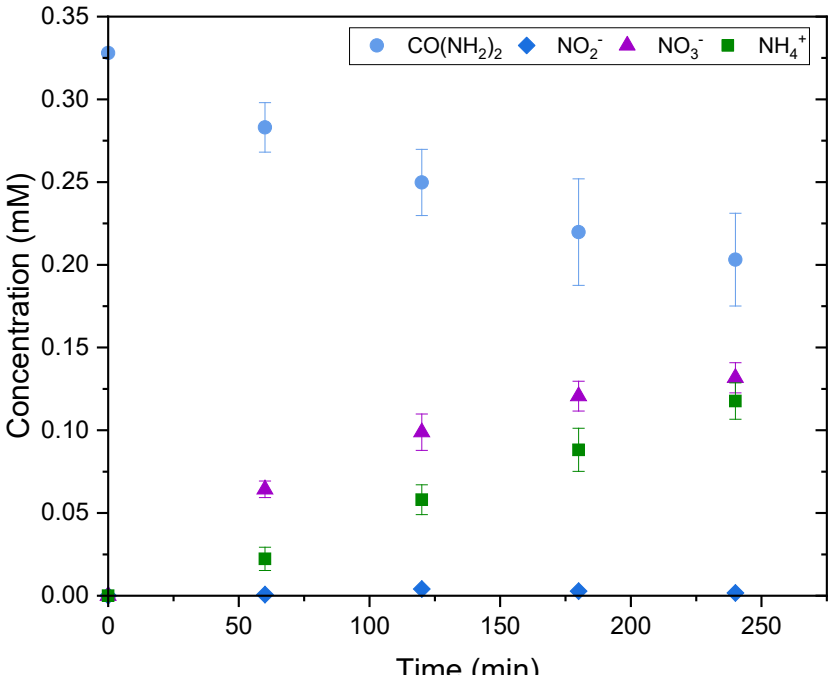

Figure 4-30. Degradation of urea and corresponding conversion to NH_4^+, NO_3^- and NO_2^- using P25 photoanode. I_0 (280-400 nm) = 47 W m^{-2}. Electrolyte = 50mM $KClO_4$ and 0.33 mM Urea.

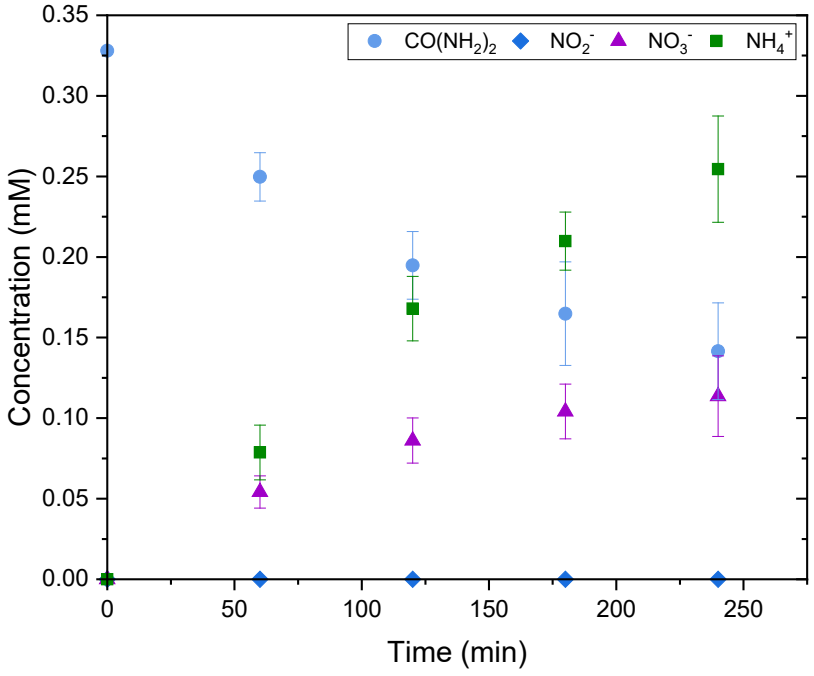

Figure 4-31. Degradation of urea and corresponding conversion to NH_4^+, NO_3^- and NO_2^- using TiNT photoanode. I_0 (280-400 nm) = 47 W m^{-2}. Electrolyte = 50mM $KClO_4$ and 0.33 mM Urea.

4.5 Conclusions

The present study has compared the use of two different TiO_2 nanostructured electrodes proving valuable insight on the oxidation of urea using several photoelectrochemical and analytical techniques. From both electrodes, the TiNT showed the highest IPCE reaching 43 % at 350 nm, compared to maximum of 12 % recorded with P25 at 340 nm. The better performance of the TiNT was attributed to the nanotubes providing a pathway along the longitudinal direction which aids the charger transfer. Moreover, higher band bending could be induced by applied potential, improving further the separation of charges. An enhancement of the PEC process in the presence of ammonia and urea was demonstrated, showing a considerable increment in photocurrent for both TiO_2 photoanodes. This improvement in photocurrent was explained by a more efficient scavenging of the photogenerated holes by urea and ammonia, which results in more electrons reaching the conductive substrate and being transferred to the counter electrode. The highest IPCE was obtained with TiNT, recording 55 % in presence of urea and 65 % with ammonia. The pH study revealed the increment in photocurrent in presence of ammonia occurs only at alkaline pH, which would involve a preliminary step in order to apply this technology to wastewater.

The TiNT mesh electrode showed the highest urea oxidation, with a rate of 0.0037 min^{-1}. The activity of both P25 and TiNT for the oxidation of urea in PEC configuration was compared to PC configuration. The TiNT electrode recorded 15 times higher urea oxidation rate with applied bias, while for P25 the rate was 1.8 higher. This increment highlights the enhancement in charge separation that can be produced by the application of a bias.

References

[1] M. Pelaez, N.T. Nolan, S.C. Pillai, M.K. Seery, P. Falaras, A.G. Kontos, P.S.M. Dunlop, J.W.J. Hamilton, J.A. Byrne, K. O'Shea, M.H. Entezari, D.D. Dionysiou, A review on the visible light active titanium dioxide photocatalysts for environmental applications, Appl. Catal. B Environ. 125 (2012) 331–349. https://doi.org/10.1016/j.apcatb.2012.05.036.

[2] K. Fujishima, A., Honda, Electrochemical Photolysis of Water at a Semiconductor Electrode, Nature. 238 (1972) 37–38. https://doi.org/10.1038/238037a0.

[3] S. Malato, P. Fernández-Ibáñez, M.I. Maldonado, J. Blanco, W. Gernjak, Decontamination and disinfection of water by solar photocatalysis: Recent overview and trends, Catal. Today. 147 (2009) 1–59. https://doi.org/10.1016/j.cattod.2009.06.018.

[4] D. Bahnemann, Photocatalytic water treatment: Solar energy applications, Sol. Energy. 77 (2004) 445–459. https://doi.org/10.1016/j.solener.2004.03.031.

[5] M. Ni, M.K.H. Leung, D.Y.C. Leung, K. Sumathy, A review and recent developments in photocatalytic water-splitting using TiO_2 for hydrogen production, Renew. Sustain. Energy Rev. 11 (2007) 401–425. https://doi.org/10.1016/j.rser.2005.01.009.

[6] W. Yang, R.R. Prabhakar, J. Tan, S.D. Tilley, J. Moon, Strategies for enhancing the photocurrent, photovoltage, and stability of photoelectrodes for photoelectrochemical water splitting, Chem. Soc. Rev. 48 (2019) 4979–5015. https://doi.org/10.1039/C8CS00997J.

[7] M. Pelaez, N.T. Nolan, S.C. Pillai, M.K. Seery, P. Falaras, A.G. Kontos, P.S.M. Dunlop, J.W.J. Hamilton, J.A. Byrne, K.O. Shea, M.H. Entezari, D.D. Dionysiou, Applied Catalysis B: Environmental A review on the visible light active titanium dioxide photocatalysts for environmental applications, "Applied Catal. B, Environ. 125 (2012) 331–349. https://doi.org/10.1016/j.apcatb.2012.05.036.

[8] T. Bobrowski, F. Conzuelo, A. Ruff, V. Hartmann, A. Frank, T. Erichsen, M.M. Nowaczyk, W. Schuhmann, Scalable Fabrication of Biophotoelectrodes by Means of Automated Airbrush Spray-Coating, Chempluschem. 85 (2020) 1396–1400. https://doi.org/10.1002/cplu.202000291.

[9] S. Hernández, G. Saracco, G. Barbero, A.L. Alexe-Ionescu, Role of the electrode morphology on the optimal thickness of $BiVO_4$ anodes for photoelectrochemical water splitting cells, J. Electroanal. Chem. 799 (2017) 481–486. https://doi.org/10.1016/j.jelechem.2017.06.057.

[10] E.G. Galindo, M.J. Ariza, F.J. De las Nieves, M.J. García-Salinas, Effects of multilayer coating and calcination procedures on the morphology of dye-sensitized solar cell semiconductor photoelectrodes, Thin Solid Films. 590 (2015) 230–240. https://doi.org/10.1016/j.tsf.2015.07.078.

[11] S.G. Hashmi, M. Özkan, J. Halme, S.M. Zakeeruddin, J. Paltakari, M. Grätzel, P.D. Lund, Dye-sensitized solar cells with inkjet-printed dyes, Energy Environ. Sci. 9 (2016) 2453–2462. https://doi.org/10.1039/C6EE00826G.

[12] I. Paramasivam, H. Jha, N. Liu, P. Schmuki, A review of photocatalysis using self-organized TiO_2 nanotubes and other ordered oxide nanostructures, Small. 8 (2012) 3073–3103. https://doi.org/10.1002/smll.201200564.

[13] Y. Fu, A. Mo, A Review on the Electrochemically Self-organized Titania Nanotube Arrays: Synthesis, Modifications, and Biomedical Applications, Nanoscale Res. Lett. 13 (2018) 187. https://doi.org/10.1186/s11671-018-2597-z.

[14] V. Zwilling, E. Darque-Ceretti, A. Boutry-Forveille, D. David, M.Y. Perrin, M. Aucouturier, Structure and physicochemistry of anodic oxide films on titanium and TA6V alloy, Surf. Interface Anal. 27 (1999) 629–637. https://doi.org/10.1002/(SICI)1096-9918(199907)27:7<629::AID-SIA551>3.0.CO;2-0.

[15] M. Paulose, H.E. Prakasam, O.K. Varghese, L. Peng, K.C. Popat, G.K. Mor, T.A. Desai, C.A. Grimes, TiO_2 Nanotube Arrays of 1000 μm Length by Anodization of Titanium Foil: Phenol Red Diffusion, J. Phys. Chem. C. 111 (2007) 14992–14997. https://doi.org/10.1021/jp075258r.

[16] Y. Feng, H.H.M. Rijnaarts, D. Yntema, Z. Gong, D.D. Dionysiou, Z. Cao, S. Miao, Y. Chen, Y. Ye, Y. Wang, Applications of anodized TiO_2 nanotube arrays on the removal of aqueous contaminants of emerging concern: A review, Water Res. 186 (2020) 116327. https://doi.org/10.1016/j.watres.2020.116327.

[17] A. Bervian, E. Coser, S. Khan, S.A. Pianaro, C. Aguzzoli, J.S. Marcuzzo, M.R. Baldan, C. de F. Malfatti, Evolution of TiO_2 Nanotubular Morphology Obtained in Ethylene Glycol/Glycerol Mixture and its Photoelectrochemical Performance, Mater. Res. 20 (2017).

[18] L. Özcan, T. Mutlu, S. Yurdakal, Photoelectrocatalytic Degradation of Paraquat by Pt Loaded TiO_2 Nanotubes on Ti Anodes, Materials (Basel). 11 (2018). https://doi.org/10.3390/ma11091715.

[19] A. Tighineanu, T. Ruff, S. Albu, R. Hahn, P. Schmuki, Conductivity of TiO_2 nanotubes: Influence of annealing time and temperature, Chem. Phys. Lett. 494 (2010) 260–263. https://doi.org/10.1016/j.cplett.2010.06.022.

[20] E. Pelizzetti, P. Calza, G. Mariella, V. Maurino, C. Minero, H. Hidaka, Different photocatalytic fate of amido nitrogen in formamide and urea, Chem. Commun. 4 (2004) 1504–1505. https://doi.org/10.1039/b404574b.

[21] P. Calza, E. Pelizzetti, C. Minero, The fate of organic nitrogen in photocatalysis: An overview, J. Appl. Electrochem. 35 (2005) 665–673. https://doi.org/10.1007/s10800-005-1626-7.

[22] S. Park, J.T. Lee, J. Kim, Photocatalytic oxidation of urea on TiO_2 in water and urine: mechanism, product distribution, and effect of surface platinization, Environ. Sci. Pollut. Res. 26 (2019) 1044–1053. https://doi.org/10.1007/s11356-017-8380-3.

[23] M. Altomare, E. Selli, Effects of metal nanoparticles deposition on the photocatalytic oxidation of ammonia in TiO_2 aqueous suspensions, Catal. Today. 209 (2013) 127–133. https://doi.org/10.1016/j.cattod.2012.12.001.

[24] J. Nemoto, N. Gokan, H. Ueno, M. Kaneko, Photodecomposition of ammonia to dinitrogen and dihydrogen on platinized TiO_2 nanoparticules in an aqueous solution, J. Photochem. Photobiol. A Chem. 185 (2007) 295–300. https://doi.org/10.1016/j.jphotochem.2006.06.024.

[25] X. Zhu, S.R. Castleberry, M.A. Nanny, E.C. Butler, Effects of pH and catalyst concentration on photocatalytic oxidation of aqueous ammonia and nitrite in titanium dioxide suspensions, Environ. Sci. Technol. 39 (2005) 3784–3791. https://doi.org/10.1021/es0485715.

[26] M. Kaneko, J. Nemoto, H. Ueno, N. Gokan, K. Ohnuki, M. Horikawa, R. Saito, T. Shibata, Photoelectrochemical reaction of biomass and bio-related compounds with nanoporous TiO_2 film photoanode and O_2-reducing cathode, Electrochem. Commun. 8 (2006) 336–340. https://doi.org/10.1016/j.elecom.2005.12.004.

[27] L.C. Pop, I. Tantis, P. Lianos, Photoelectrocatalytic hydrogen production using nitrogen containing water soluble wastes, Int. J. Hydrogen Energy. 40 (2015) 8304–8310. https://doi.org/10.1016/j.ijhydene.2015.04.116.

[28] G. Wang, Y. Ling, X. Lu, H. Wang, F. Qian, Y. Tong, Y. Li, Solar driven hydrogen releasing from urea and human urine, Energy Environ. Sci. 5 (2012) 8215–8219. https://doi.org/10.1039/c2ee22087c.

[29] D. Dector, D. Ortega-Díaz, J.M. Olivares-Ramírez, A. Dector, J.J. Pérez-Bueno, D. Fernández, D.M. Amaya-Cruz, A. Reyes-Rojas, Harvesting energy from real human urine in a photo-microfluidic fuel cell using TiO_2–Ni anode electrode, Int. J. Hydrogen Energy. 46 (2021) 26163–26173. https://doi.org/10.1016/j.ijhydene.2021.02.148.

[30] D. Jung, H. Biggs, J. Erikson, P.U. Ledyard, New colorimetric reaction for end point, continuous flow, and kinetic measurement of urea, Clin. Chem. 21 (1975) 1136–1140. https://doi.org/10.1093/clinchem/21.8.1136.

[31] R.J.X. Zawada, P. Kwan, K.L. Olszewski, M. Llinas, S.G. Huang, Quantitative determination of urea concentrations in cell culture medium, Biochem. Cell Biol. 87 (2009) 541–544. https://doi.org/10.1139/O09-011.

[32] C. Pablos, J. Marugán, R. Van Grieken, P.S. Dunlop, J.W. Hamilton, D.D. Dionysiou, J.A. Byrne, Electrochemical Enhancement of Photocatalytic Disinfection on Aligned TiO_2 and Nitrogen Doped TiO_2 Nanotubes, Molecules. 22 (2017). https://doi.org/10.3390/molecules22050704.

[33] S. McMichael, A. Tolosana-Moranchel, M.A.L.R.M. Cortes, J.W.J. Hamilton, P. Fernandez-Ibanez, J.A. Byrne, An investigation of photoelectrocatalytic disinfection of water using titania nanotube photoanodes with carbon cathodes and determination of the radicals produced, Appl. Catal. B Environ. 311 (2022) 121339. https://doi.org/10.1016/j.apcatb.2022.121339.

[34] M.A.L.R.M. Cortes, S. McMichael, J.W.J. Hamilton, P.K. Sharma, A. Brown, J.A. Byrne, Photoelectrochemical reduction of CO_2 with TiNT, Mater. Sci. Semicond. Process. 108 (2020) 104900. https://doi.org/10.1016/j.mssp.2019.104900.

[35] P. Makuła, M. Pacia, W. Macyk, How To Correctly Determine the Band Gap Energy of Modified Semiconductor Photocatalysts Based on UV–Vis Spectra, J. Phys. Chem. Lett. 9 (2018) 6814–6817. https://doi.org/10.1021/acs.jpclett.8b02892.

[36] D. Monllor-Satoca, R. Gómez, A photoelectrochemical and spectroscopic study of phenol and catechol oxidation on titanium dioxide nanoporous electrodes, Electrochim. Acta. 55 (2010) 4661–4668. https://doi.org/10.1016/j.electacta.2010.03.045.

[37] Z.-D. Gao, Y.-F. Qu, X. Zhou, L. Wang, Y.-Y. Song, P. Schmuki, Pt-Decorated g-C_3N_4/TiO_2 Nanotube Arrays with Enhanced Visible-Light Photocatalytic Activity for H2 Evolution, ChemistryOpen. 5 (2016) 197–200. https://doi.org/10.1002/open.201500219.

[38] X. Zhou, N. Denisov, G. Cha, I. Hwang, P. Schmuki, Photoelectrochemical performance of TiO_2 photoanodes: Nanotube versus nanoflake electrodes, Electrochem. Commun. 124 (2021) 106937. https://doi.org/10.1016/j.elecom.2021.106937.

[39] C. Haisch, J. Schneider, M. Fleisch, H. Gutzmann, T. Klassen, D.W. Bahnemann, Cold sprayed WO_3 and TiO_2 electrodes for photoelectrochemical water and methanol oxidation in renewable energy applications, Dalt. Trans. 46 (2017) 12811–12823. https://doi.org/10.1039/c7dt02063e.

[40] Z. Yang, Y. Jiang, W. Zhang, Y. Ding, Y. Jiang, J. Yin, P. Zhang, H. Luo, Solid-State, Low-Cost, and Green Synthesis and Robust Photochemical Hydrogen Evolution Performance of Ternary TiO2/MgTiO3/C Photocatalysts, IScience. 14 (2019) 15–26. https://doi.org/10.1016/j.isci.2019.03.009.

[41] K. Ranganathan, A. Morais, I. Nongwe, C. Longo, A.F. Nogueira, N.J. Coville, Study of photoelectrochemical water splitting using composite films based on TiO_2 nanoparticles and nitrogen or boron doped hollow carbon spheres as photoanodes, J. Mol. Catal. A Chem. 422 (2016) 165–174. https://doi.org/10.1016/j.molcata.2015.10.024.

[42] A. Tolosana-Moranchel, N. Pichel, H. Lubarsky, J.A. Byrne, P. Fernández-Ibañez, Photoelectrocatalytic degradation of pharmaceuticals and inactivation of viruses

in water with tungsten oxide electrodes, J. Environ. Chem. Eng. 10 (2022) 107955. https://doi.org/10.1016/j.jece.2022.107955.

[43] P.K. Sharma, M.A.L.R.M. Cortes, J.W.J. Hamilton, Y. Han, J.A. Byrne, M. Nolan, Surface modification of TiO_2 with copper clusters for band gap narrowing, Catal. Today. 321–322 (2019) 9–17. https://doi.org/10.1016/j.cattod.2017.12.002.

[44] T.A. Larsen, K.M. Udert, J. Lienert, Source Separation and Decentralization for Wastewater Management, (2013). https://doi.org/10.2166/9781780401072.

[45] J. Kim, D. Monllor-Satoca, W. Choi, Simultaneous production of hydrogen with the degradation of organic pollutants using TiO_2 photocatalyst modified with dual surface components, Energy Environ. Sci. 5 (2012) 7647–7656. https://doi.org/10.1039/c2ee21310a.

[46] J.A. Byrne, B.R. Eggins, Photoelectrochemistry of oxalate on particulate TiO_2 electrodes, J. Electroanal. Chem. 457 (1998) 61–72. https://doi.org/10.1016/S0022-0728(98)00304-0.

[47] J. Anthony Byrne, B. R. Eggins, P. S. M. Dunlop, S. Linquette-Mailley, The effect of hole acceptors on the photocurrent response of particulate TiO_2 anodes, Analyst. 123 (1998) 2007–2012. https://doi.org/10.1039/A803885F.

[48] N. Hykaway, W.M. Sears, H. Morisaki, S.R. Morrison, Current-doubling reactions on titanium dioxide photoanodes, J. Phys. Chem. 90 (1986) 6663–6667. https://doi.org/10.1021/j100283a014.

[49] Y. Maeda, A. Fujishima, K. Honda, The Investigation of Current Doubling Reactions on Semiconductor Photoelectrodes by Temperature Change Measurements, J. Electrochem. Soc. 128 (1981) 1731. https://doi.org/10.1149/1.2127720.

[50] B. O'Regan, M. Grätzel, A low-cost, high-efficiency solar cell based on dye-sensitized colloidal TiO_2 films, Nature. 353 (1991) 737–740. https://doi.org/10.1038/353737a0.

Chapter 5. Surface modification of TiO_2 with Cu_xO clusters using Atomic Layer Deposition and its performance for the oxidation of urea

5.1 Aim and Objectives

5.1.1 Aim

The main objective of this study is to modify the surface of TiO_2 depositing Cu_xO nanoclusters using atomic layer deposition and evaluate the performance of the modified TiO_2/Cu_xO nanoparticles for the oxidation of urea.

5.1.2 Objectives

The specific objectives of this research are the following:

- Development of an atomic layer deposition (ALD) process for the modification of TiO_2, with Cu_xO nanoclusters controlling the loading.
- Characterization of the ALD deposited Cu_xO nanoparticle size distribution and dispersion.
- Identification of oxidation state of copper clusters.
- Study the optical band gap using UV-DRS.
- Assessment of the photoelectrochemical properties of the ALD modified materials.
- Study effective band gap of ALD modified samples through spectral photocurrent response.
- Performance evaluation of the modified TiO_2 for photocatalytic the oxidation of urea.

5.2 Introduction

TiO_2 is a material widely used in photocatalysis due to its high photo-activity, low cost, and good chemical stability [1]. However, it has a wide band gap (3.2 eV), only absorbing 4% of the total solar irradiation. Some of the strategies reported to enhance the photocatalytic activity of TiO_2 include the modification of its surface with metals, metal oxides or sulphides [1]. Among these options, surface modification with copper oxide has been reported to enhance the photocatalytic performance of TiO_2.

Copper oxides are abundant in nature and inexpensive. Their electrical conductivity and hole density varies depending on the copper vacancy density, generally showing p-type semiconducting behaviour [2]. Several studies have reported the coupling of Cu_xO with TiO_2 to improve the charge separation and in some cases also the light absorption. Benz *et al*. reported the enhanced performance of Cu_xO modified TiO_2 for the degradation of organic dyes, attributing the improvement to the efficient charge transfer between Cu_2O and TiO_2 which reduced the charge recombination [3]. Saedy *et al.* studied the use of TiO_2 modified with 1.7 nm Cu_2O clusters for the photocatalytic production of hydrogen from ethanol. The study identified a reduction of Ti^{4+} to Ti^{3+} caused by the addition of the Cu_xO clusters, showing a correlation between performance and percentage of Ti^{3+}[4]. In addition, theoretical studies have suggested that the formation of Ti-O-Cu bonds due to the presence of Cu on the surface, promotes the shift in the valence band edge mainly via formation of the sub-band gap states of Cu 3d [5]. Concurring with these theoretical studies, Sharma *et al*. performed spectral photocurrent measurements reporting an effective band gap change of 0.11 eV with the addition of Cu_2O clusters [6]. Wang. *et al.* reported that Cu_xO modified TiO_2 can work as stable photocatalysts avoiding the formation of the CuO [7].

The modification of TiO_2 with Cu_xO clusters have usually been reported using wet-synthesis methods as precipitation [8], sol-gel [9], solvothermal [10], electrodeposition [11] and impregnation [12]. In contrast, Atomic Layer Deposition (ALD) can be applied to particulate materials providing control, uniformity, and precision for deposition of nanolayers and nanoclusters. In particular, the use of ALD for the modification of semiconductor materials is an attractive alternative to enhance the photocatalyst properties as: band edges position, light absorption, charge transport, overpotential or chemical and photochemical stability. The deposition of Cu_xO clusters onto TiO_2 nanoparticles have been reported feasible in previous studies [3,4].

This chapter aimed to study the deposition of Cu_xO clusters on the surface of TiO_2 in a controlled manner using ALD and assess its performance for photocatalysis and photoelectrochemistry. This work included the material characterization of the modified samples for the different loadings with special focus in the copper clusters particle size and oxidation state. The possible enhancement in the visible light absorption was also studied through the use of diffuse reflectance spectroscopy and spectral photocurrent

measurements. The photoelectrochemical properties of the modified samples were also assessed together with the photocatalytic performance for the oxidation of urea.

5.3 Experimental section

5.3.1 Atomic Layer deposition

The ALD experiments were carried out in a fluidized bed reactor (FBR) operated at atmospheric pressure. Cu_xO was deposited onto the commercial TiO_2 (P25) substrate using, copper hexafluoroacetylacetonate trimethylvinylsilane, Cu(I)(hfac)(tmvs) as precursor and H_2O as oxidizer. The bubbler containing the Cu precursor was maintained at 60 °C, whereas the H_2O bubbler was kept at room temperature. The deposition temperature was 150 °C. For each ALD deposition batch, 1 g of TiO_2 was used, fluidized using inert N_2 with a flow of 0.5 L min^{-1} (Chapter 3. Materials and methods).

5.3.2 Material Characterization

Inductively coupled plasma optical emission spectroscopy (ICP-OES) was utilized to determine the Cu metal content in the ALD deposited materials. The high-resolution images of the materials were acquired using transmission electron microscopy (TEM) (JEOLJEM1400) and the cluster size was measured using the software ImageJ. The elemental composition of the electrodes was determined using X-ray photoelectron spectroscopy (XPS) (Kratos Axis Ultra). The wide energy survey scans (WESS) were measured for all samples in the binding energy range of 0-1250 eV, with a pass energy of 160 eV. High resolution (HR) scans of each target element (C, Ti, Cu and O) were recorded with a pass energy of 14.2 eV. The UV-vis diffuse reflectance spectra were measured with a LAMBDA 365 UV/Vis spectrometer (PerkinElmer) equipped with an integrating sphere and the optical band gap was estimated using the Kubelka-Munk method.

5.3.3 Electrode fabrication

The TiO_2 and modified Cu_xO/TiO_2 samples were immobilized on a FTO glass using spray coating (Chapter 3. Materials and methods). A FTO size of 2 cm x 1.5 cm was used. The electrical contact was made by attaching a copper wire to an uncoated section of the FTO, using silver epoxy. A negative photoresist was used as insulator of the contact and any area of the conductive substrate not covered with nanoparticles.

5.3.4 Photoelectrochemical Characterization

A potentiostat (AUTOLAB PGSTAT 30) and a 450 W Xe lamp (Horiba Jobin Yvon FL-1039/40) equipped with a monochromator (Horiba Jobin Yvon microHR), a chopper (Uniblitz) and an infra-red (IR) filter were utilized to perform the photoelectrochemical characterization experiments. These experiments were performed in a cylindrical water jacketed quartz cell with a total volume of 30 mL. A three-electrode configuration was employed with the Cu_xO/TiO_2 electrodes used as working electrodes, a Saturated Calomel Electrode (SCE) as reference and a platinum gauze as counter electrode (Chapter 3.Materials and methods). The electrolyte was of 0.05 M of $KClO_4$.

The spectral photocurrent response measurements were performed from a wavelength ranging from 280 nm to 420 nm in steps of 10 nm with chopped irradiation intervals of 30 s under illumination and 80 s in the dark and a fixed potential of +1.0 V vs SCE. The photocurrent was determined using amperometry with fixed potentials of 0.0 V, +0.5 V and +1.0 V. The open circuit potential and open circuit photo-potential were measured using potentiometry.

5.3.5 Photocatalytic experiments

The photocatalytic experiments were performed using a glass water jacket reactor with a total volume of 22 mL and the irradiation source was a 1000 W Xe lamp (Chapter 3, Figure 3-1). The experiments were performed with constant air bubbling and stirring. A photocatalyst loading of 0.2 mg $L^{-1}$was selected as it resulted in the highest urea oxidation in preliminary experiments where loading was varied from 0.15 mg L^{-1} to 0.3 mg L^{-1}. Samples of 0.7 mL were collected in time with a pipette and analysed following the UV-vis methods detailed in Chapter 3.3.5 Quantification of reactants and products.

5.4 Results and discussion

5.4.1 Atomic Layer Deposition experiments

The goal of this study was to use ALD to improve the photocatalytic properties of TiO_2 by depositing copper oxide nanoclusters. The precursor chosen, copper hexafluoroacetylacetonate trimethylvinylsilane, also referred as Cu(I) (hfac) (tmvs), or CupraSelect, have been previously used in several studies for the deposition of Cu, obtaining usually copper oxides [13,14]. The ALD mechanism for the deposition of Cu

using Cu(I) (hfac) (tmvs) as precursor has been reported for ALD deposition on flat substrates. This mechanism differs depending on the required Cu oxidation state product [15]. For metallic copper, the Cu(I) (hfac) (tmvs) is believed to suffer a disproportionation due to its low stability at temperatures above 60 °C [15], with two molecules of precursor reacting to give an atom of metallic coper together with the volatile by-products of 2(tmvs) and Cu(II)$(hfac)_2$. For this process to occur, it is necessary to avoid presence or air or humidity. For copper oxide, H_2O vapour is used as co-reactant, in this process Cu(I) (hfac) (tmvs) experiences hydrolysis reaction, resulting in the deposition of Cu_2O together with the volatile by-products of tmvs and hfacH. As the aim of this study was to deposit Cu_2O, H_2O vapor was used a co-reactant. This process is represented in Figure 5-1 for a conventional ALD process with deposition on flat substrates.

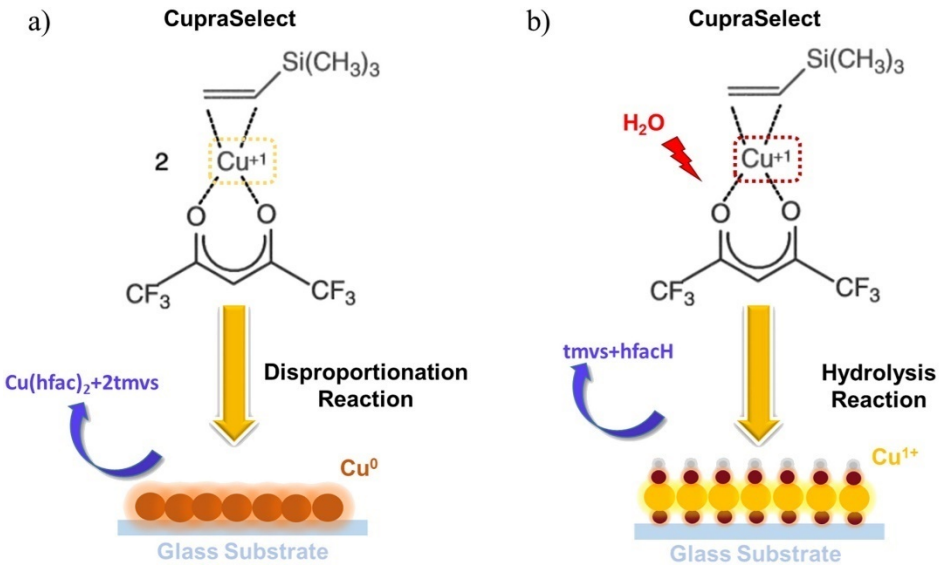

Figure 5-1. Schematic representation of the ALD deposition of a) Cu(0) and b) Cu(I) using Cu(I) (hfac) (tmvs), (CupraSelect), as precursor in a flat substrate ALD conventional process. Figure reproduced from [15].

Previous ALD studies have demonstrated the possibility of controlling the dispersion and size distribution of the deposited nanoclusters in the unsaturated ALD regime conditions [3,4]. Therefore, in this study, the fabrication of the desired nanoclusters (<5 nm) was achieved selecting dosing times in the unsaturated regime or growth region (i.e., shorter times than the saturation region). These deposition times ranged between 1.5 to 5 min. When comparing the dosing times of this study (fluidized nanoparticles) to literature for

the deposition of Cu_xO using conventional ALD processes (flat substrates), literature reports shorter deposition times ranging from ms to s for flat substrates [16]. This is due to the fact that suspension nanoparticle substrates, have larger surface areas, therefore requiring dosing times in the range of minutes. In this study, with 1 g of P25 used as a substrate for each ALD batch, considering a P25 specific surface area of 54 m^2g^{-1}, the surface area to coat was 54 m^2. A schematic representation of both ALD conventional and FBR systems is shown in Figure 5-2.

Concerning the oxidizer dosing time, preliminary tests showed no increase in Cu loading when oxidizer exposure (H_2O vapor) was increased from 5 to 10 min, therefore 5 min was selected as oxidant dosing time and was kept constants for all the depositions.

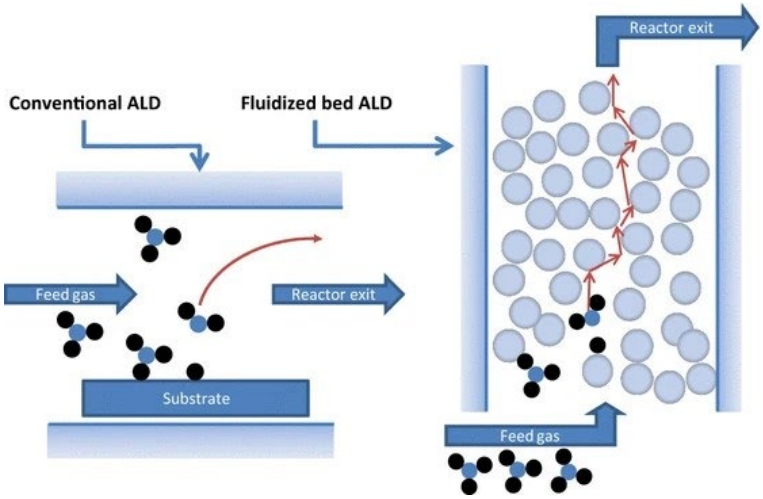

Figure 5-2. Schematic representation of a conventional ALD process for deposition on flat substrates (left) and a fluidized bed reactor ALD process for the deposition on suspended particles (right). Figure reproduced from [17].

5.4.2 Material Characterization

5.4.2.1 Inductively Coupled Plasma-Optical Emission Spectrosocopy Analysis

ICP measurements were used to quantify the elemental composition of the Cu_xO/TiO_2 particles and thus corroborating the success of the deposition of Cu_xO and studying the effect of the modification of ALD process parameters. Figure 5-3 shows the copper loading given by ICP as a function of the ALD number of cycles used, when a precursor dosing time of 5 min was used. These results demonstrate a linear growth of the Cu loading with increasing number of cycles, which is characteristic of the unsaturated ALD region. These results proved the possibility of controlling the loading by the number ALD

cycles. To achieve even smaller loadings, the Cu precursor dosing time was reduced to 3 min, resulting in a loading as small as 0.1 wt.% of Cu. The observed results agree with the obtained conclusions in a previous study in which a similar ALD system for the deposition of Cu_xO on P25 [3]. Benz *et al.* reported an increase of Cu loading with increasing number of cycles. In addition, the study reported an ALD saturation regime with precursor dosing times longer than 15 min.

In the following section, the investigation of the properties and performance of Cu_xO/TiO_2 photocatalysts was carried out selecting 4 samples with Cu loadings, 0.1 %, 0.4 %, 1.0 % and 2.6 %. These samples will be referred in the following sections as Cu_xO/TiO_2 (0.1 %), Cu_xO/TiO_2 (0.4 %), Cu_xO/TiO_2 (1.0 %) and Cu_xO/TiO_2 (2.6 %), with the % being the obtained ICP quantification of the metallic Cu.

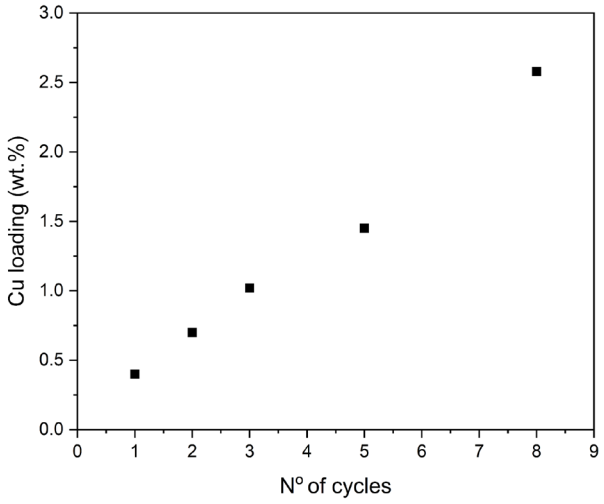

Figure 5-3. Cu concentration as function of the number of ALD cycles with the Cu-precursor and H_2O dose time of 5 min and 5 min respectively.

5.4.2.2 Transmission electron microscopy analysis

The TEM images and cluster size distribution are shown in Figure 5-4 to Figure 5-7, these results confirmed the successful deposition of Cu_xO nanoparticles on P25, revealing highly dispersed nanoclusters with a well-controlled size. The Cu_xO clusters had an average particle size between 1.7 nm and 2.1 nm as shown in Figure 5-8.

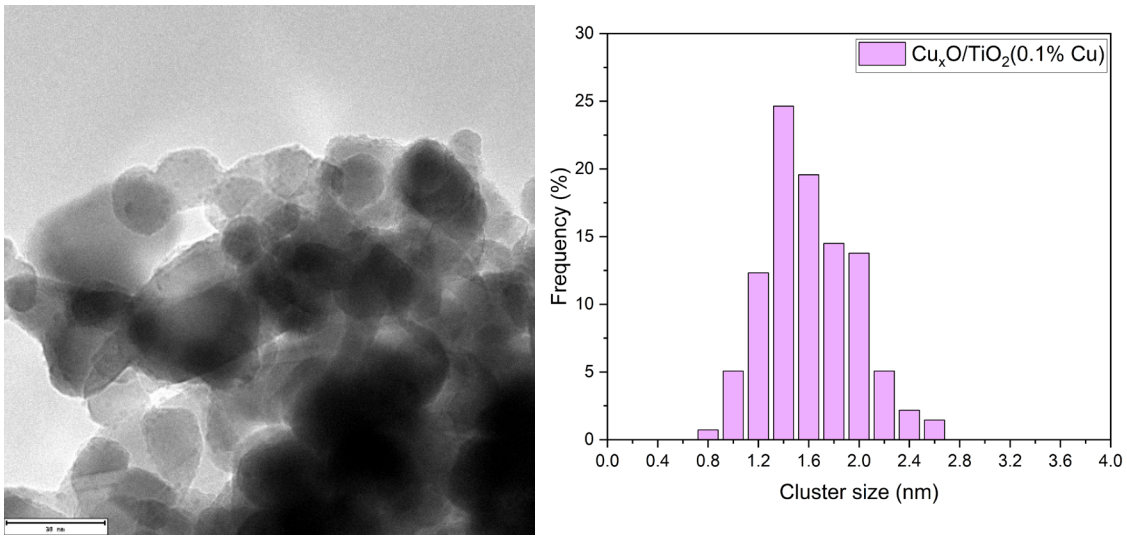

Figure 5-4. TEM image of the ALD synthesized Cu_xO/TiO_2 with Cu content of 0.1 wt.% and the Cu_xO cluster size distribution.

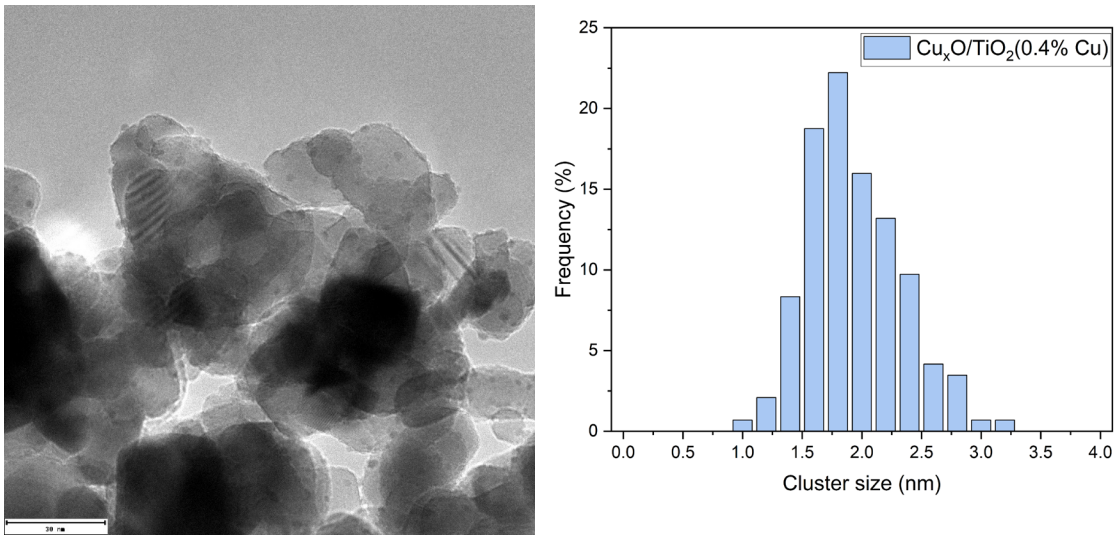

Figure 5-5. TEM image of the ALD synthesized Cu_xO/TiO_2 with Cu content of 0.4 wt.% and the Cu_xO cluster size distribution.

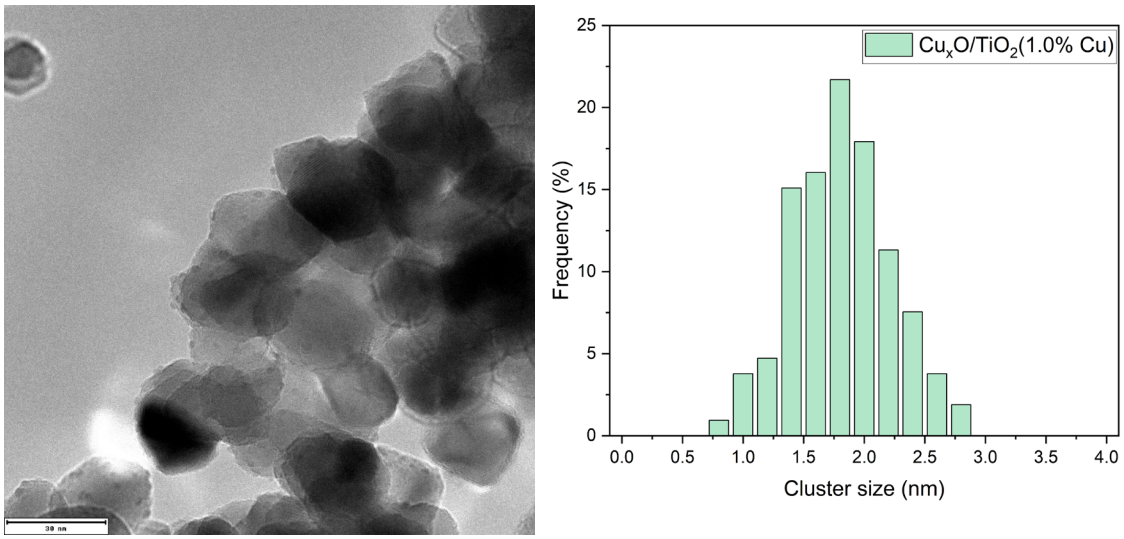

Figure 5-6. TEM image of the ALD synthesized Cu_xO/TiO_2 with Cu content of 1.0 wt.% and the Cu_xO cluster size distribution.

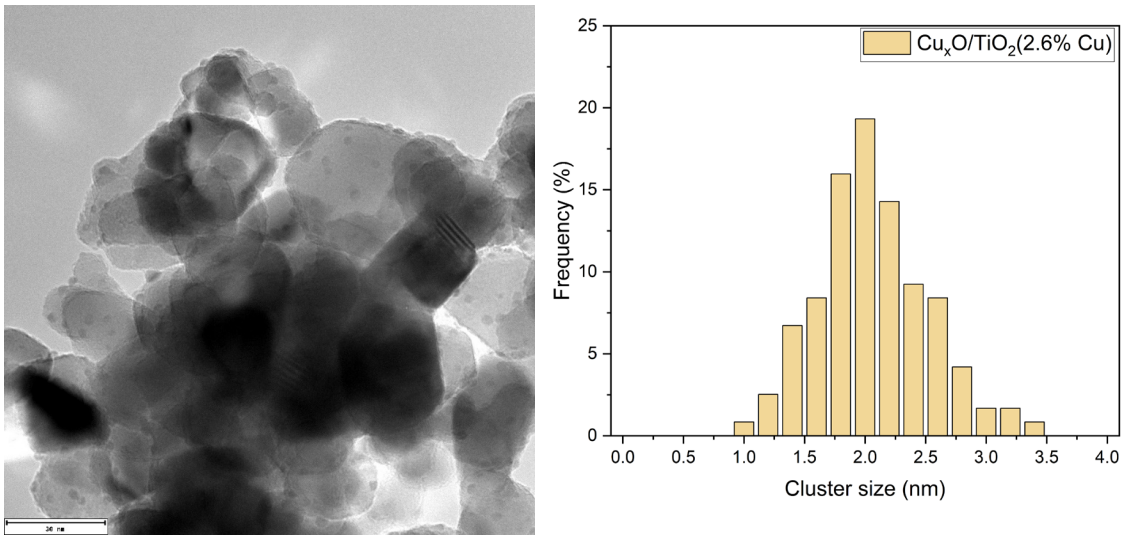

Figure 5-7. TEM image of the ALD synthesized Cu_xO/TiO_2 with Cu content of 2.6 wt.% and the Cu_xO cluster size distribution.

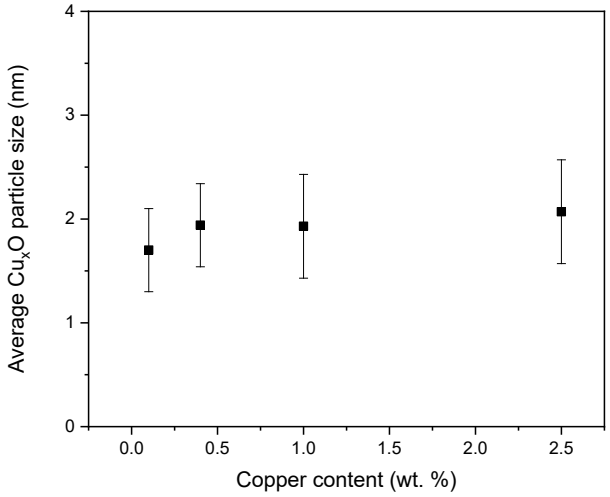

Figure 5-8. Average size of the Cu_xO and standard deviation as function of copper loading (wt.%) measured by ICP.

5.4.2.3 X-Ray Photoelectron Spectroscopy

The study of the surface chemistry of the samples and the oxidation state of the deposited Cu_xO nanoclusters was performed using XPS (Figure 5-9). The copper 2p spectra revealed a characteristic spin-orbit splitting of ~ 19.75 eV; while only the $2p_{3/2}$ spectrum is commonly used for quantification. The distinction between metallic copper Cu(0), and Cu(I) oxide based on the $2p_{3/2}$ spectra results rather difficult, as their binding energies are very similar, i.e. 932.6 eV and 932.2 eV respectively. For this purpose, the LMM Auger peak is usually studied to discriminate between Cu(0) and Cu(I). However, in the present study this was not possible due to the presence of the Ti substrate, with Ti 1s overlapping the spectral region of Cu LMM. Nevertheless, considering the the oxidative condition of the synthesis process in which H_2O is used as co-reactant (as disccussed in section 5.4.1 Atomic Layer Deposition experiments), the copper is assumed to be in Cu(I) form.

Cu(II) oxide reveals a $2p_{3/2}$ peak at binding energy of 933.1 eV, which can be easily distinguished from Cu(0) and Cu(I). Moreover, the Cu(II) species show a $2p_{3/2}$ shake-up satellite peak in the binding energy range between 940 and 945 eV. In Figure 5-9, the lower Cu_xO loadings (0.1 wt.% and 0.4 wt.%), showed no satellite, suggesting that in these samples copper is in Cu(I) oxidation state, while at higher loadings (1 wt.% and 2.6 wt.%) the presence of Cu(II) is confirmed by its characteristic satellite peak. This indicates that for Cu co-catalyst loading lower than 1 wt% Cu(I) is the majority phase, while at higher loadings part of the Cu is further oxidised to Cu(II). In order to quantify the various Cu species (with different oxidation state) and corroborate the observations

from Figure 5-9, the Cu $2p_{3/2}$ spectra for each sample were fitted with the corresponding components. Figure 5-10 and Figure 5-11 showed a 100 at.%. for Cu(I) corroborating the conclusions obtained from Figure 5-9. For the sample Cu_xO/TiO_2 (1.0 % Cu), the fitting showed almost equal contributions of Cu(I) and Cu(II) (Figure 5-12). While for the sample Cu_xO/TiO_2 (2.6 % Cu), a dominant contribution from Cu(II) was obtained (Figure 5-13). These results were summarised in Table 5-1.

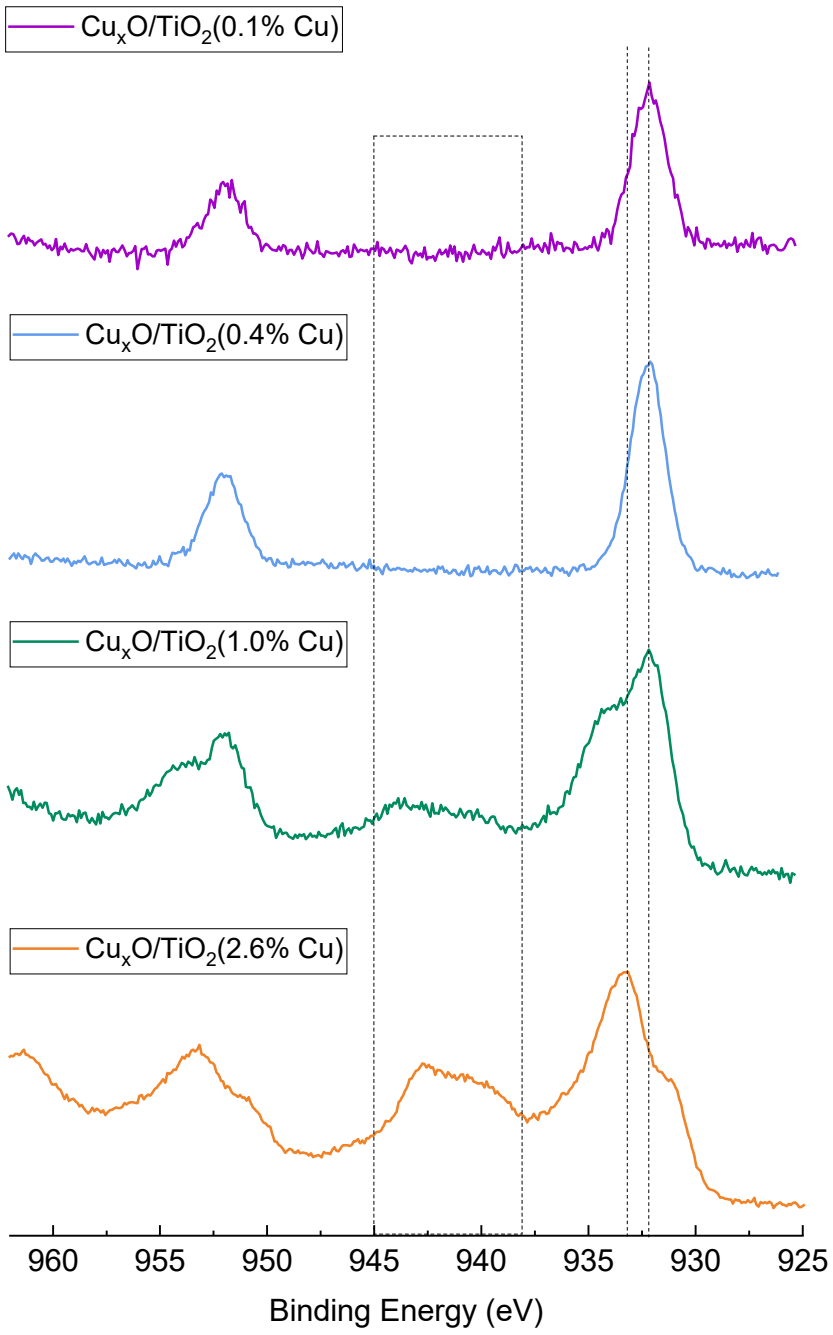

Figure 5-9. Cu 2p XPS spectra of Cu_xO/TiO_2 with different Cu loadings.

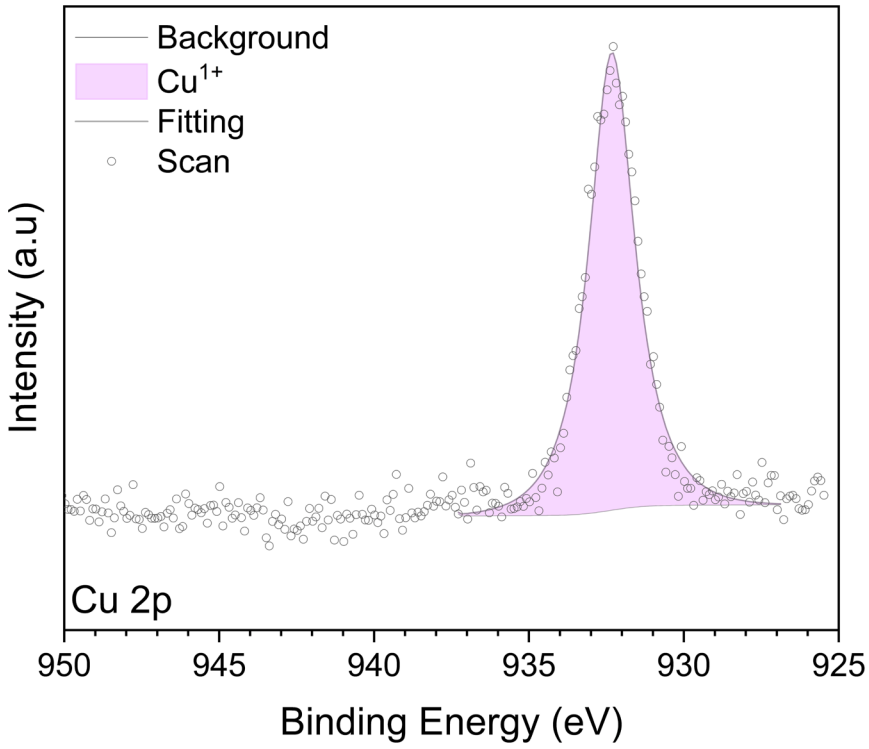

Figure 5-10. XPS spectra corresponding to Cu 2p for the Cu_xO/ TiO_2 (0.1 wt.% Cu).

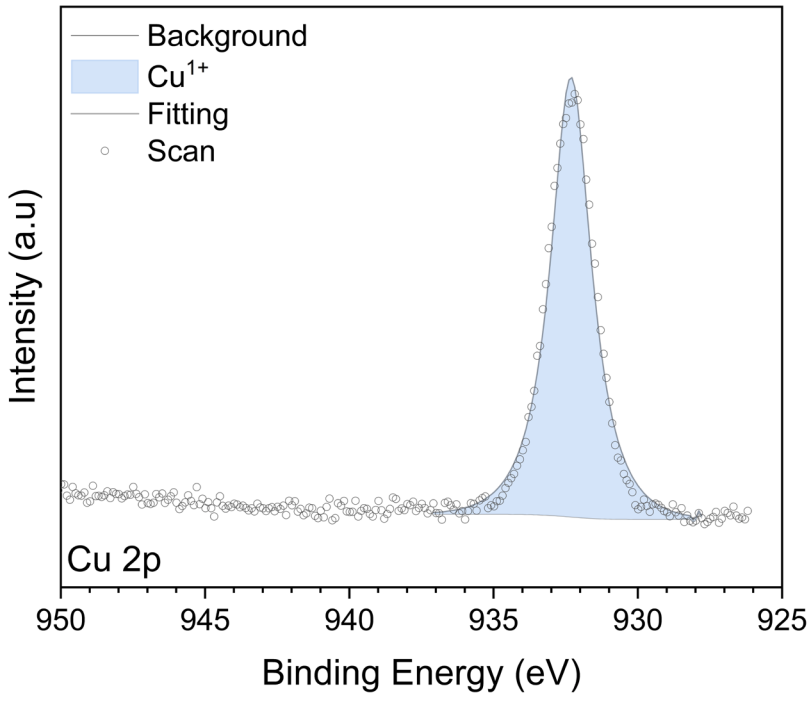

Figure 5-11. XPS spectra corresponding to Cu 2p for the Cu_xO/ TiO_2 (0.4 wt.% Cu).

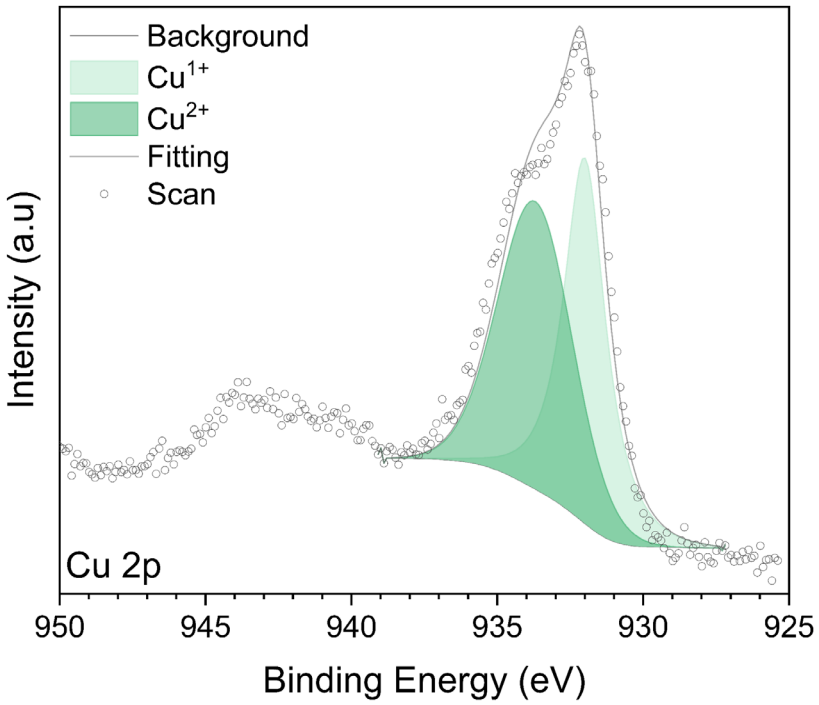

Figure 5-12. XPS spectra corresponding to Cu 2p for the Cu_xO/ TiO_2 (1.0 wt.% Cu).

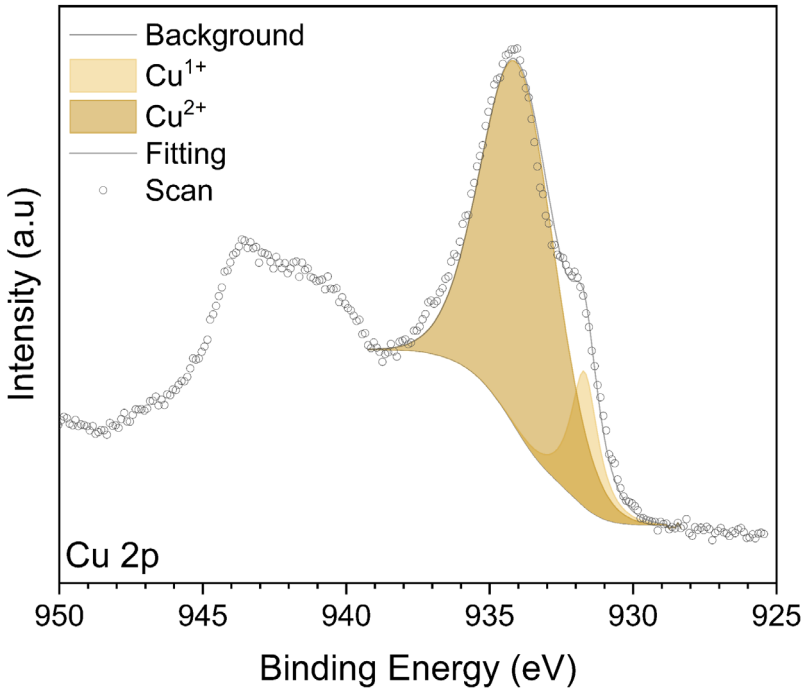

Figure 5-13. XPS spectra corresponding to Cu 2p for the Cu_xO/ TiO_2 (2.6 wt.% Cu).

Table 5-1. Relative atomic percentage of Cu(I) and Cu(II) derived from the fitting of the Cu 2p XPS spectra.

Sample	Cu(I) (at.%)	Cu(II) (at.%)
Cu_xO/TiO_2 (0.1 wt.% Cu)	100	0
Cu_xO/TiO_2 (0.4 wt.% Cu)	100	0
Cu_xO/TiO_2 (1.0 wt.% Cu)	52	48
Cu_xO/TiO_2 (2.6 wt.% Cu)	13	87

In addition to the identification of the copper oxidation state, high resolution XPS of the valence band region was carried out to study the possible shift in valence band edge position resulting from the addition of the Cu_xO clusters (Figure 5-14). A linear fitting was performed to estimate the valence band position, and the obtained results are summarised in Table 5-2. The VB shifted towards lower energy with the copper oxide clusters loaded, with a maximum shift of 1.22 eV observed with the sample with Cu_xO/TiO_2 (1.0 wt% Cu). Sharma *et al.* reported a shift in the valence band edge when depositing Cu_2O clusters on P25 and resulting in a band gap reduction of 0.62 eV [6]. However, it is important to consider that in this method is not possible to differentiate between the real band gap narrowing and the contribution from overlapping valence band edges in both materials.

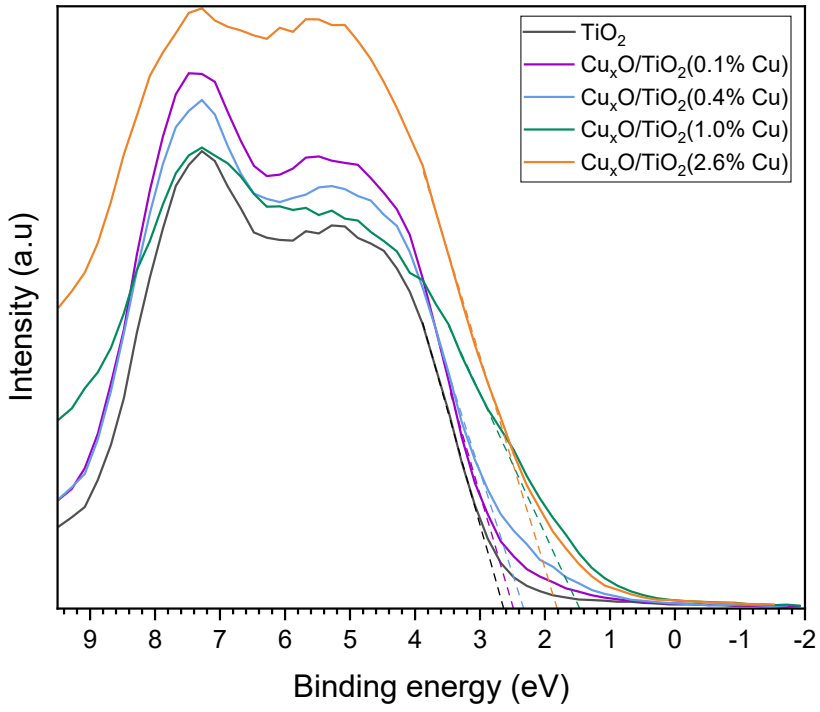

Figure 5-14. VB XPS spectra of TiO_2 and Cu_xO/TiO_2 for different Cu loadings and linear fitting.

Table 5-2. Obtained VB values from the XPS spectra.

Sample	VB (eV)
TiO_2(P25)	2.65
Cu_xO/TiO_2 (0.1% Cu)	2.5
Cu_xO/TiO_2 (0.4% Cu)	2.32
Cu_xO/TiO_2 (1.0% Cu)	1.46
Cu_xO/TiO_2 (2.6% Cu)	1.81

5.4.2.4 Diffuse reflectance spectroscopy

The optical properties of the Cu_xO/ TiO_2 samples were studied by UV-visible diffuse reflectance spectroscopy. The absorbance for all the Cu_xO/ TiO_2 and TiO_2 samples was calculated from the collected spectra using the Kubelka-Munk function (procedure explained in section 3.3.3.6 Ultraviolet-visible diffuse reflectance spectroscopy). The results showed a slight increase in visible light absorption for the samples modified with Cu_xO, which has been reported in literature as one of the reasons for enhanced photocatalytic and photoelectrochemical performance after the modification of TiO_2 with Cu_xO [4,19]. To estimate the band gap energy of the different samples, the Tauc plot was employed (Figure 5-15). For a better estimation, a baseline was introduced to intercept with the linear fitting [20]. The obtained band gaps were: 3.19 eV, 3.16 eV, 3.12 eV, 3.12 eV and 3.24 eV for TiO_2(P25), Cu_xO/TiO_2 (0.1% Cu), Cu_xO/TiO_2 (0.4% Cu), Cu_xO/TiO_2 (1.0% Cu) and Cu_xO/TiO_2 (2.6% Cu) respectively. The shift ranged from 0.05 eV to 0.07 eV (Figure 5-15) with the biggest shift obtained with Cu_xO/TiO_2 (0.4% Cu) and Cu_xO/TiO_2 (1.0% Cu) (results summarised in Table 5-3). The use of UV-vis spectroscopy to determine the optical band gap can result in considerable deviations caused by the absorption of non-interacting optical states. The band gap value extracted from the Tauc plot depends on the use of a function that matches the electronic transition and a sufficient film thickness. Since the samples contain anatase, rutile and copper oxide materials, neither direct nor indirect fit can precisely describe all states, possibly causing deviations in the optical data treatment. However, the observed red shift with a value of around 0.1 eV matches with previous works in Cu_xO modified TiO_2 reported in literature and DFT simulations [4,19].

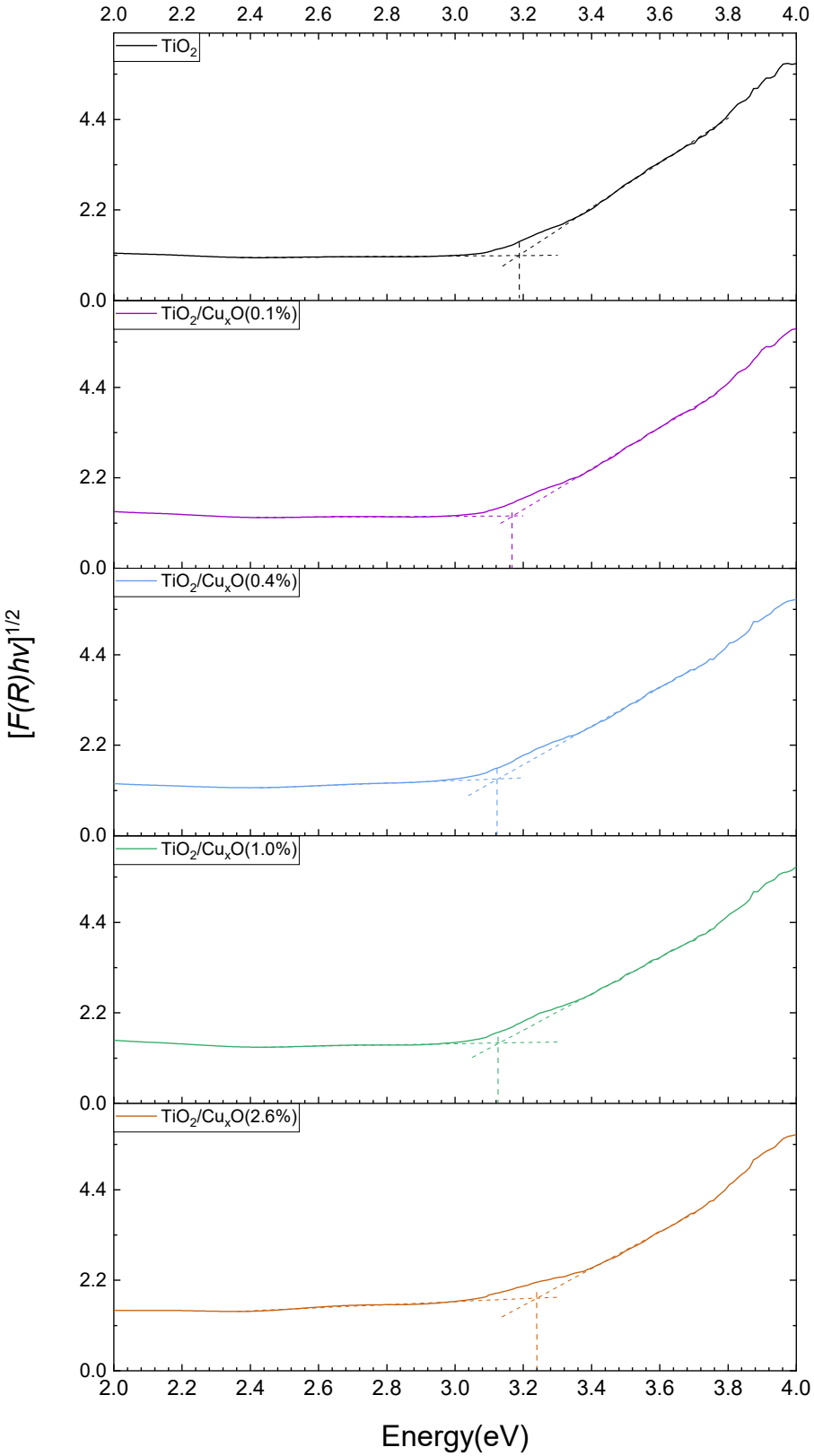

Figure 5-15. Tauc plot for Cu_xO/TiO_2 and TiO_2 samples considering an indirect band gap.

Table 5-3. Estimated band gaps obtained from Tauc plots.

Sample	Estimated band gap (eV) Intercept with baseline
TiO_2(P25)	3.19
Cu_xO/TiO_2 (0.1% Cu)	3.16
Cu_xO/TiO_2 (0.4% Cu)	3.12
Cu_xO/TiO_2 (1.0% Cu)	3.12
Cu_xO/TiO_2 (2.6% Cu)	3.24

5.4.3 Photoelectrochemical characterization

Photoelectrochemical characterization experiments were performed with a dual purpose i.e., as analytical tool to gain fundamental knowledge into the modified TiO_2 nanoparticles, as well as, evaluating its use as photoanode under the action of an externally applied electrical field.

5.4.3.1 Spectral photocurrent response

To study the possible improvement in light absorption due to the surface modification of TiO_2 with Cu_xO clusters, spectral photocurrent response measurements were performed (Figure 5-16).

The samples in this study are a combination of P25 which is formed by 20% rutile and 80% anatase, and the copper clusters which are present in different oxidation states (Cu_2O and CuO). The approximated reported band gap for rutile is 3 eV and for anatase 3.2 eV, which translates to light absorption up to wavelengths of 413 nm and 387 nm respectively [21]. While for Cu_2O, reported values vary between 2.0-2.5 eV, which equals to light absorption until wavelengths of 495 nm or 619 nm [22]. For CuO, the reported bad gap values vary between 1.3 and 1.7 eV, with wavelength up to 729 nm or 953 nm reported [22]. A previous work by Sharma *et al.* studied the spectral photocurrent response of a photoanode formed by Cu_2O/P25, reporting a spectral photocurrent response up to 500 nm. In contrast, the present study found no observable photocurrent response for wavelengths > 420 nm (Figure 5-16). Therefore, the effective band gap values obtained through spectral photocurrent measurements differ from the optical band gap obtained through diffuse reflectance spectroscopy.

The spectral photocurrent response results exhibited a higher photocurrent for TiO_2 than for the modified samples up to a wavelength of 360 nm. In this range (280 nm – 360 nm), the lowest photocurrent was obtained with the sample containing the highest Cu loading (2.6 %), and the highest photocurrent was achieved with the sample containing a loading of 0.4 wt.%. These results showed how the addition of Cu_xO clusters have a negative effect in the photocurrent generation for wavelengths between 280 nm and 360 nm, with a lower number of photogenerated electrons reaching the conductive substrate once Cu_xO is added.

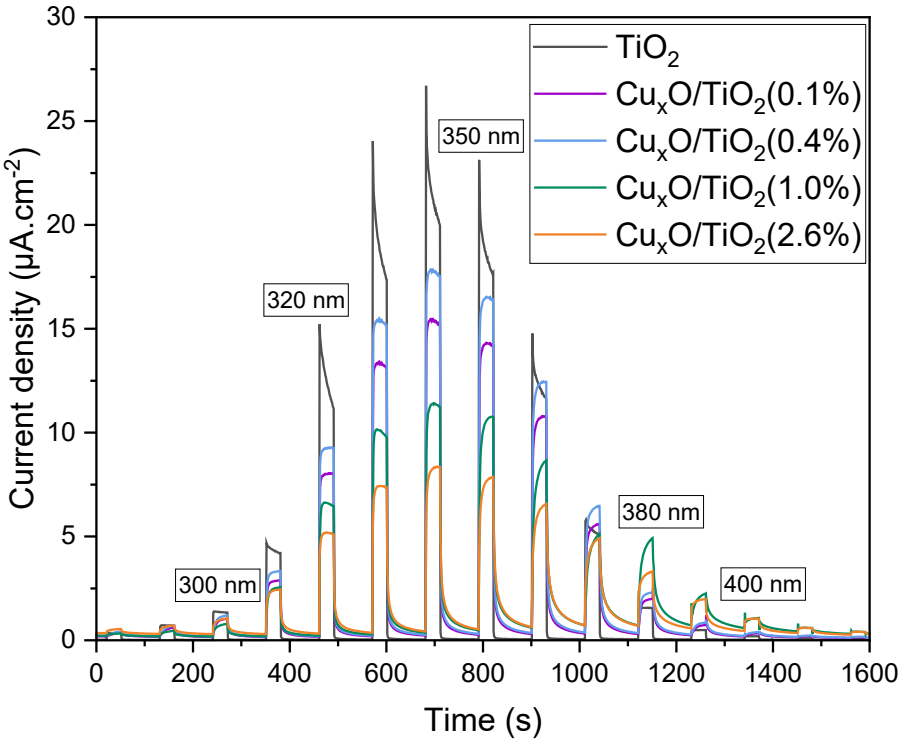

Figure 5-16. Spectral current response at fixed potential of + 1.0 V with monochromatic irradiation (280 nm to 420 nm). I_0 (280-420 nm) = 44 W m^{-2}. Electrolyte = 50 mM $KClO_4$.

On the contrary, at wavelengths from 360 nm to 420 nm the Cu_xO modified TiO_2 samples showed a higher photocurrent when compared than the unmodified TiO_2 electrode. For a better study of the region 380nm and 390 nm, further experiments were performed with fixed monochromatic irradiation and an increased time of dark current stabilisation before the measurement, the results from these experiments are shown in Figure 5-18 and Figure

5-19. At these wavelengths, all the Cu_xO modified samples showed a higher photocurrent than TiO_2, with the highest photocurrent response corresponding to the sample with a Cu loading of 1.0 wt.%. This could indicate that the Cu_xO clusters are providing photogenerated electrons to the TiO_2 or conductive substrate or improving charge separation lowering recombination.

Moreover, Figure 5-18 and Figure 5-19 showed a different photocurrent transient response for the electrodes modified with Cu_xO compared to TiO_2. A schematic representation of photocurrent transient response for a typical n-type semiconductor is shown in Figure 5-17. In this process, the semiconductor is irradiated, generating electron-hole pairs. For a single crystal n-type semiconductor, the holes migrate towards the semiconductor/electrolyte interface where they can get trapped or participate in oxidation reactions with species present in the electrolyte. The electrons migrate to the back contact. In the typical photocurrent transient, the current then decreases until a steady state is achieved, which could be an indication of the occurrence of recombination processes [5]. In nanoparticulate electrodes, the electron hole pair separation is mainly driven by diffusion, in contrast to single crystal electrodes where the formation of the space charge layer occurs. For nanoparticulate semiconductor anodes, surface recombination can occur when the holes accumulate at the semiconductor surface and recombine with electrons from the conduction band. Another process which can contribute to the current decay, is electrons from the conduction reducing the oxidized species in the electrolyte. At light off, a cathodic peak may be observed as conduction band electrons reduce holes trapped at the surface.

At wavelengths between 380 and 390 nm the TiO_2 sample showed a steady state photocurrent after irradiation, which differs from the transient of the Cu_xO modified samples, which in general showed a gradual photocurrent increase until achieving steady state. In addition, the samples with Cu_xO loadings of 0.1 % and 0.4 %, in the oxidation state Cu(I), showed an anodic peak whenever the irradiation was switched off. This peak could indicate the transfer of electrons from the Cu_2O the TiO_2 or conductive substrate once the irradiation is interrupted. Another interesting feature was observed in the spectral photocurrent response transient at 390 nm for the sample with loading Cu_xO (1.0%), which has a mixture of both Cu_2O and CuO. In this measurement, once the electrode is irradiated, an anodic peak occurred which then decreased and then showed a gradual increase during the irradiation time. In addition, once the irradiation is stopped, a sudden

decrease of current was observed followed by an anodic peak and a gradual decrease of current in time. These suggests the differentiation of two distinguishable process, a faster one which is seen right after light is switched on and off and a slower one which is gradual in time. The fast one could be due the electron transport from the charge separation to the conductive substrate, while the slower one, could be related to the transfer of electrons between the different phases of TiO_2 and Cu_xO which then reached the conductive substrate.

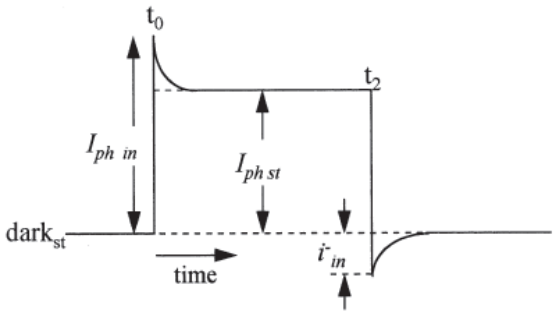

Figure 5-17. Schematic representation photocurrent transient response for a typical single crystal n-type semiconductor. Image reproduced from [23].

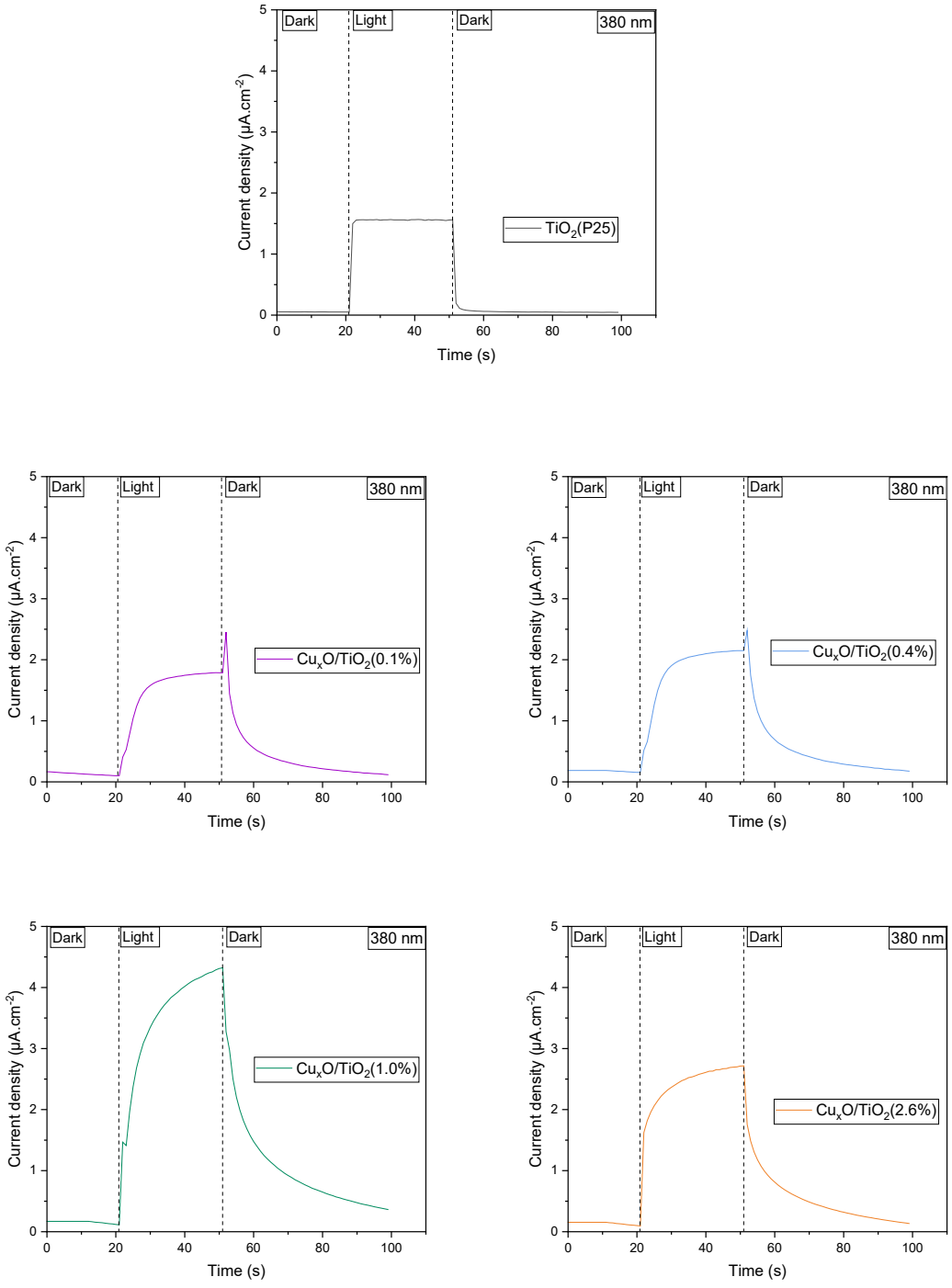

Figure 5-18. Photocurrent time response with monochromatic irradiation at 380 nm +1.0 V.

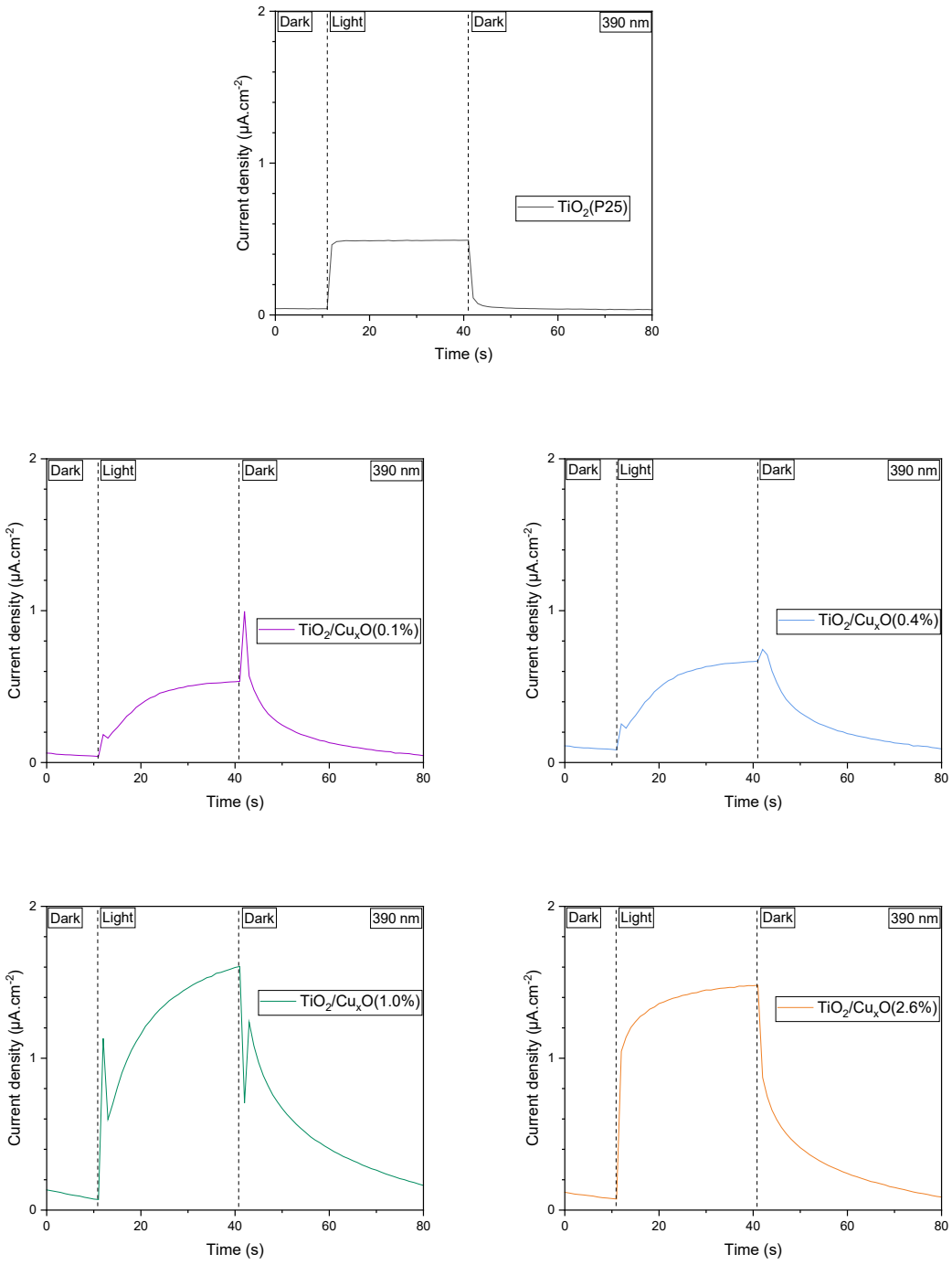

Figure 5-19. Photocurrent time response with monochromatic irradiation at 390 nm, and +1.0 V.

5.4.3.2 Photocurrent response at fixed potential

The photocurrent response from the surface modified TiO_2 immobilized electrodes was studied measuring the current at fixed potentials of 0.0, + 0.5 and + 1.0 V (Figure 5-20 to Figure 5-22).

The deposition of Cu_xO clusters on the TiO_2 surface led to a reduction in photocurrent compared to pure TiO_2 under applied potentials of 0.0 and + 0.5 V. This might indicate that the presence of Cu_xO clusters enhances recombination or drives electrons to the electrolyte, resulting in both cases in fewer electrons reaching the conductive substrate. The sample with loading of 2.6 % and Cu (II) oxidation state consistently exhibits the lowest photocurrent, while the highest photocurrent is observed with 0.4% loading and Cu(I) oxidation state.

When applying a potential of +1.0 V the photocurrent obtained for all the Cu_xO modified sample increased significantly. The sample modified with Cu(I) oxidation state and loading of 0.1% reached a similar photocurrent than TiO_2 while the sample modified with Cu(I) with 0.4% loading exhibited a slightly higher photocurrent than TiO_2 sample. These results agree with the spectral photocurrent results studied in the previous section, since it was seen how the addition of Cu_xO improved slightly the light absorption at wavelengths from 370 nm to 420 nm, however, they did not extend absorption to wavelength > 420 nm neither enhance the photocurrent obtained from 300 nm to 360 nm.

Therefore, it could be concluded that the modification of P25 nanoparticles with Cu_xO clusters did not result in an enhancement the P25 properties when used as photoanode. The addition of Cu_xO to TiO_2 might form of a p-n junction between both semiconductors, rectifying the current cathodically, with some electrons flowing to the electrolyte instead of to the conductive substrate, therefore reducing the observed anodic current. In addition, the Cu_xO clusters might also slow the electron transfer to the conductive substrate and provide higher interfaces for recombination for the photogenerated electrons and holes.

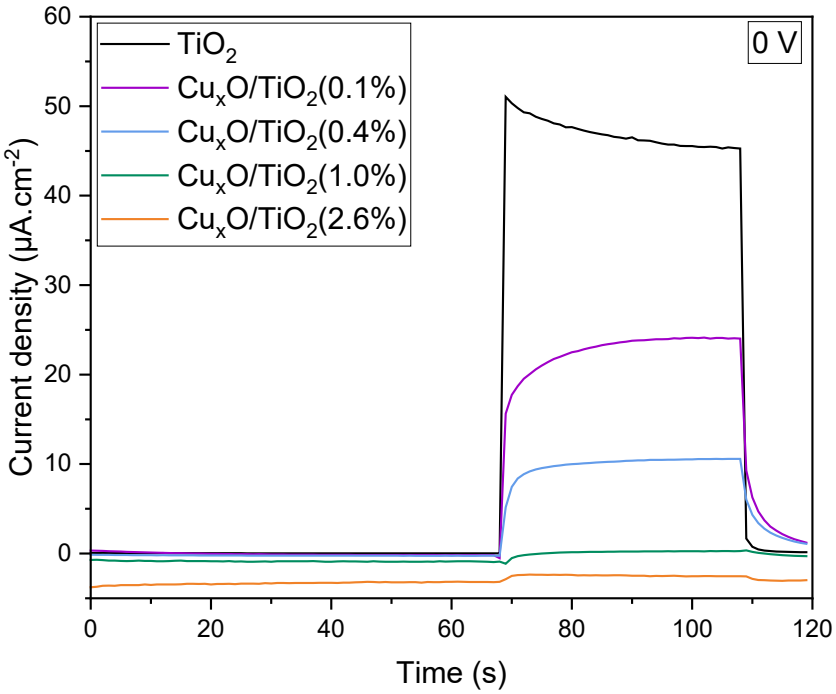

Figure 5-20. Photocurrent response at fixed potential of 0.0 V. Electrolyte = 0.05 M $KClO_4$. I_0 (280-420 nm) = 44 W m^{-2}.

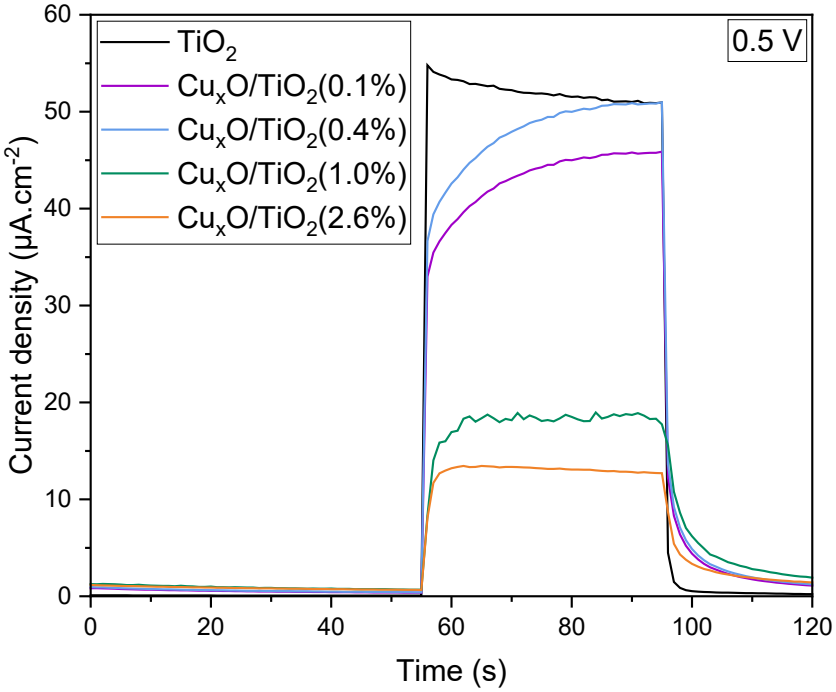

Figure 5-21. Photocurrent response at fixed potential of + 0.5 V. Electrolyte = 0.05 M $KClO_4$. I_0 (280-420 nm) = 44 W m^{-2}.

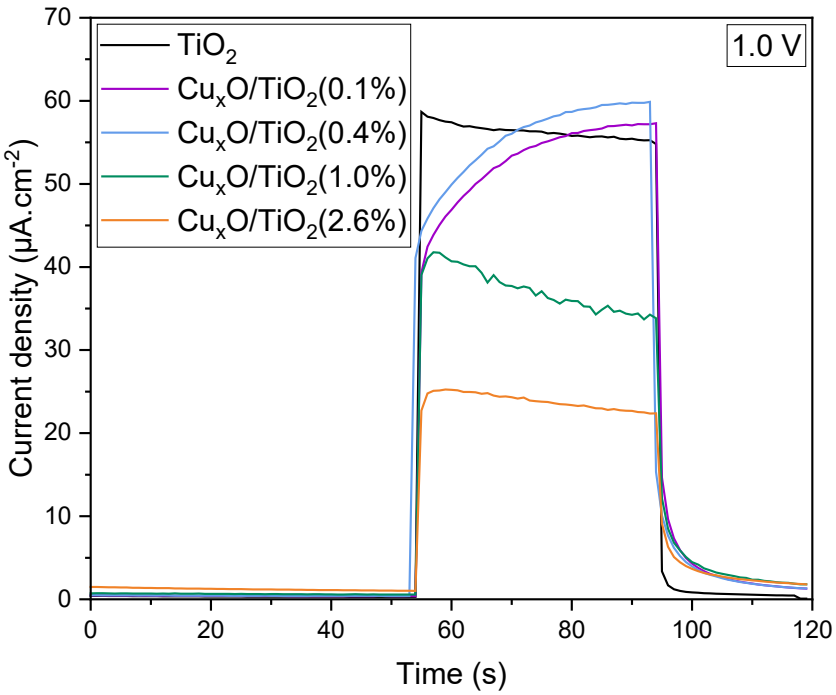

Figure 5-22. Photocurrent response at fixed potential of +1.0 V Electrolyte = 0.05 M $KClO_4$. I_0 (280-420 nm) = 44 W m^{-2}.

5.4.3.3 Open-circuit potential (E_{ocp}) and Open circuit Photopotential (E_{pho})

The effect that modifying TiO_2 with Cu_xO clusters had on the E_{ocp} and E_{pho} was studied and shown in Figure 5-23. The results obtained from the OCP measurements, revealed the presence of four distinct regions. In this technique, as there is no applied bias, the conducting substrate (in this case FTO) does not behave as electron sink as in the photocurrent measurements. Therefore, the potential measured corresponds to the potential of the conducting substrate equilibrated with the deposited TiO_2 or Cu_xO/TiO_2 layer. In the first region, the electrode is in steady state in the dark. In the second region, which occurs when the semiconductor electrode is irradiated and in non-steady conditions, the holes are either trapped at the interface or transferred to the solution with a faster rate than electrons. Therefore, this process produces a surplus of negative charge that causes a rise in the fermi level of the conducting substrate, until it equilibrates with the quasi-Fermi level of the produced electrons of the photoanode, resulting in a negative photo-potential [24]. In the case of the surface modified TiO_2 electrodes, two trends can be observed for the different loadings. For the high Cu_xO loading content and a mixture of Cu(I) and Cu(II), electrons might be easily transferred to Cu_xO leaving the conduction band of the TiO_2, resulting in a photopotential less negative than for unmodified TiO_2.

On the other hand, for low loadings of Cu_xO and Cu(I) oxidation state, the holes are easily transferred to the solution or the Cu_xO generating a higher excess of negative charge and generating a more negative photopotential than unmodified TiO_2. After some time, a steady state under illumination is reached (E_{pho}), representing region 3. Upon turning off the irradiation, the electrode will eventually return to a steady state in the dark. The duration of this transition varies depending on the redox processes occurring at the solid electrolyte interface. The values obtained are summarized in Table 5-4.

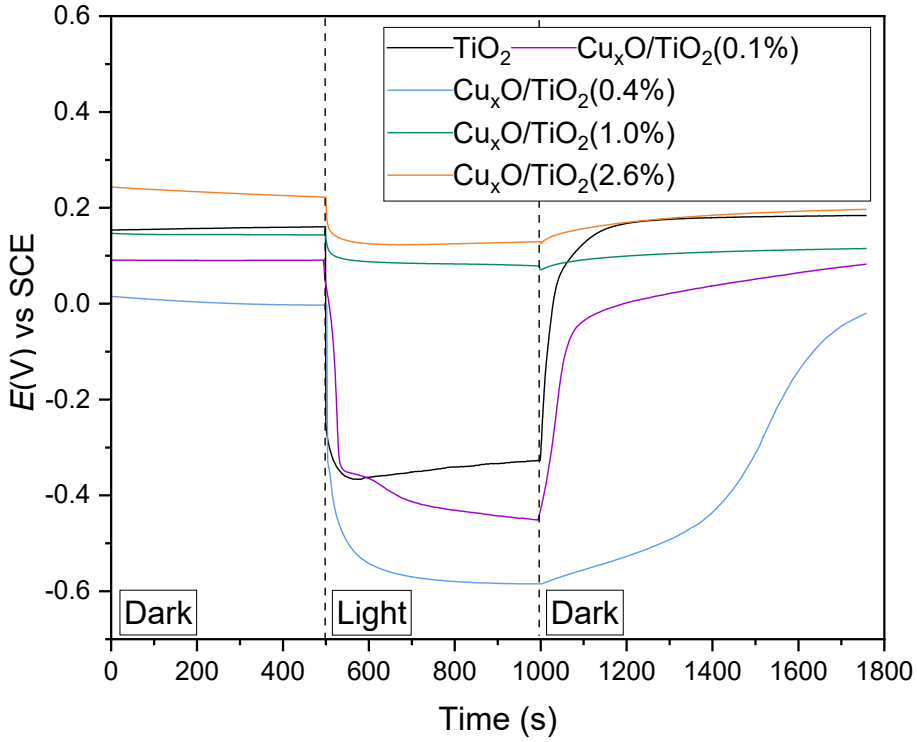

Figure 5-23. Open circuit potential for TiO_2 and Cu_xO/TiO_2 under dark and irradiation. I_0 (280-400 nm) = 44 W m^{-2}. Electrolyte = 0.05 M $KClO_4$.

Table 5-4. Open-circuit potential and Open circuit photo-potential.

Sample	E_{ocp}	E_{pho}
TiO_2 (P25)	0.156	-0.324
Cu_xO(0.1%)/TiO_2	-0.004	-0.584
Cu_xO(0.4%)/TiO_2	0.096	-0.444
Cu_xO(1.0%)/TiO_2	0.146	0.086
Cu_xO(2.6%)/TiO_2	0.226	0.126

5.4.4 Photocatalytic oxidation of urea

The photocatalytic performance of the Cu_xO modified TiO_2 samples was evaluated for the oxidation of urea and compared to the performance of unmodified TiO_2 (P25) (Figure 5-24). The oxidation of urea was fitted to a zero order kinetic model, these results are shown in Figure 5-25 and Table 5-5.

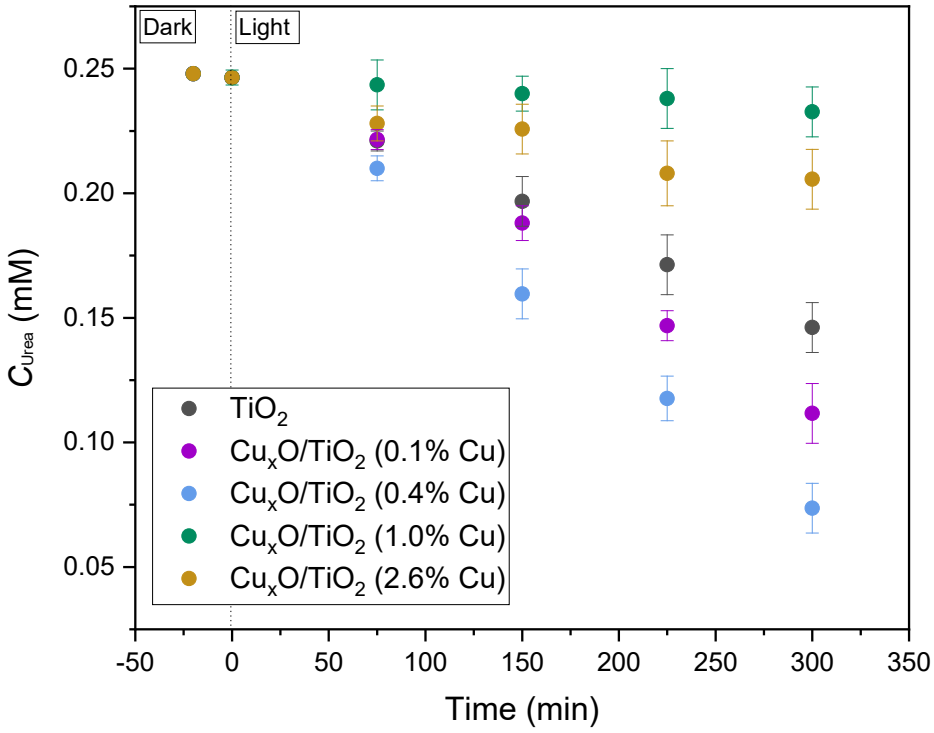

Figure 5-24. Photocatalytic urea oxidation in time for different Cu_xO/TiO_2, using 1000 W Xe lamp, under air bubbling.

Previous studies have reported urea showing small or no adsorption on the surface of TiO_2, being this a possible reason for not experiencing hole mediated oxidation [25]. In the present study, no significant adsorption can be observed in the dark in either TiO_2 or Cu_xO/TiO_2 samples (Figure 5-24). The oxidation of urea has been reported to be primarily driven by •OH radicals [26]. In urea, the C atom is in +4 oxidation state, and there is no C-H extractable bond present, therefore, the •OH has been proposed to attack the $-NH_2$, resulting in a slow process when compared to the oxidation of other nitrogen waste as e.g. formamide [26]. Pelizzetti *et al.* reported a 60 % urea oxidation with a starting

concentration of 0.83 mM using and 0.5 g/L of TiO_2 as photocatalyst [27]. Park *et al.* reported the enhancement in urea oxidation using Pt modified TiO_2 photocatalysts when compared to TiO_2 [25].

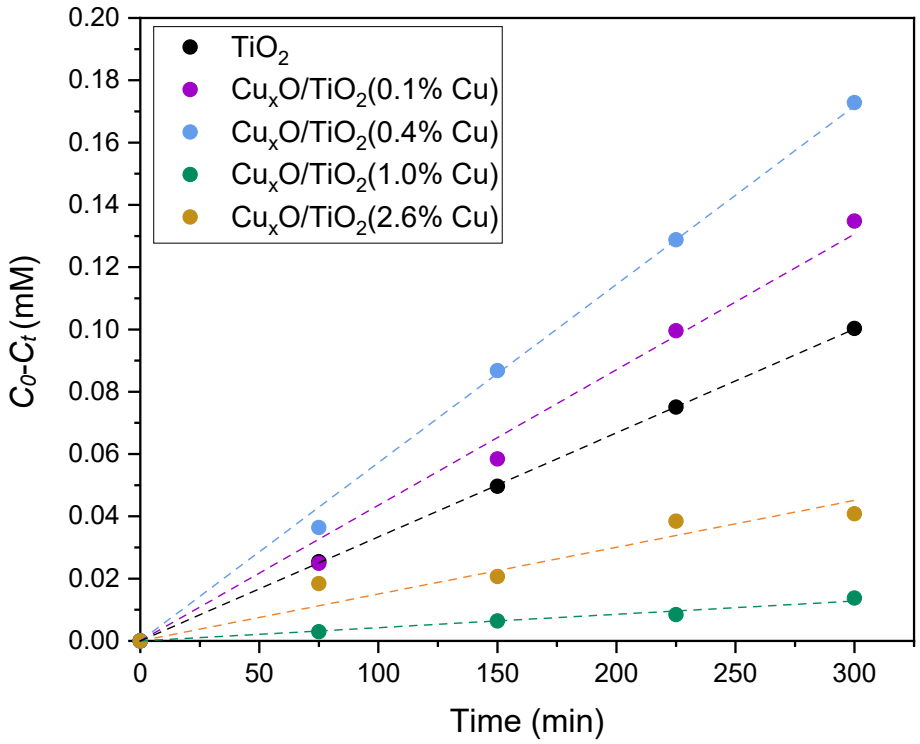

Figure 5-25. Linear 0-order fitting for the photocatalytic urea oxidation in time for different Cu_xO/TiO_2.

Table 5-5. Rate constant and R-square (COD) for urea oxidation.

Sample	*k (mM min^{-1})*	R^2
TiO_2 (P25)	$3.3.10^{-4}$	0.9998
Cu_xO(0.1%)/TiO_2	$4.4.10^{-4}$	0.9950
Cu_xO(0.4%)/TiO_2	$5.7.10^{-4}$	0.9989
Cu_xO(1.0%)/TiO_2	$4.3.10^{-5}$	0.9905
Cu_xO(2.6%)/TiO_2	$1.5.10^{-4}$	0.9684

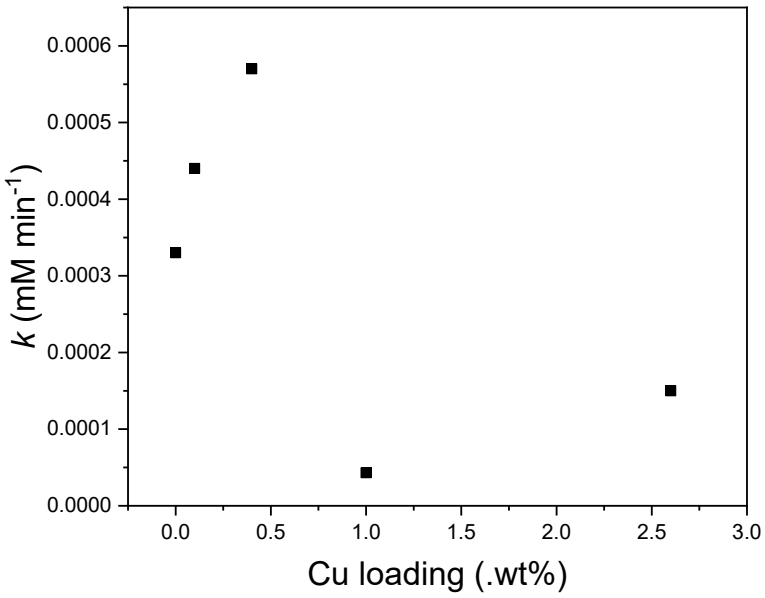

Figure 5-26. Rate constant for photocatalytic urea oxidation vs the Cu loading (wt.%).

The results showed improved urea oxidation rates for the samples modified with oxidation state Cu(I) and loadings of 0.1% and 0.4% when compared to unmodified TiO_2(P25) (Figure 5-26). However, the samples modified with mixtures of Cu(I) and Cu(II) and loadings of 1.0% and 2.6% exhibited worse performance than TiO_2(P25) (Figure 5-26). The best performance was obtained with the sample Cu_xO/TiO_2 (0.4%) with an oxidation rate of $5.7.10^{-4}$ mM min^{-1} which is 1.7 better than for TiO_2 ($3.3.10^{-4}$ mM min^{-1}). In addition, the sample modified with just 0.1% of loading also showed a rate of $4.4.10^{-4}$ mM min^{-1} which is 1.3 better than for TiO_2. This suggest that surface modification with Cu_2O in low loadings enhances the charge separation and contributes to lower the recombination charge carriers, showing improved oxidation of urea. However, the presence of higher Cu_xO loadings (> 1wt.%) which are present with different copper oxidation states result in a poor photocatalytic performance. This could be due to the CuO providing recombination centres for the photogenerated charges, worse stability occasioned by the oxidation and reduction between both Cu oxidation states or high loading creating shielding effect, which reduces the light absorption of TiO_2 and photogenerated charges generated. When comparing the samples with Cu loadings of 1 wt.% and 2.6 wt.%, the worse performance is obtained with the loading of 1 wt%. This could be due to the 52 at.% of Cu_2O and 48 at.% CuO present in the clusters compared to the 87 at.% found in the clusters with loading 2.6 wt.%.

The use of Cu_xO modified TiO_2 has been reported for the oxidation of other wastes [3,4,28]. Feng *et al.* reported the use of Cu_2O modified TiO_2 fabricated using photo-deposition for the oxidation of ammonia. The study showed an increased ammonia oxidation with the addition of Cu_2O clusters [29]. Benz *et al.* studied the photocatalytic degradation of organic dyes using Cu_2O modified TiO_2 fabricated through ALD [3]. The study showed an oxidation rate of 2 times the P25 at 0.4 wt.% loading, with loadings higher than 1.2 wt.% showing worse oxidation rate than P25. Saedy *et al.* used ALD modified TiO_2 with Cu_2O clusters for the photocatalytic production of hydrogen from ethanol [4]. The study showed highest H_2 production with 2 wt.%.

The surface modification of TiO_2 with Cu_xO clusters did not show any enhancement when used as a photoanode compared to unmodified TiO_2, therefore, no products quantification was performed for these experiments The Cu_xO modified TiO_2 showed improved photocatalytic activity for the oxidation of urea. This was probably due to the improvement in charge separation which lowers the recombination of photogenerated electron-hole pairs. However, the performance of the surface modified TiO_2 was found to be dependent on the loading and the degree of oxidation of the copper clusters.

In addition, the photoelectrochemical measurements showed that the best performance between the modified samples was achieved with the sample with 0.4 wt.% loading, which was also the best performing sample for photocatalysis.

5.5 Conclusions

The use of particle suspension ALD resulted on the deposition of Cu_xO nanoclusters with a narrow particle size and controlled loading onto TiO_2(P25) substrate. The particle size distribution and loading were studied by the use of ICP and TEM. In addition, the XPS revealed different Cu oxidation states for the different loadings, showing the presence of Cu(I) and Cu(II) for higher loadings (>1.0 wt/%). The effect of the deposition of Cu_xO clusters on the TiO_2 band gap was studied by UV-DRS and VB XPS, with the results suggesting a reduction in the TiO_2 band gap. However, photoelectrochemical characterization and determination of light absorbance differences using spectral photocurrent response showed no increase in absorption to the visible region of the spectrum for the Cu_xO modified TiO_2, showing no effective band-gap reduction, in contrast to the estimations obtained with the optical band-gap measurements.

The surface modification of TiO_2 with Cu_xO clusters did not enhance the photoelectrochemical properties. However, the photocatalytic experiments showed the deposition of Cu_xO on TiO_2 to have the ability to enhance the oxidation of urea, probably due to the improvement in charge separation resulting in lower recombination. The performance of the surface modified TiO_2 was found to be dependent on the loading and the degree of oxidation of the copper clusters. The best performing sample was the one containing a Cu wt.% loading of 0.4 and oxidation state Cu(I), achieving 1.7 times the oxidation rate of unmodified TiO_2.

Future studies should focus on the control of the Cu oxidation state during the ALD synthesis process, to avoid further oxidation to Cu(II) at higher loadings. In addition, the long-term stability of the photocatalysts and the possible oxidation and reduction of the Cu during the photocatalytic reaction should be assessed. Besides, further work could explore the use of photoelectrochemistry for the evaluation of semiconductor heterojunctions as p-n or n-p, studying their photocurrent response to chopped illumination.

References

[1] M. Pelaez, N.T. Nolan, S.C. Pillai, M.K. Seery, P. Falaras, A.G. Kontos, P.S.M. Dunlop, J.W.J. Hamilton, J.A. Byrne, K.O. Shea, M.H. Entezari, D.D. Dionysiou, Applied Catalysis B : Environmental A review on the visible light active titanium dioxide photocatalysts for environmental applications, "Applied Catal. B, Environ. 125 (2012) 331–349. https://doi.org/10.1016/j.apcatb.2012.05.036.

[2] A.S. Zoolfakar, R.A. Rani, A.J. Morfa, A.P. O'Mullane, K. Kalantar-zadeh, Nanostructured copper oxide semiconductors: a perspective on materials, synthesis methods and applications, J. Mater. Chem. C. 2 (2014) 5247–5270. https://doi.org/10.1039/C4TC00345D.

[3] D. Benz, Y.N.T. Nguyen, T.L.T. Le, T.H.T. Le, V.T. Le, J.R. van Ommen, H. van Bui, Controlled growth of ultrasmall Cu_2O clusters on TiO_2 nanoparticles by atmospheric-pressure atomic layer deposition for enhanced photocatalytic activity, Nanotechnology. 32 (2021). https://doi.org/10.1088/1361-6528/ac10e2.

[4] J.R. van O. Saeed Saedy, Nico Hiemstra, Dominik Benz, Hao Van Bui, Michael Nolan, Dual promotional effect of Cu_xO clusters grown with atomic layer deposition on TiO2 for photocatalytic hydrogen production, Cambridge Open Engag. (2021) 1–20.

[5] Q. Jin, M. Fujishima, A. Iwaszuk, M. Nolan, H. Tada, Loading Effect in Copper (II) Oxide Cluster-Surface-Modified Titanium (IV) Oxide on Visible- and UV-Light Activities, J. Phys. Chem. C. 117 (2013) 23848–23857. https://doi.org/10.1021/jp4085525.

[6] P.K. Sharma, M.A.L.R.M. Cortes, J.W.J. Hamilton, Y. Han, J.A. Byrne, M. Nolan, Surface modification of TiO_2 with copper clusters for band gap narrowing, Catal. Today. 321–322 (2019) 9–17. https://doi.org/10.1016/j.cattod.2017.12.002.

[7] Z. Wang, D. Brouri, S. Casale, L. Delannoy, C. Louis, Exploration of the preparation of Cu/TiO_2 catalysts by deposition–precipitation with urea for selective hydrogenation of unsaturated hydrocarbons, J. Catal. 340 (2016) 95–106. https://doi.org/10.1016/j.jcat.2016.05.011.

[8] L. Huang, F. Peng, H. Wang, H. Yu, Z. Li, Preparation and characterization of Cu_2O/TiO_2 nano–nano heterostructure photocatalysts, Catal. Commun. 10 (2009) 1839–1843. https://doi.org/10.1016/j.catcom.2009.06.011.

[9] K. Zhao, S. Zhao, J. Qi, H. Yin, C. Gao, A.M. Khattak, Y. Wu, A. Iqbal, L. Wu, Y. Gao, Cu_2O clusters grown on TiO_2 nanoplates as efficient photocatalysts for hydrogen generation, Inorg. Chem. Front. 3 (2016) 488–493.

[10] Z. Xi, C. Li, L. Zhang, M. Xing, J. Zhang, Synergistic effect of Cu_2O/TiO_2 heterostructure nanoparticle and its high H_2 evolution activity, Int. J. Hydrogen Energy. 39 (2014) 6345–6353. https://doi.org/10.1016/j.ijhydene.2014.01.209.

[11] J. Li, L. Liu, Y. Yu, Y. Tang, H. Li, F. Du, Preparation of highly photocatalytic active nano-size TiO_2–Cu_2O particle composites with a novel electrochemical method, Electrochem. Commun. 6 (2004) 940–943. https://doi.org/10.1016/j.elecom.2004.06.008.

[12] D. Praveen Kumar, N. Lakshmana Reddy, M. Mamatha Kumari, B. Srinivas, V. Durga Kumari, B. Sreedhar, V. Roddatis, O. Bondarchuk, M. Karthik, B. Neppolian, M. V Shankar, Cu_2O-sensitized TiO_2 nanorods with nanocavities for highly efficient photocatalytic hydrogen production under solar irradiation, Sol. Energy Mater. Sol. Cells. 136 (2015) 157–166. https://doi.org/10.1016/j.solmat.2015.01.009.

[13] M. Zhang, A. Kobayashi, T. Koide, A. Sekiguchi, O. Okada, N. Hosokawa, Optimization of copper CVD film properties using the precursor of Cu(hfac)(tmvs) with variations of additive content, in: Proc. IEEE 1999 Int. Interconnect Technol. Conf. (Cat. No.99EX247), 1999: pp. 170–172. https://doi.org/10.1109/IITC.1999.787112.

[14] R. Izquierdo, J. Bertomeu, M. Suys, E. Sacher, M. Meunier, Excimer laser-induced deposition of copper from Cu(hfac) (TMVS), Appl. Surf. Sci. 86 (1995) 509–513. https://doi.org/10.1016/0169-4332(94)00439-0.

[15] A. Sekkat, M. Weber, J. López-Sánchez, H. Rabat, D. Hong, J. Rubio-Zuazo, D. Bellet, G. Chichignoud, A. Kaminski-Cachopo, D. Muñoz-Rojas, Selective spatial atomic layer deposition of Cu, Cu_2O, and CuO thin films in the open air: reality or fiction?, Mater. Today Chem. 29 (2023) 101431. https://doi.org/10.1016/j.mtchem.2023.101431.

[16] T. Iivonen, M.J. Heikkilä, G. Popov, H.-E. Nieminen, M. Kaipio, M. Kemell, M. Mattinen, K. Meinander, K. Mizohata, J. Räisänen, M. Ritala, M. Leskelä, Atomic Layer Deposition of Photoconductive Cu_2O Thin Films, ACS Omega. 4 (2019) 11205–11214. https://doi.org/10.1021/acsomega.9b01351.

[17] A. Didden, P. Hillebrand, M. Wollgarten, B. Dam, R. van de Krol, Deposition of conductive TiN shells on SiO_2 nanoparticles with a fluidized bed ALD reactor, J. Nanoparticle Res. 18 (2016) 35. https://doi.org/10.1007/s11051-016-3343-z.

[18] D. Muñoz-Rojas, M. Jordan, C. Yeoh, A.T. Marin, A. Kursumovic, L.A. Dunlop, D.C. Iza, A. Chen, H. Wang, J.L. MacManus Driscoll, Growth of ∼5 cm2V−1s−1 mobility, p-type Copper(I) oxide (Cu_2O) films by fast atmospheric atomic layer deposition (AALD) at 225°C and below, AIP Adv. 2 (2012) 42179. https://doi.org/10.1063/1.4771681.

[19] P.K. Sharma, M.A.L.R.M. Cortes, J.W.J. Hamilton, Y. Han, J.A. Byrne, M. Nolan, Surface modification of TiO_2 with copper clusters for band gap narrowing, Catal. Today. 321–322 (2019) 9–17. https://doi.org/10.1016/j.cattod.2017.12.002.

[20] P. Makuła, M. Pacia, W. Macyk, How To Correctly Determine the Band Gap Energy of Modified Semiconductor Photocatalysts Based on UV–Vis Spectra, J. Phys. Chem. Lett. 9 (2018) 6814–6817. https://doi.org/10.1021/acs.jpclett.8b02892.

[21] M. Pelaez, N.T. Nolan, S.C. Pillai, M.K. Seery, P. Falaras, A.G. Kontos, P.S.M. Dunlop, J.W.J. Hamilton, J.A. Byrne, K. O'Shea, M.H. Entezari, D.D. Dionysiou, A review on the visible light active titanium dioxide photocatalysts for environmental applications, Appl. Catal. B Environ. 125 (2012) 331–349. https://doi.org/10.1016/j.apcatb.2012.05.036.

[22] D. Gupta, S.R. Meher, N. Illyaskutty, Z.C. Alex, Facile synthesis of Cu_2O and CuO nanoparticles and study of their structural, optical and electronic properties, J. Alloys Compd. 743 (2018) 737–745. https://doi.org/10.1016/j.jallcom.2018.01.181.

[23] J.A. Byrne, B.R. Eggins, Photoelectrochemistry of oxalate on particulate TiO_2 electrodes, J. Electroanal. Chem. 457 (1998) 61–72. https://doi.org/10.1016/S0022-0728(98)00304-0.

[24] T. Berger, D. Monllor-Satoca, M. Jankulovska, T. Lana-Villarreal, R. Gómez, The Electrochemistry of Nanostructured Titanium Dioxide Electrodes, ChemPhysChem. 13 (2012) 2824–2875. https://doi.org/10.1002/cphc.201200073.

[25] S. Park, J.T. Lee, J. Kim, Photocatalytic oxidation of urea on TiO_2 in water and urine: mechanism, product distribution, and effect of surface platinization, Environ. Sci. Pollut. Res. 26 (2019) 1044–1053. https://doi.org/10.1007/s11356-017-8380-3.

[26] P. Calza, E. Pelizzetti, C. Minero, The fate of organic nitrogen in photocatalysis: An overview, J. Appl. Electrochem. 35 (2005) 665–673. https://doi.org/10.1007/s10800-005-1626-7.

[27] E. Pelizzetti, P. Calza, G. Mariella, V. Maurino, C. Minero, H. Hidaka, Different photocatalytic fate of amido nitrogen in formamide and urea, Chem. Commun. (2004) 1504–1505. https://doi.org/10.1039/B404574B.

[28] J. Feng, X. Zhang, G. Zhang, J. Li, W. Song, Z. Xu, Improved photocatalytic conversion of high−concentration ammonia in water by low−cost Cu/TiO_2 and its mechanism study, Chemosphere. 274 (2021) 129689. https://doi.org/10.1016/j.chemosphere.2021.129689.

[29] J. Feng, X. Zhang, G. Zhang, J. Li, W. Song, Z. Xu, Improved photocatalytic conversion of high−concentration ammonia in water by low−cost Cu/TiO_2 and its mechanism study, Chemosphere. 274 (2021). https://doi.org/10.1016/j.chemosphere.2021.129689.

Chapter 6. Tungsten oxide photoanodes for the oxidation of urea coupled to simultaneous hydrogen production

The contents of this chapter have been published in part in "Rioja-Cabanillas, A., McMichael, S., Tolosana-Moranchel, A., Alkharabsheh, S., Skillen, N., Fernandez-Ibanez, P., Byrne, J. A. (2023). Solar photoelectrocatalytic oxidation of urea in water coupled to green hydrogen production. Journal of Cleaner Production, (2023) 138200. https://doi.org/10.1016/j.jclepro.2023.138200"

6.1 Aim and Objectives

6.1.1 Aim

The overall objective of this work is to fabricate tungsten oxide (WO_3) nanostructured photoanodes and assess their performance for the oxidation of urea with simultaneous hydrogen production. The photoelectrochemical performance was compared with P25 (TiO_2) as benchmark.

6.1.2 Objectives

The specific objectives of this research are the following:

- Fabrication nanostructured WO_3 photoanode.
- Analysis of material properties of the fabricated electrode e.g. morphology, chemical composition, crystalline phase and optical properties.
- Evaluation of photoelectrochemical response of the WO_3 electrode and comparison to TiO_2(P25) as benchmark.
- Study of the photoelectrochemical performance of the electrodes in the presence of urea.
- Determination of IPCE efficiency in presence of urea.
- Evaluation of the use of WO_3 for the oxidation of urea compared to TiO_2 in scaled-up customized photoelectrochemical cell and determination of oxidation kinetics.
- Identification of all products from the oxidation of urea.
- Assessment of use of one or two compartment cell on urea conversion and byproducts.

- Detection and quantification of hydrogen produced at the cathode in a two compartment PEC cell
- Evaluation of hydrogen production performance parameters as Faradaic and Solar to hydrogen conversion efficiencies.

6.2 Introduction

Coupling the photoelectrochemical oxidation of organic and inorganic compounds to the production of hydrogen is an interesting approach to recovering energy from, and with the simultaneous treatment of, wastewater. Among the different semiconductors, TiO_2 has been widely used due to its high photo-activity, low cost and good chemical and thermal stability. While TiO_2 has been studied for a range of diverse applications including hydrogen production [1] and degradation of organic pollutants [2], there are fewer examples for the photocatalytic oxidation of urea [3–5]. In addition, TiO_2 has a wide bandgap (3.2 eV), only absorbing 4% of the total solar irradiation. Alternatively, WO_3 has been proposed as a promising alternative to TiO_2, due to its narrower band gap, which extends into the visible region of the solar spectrum. It also presents good stability and charge carrier mobility, and resistance to photo-corrosion [6]. WO_3 photoanodes have been widely studied for water splitting [7], however to date, only few works have investigated urea oxidation [8–10].

A variety of WO_3 nanostructures have been studied, including 1-D structures as nanotubes or nanowires and 2-D structures as nanoplates or nanosheets [7]. WO_3 2-D structures have showed high photocurrent due to shorter charge diffusion length and exposed highly reactive facets [11–13]. Some of these nanostructures have been fabricated by anodization of W foil, with the foil acting as the conductive substrate. However, when using non-transparent substrates with front-face configuration in wastewater applications, the irradiation can be attenuated by the water matrix. Therefore, the use transparent conductive substrates as fluorine doped tin oxide (FTO) or indium doped tin oxide (ITO) is beneficial. WO_3 nanostructures synthesized using sol-gel or hydrothermal methods followed by an immobilization step into the conductive substrate have been studied [7]. Alternatively, it is also possible the in situ synthesis of nanostructures on the conductive substrate using hydrothermal method, resulting in a simple one step process.

While most photoelectrochemical works have focused on either hydrogen production from water splitting or on the degradation of pollutants, only limited studies have investigated the production of energy coupled with wastewater treatment. In 2006, Kaneko et al. demonstrated the possibility of generating electricity by decomposing different pollutants (including urea) using a TiO_2 photoanode and a O_2-reducing cathode. Since then, very few studies have highlighted the recovery of energy in the form of electricity [15] or H_2 from urea using TiO_2 based photoanodes [16,17]. The low photo-current densities reached using TiO_2 under simulated solar irradiation, however, limit the applicability of this approach.

The aim of this work is to showcase the simultaneous photoelectrochemical oxidation of urea and the production of hydrogen using a WO_3 photoanode with a platinized titanium cathode in a two compartment photoelectrochemical cell. The photoelectrochemical behaviour of WO_3 was compared to TiO_2 as benchmark. Urea oxidation kinetics and product distribution were investigated using two custom-made photoelectrochemical cells. The findings presented in this study demonstrate the proof of concept of oxidizing common pollutants present in wastewater as urea, coupled to the simultaneous generation of hydrogen in a photoelectrochemical cell.

6.3 Experimental Methodology

6.3.1 Photoanode fabrication

The TiO_2 photoanode was fabricated by the immobilization of commercial Evonik Aeroxide P25 on a fluorine doped tin oxide (FTO) coated glass using spray coating, achieving a desired loading of 1 mg cm^{-2}. The WO_3 photoanode was synthesized directly on the FTO glass using a hydrothermal method [18]. For the photoelectrochemical characterization experiments, FTO glasses with a size of 2 x 1.5 cm were employed. The electrical contact was made by attaching a copper wire to an uncoated section of the FTO employing silver epoxy. A negative photoresist was use as insulator of the contact and any area of the conductive substrate not covered with semiconductor. (Detailed fabrication methods are given in Chapter 3, 3.3.2 Electrode fabrication).

6.3.2 Material characterization

The surface morphology of the photoanodes was characterized using scanning electron microscope (Hitachi SU500 FE-SEM) with an accelerating voltage of 10 kV and a high

vacuum pressure of 10^{-8} bar. The size of the nanoparticles was determined using the software ImageJ averaging more than 50 measurements.

The elemental composition of the electrodes was determined by X-ray photoelectron spectroscopy (XPS) (Kratos Axis Ultra). The wide energy survey scans (WESS) were measured for all samples in the binding energy range of 0-1250 eV, with a pass energy of 160 eV. High resolution (HR) scans of each target element (C, Ti, W and O) were recorded with a pass energy of 14.2 eV.

The crystalline phase of the WO_3 photoanode was characterized using X-ray diffraction (XRD) (Malvern Panalytical) with Cu Kα (λ= 1.560 Å) radiation at a scanning angle between 20° and 70°.

The UV-vis diffuse reflectance spectra were measured with a LAMBDA 365 UV/Vis spectrometer (PerkinElmer) equipped with an integrating sphere and the optical band gap was estimated using the Kubelka-Munk method.

6.3.3 Electrochemical characterization

The photoelectrochemical characterization was performed using an electrochemical workstation (AUTOLAB PGSTAT 30) and a 450 W Xe lamp (Horiba Jobin Yvon FL-1039/40, Figure 3-1) equipped with a monochromator (Horiba Jobin Yvon microHR), a chopper (Uniblitz) for interrupted irradiation and an infra-red (IR) filter. In each photoelectrochemical measurement, the photoanode was used as the working electrode with a Pt mesh as counter and a saturated calomel electrode (SCE) as reference. The experiments were performed in a 30 mL one compartment cylindrical cell made of quartz glass, using 0.05 M $KClO_4$ as electrolyte.

The linear sweep voltammetry (LSV) and spectral photocurrent were performed to evaluate the performance of the photoanodes under different potential and spectral conditions. In the LSV, a scan rate of 5 mV s^{-1} was used. The spectral photocurrent response measurements were performed from a wavelength ranging from 280 nm to 500 nm in steps of 10 nm with chopped irradiation intervals of 20 s and a fixed potential of +1 V vs SCE. The incident photon to current efficiency (IPCE) was determined using Equation (**3-4**) described in Chapter 3, section 3.3.4.2 Photoelectrochemical characterization.

6.3.4 Urea degradation and hydrogen production experiments

For these experiments custom-made 3D printed cells with one and two compartments were used (Figure 3-6 and Figure 3-7). A commercial platinized (2.5 ± 0.3 μm) titanium mesh was used as cathode. The cells were equipped with septum ports to facilitate the extraction of liquid samples using syringes. The one-compartment cell, shown Figure 3-6, had a total volume of 33 mL and an electrode separation of 10 mm. In the two-compartment PEC cell (Figure 3-7), a Nafion membrane, placed between two silicon gaskets, was used to separate the anolyte from the catholyte. Each compartment had a volume of 33 mL and the distance between electrodes was 15 mm. The electrolyte consisted of 0.05 M $KClO_4$ and known concentrations of either urea, nitrate or ammonium with an initial pH of 6.2. The starting concentration of urea was adapted to the capabilities of the detection method.

The irradiation source was a 1000 W Xe lamp (Quantum Design, Figure 3-1). A power supply (PHL120 DC Aim-TTi) was used to provide the external electrical bias and multimeters were used to record the potential and current (1351 Data precision).

The quantification of the N-species in aqueous phase including, NH_4^+, NO_3^-, NO_2^- and urea was performed following the spectrophotometric methods described chapter 3, section 3.3.5 Quantification of reactants and products. The detection of hydrogen gas was performed using a gas chromatograph (GC - Agilent Technologies 7280 A) equipped with a thermal conductivity detector (TCD). Gas samples with a volume of 0.1 mL were injected into the GC using a gas tight syringe. The quantification of the total volume of gas produced during the urea degradation experiments was carried out by water displacement through a gas tight connection of the catholyte headspace to an inverted graduated cylinder. The gas generated in the cathode compartment was collected in a Tedlar sampling bag (Restek). Before performing experiments, the catholyte compartment was purged for 20 min with N_2 gas to remove the oxygen from the electrolyte.

6.4 Results and Discussion

6.4.1 Material Characterization

SEM was performed to analyse the surface morphology of the WO_3 electrode (Figure 6-1). The image at low magnification shows he FTO glass to be uniformly covered with a

plate-like structures. The high magnification image shows the plate-like structure with an average plate length of 1000 nm and average thickness of 200 nm. SEM images for the electrode formed by P25 were presented and studied in Chapter 4, section 4.4.1 Electrode morphology. These images are again given in Figure 6-1 for the purpose of comparison.

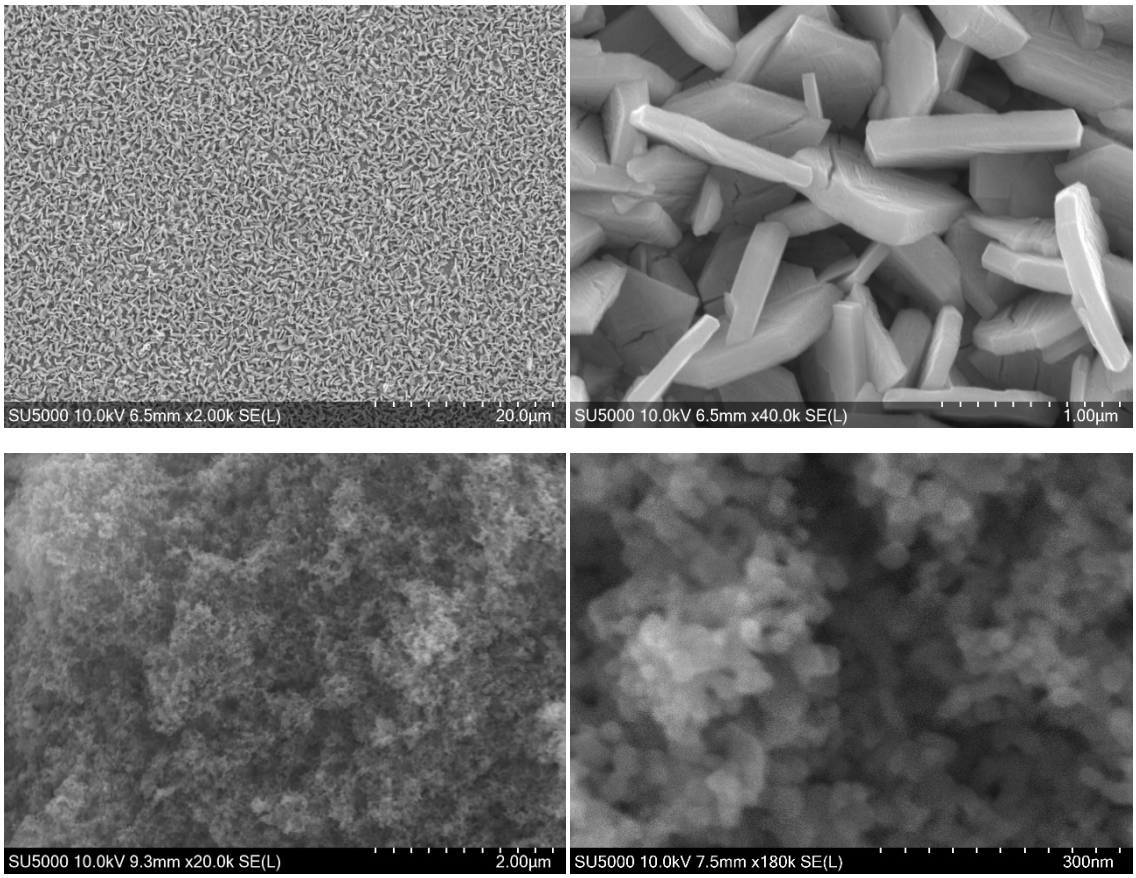

Figure 6-1. SEM images and for the WO_3 electrode at 2k magnification (left top) and 40 k magnification (top right) and the P25 electrode at 20 k magnification (left bottom) and 180k magnification (right bottom).

The XRD patterns of the WO_3 grown film after calcination are shown in Figure 6-2, with the FTO glass patterns also shown for easier identification of WO_3 peaks. All the diffraction peaks of the WO_3 plates agree well with the monoclinic crystal phase of WO_3, (PDF no.43-1035) with lattice constants of a=7.297, b=7.539 and c=7.688 Å.

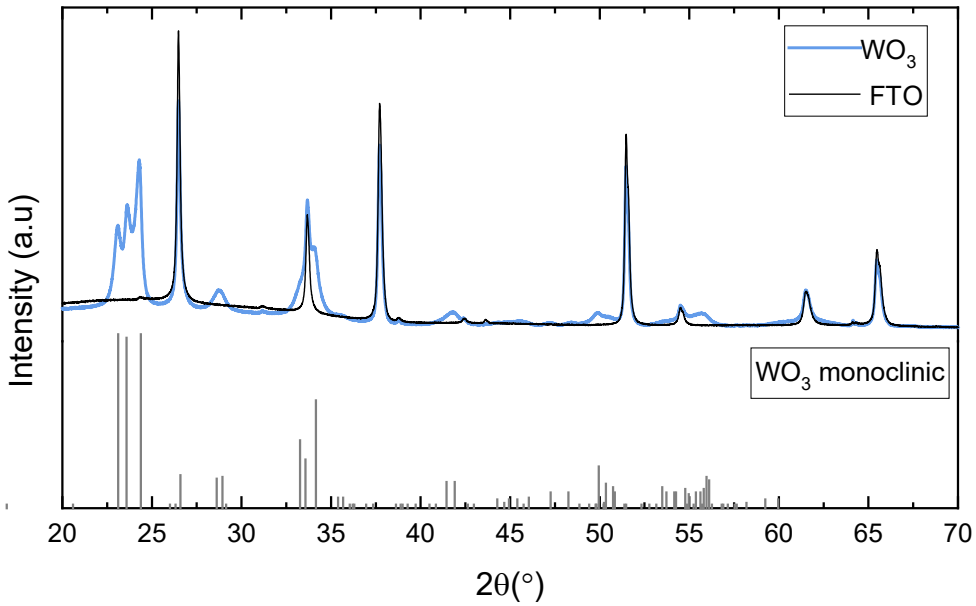

Figure 6-2. XRD patterns of FTO and WO_3.

The chemical composition of both photoanodes was analysed by XPS. The survey spectra (Figure 6-3) showed the presence of Ti, O and C on the TiO_2 electrode and W, O and C on the WO_3 electrode, with no significant contamination. The Ti 2p spectra corresponding to the TiO_2 photoanode shows the clearly defined Ti(IV) 2 $p_{3/2}$ peak located at a binding energy (BE) of 458.6 eV, and the Ti $2p_{1/2}$ at 464.3 eV, separated by 5.7 eV (Figure 6-4) [19]. The observed Ti^{4+} confirms, with the corresponding O 1s component, the presence of TiO_2. Additionally, the doublet $2p_{3/2}$ and $2p_{1/2}$ located at BE of 457.2 and 461.6 respectively, reveals a minor contribution from the lower oxidation state (+3) due to oxygen vacancies [20]. The W 4f spectra of the WO_3 photoanode shows two main peaks separated by 2.2 eV and attributed to the doublet W $4f_{7/2}$ and $4f_{5/2}$ (Figure 6-5). These contributions positioned at BE of 35.8 eV and 38 eV, are characteristic of the electronic state of W^{6+} in WO_3. Moreover, the presence of two minor contributions at slightly lower BE of 34.6 eV and 36.9 eV can be attributed to the doublet $4f_{7/2}$ and $4f_{5/2}$ from the electronic structure of W^{5+}, originated by the presence of oxygen vacancies [21,22]. In addition, the O1s XPS spectra from WO_3 was fitted and deconvoluted into three peaks at binding energies of 530.4 eV, 531.6 eV and 532.4 eV (Figure 6-6). The most intense peak is attributed to lattice oxygen (O_2^-) in WO_3. The peak at binding energy of 531.6 eV could be associated to O_2^- in the oxygen deficient region within WO_3 [23-25]. While the

peak at binding energy of 532.4 eV corresponds to the H_2O species on the surface of WO_3.

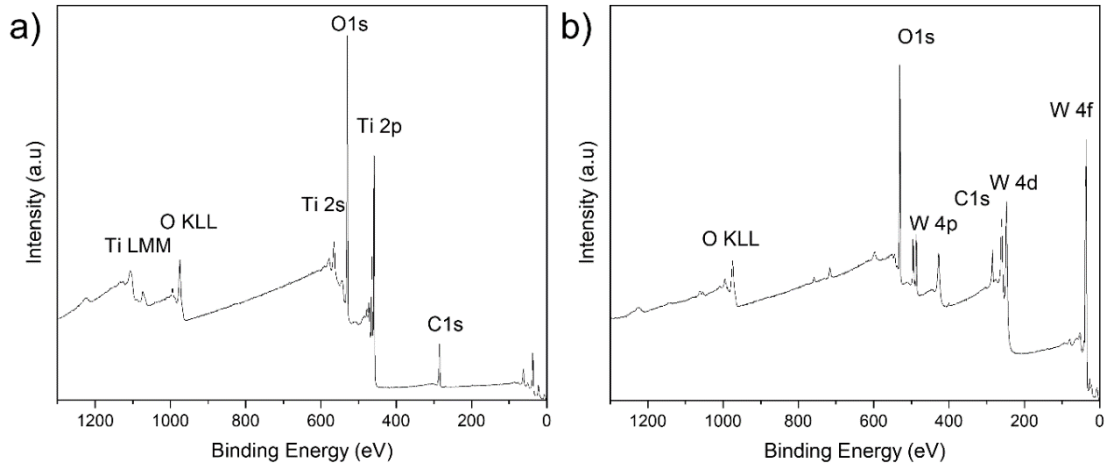

Figure 6-3. XPS survey spectra for a) TiO_2 electrode and b) WO_3 electrode.

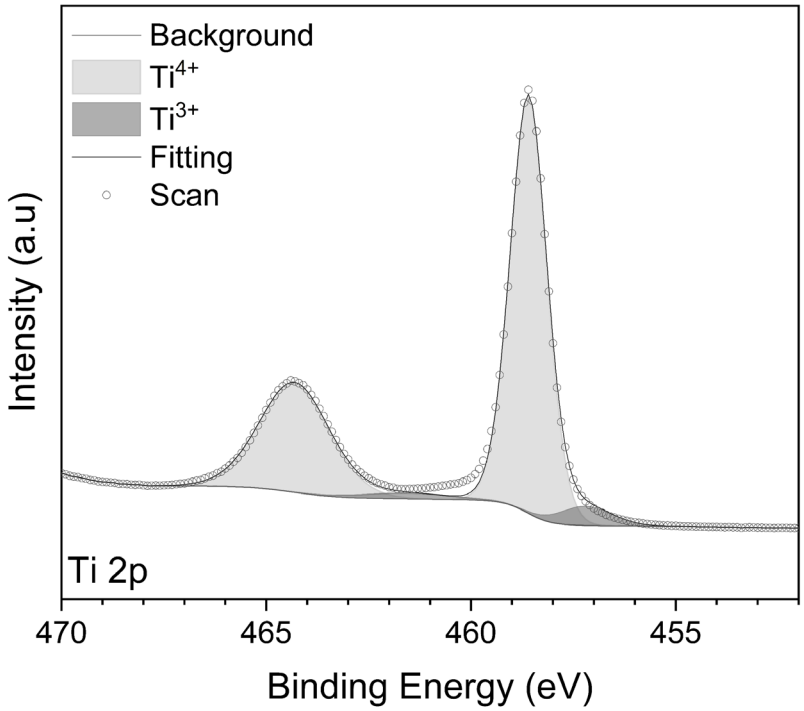

Figure 6-4. XPS spectra corresponding to Ti 2p for the TiO_2 photoanode.

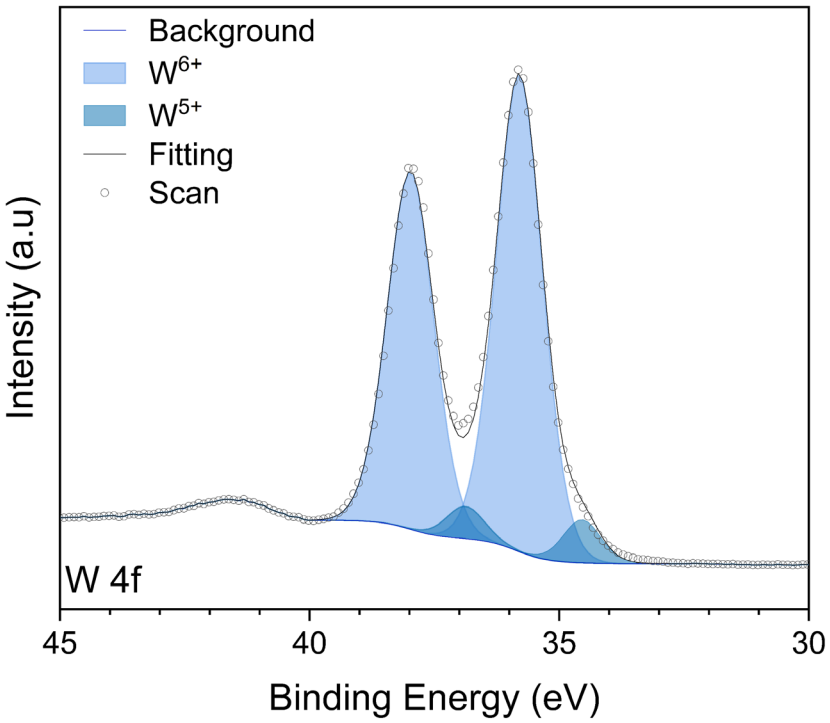

Figure 6-5. XPS spectra corresponding to W4f for the WO_3 photoanode.

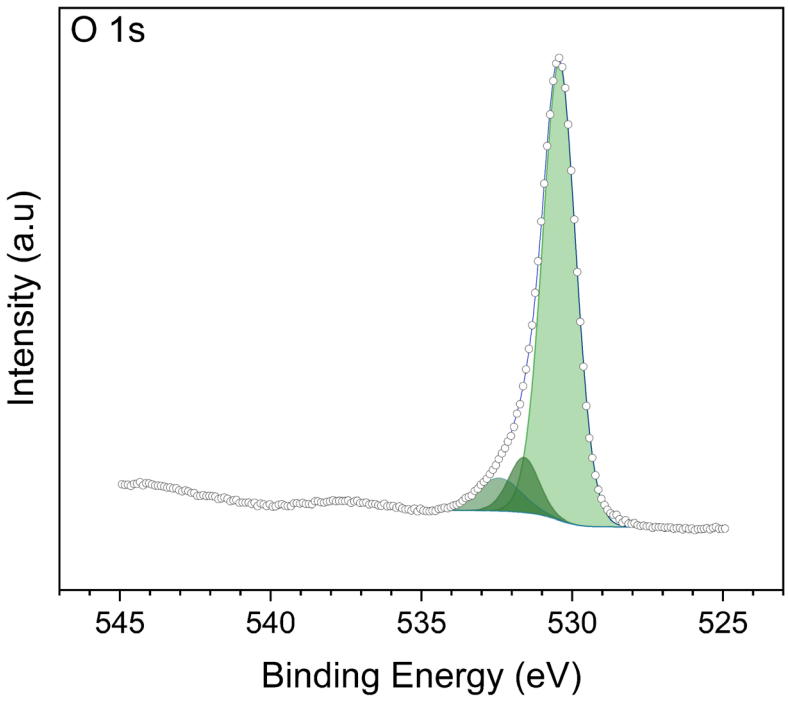

Figure 6-6. XPS spectra corresponding to O 1s for the WO_3 photoanode.

The optical band gap energies were estimated from the diffuse reflectance measurements using the Tauc plots shown in Figure 6-7. An optical band gap of 3.2 eV was obtained for the electrode formed by P25 deposited on FTO, which agrees with previous literature values of 3.2 eV for anatase and 3.0 eV for rutile, with P25 being a mixture of 80% anatase and 20% rutile [2]. The optical band gap for the WO_3 plates grown on FTO was 2.7 eV which, correlates to previously reported values for WO_3 nanostructures of 2.5-2.8 eV [2,26,27].

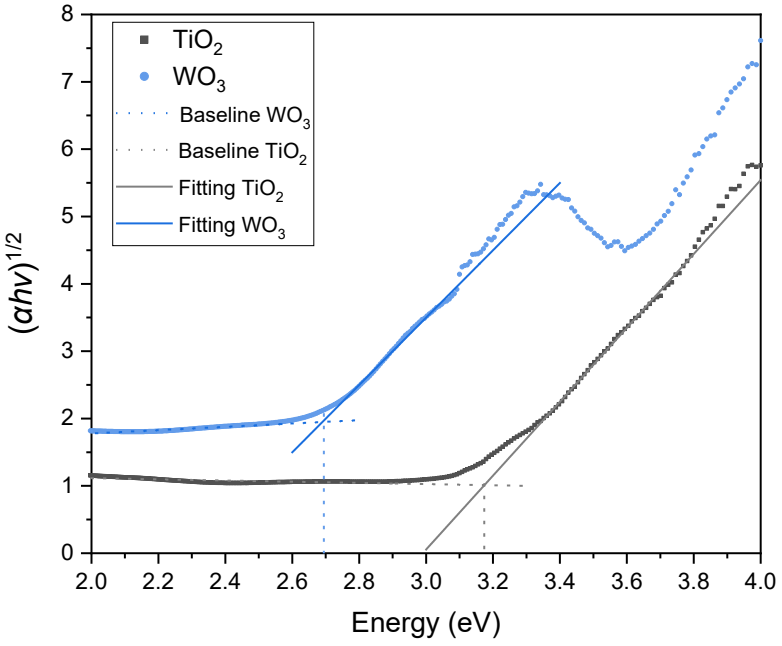

Figure 6-7. Tauc plots for the TiO_2 photoanode (black) and the WO_3 photoanode (blue).

6.4.2 Photoelectrochemical characterization

The photoelectrochemical characteristics of the fabricated electrodes were evaluated by LSV under chopped irradiation, spectral photocurrent response and IPCE. The current response of both anodes was measured in a potential ranging from 0 to + 1.5 V vs SCE (Figure 6-8). The TiO_2 photoanode showed a photocurrent density of 40 μA cm^{-2}, which is stable in the studied potential range, while the WO_3 photoanode showed an increasing photocurrent density, reaching a saturation current density of 402 μA cm^{-2} at + 1.5 V. The maximum current value obtained with WO_3 is 10 times higher than the one measured

with TiO_2. Different current densities have been reported for different WO_3 structures, varying from 150 μA cm^{-2} to 2500 μA cm^{-2} [2,26,27], while reported values for P25 photoanodes vary from 1 μA cm^{-2} to 1000 μA cm^{-2} [17,33–37]. A direct comparison of these values is unfortunately not possible due to the different experimental conditions, such as the radiation intensity, spectral output of the irradiation source, the electrolyte and the photoelectrochemical cell design.

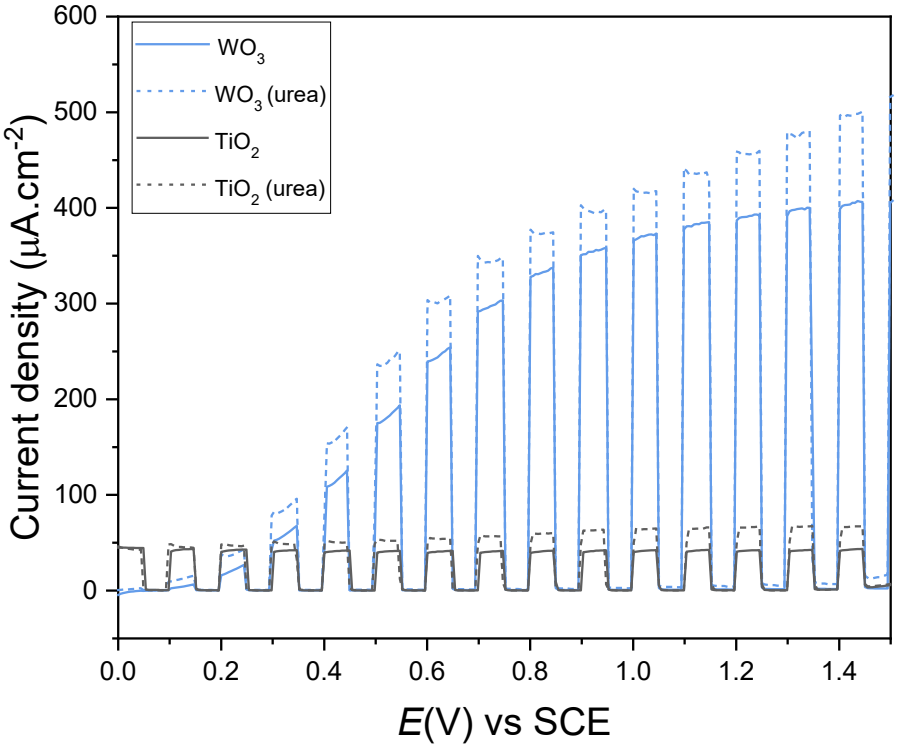

Figure 6-8. Linear sweep voltammograms under chopped irradiation, working window: 0 to +1.5 V, scan rate = 5 mV s^{-1}. I_0 (280-500 nm) = 178 W m^{-2}. Electrolyte = 50 mM $KClO_4$ with (dash) or without 6.6 mM urea (solid).

To study the current response of both photoanodes in time, amperometry measurements in presence of urea for both electrodes were performed and are shown in Figure 6-9. Both photoanodes remain stable for the studied time range.

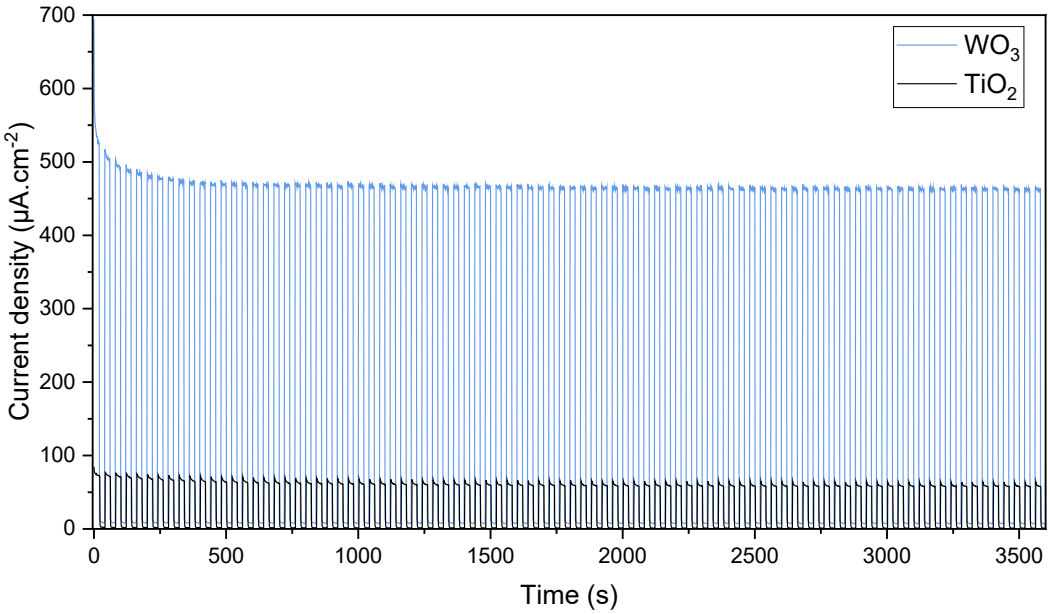

Figure 6-9. Chronoamperometry under chopped irradiation for prolonged time period, Io (280-500 nm) = 178 W m^{-2}. Electrolyte = 0.05M $KClO_4$ and 6.6 mM urea. Applied potential for TiO_2 +1.0 V vs SCE and for WO_3 +1.5 V vs SCE.

To study the electrode behaviour at negative potentials and measure the onset photocurrent potential, a LSV performed from -1.0 to +1.5 V vs SCE (Figure 6-10) is used, for TiO_2 photoanode the onset potential for anodic current was -0.6 V vs SCE, while for WO_3 the onset potential for anodic current was + 0.15 V vs SCE. The critical band bending ($\varnothing_s$) is the difference between the onset potential (close to flat band E_{fb}) and the potential required to obtain the maximum or saturated photocurrent (where all charge carriers are separated). For TiO_2 $\varnothing_s$ is around + 0.5 V (Figure 6-10) while for the WO_3 the photocurrent continues to increase asymptotically up to + 1.5 V ($\varnothing_s$ ~ 1.35 V), but a much larger photocurrent is observed. Multiple factors can account for the better performance of the WO_3 photoanode at more positive potentials, compared to the TiO_2. The plate-like structure of WO_3 presents a direct pathway for the photogenerated charges to the current collector [27,38]. On the other hand, the TiO_2 photoanode has a porous structure formed from P25 independent particles. This structure limits photogenerated charge transfer efficiency through the particles and to the collector electrode (FTO glass), increasing the interparticle charge recombination [39,40].

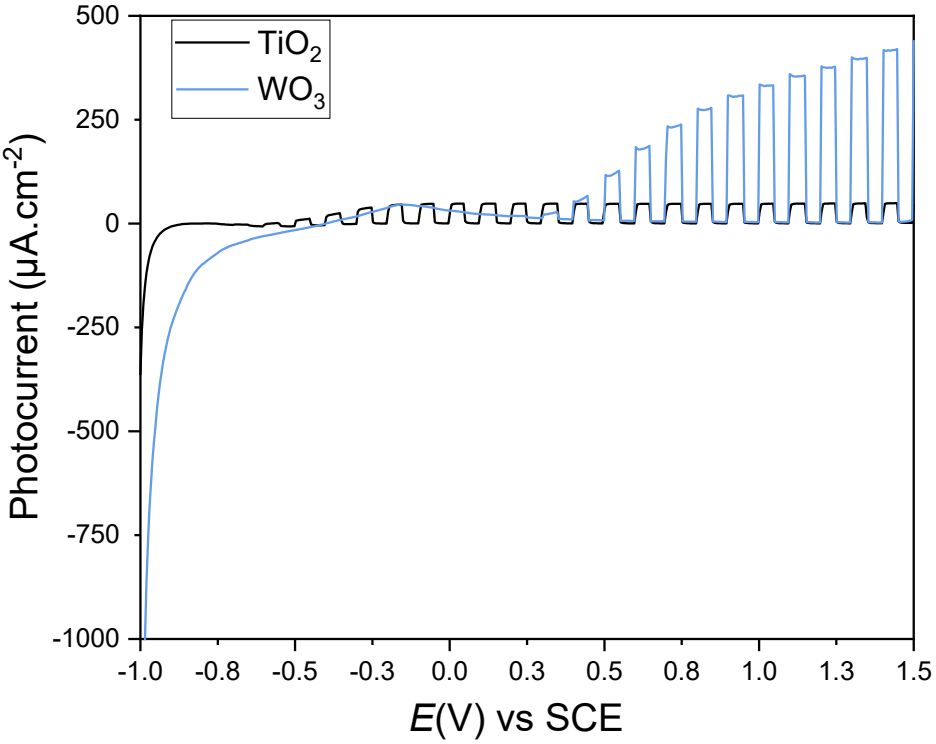

Figure 6-10. Linear sweep voltammograms under chopped irradiation, working window: -1.0 to +1.5 V, scan rate = 5 mV s^{-1}. I_0 (280-500 nm) = 178 W m^{-2}. Electrolyte = 50 mM $KClO_4$.

In addition to morphological differences, when comparing the spectral photocurrent response (Figure 6-11), WO_3 showed a superior photocurrent density than TiO_2, at any point in the spectrum. Furthermore, WO_3 exhibited visible light activity up to 470 nm while TiO_2 gave photocurrent up to 390 nm. These wavelengths correspond to an effective bandgap of 2.63 eV for WO_3 and 3.18 eV for TiO_2, which are consistent with the optical band gap determined from the Tauc plots, and correlate to values previously reported [1,2]. The IPCE efficiency of WO_3 peaks with 37% at a wavelength of 360 nm, while TiO_2 peaks with 12 % at 340 nm **(**Figure 6-12). The IPCE values obtained for WO_3 are in line with several studies using WO_3 nanoparticulate photoanodes [28–30,38]. The IPCE values reported in previous studies for P25 photoanodes vary widely (10 – 25 %) [32–35], due to the different experimental conditions, including the electrode thickness, immobilization process, electrolyte and testing conditions; nevertheless, the value reported in this work is within the range reported in comparable studies.

An increase in the photocurrent density due to the addition of urea was observed for both electrodes, which may be attributed to the oxidation of urea via direct hole transfer or via hydroxyl radical mediated hole transfer (Figure 6-10) both resulting in hole capture and reduced rates of charge carrier recombination. The photocurrent magnitude depends on the concentration of urea in solution. An increase in photocurrent due to the presence of urea has been previously reported in two studies using TiO_2 photoanodes. Kim *et al*. (2012) reported a 3-fold increase in photocurrent with a concentration of 0.33 M urea [41] and Pop *et al*. (2015) reported an enhancement varying from 15% to 35% with urea concentrations ranging from 0.1 to 1 M [17]. In this work, with urea concentration of 6.6 mM, a 45% increase in photocurrent for the TiO_2 photoanode is reported. Moreover, this study also tested a WO_3 photoanode in the presence of urea, observing a 25% increase in photocurrent. The spectral photocurrent response was also measured in presence of urea (Figure 6-11). For WO_3 the peak efficiency increased to 43% at a wavelength of 360 nm, while TiO_2 improved to 16% at 340 nm. Overall, the photoelectrochemical results showed an improved performance for WO_3, when compared to TiO_2, which is attributed to an increased light absorption range in the UV-vis due to the lower bandgap energy and an enhanced pathway for the charge carrier migration.

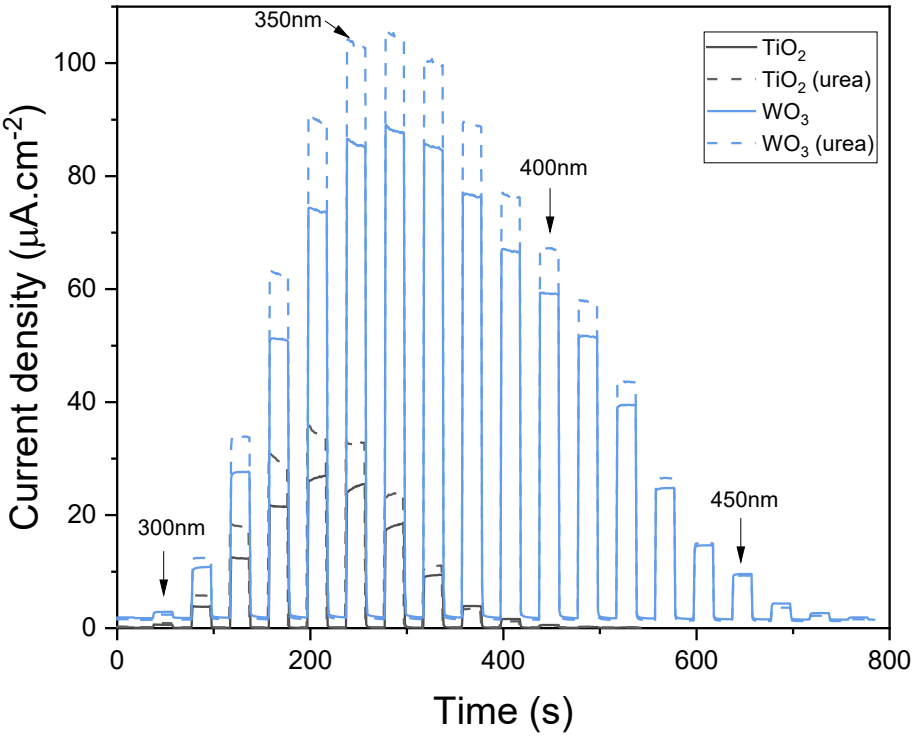

Figure 6-11. Spectral current response at fixed potential (+ 1.0 V vs SCE) with monochromatic irradiation (280 nm to 500 nm). I_0 (280-500 nm) = 178 W m^{-2}. Electrolyte = 50 mM $KClO_4$ with or without 6.6 mM urea.

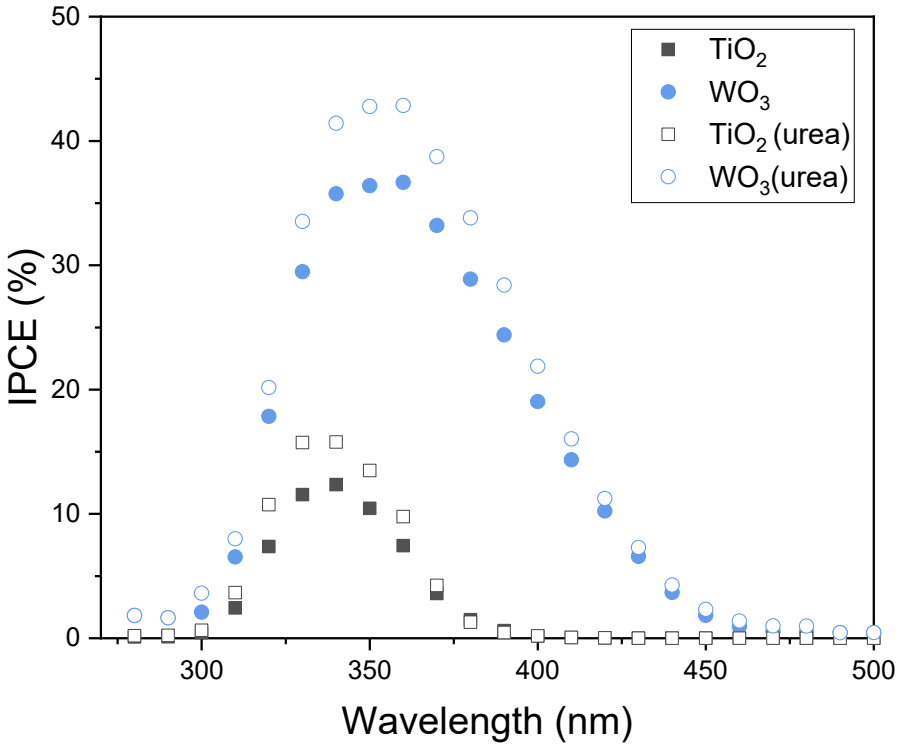

Figure 6-12. Incident photon-to-current efficiency (IPCE). I_0 (280-500 nm) = 178 W m^{-2}. Electrolyte = 50 mM $KClO_4$ with or without 6.6 mM urea.

6.4.3 One-compartment cell: Urea degradation experiments

The performance of TiO_2 and WO_3 photoanodes in the custom-made PEC cell (Figure 6-13 and Figure 6-14) was investigated by varying the applied cell potential between the photoanode and the platinized titanium mesh cathode. Simultaneously, the photoanode potential was measured using a reference electrode as shown in Figure 6-15 and Figure 6-16. The current generated under irradiation by the TiO_2 photoanode increases slightly with increasing applied cell potential (Figure 6-15 and Figure 6-16), for the dark current, breakdown was observed at a potential of +1.2 V. The chosen operating cell potential for TiO_2 was +1.2 V with a photoanode potential of +1.14 V vs SCE, as this was the point of current saturation.

The saturation current for the WO_3 photoanode was substantially higher than for TiO_2, however a greater applied potential is also required to achieve this current (Figure 6-16). The breakdown current for WO_3 photoanode is observed at a cell potential of + 2.5 V, corresponding to a photoanode potential of +1.55 V vs SCE. Under irradiation, for increasing cell potential between + 0.5 and + 1.25 V (Figure 6-14), the anode potential remains fairly constant (+ 0.31 to + 0.32 V vs SCE) (Figure 6-16). Similarly, in the dark for cell potential between + 2.0 and + 2.5 V (Figure 6-14) the anode potential remains between +1.79 to +1.81 V vs SCE (Figure 6-16). This trend is attributed to the contribution of the cathode and the ohmic drop to the cell potential. The cell potential of + 2.4 V was chosen within the saturation region, corresponding to an anode potential of + 1.37 V vs SCE.

The current densities recorded using the one-compartment custom-made PEC cell (Figure 6-16) were higher compared to the quartz cell (Figure 6-8), in the whole range of the applied potentials. This enhancement is caused by the design of the photoelectrochemical cell (Figure 3-7), including lower reflective losses due to planar FTO compared to the cylindrical water-jacketed quartz cell.

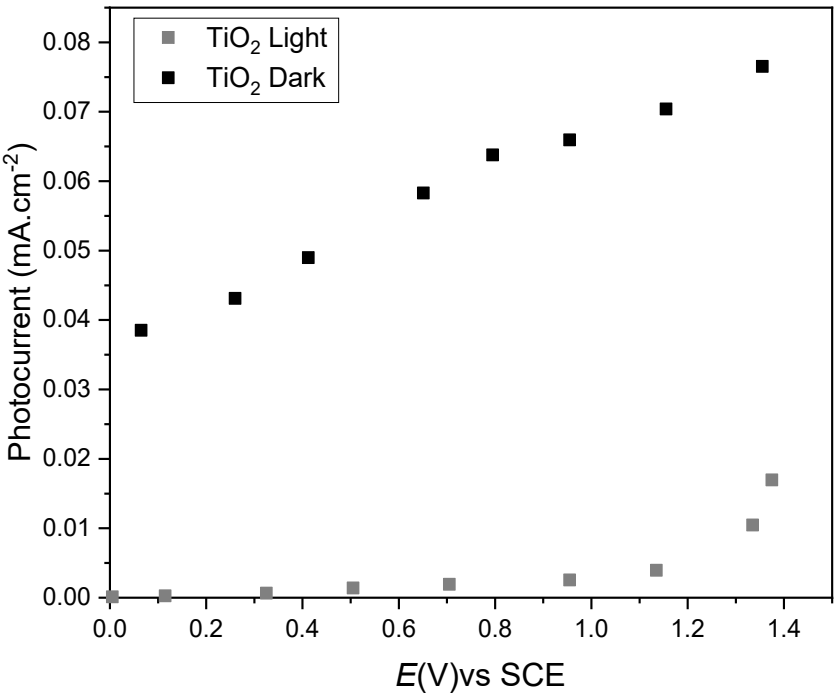

Figure 6-13. Measured current for TiO_2 at different cell potentials. One-compartment photoelectrochemical cell. I_0 (280-500 nm) = 173 W m^{-2}. Electrolyte = 50mM $KClO_4$ and 0.83 mM Urea.

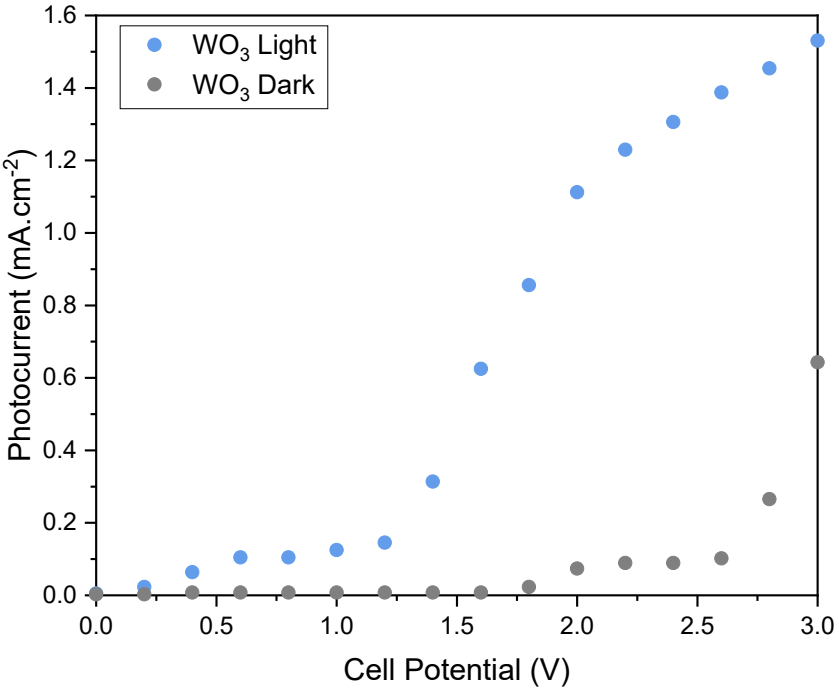

Figure 6-14. Measured current for WO_3 at different cell potentials. One-compartment photoelectrochemical cell. I_0 (280-500 nm) = 173 W m^{-2}. Electrolyte = 50mM $KClO_4$ and 0.83 mM Urea.

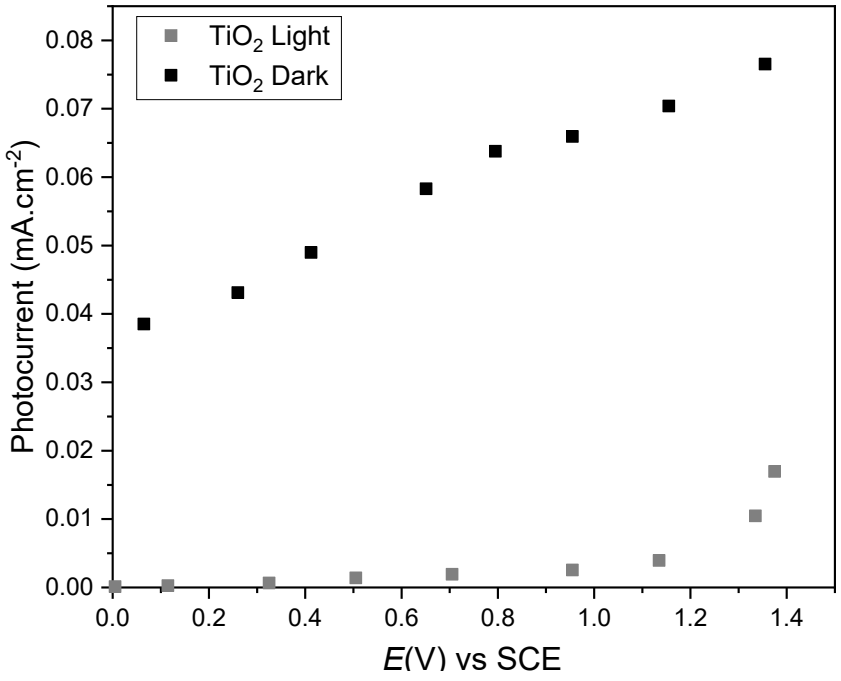

Figure 6-15. Current for anode potential measured while varying cell potential for TiO_2. One-compartment photoelectrochemical cell. I_0 (280-500 nm) = 173 W m^{-2}. Electrolyte = 50mM $KClO_4$ and 0.83 mM Urea.

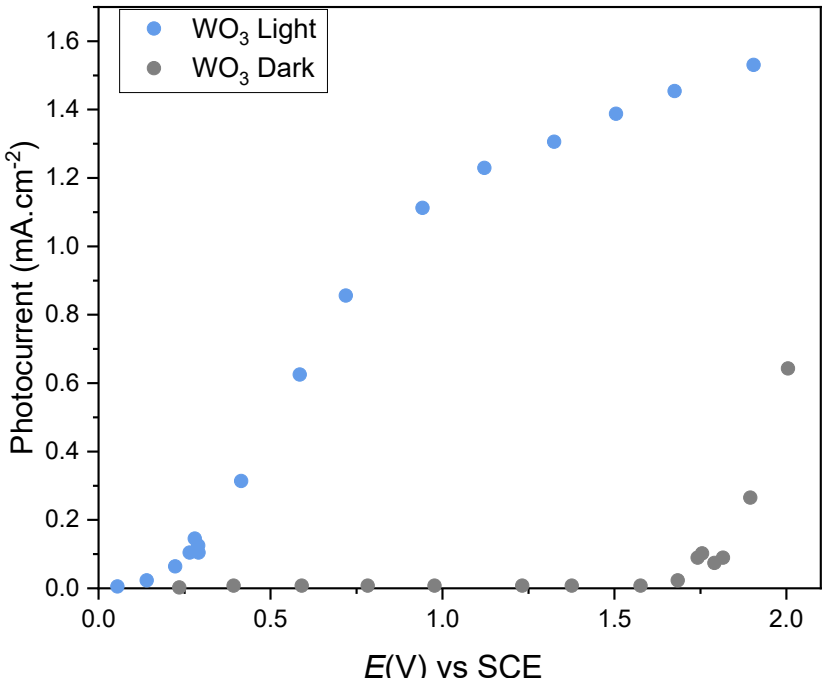

Figure 6-16. Current for anode potential measured while varying cell potential for WO_3. One-compartment photoelectrochemical cell. I_0 (280-500 nm) = 173 W m^{-2}. Electrolyte = 50mM $KClO_4$ and 0.83 mM Urea.

The activity of the TiO_2 and WO_3 photoanodes for urea removal was studied over a period of 2.4 h (Figure 6-17). The experimental data are fitted to a pseudo-first-order kinetic model (Figure 6-18), where C_0 is the initial concentration and C_t the concentration measured at time t. The obtained rate constant (k_1) for WO_3 is 1.47×10^{-2} min^{-1}, is 15 times higher than the one obtained for TiO_2 (1.1×10^{-3} min^{-1}). The TiO_2 photoanode achieved only 13% of urea oxidation while the WO_3 photoanode showed 90 % of urea oxidation after 2.4 h.

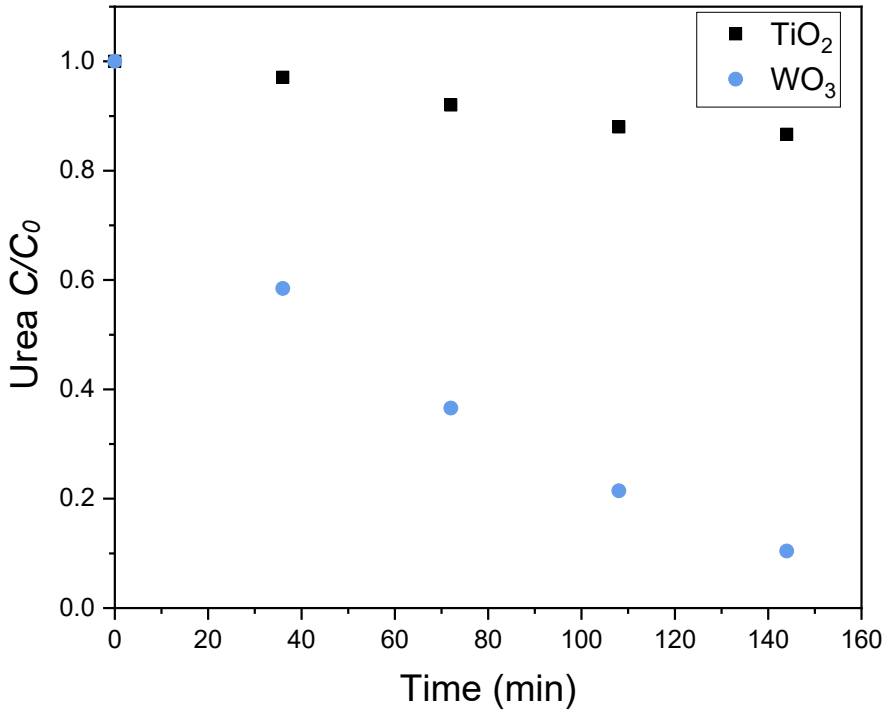

Figure 6-17. Normalized urea concentration vs time for TiO_2 and WO_3 electrodes. $[Urea]_0$ = 0.83 mM. Electrolyte = 0.05M $KClO_4$. I_0 (280-500 nm) = 173 W m^{-2}.

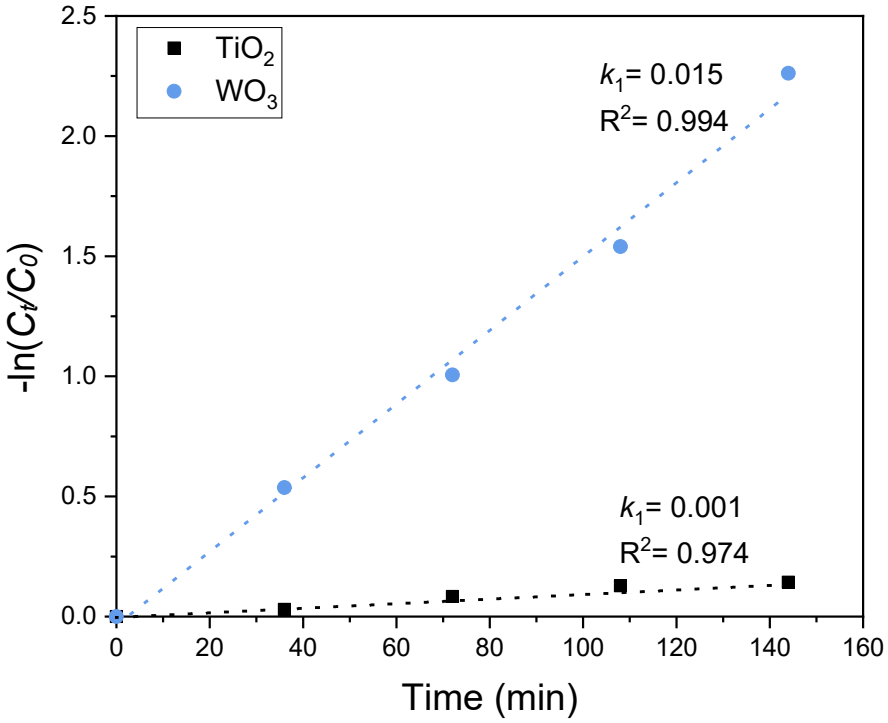

Figure 6-18. Negative natural log of normalized concentration vs time for TiO_2 and WO_3. $[Urea]_0$ = 0.83 mM. Electrolyte = 0.05M $KClO_4$. I_0 (280-500 nm) = 173 W m^{-2}.

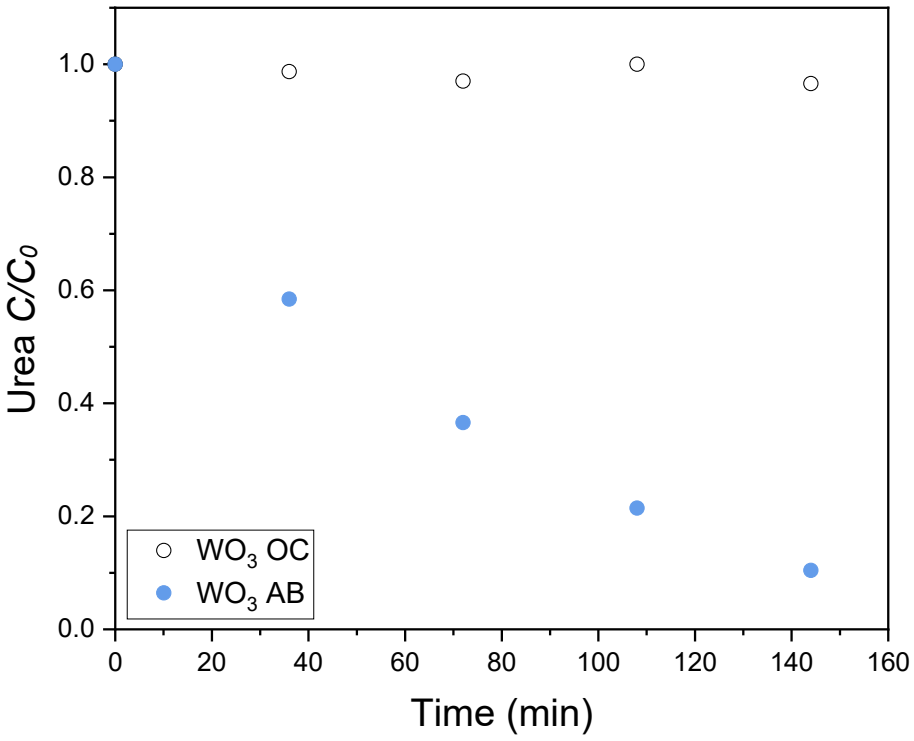

Figure 6-19. Normalized urea concentration vs time for WO_3 electrodes at open circuit (OC) and with applied bias (AB). $[Urea]_0$ = 0.83 mM. Electrolyte = 0.05M $KClO_4$. I_0 (280-500 nm) = 173 W m^{-2}.

To further investigate the difference in performance between WO_3 and TiO_2, additional experiments with the PEC in open circuit configuration (photocatalysis) were performed. For WO_3, the results showed urea removal rate constant of $3x10^{-4}$ min^{-1} which results in less than 5% after 2.4 h (Figure 6-19). The negligible urea oxidation is due to the positive conduction band edge potential of WO_3 which is not negative enough to reduce molecular oxygen to superoxide, leading to a build-up of photogenerated electrons and recombination of charge carriers dominates. On the contrary, when a bias is applied, electrons are driven to the cathode, and the recombination is reduced, leading to improved performance. In the case of TiO_2, (Figure 6-20), a rate constant of $5x10^{-4}$ min^{-1} was obtained at open circuit, with a decrease in urea concentration of 7%, showing just a small difference between the open circuit and applied bias. The favourable position of P25-TiO_2 conduction band edge enables the use of the photogenerated electrons to reduce molecular oxygen, with the holes being used for urea oxidation [2]. However, when a bias is applied, the morphology of P25-TiO_2 hinders electron transfer, and favours surface recombination. This recombination hampers TiO_2 photoanode performance in comparison to WO_3, as discussed in section 6.4.2 Photoelectrochemical characterization.

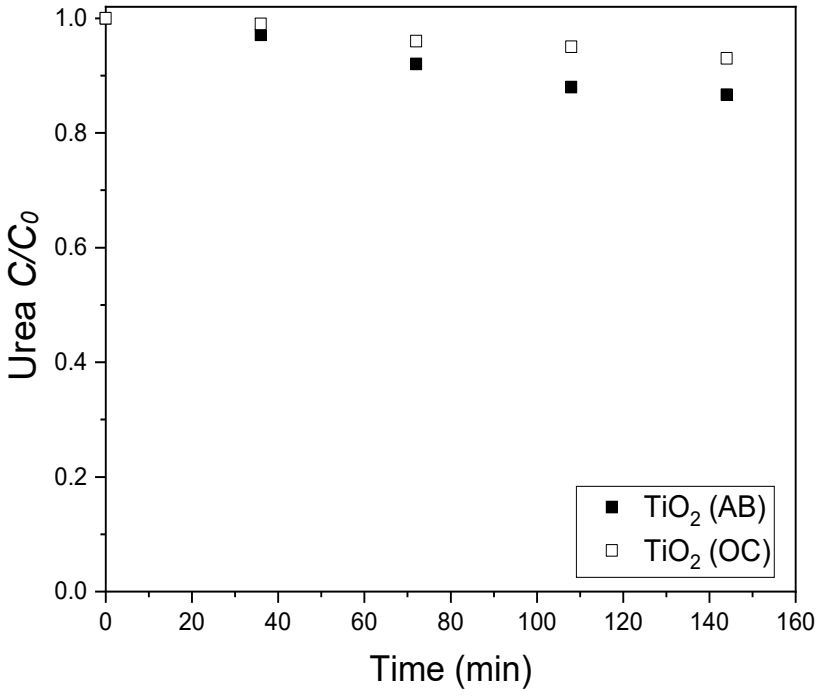

Figure 6-20. Normalized urea concentration vs time for TiO_2 electrodes at open circuit (OC) and with applied bias (AB). $[Urea]_0$ = 0.83 mM. Electrolyte = 0.05M $KClO_4$. I_0 (280-500 nm) = 173 W m^{-2}.

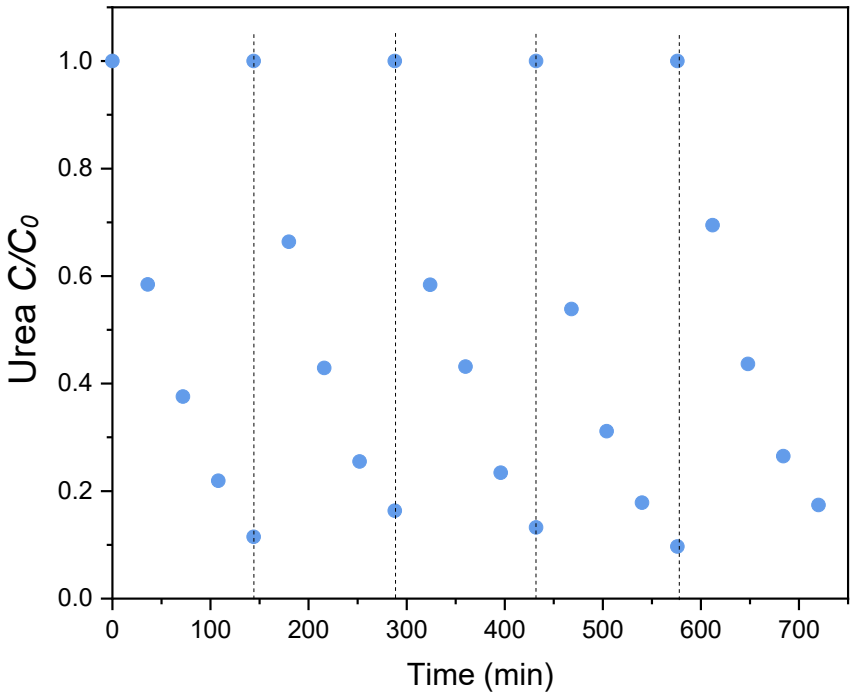

Figure 6-21. Normalized urea concentration vs time for 5 consecutive experiments with the WO_3 electrode. $[Urea]_0$ = 0.83 mM. Electrolyte = 0.05M $KClO_4$. I_0 (280-500 nm) = 173 W m^{-2}.

The reusability of the WO_3 photoanode for urea oxidation is studied over 5 consecutive cycles each 2.4 h, as shown in Figure 6-21**.** The photoanode reveals similar activity with urea oxidation rates ranging from $1.47x10^{-2}$ min^{-1} to $1.2x10^{-2}$ min^{-1}, with the concentration decrease varying by between 90% and 82% at the end of each cycle. Only a slight decrease can be observed in the last cycle after 12 hours.

The analysis of the time distribution of the nitrogen ionic species present in the solution from the oxidation of urea in the custom-made one-compartment PEC cell reveals that the prevalent species are NH_4^+ and NO_3^-, reaching up to 0.86 mM and 0.70 mM, respectively at the end of the experiment, and nearly non-detectable concentrations of NO_2^- ($8x10^{-3}$ mM) (Figure 6-22). The totality of the quantified N-ionic species balances the nitrogen content in this process, suggesting that no N_2 gas or other aqueous N-species were originated from the oxidation of urea under these conditions (Figure 6-22).

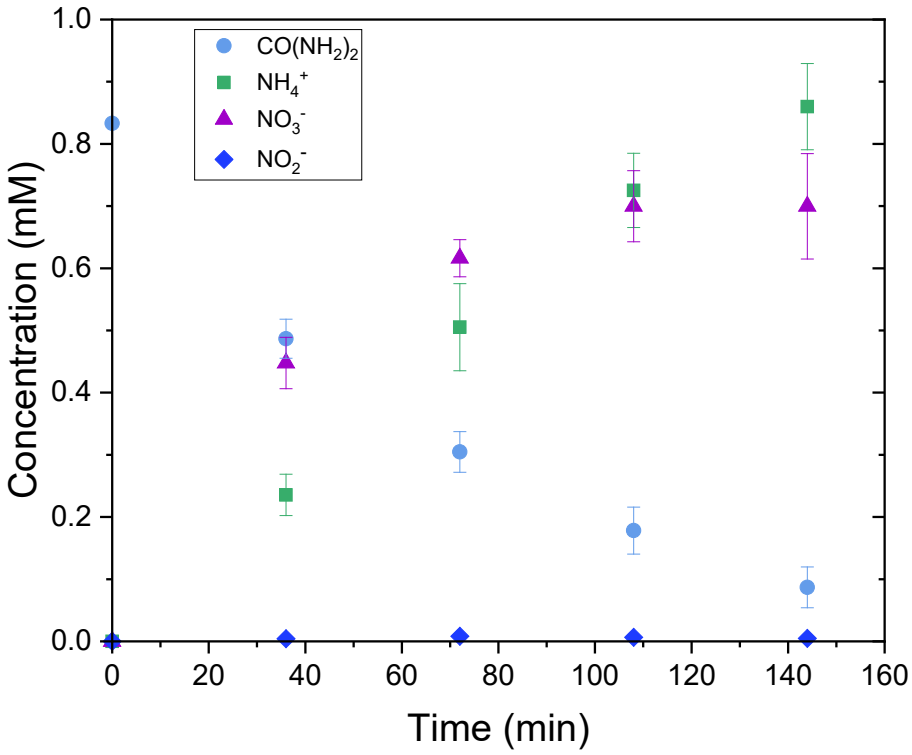

Figure 6-22. Concentration of NH_4^+, NO_3^- and NO_2^- vs time in the one-compartment cell with WO_3 photoanode under irradiation. $[Urea]_0 = 0.83$ mM. Electrolyte = 0.05M $KClO_4$. I_0 (280-500 nm) = 173 W m^{-2}.

Hydroxyl radicals (•OH) have been reported to have a major role in the oxidation of urea to form NO_3^- and NH_4^+ [3–5]. Previous studies described a detailed mechanism for the photocatalytic oxidation of urea using TiO_2 [3–5]. Pelizzetti et al. (2004) proposed a mechanism for urea degradation using TiO_2, where, one of the amino groups of urea initially converts into a nitroso group and later to a nitro group by •OH [3]. Subsequentially, the nitroformamide is hydrolysed, releasing NO_2^- ions, which are rapidly transformed into NO_3^- by •OH [42]. The remaining carbamic acid, which occurs as a zwitterion can undergo two different oxidation pathways. One of the possible pathways is the oxidation to CO_2 and NH_2OH by •OH radicals, NH_2OH undergoes further •OH oxidation to NO_2^- and NO_3^-. The other possible pathway is the decomposition of carbamic acid to form HCO_3^- and NH_3 by simultaneous •OH and e^- attacks. The molar ratio of NO_3^- to NH_4^+ is indicative of which reactions are favoured. NO_3^-/NH_4^+ ratios of 2 [4] and 1.9 [5] have been reported for photocatalytic degradation of urea using TiO_2. Alternatively, Kim et al. (2012) reported no NO_3^- production in anoxic conditions, suggesting that the

presence of O_2 is essential for the generation of NO_3^- from the photocatalytic degradation of urea in TiO_2 [41].

In this study, with the WO_3 photoanode, the production of NO_2^- in time peaks at $8x10^{-3}$ mM after 72 min and then decreases, indicating that NO_2^- is a reaction intermediate (Figure 6-23), which is consistent with the proposed rapid oxidation of NO_2^- to NO_3^- [42]. However, a higher molar concentration of NH_4^+ than NO_3^- was obtained with a ratio of 0.81 $[NO_3^-]/[NH_4^+]$, which deviates from the previously obtained results in photocatalytic tests using TiO_2 [4,5]. This suggests that even though the urea oxidation via •OH radicals in solution could follow the pathway proposed by Pelizzetti et al. (2004), there might be another mechanisms contributing to preferential decomposition to NH_4^+ [3].

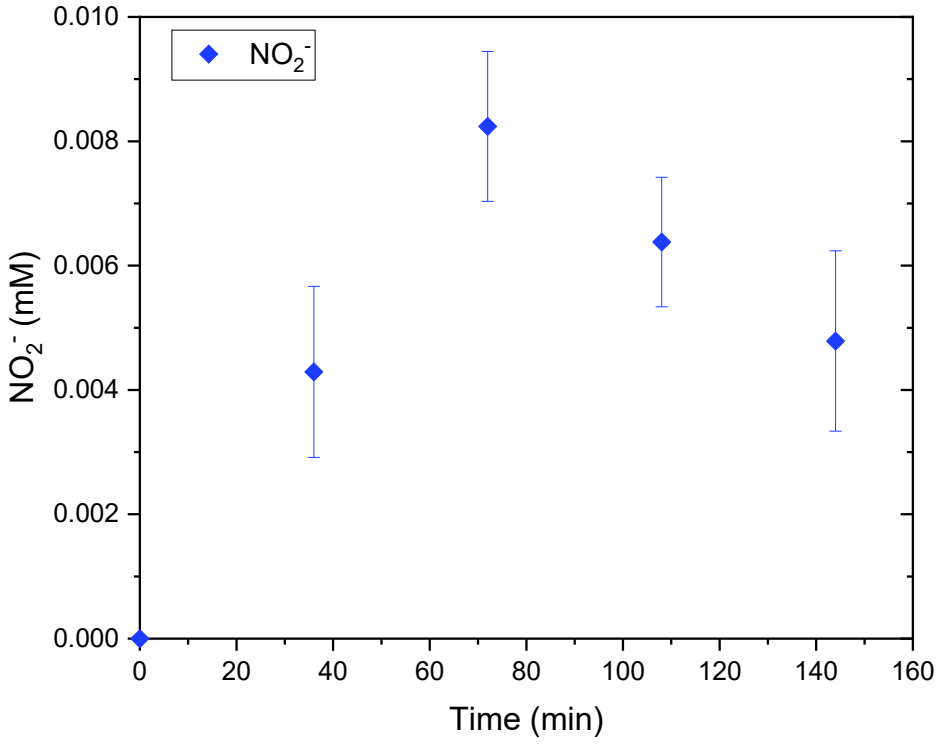

Figure 6-23. Concentration of NO_2^- vs time during oxidation of urea with WO_3 under irradiation in the one-compartment cell. I_0 (280-500 nm) = 173 W m^{-2}. Electrolyte = 0.05M $KClO_4$. $[Urea]_0$ = 0.83 mM.

To gain knowledge depth on the mechanism and potential side reactions, the reduction of NO_3^- to NH_4^+ at the cathode, or by conduction band electrons at the photoanode, was investigated by performing experiments starting with a 0.55 mM NO_3^- solution. The

results show that 25% of the NO_3^- was converted to NH_4^+ (Figure 6-24), confirming the viability of this reduction reaction in the final product distribution.

Similarly, to obtain more insight into the possible oxidation of NH_4^+ to NO_3^- and its role in the main mechanism, experiments starting with a 0.58 mM NH_4^+ solution were performed (Figure 6-25). The results proved that NH_4^+ was not oxidized under these experimental conditions. Several studies have reported the oxidation to occur only when the un-ionized form ammonia (NH_3) is predominant for which the pH needs to be higher than 9.25 (pKa) [43–45]. In the pH used in this study, the protonated form ammonium (NH_4^+) will predominate.

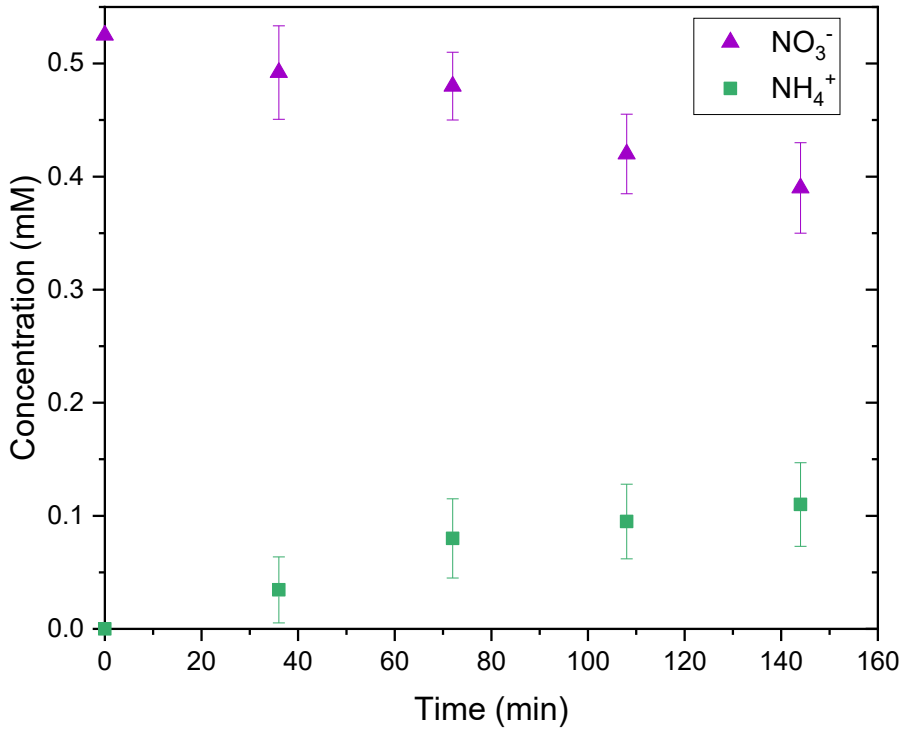

Figure 6-24. Evolution of NO_3^- in time and conversion to NH_4^+ ($[NO_3^-]_0$= 0.55 mM). One-compartment cell. WO_3 photoanode. I_0 (280-500 nm) = 173 W m^{-2}. Electrolyte = 0.05M $KClO_4$.

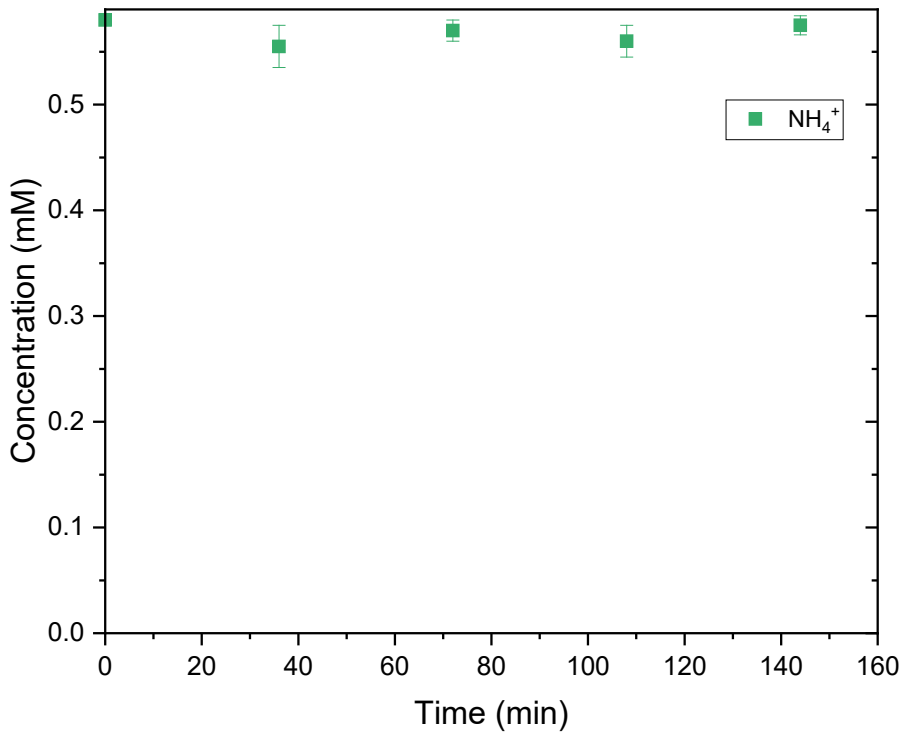

Figure 6-25. Evolution of NH_4^+ in time. ($[NH_4^+]_0$= 0.58 mM). One-compartment cell. WO_3 photoanode. I_0 (280-500 nm) = 173 W m^{-2}. Electrolyte = 0.05M $KClO_4$.

6.4.4 Two-compartment cell: Urea degradation coupled to hydrogen production

In order to couple the production of hydrogen with the degradation of urea a two-compartment gas tight PEC cell was designed, with the compartments separated by a proton exchange membrane (Figure 3-7). This configuration was chosen to separate the H_2 gas evolving at the cathode from the possible gases produced at the photoanode, as well as to eliminate the potential reduction of urea intermediates in the cathode. The two-compartment cell was tested using a WO_3 photoanode as it was the best performing photoelectrode in the initial experiments.

An operational cell potential of 2.4 V, was chosen to perform the experiments in the two-compartment cell since no considerable increase of photocurrent was observed above this potential (Figure 6-26). The cell potential of 2.4 V corresponds to a potential at the photoanode of +1.15 V vs SCE (Figure 6-27). The current generated from WO_3 photoanode under irradiation and in the dark were plotted against potential of cathode vs SCE (Figure 6-28). For the chosen working applied cell potential of +2.4 V, the potential measured between cathode and reference was -1.0 V vs SCE.

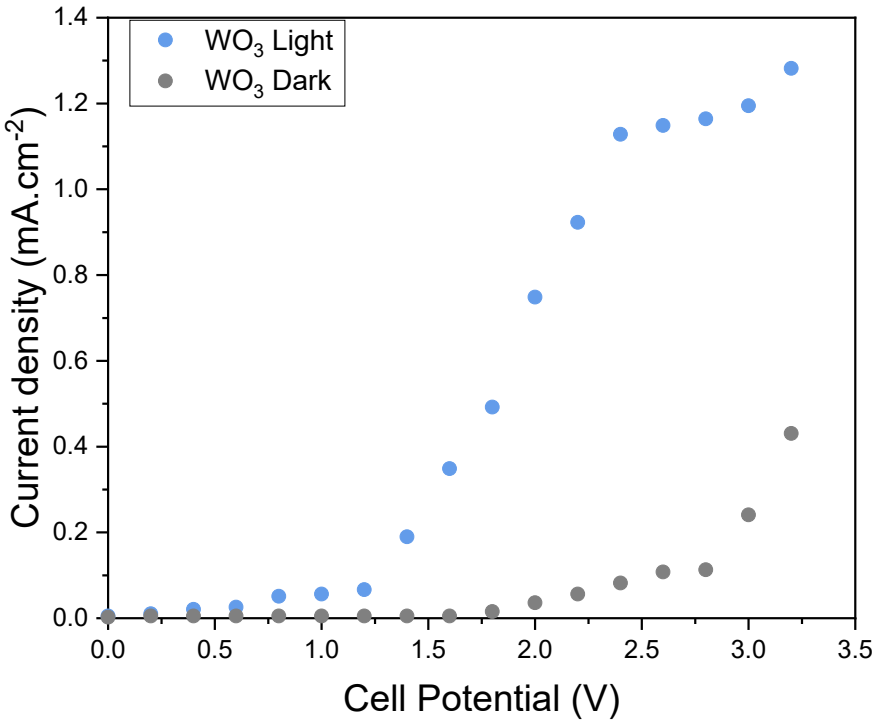

Figure 6-26. Current vs cell potential for WO_3. Two-compartment photoelectrochemical cell. I_0 (280-500 nm) = 173 W m^{-2}. Anolyte electrolyte= 0.83 mM Urea and 50 mM $KClO_4$.

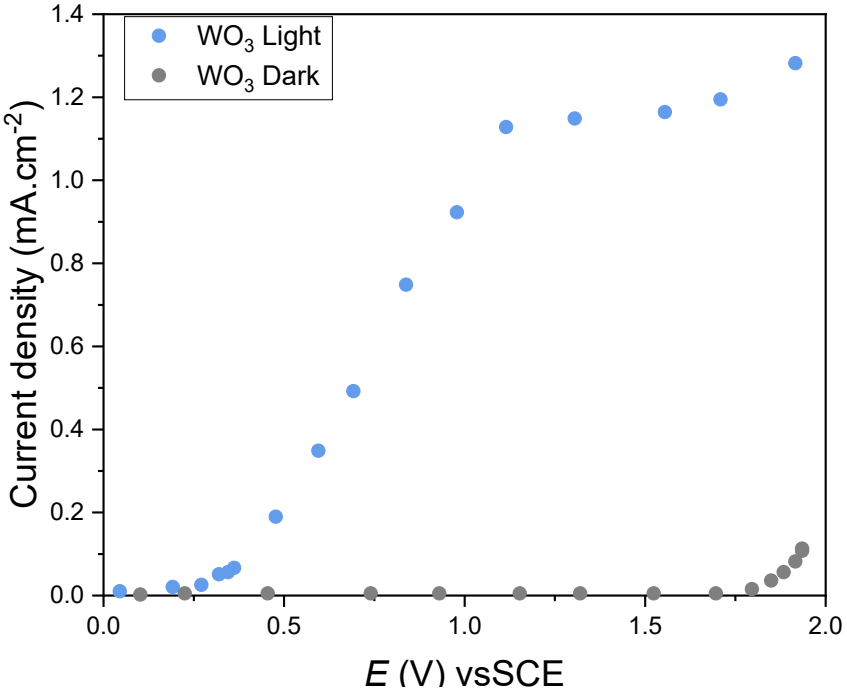

Figure 6-27. Anode potential vs SCE for different applied cell potentials. I_0 (280-500 nm) = 173 W m^{-2}. Anolyte electrolyte= 0.83 mM Urea and 50 mM $KClO_4$.

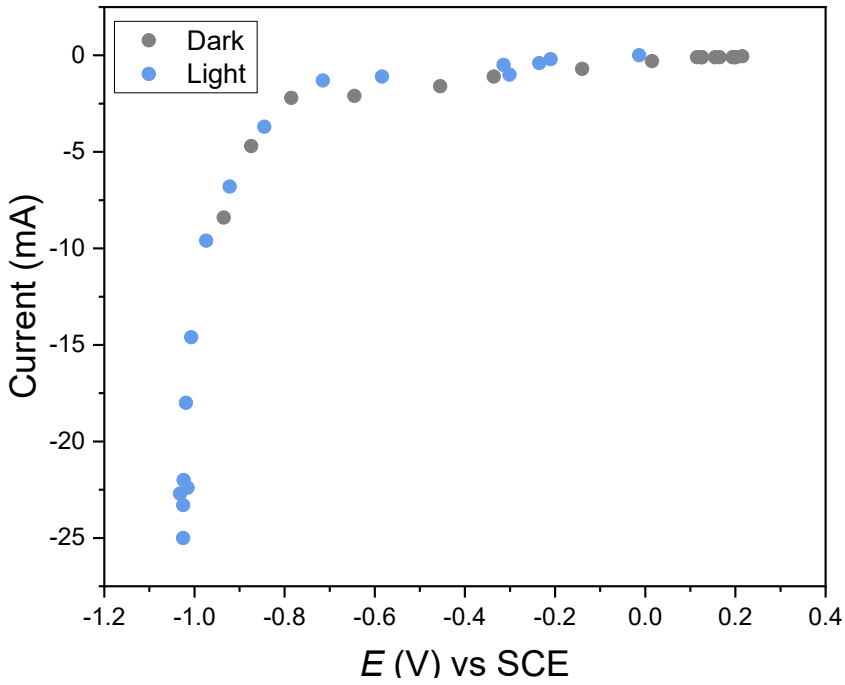

Figure 6-28. Cathode potential vs SCE while cell potential is varied. I_0 (280-500 nm) = 173 W m^{-2}. Catholyte electrolyte = 50 mM $KClO_4$.

In the two-compartment cell, a urea removal rate constant of $1.34x10^{-2}$ min^{-1} was obtained, with 86 % decrease after 2.4 h in the anolyte compartment (Figure 6-29). This slight reduction compared to the $1.47x10^{-2}$ min^{-1} (90 %) obtained with the one-compartment cell is attributed to the reduced photoanode potential. Simultaneously, the production of H_2 gas was studied at the catholyte compartment. Hydrogen production reached 3.09 $x10^{-1}$ mmol after 1 h irradiation and was confirmed by GC-TCD. This would result in an average 309 µmol h^{-1} rate if a zero order H_2 production rate is assumed. This corresponds to a faradaic efficiency of 87.3 %, calculated considering the theoretical moles produced by the recorded current during this hour, 3.54 $x10^{-1}$ mmol (Equation (**3-5**), Chapter 3).

The solar-to-hydrogen conversion efficiency (STH) was calculated by comparing the energy content of the produced hydrogen with the energy supplied by the simulated solar light source (section 3.3.4.1, Figure 3-1). Using 237 KJ for the energy content of 1 mol of hydrogen and with photoanode area of 19.6 cm^2, an efficiency of 1.1% was obtained (Equation (**3-6**), Chapter 3). Even the calculated value might seem low, it is important to consider that the maximum theoretical STH for WO_3 is just 4.5% [46]. Raptis et al. (2017) reported STH efficiency varying from 1.2-1.7% using WO_3 in presence of ethanol. It is also important to consider that the presence of ethanol influences the STH because of its

known current-doubling effect, which it is unlikely to be present in wastewater. Recently, studies have reported the generation of hydrogen and urea oxidation using photoelectrochemistry [48–50]. Bezboruah et al. (2023) reported the production of H_2 when urea is present in the electrolyte [48]. This study used a Ni–TiO_2/p-NDIHBT photoanode and a Pt cathode in a one compartment cell, achieving a faradaic efficiency of 83.3 % and STH efficiency of 0.34 %, when using a 0.5 M KOH electrolyte. Tao et al. (2022) demonstrated the oxidation of urea linked to the production of H_2. The study achieved a H_2 production rate of 128 μmol cm^{-2} h^{-1} when employing a La-Ni-based perovskite photoanode and a Pt cathode in a H-cell reactor with 1 M KOH [49]. In a recent study, Tao et al. (2023) studied the oxidation of urea and hydrogen production, reporting H_2 rate of 200 μmol h^{-1} when using Ni_2P clusters sensitized TiO_2 nanotube arrays photoanode (Ni_2P/TiO_2-NTAs) in a 1 M KOH electrolyte [50]. However, a direct comparison of the performance with the present is not possible due to different experimental testing conditions (as irradiation source, cell configuration and electrolyte). In addition, these studies were performed at alkaline pH (13-14), which if used for wastewater treatment, this process would require pH adjustment of the wastewater with consumable chemicals before treatment and correction before discharge.

In the present study, both the anolyte and catholyte compartment were periodically sampled to identify possible membrane crossover of species. Similar to the observations drawn from the one-compartment cell experiments, the molar nitrogen balance was closed by the summation of the products in solution from both compartments. The products were mostly NH_4^+ and NO_3^-, with a small amount of NO_2^- (Figure 6-29). Small amounts of NH_4^+ are detected in the catholyte compartment, suggesting some NH_4^+ crossover through the membrane. In the case of the two-compartment cell, the measured ratio of NO_3^-/NH_4^+ is equal to 0.76, in close agreement with the 0.81 observed in the one compartment cell.

The NO_2^- concentrations remained below 0.002 mM for the first half of the experiment (Figure 6-30), before decreasing below instrumental detection limit (LOD_{NO2}=2x10^{-4} mM). To verify if the observed conversion of NO_3^- to NH_4^+ in the one-compartment cell occurs at the cathode, additional experiments were carried out starting with an initial NO_3^- concentration of 0.55 mM in the anolyte compartment. The concentration of NO_3^- remains unchanged throughout the duration of the experiments and no detectable concentration of NH_4^+ is found, indicating that the cathode is responsible for the conversion of NO_3^- to

NH_4^+ in the one-compartment cell experiments (Figure 6-31). Additionally, experiments with an initial concentration of 0.58 mM NH_4^+ were performed, similarly to the one-compartment cell no NH_4^+ removal was observed (Figure 6-32).

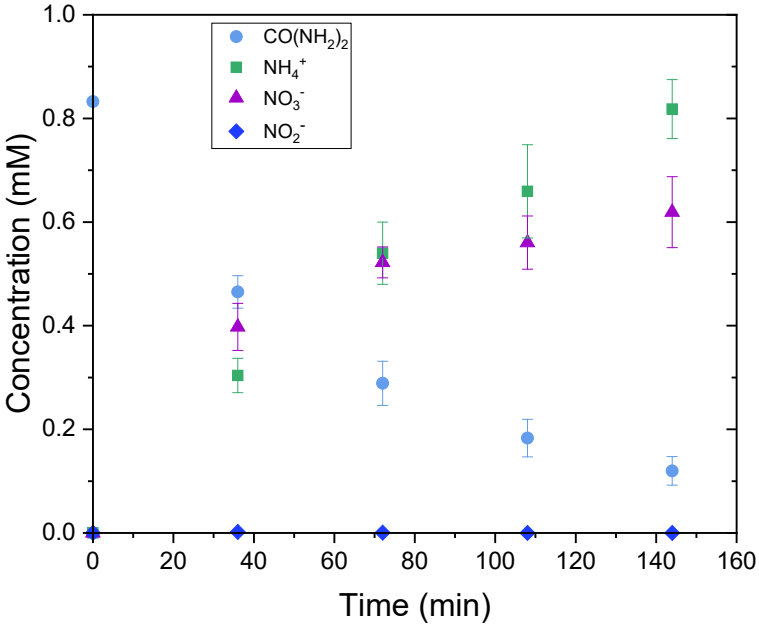

Figure 6-29. Degradation of urea and corresponding conversion to NH_4^+, NO_3^- and NO_2^- using WO_3 photoanode. Two-compartment cell. $[Urea]_0 = 0.83$ mM. Electrolyte = 0.05 M $KClO_4$. I_0 (280-500 nm) = 173 W m^{-2}.

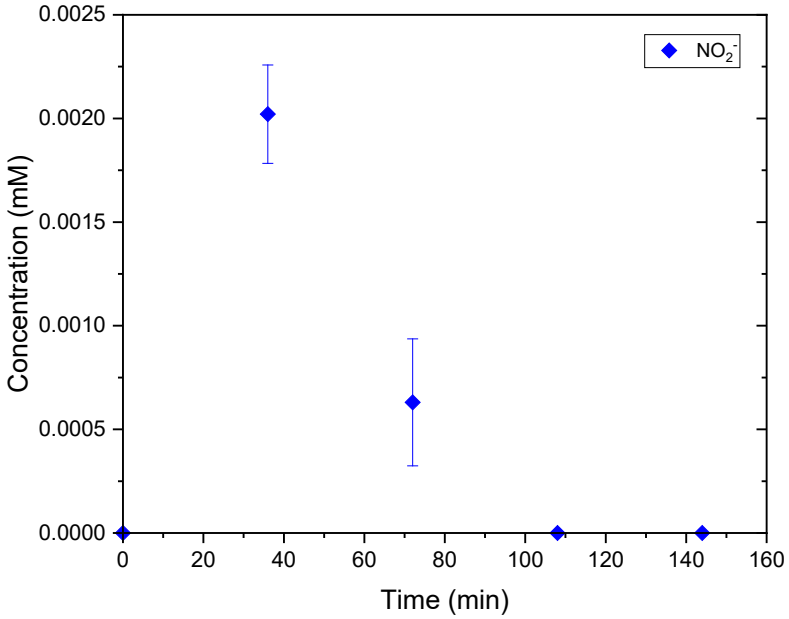

Figure 6-30.Evolution of NO_2^- concentration in time during oxidation of urea with WO_3. Two-compartment cell. WO_3 photoanode. I_0 (280-500 nm) = 173 W m^{-2}. Electrolyte = 0.05M $KClO_4$. $[Urea]_0 = 0.83$ mM.

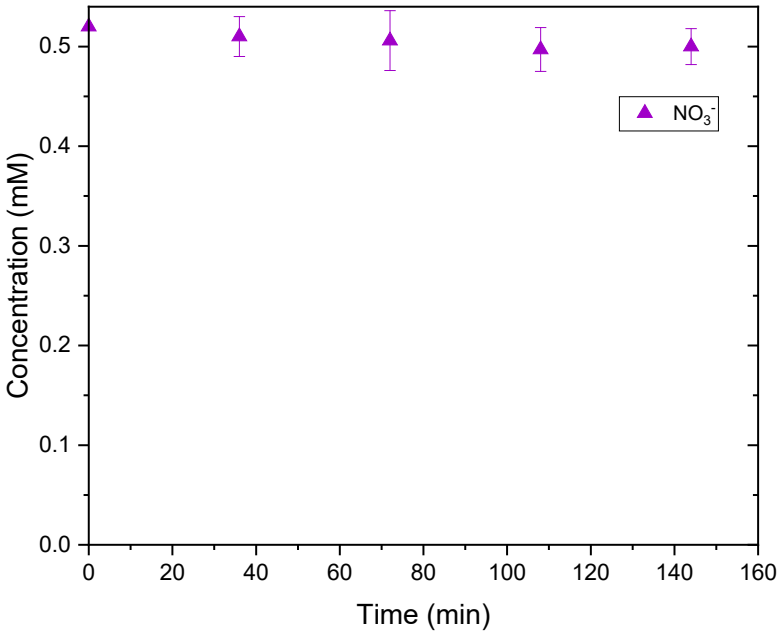

Figure 6-31. Evolution of NO_3^+ in time ($[NO_3^-]_0$= 0.55 mM). One-compartment cell. WO_3 photoanode. I_0 (280-500 nm) = 173 W m^{-2}. Electrolyte = 0.05M $KClO_4$.

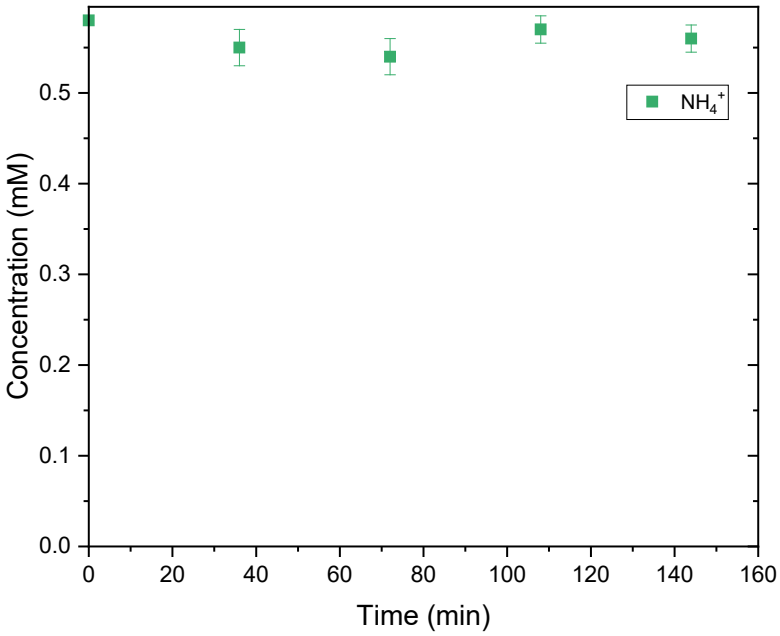

Figure 6-32. Evolution of NH_4^+ in time. ($[NH_4^+]_0$= 0.58 mM). Two-compartment cell. WO_3 photoanode. I_0 (280-500 nm) = 173 W m^{-2}. Electrolyte = 0.05M $KClO_4$.

This study has shown the potential of simultaneous photoelectrochemical urea oxidation and hydrogen generation from wastewater. In order to progress from the laboratory scale testing, further work in reactor design is needed. Specifically, a scale-up version of this technology needs to be evaluated in further studies, together with testing with real wastewater, to assess electrode fouling and long-term operation at these conditions. In addition, techno-economic assessment should be carried out before deployment.

6.5 Conclusions

This work demonstrates the feasibility of coupling urea oxidation to energy recovery as hydrogen. This investigation focuses on the utilization of WO_3 monoclinic plates as photoanode. This visible light active electrode outperformed the UV active TiO_2 electrode for the oxidation of urea without the addition of external oxidizing radicals. WO_3 proved superior urea removal with a rate constant 15 times higher the one obtained for TiO_2.

The coupling of urea oxidation to hydrogen production, besides providing additional value to each individual process, can represent a more desirable anodic process than water splitting to produce hydrogen. This was demonstrated by the increase in photocurrent and IPCE in the presence of urea.

The investigation of the mechanisms of the N-species reactions and product distribution in liquid and gas phase, showed a closed nitrogen balance with nitrate and ammonium as main by-products and the production of hydrogen with a faradaic efficiency of 87.3% and a STH efficiency of 1.1%. Moreover, the use of a two-compartment PEC cell should be considered to separate gas products and to limit the side reactions at the cathode derived by anode by-products. Further work is needed to address the preferential and selective oxidation of urea to dinitrogen.

This study showcases the potential of photoelectrochemical urea oxidation and hydrogen generation from wastewater. This technology can achieve the recovery of resources from wastewater, generating a clean fuel, which aids in the implementation of the circular economy concept and the development of sustainable approaches in the environmental and energy fields.

References

[1] C.V. Reddy, K.R. Reddy, N.P. Shetti, J. Shim, T.M. Aminabhavi, D.D. Dionysiou, Hetero-nanostructured metal oxide-based hybrid photocatalysts for enhanced photoelectrochemical water splitting – A review, Int. J. Hydrogen Energy. 45 (2020) 18331–18347. https://doi.org/10.1016/j.ijhydene.2019.02.109.

[2] M. Pelaez, N.T. Nolan, S.C. Pillai, M.K. Seery, P. Falaras, A.G. Kontos, P.S.M. Dunlop, J.W.J. Hamilton, J.A. Byrne, K. O'Shea, M.H. Entezari, D.D. Dionysiou, A review on the visible light active titanium dioxide photocatalysts for environmental applications, Appl. Catal. B Environ. 125 (2012) 331–349. https://doi.org/10.1016/j.apcatb.2012.05.036.

[3] E. Pelizzetti, P. Calza, G. Mariella, V. Maurino, C. Minero, H. Hidaka, Different photocatalytic fate of amido nitrogen in formamide and urea, Chem. Commun. 4 (2004) 1504–1505. https://doi.org/10.1039/b404574b.

[4] P. Calza, E. Pelizzetti, C. Minero, The fate of organic nitrogen in photocatalysis: An overview, J. Appl. Electrochem. 35 (2005) 665–673. https://doi.org/10.1007/s10800-005-1626-7.

[5] S. Park, J.T. Lee, J. Kim, Photocatalytic oxidation of urea on TiO2 in water and urine: mechanism, product distribution, and effect of surface platinization, Environ. Sci. Pollut. Res. 26 (2019) 1044–1053. https://doi.org/10.1007/s11356-017-8380-3.

[6] X. Liu, F. Wang, Q. Wang, Nanostructure-based WO_3 photoanodes for photoelectrochemical water splitting, Phys. Chem. Chem. Phys. 14 (2012) 7894–7911. https://doi.org/10.1039/c2cp40976c.

[7] S.S. Kalanur, L.T. Duy, H. Seo, Recent Progress in Photoelectrochemical Water Splitting Activity of WO_3 Photoanodes, Top. Catal. 61 (2018) 1043–1076. https://doi.org/10.1007/s11244-018-0950-1.

[8] Z. Shen, J. Bai, Y. Zhang, J. Li, T. Zhou, J. Wang, Q. Xu, B. Zhou, Efficient purification and chemical energy recovery from urine by using a denitrifying fuel cell, Water Res. 152 (2019) 117–125. https://doi.org/10.1016/j.watres.2018.12.066.

[9] Z. Shen, J. Li, Y. Zhang, J. Bai, X. Tan, X. Li, L. Qiao, Q. Xu, B. Zhou, Highly efficient total nitrogen and simultaneous total organic carbon removal for urine based on

the photoelectrochemical cycle reaction of chlorine and hydroxyl radicals, Electrochim. Acta. 297 (2019). https://doi.org/10.1016/j.electacta.2018.11.087.

[10] Z. Shen, Y. Zhang, C. Zhou, J. Bai, S. Chen, J. Li, J. Wang, X. Guan, M. Rahim, B. Zhou, Exhaustive denitrification via chlorine oxide radical reactions for urea based on a novel photoelectrochemical cell, Water Res. 170 (2020) 115357. https://doi.org/10.1016/j.watres.2019.115357.

[11] G. Cai, J. Tu, D. Zhou, L. Li, J. Zhang, X. Wang, C. Gu, The direct growth of a WO_3 nanosheet array on a transparent conducting substrate for highly efficient electrochromic and electrocatalytic applications, CrystEngComm. 16 (2014) 6866–6872.

[12] R.M. Fernández-Domene, R. Sánchez-Tovar, B. Lucas-granados, M.J. Muñoz-Portero, J. García-Antón, Elimination of pesticide atrazine by photoelectrocatalysis using a photoanode based on WO3 nanosheets, Chem. Eng. J. 350 (2018) 1114–1124. https://doi.org/10.1016/j.cej.2018.06.015.

[13] N. Li, H. Teng, L. Zhang, J. Zhou, M. Liu, Synthesis of Mo-doped WO_3 nanosheets with enhanced visible-light-driven photocatalytic properties, RSC Adv. 5 (2015) 95394–95400.

[14] M. Kaneko, J. Nemoto, H. Ueno, N. Gokan, K. Ohnuki, M. Horikawa, R. Saito, T. Shibata, Photoelectrochemical reaction of biomass and bio-related compounds with nanoporous TiO_2 film photoanode and O_2-reducing cathode, Electrochem. Commun. 8 (2006) 336–340. https://doi.org/10.1016/j.elecom.2005.12.004.

[15] D. Dector, D. Ortega-Díaz, J.M. Olivares-Ramírez, A. Dector, J.J. Pérez-Bueno, D. Fernández, D.M. Amaya-Cruz, A. Reyes-Rojas, Harvesting energy from real human urine in a photo-microfluidic fuel cell using TiO_2–Ni anode electrode, Int. J. Hydrogen Energy. 46 (2021) 26163–26173. https://doi.org/10.1016/j.ijhydene.2021.02.148.

[16] G. Wang, Y. Ling, X. Lu, H. Wang, F. Qian, Y. Tong, Y. Li, Solar driven hydrogen releasing from urea and human urine, Energy Environ. Sci. 5 (2012) 8215–8219. https://doi.org/10.1039/c2ee22087c.

[17] L.C. Pop, I. Tantis, P. Lianos, Photoelectrocatalytic hydrogen production using nitrogen containing water soluble wastes, Int. J. Hydrogen Energy. 40 (2015) 8304–8310. https://doi.org/10.1016/j.ijhydene.2015.04.116.

[18] J. Yang, W. Li, J. Li, D. Sun, Q. Chen, Hydrothermal synthesis and photoelectrochemical properties of vertically aligned tungsten trioxide (hydrate) plate-like arrays fabricated directly on FTO substrates, J. Mater. Chem. 22 (2012) 17744–17752. https://doi.org/10.1039/C2JM33199C.

[19] N. V. Alov, Determination of the states of oxidation of metals in thin oxide films by X-ray photoelectron spectroscopy, J. Anal. Chem. 60 (2005) 431–435. https://doi.org/10.1007/s10809-005-0114-x.

[20] B. Bharti, S. Kumar, H.N. Lee, R. Kumar, Formation of oxygen vacancies and Ti^{3+} state in TiO_2 thin film and enhanced optical properties by air plasma treatment, Sci. Rep. 6 (2016) 1–12. https://doi.org/10.1038/srep32355.

[21] M.T. Greiner, L. Chai, M.G. Helander, W.-M. Tang, Z.-H. Lu, Transition Metal Oxide Work Functions: The Influence of Cation Oxidation State and Oxygen Vacancies, Adv. Funct. Mater. 22 (2012) 4557–4568. https://doi.org/10.1002/adfm.201200615.

[22] S. Corby, L. Francàs, A. Kafizas, J.R. Durrant, Determining the role of oxygen vacancies in the photoelectrocatalytic performance of WO_3 for water oxidation, Chem. Sci. 11 (2020) 2907–2914. https://doi.org/10.1039/c9sc06325k.

[23] W. Kong, R. Zhang, X. Zhang, L. Ji, G. Yu, T. Wang, Y. Luo, X. Shi, Y. Xu, X. Sun, WO_3 nanosheets rich in oxygen vacancies for enhanced electrocatalytic N_2 reduction to NH3, Nanoscale. 11 (2019) 19274–19277. https://doi.org/10.1039/C9NR03678D.

[24] E. Ciftyurek, Z. Li, K. Schierbaum, Adsorbed Oxygen Ions and Oxygen Vacancies: Their Concentration and Distribution in Metal Oxide Chemical Sensors and Influencing Role in Sensitivity and Sensing Mechanisms, Sensors. 23 (2023). https://doi.org/10.3390/s23010029.

[25] S. Rahimnejad, J. Hui He, F. Pan, X. Lee, W. Chen, K. Wu, G. Qin Xu, Enhancement of the photocatalytic efficiency of WO_3 nanoparticles via hydrogen plasma treatment, Mater. Res. Express. 1 (2014) 45044. https://doi.org/10.1088/2053-1591/1/4/045044.

[26] V. Dutta, S. Sharma, P. Raizada, V. Kumar, An overview on WO_3 based photocatalyst for environmental remediation, J. Environ. Chem. Eng. 9 (2021) 105018. https://doi.org/10.1016/j.jece.2020.105018.

[27] G. Zheng, J. Wang, H. Liu, V. Murugadoss, G. Zu, H. Che, C. Lai, H. Li, T. Ding, G. Qiang, Guo Zhanhu, Tungsten oxide nanostructures and nanocomposites for photoelectrochemical water splitting, Nanoscalenoscale. 18968 (2019) 18968–18994. https://doi.org/10.1039/c9nr03474a.

[28] Y. Li, X. Wei, X. Yan, J. Cai, A. Zhou, M. Yang, K. Liu, Construction of inorganic-organic 2D/2D WO_3/g-C_3N_4 nanosheet arrays toward efficient photoelectrochemical splitting of natural seawater, Phys. Chem. Chem. Phys. 18 (2016) 10255–10261. https://doi.org/10.1039/c6cp00353b.

[29] J. Liu, S.M. Xu, Y. Li, R. Zhang, M. Shao, Facet engineering of WO_3 arrays toward highly efficient and stable photoelectrochemical hydrogen generation from natural seawater, Appl. Catal. B Environ. 264 (2020) 118540. https://doi.org/10.1016/j.apcatb.2019.118540.

[30] Y. Liu, Y.S. Chang, Y.J. Hsu, B.J. Hwang, C.H. Hsueh, Fabrication of WO_3 photoanode decorated with Au nanoplates and its enhanced photoelectrochemical properties, Electrochim. Acta. 321 (2019) 134674. https://doi.org/10.1016/j.electacta.2019.134674.

[31] W. Li, P. Da, Y. Zhang, Y. Wang, X. Lin, X. Gong, Z. Gengfeng, WO_3 Nanoflakes for Enhanced Photoelectrochemical Conversion, ACS Nano. 8 (2014) 11770–11777.

[32] A. Tolosana-Moranchel, N. Pichel, H. Lubarsky, J.A. Byrne, P. Fernández-Ibañez, Photoelectrocatalytic degradation of pharmaceuticals and inactivation of viruses in water with tungsten oxide electrodes, J. Environ. Chem. Eng. 10 (2022) 107955. https://doi.org/10.1016/j.jece.2022.107955.

[33] C. Haisch, J. Schneider, M. Fleisch, H. Gutzmann, T. Klassen, D.W. Bahnemann, Cold sprayed WO_3 and TiO_2 electrodes for photoelectrochemical water and methanol oxidation in renewable energy applications, Dalt. Trans. 46 (2017) 12811–12823. https://doi.org/10.1039/c7dt02063e.

[34] Z. Yang, Y. Jiang, W. Zhang, Y. Ding, Y. Jiang, J. Yin, P. Zhang, H. Luo, Solid-State, Low-Cost, and Green Synthesis and Robust Photochemical Hydrogen Evolution

Performance of Ternary $TiO_2/MgTiO_3/C$ Photocatalysts, IScience. 14 (2019) 15–26. https://doi.org/10.1016/j.isci.2019.03.009.

[35] K. Ranganathan, A. Morais, I. Nongwe, C. Longo, A.F. Nogueira, N.J. Coville, Study of photoelectrochemical water splitting using composite films based on TiO_2 nanoparticles and nitrogen or boron doped hollow carbon spheres as photoanodes, J. Mol. Catal. A Chem. 422 (2016) 165–174. https://doi.org/10.1016/j.molcata.2015.10.024.

[36] K. Kim, M.J. Kim, S.I. Kim, J.-H. Jang, Towards visible light hydrogen generation: Quantum dot-sensitization via efficient light harvesting of hybrid-TiO_2, Sci. Rep. 3 (2013) 1–8. https://doi.org/10.1038/srep03330.

[37] H. Yu, Y. Zhao, C. Zhou, L. Shang, Y. Peng, Y. Cao, L.Z. Wu, C.H. Tung, T. Zhang, Carbon quantum dots/TiO_2 composites for efficient photocatalytic hydrogen evolution, J. Mater. Chem. A. 2 (2014) 3344–3351. https://doi.org/10.1039/c3ta14108j.

[38] Q. Zeng, J. Li, J. Bai, X. Li, L. Xia, B. Zhou, Preparation of vertically aligned WO_3 nanoplate array films based on peroxotungstate reduction reaction and their excellent photoelectrocatalytic performance, Appl. Catal. B Environ. 202 (2017) 388–396. https://doi.org/10.1016/j.apcatb.2016.09.045.

[39] G. Dale, Electrochemical growth and characterisation of self-organised titania nanotubes, (2009). https://search.ebscohost.com/login.aspx?direct=true&db=edsble&AN=edsble.516137&site=eds-live.

[40] Y. Wang, M. Zu, X. Zhou, H. Lin, F. Peng, S. Zhang, Designing efficient TiO_2-based photoelectrocatalysis systems for chemical engineering and sensing, Chem. Eng. J. 381 (2020) 122605. https://doi.org/10.1016/j.cej.2019.122605.

[41] J. Kim, D. Monllor-Satoca, W. Choi, Simultaneous production of hydrogen with the degradation of organic pollutants using TiO_2 photocatalyst modified with dual surface components, Energy Environ. Sci. 5 (2012) 7647–7656. https://doi.org/10.1039/c2ee21310a.

[42] A. Zafra, J. Garcia, A. Milis, X. Domènech, Kinetics of the catalytic oxidation of nitrite over illuminated aqueous suspensions of TiO_2, J. Mol. Catal. 70 (1991) 343–349. https://doi.org/10.1016/0304-5102(91)80129-Q.

[43] X. Zhu, S.R. Castleberry, M.A. Nanny, E.C. Butler, Effects of pH and catalyst concentration on photocatalytic oxidation of aqueous ammonia and nitrite in titanium dioxide suspensions, Environ. Sci. Technol. 39 (2005) 3784–3791. https://doi.org/10.1021/es0485715.

[44] J. Nemoto, N. Gokan, H. Ueno, M. Kaneko, Photodecomposition of ammonia to dinitrogen and dihydrogen on platinized TiO_2 nanoparticules in an aqueous solution, J. Photochem. Photobiol. A Chem. 185 (2007) 295–300. https://doi.org/10.1016/j.jphotochem.2006.06.024.

[45] N.L. Michels, A. Kapałka, A.A. Abd-El-Latif, H. Baltruschat, C. Comninellis, Enhanced ammonia oxidation on BDD induced by inhibition of oxygen evolution reaction, Electrochem. Commun. 12 (2010) 1199–1202. https://doi.org/10.1016/j.elecom.2010.06.018.

[46] Z. Li, W. Luo, M. Zhang, J. Feng, Z. Zou, Photoelectrochemical cells for solar hydrogen production: current state of promising photoelectrodes, methods to improve their properties, and outlook, Energy Environ. Sci. 6 (2013) 347–370. https://doi.org/10.1039/c2ee22618a.

[47] D. Raptis, V. Dracopoulos, P. Lianos, Renewable energy production by photoelectrochemical oxidation of organic wastes using WO_3 photoanodes, J. Hazard. Mater. 333 (2017) 259–264. https://doi.org/10.1016/j.jhazmat.2017.03.044.

[48] J. Bezboruah, D.M. Sanke, A.V. Munde, S. Das, H.S. Karmakar, S.S. Zade, Nickel-doped TiO_2 and thiophene-naphthalenediimide copolymer-based inorganic/organic nano-heterostructure for the enhanced photoelectrochemical urea oxidation reaction, Int. J. Hydrogen Energy. 48 (2023) 7361–7373. https://doi.org/10.1016/j.ijhydene.2022.11.098.

[49] Y. Tao, L. Chen, Z. Ma, C. Zhang, Y. Zhang, D. Zhang, D. Pan, J. Wu, G. Li, Near-infrared-driven photoelectrocatalytic oxidation of urea on La-Ni-based perovskites, Chem. Eng. J. 446 (2022) 137240. https://doi.org/10.1016/j.cej.2022.137240.

[50] Y. Tao, Z. Ma, W. Wang, C. Zhang, L. Fu, Q. Zhu, Y. Li, G. Li, D. Zhang, Nickel Phosphide Clusters Sensitized TiO_2 Nanotube Arrays as Highly Efficient Photoanode for

Photoelectrocatalytic Urea Oxidation, Adv. Funct. Mater. 33 (2023) 2211169. https://doi.org/10.1002/adfm.202211169.

Chapter 7. Conclusions and future work

7.1 Conclusions

The overall aim of this research was to investigate the performance of semiconductor materials for the photocatalytic and photoelectrochemical oxidation of common nitrogen pollutants in wastewater, together with the simultaneous recovery of energy in the form of hydrogen gas.

The state-of-the-art for the use of photocatalytic and photoelectrocatalytic processes for the treatment of wastewater compounds coupled to the production of hydrogen was discussed in chapter 2. This chapter included an overview of the fundamentals, materials and the parameters used to evaluate the performance of these processes. The main section reviewed different waste compounds with a special focus in ammonia and urea and it was concluded with an evaluation of the current limitations on this field and future opportunities.

The initial work in chapter 4, studied the use of two different TiO_2 nanostructured electrodes (P25 and TiNT) for the photoelectrochemical oxidation of urea. For both electrodes, an enhancement on the photoelectrochemical process was found when urea was added to the electrolyte, shown by an increase in photocurrent. This enhancement was attributed to the holes being scavenged by the urea either via direct hole transfer or via hydroxyl radical mediated hole transfer. When comparing the performance of both electrodes in presence of urea, TiNT obtained more than 3 times the photocurrent generated with P25. In addition, in presence of urea, TiNT showed a 55.11 % IPCE at 340 nm, compared to maximum a IPCE of 21.22 % achieved with P25 at 330 nm. The better performance of the TiNT electrode was attributed to the longitudinal pathway provided by the nanotubes, which helps the charge transfer.

The oxidation of urea for both TiO_2 electrodes was studied using a custom-made photoelectrochemical cell with an irradiated area of 19.6 cm^2. The results for TiNT showed a urea oxidation rate 1.8 times the rate obtained with P25. Besides, the activity of both P25 and TiNT for the oxidation of urea in photoelectrochemical configuration

was compared to photocatalytic configuration. The TiNT electrode recorded 15 times higher urea oxidation rate with applied bias, while for P25 the rate was 1.8 higher. This increment corroborates the enhancement in charge separation that can be achieved by the application of a bias in photoelectrochemical configuration.

Following the initial results, the enhancement of the TiO_2 properties through the modification of its surface with Cu_xO clusters was studied in chapter 5. For this study, particle suspension atomic layer deposition (ALD) was utilized to deposit the Cu_xO nanoclusters on the surface of the TiO_2(P25) semiconductor particles. The deposition of Cu_xO clusters was successfully achieved with a narrow particle size distribution and a controlled loading, highlighting the possibility of using ALD for the deposition of nanoclusters to enhance particulate semiconductor properties. The oxidation state of the clusters was studied through XPS, obtaining Cu_2O for lower Cu loadings and a mixture of Cu_2O and CuO for higher Cu loadings (>1.0 wt.%). Furthermore, the optical bandgap was studied by UV-DRS, with the results suggesting a bandgap reduction for the Cu_xO/TiO_2 samples when compared to TiO_2. However, the spectral photocurrent study showed no effective bandgap modification. The photoelectrochemical measurements showed no significant enhancement for Cu_xO clusters deposition on TiO_2, when immobilized in electrode and used as photoanode. Besides, the addition of Cu_xO formed a p-n heterojunction which caused a rectification of the current catholically. On the other hand, the photocatalytic experiments in the presence of urea, showed a distinguishable enhancement in oxidation rate for the Cu_xO/TiO_2 suspension photocatalysts. This improvement was attributed to charge separation, which lowers the recombination of photogenerated electron-hole pairs. The best performing sample among the studied Cu loadings from 0.1 % to 2.4 %, was the one containing 0.4 % and oxidation state Cu(I), achieving 1.7 times the oxidation rate of unmodified TiO_2.

Subsequently, a different material than TiO_2 was studied for the oxidation of urea, WO_3. The performance of WO_3 was also compared to TiO_2(P25) as benchmark. In this study, the photoelectrochemical properties of WO_3 surpassed P25, with up to 10 times higher photocurrent. In addition, WO_3 exhibited a maximum IPCE of 43% at a wavelength of 360 nm and visible light activity up to 470 nm, while TiO_2 just showed photocurrent up to 390 nm. Similarly, to the study with TiO_2 (chapter 4), the presence of urea increased the photocurrent obtained with WO_3. Thus, it was concluded that WO_3 proved superior urea oxidation, with 15 times the urea oxidation rate of TiO_2(P25). The investigation of

the product distribution resulted in a closed nitrogen balance, with nitrate and ammonium being the majoritarian products.

To study the oxidation of urea and the simultaneous production of hydrogen, a custom-made photoelectrochemical cell, with an irradiation window of 19.6 cm^2, was designed and fabricated. The cell had 2-compartments separated by a Nafion membrane, to limit the side reactions at the cathode derived by anode by-products and separate the produced gas products. The simultaneous production hydrogen was detected, achieving a hydrogen faradaic efficiency of 87.3 % and a solar-to-hydrogen efficiency of 1.1 %.

This study showcased the potential of coupling the oxidation of urea from wastewater and hydrogen generation through the use of photoelectrochemistry. The treatment of wastewater coupled to the recovery of resources from wastewater would help in the application of the circular economy concept and the development of sustainable approaches in the environmental and energy fields.

7.2 Future work

The use of photocatalysis and photoelectrocatalysis (electrochemically assisted photocatalysis) for the treatment of urea in wastewater coupled to the generation of hydrogen was investigated in this thesis. This work investigated the performance of different semiconductor materials, TiO_2(P25), TiO_2(TiNt) and WO_3 as photoanodes, as well, as the surface modification of TiO_2 with Cu_xO clusters using atomic layer deposition. In addition, all the by-products from urea oxidation were identified and the production of hydrogen studied using custom-made photoelectrochemical cells. However, to further develop this approach, several challenges need to be considered.

Regarding the photoanode, other materials with improved visible light absorption and low applied potential, to drive their charge separation, should be investigated. Besides, the formation of nanostructures with larger surface area and reduced charge recombination should be considered to make this process more competitive**.** In addition, when selecting photoanode materials for the treatment of wastewater, it is necessary to evaluate if the material would be stable at the wastewater pH conditions. The long-term stability of the photoanode materials for the treatment of wastewater still needs to be assessed.

Additionally, consideration should also be given to the scalability, cost and sustainability of the production methods for the electrodes.

As identified in this study, the oxidation of urea requires particular attention to avoid the formation of harmful by-products. For this reason, future work should consider the incorporation of co-catalyst that favour reaction mechanisms leading to the selective production of harmless products, such as dinitrogen gas. Alternatively, it can also be considered the implementation of a second treatment step where the products of urea oxidation are converted into nitrogen gas. Future studies should also include the use of complex wastewater mixtures, which simulate real conditions, gaining further understanding on the interaction mechanisms between the distinct compounds present in wastewater, which would culminate with testing real wastewater. Besides, the possible electrode and membrane fouling, originated by wastewater components should be studied, assessing if some pre-treatment as e.g. filtration would be necessary.

Further consideration should also be given to cathode material. The use of platinum or platinized electrodes for the production of hydrogen should be substituted by inexpensive and abundant alternative materials. This research can benefit from the vastly explored field water electrolysis. In addition, the treatment of wastewater compounds through photoelectrochemical oxidation could be potentially also coupled to other reduction reactions instead of H_2, as the production of H_2O_2 (a valuable chemical which could also be used as oxidizer for wastewater treatment), or the reduction of CO_2 (which might be liberated from the oxidation of organic compounds in the anode, to form valuable products).

In order to scale-up this technology, a part of further research into the photoanode and cathode materials, more research is needed to improve the design of photoelectrochemical cells, leading to improved light absorption and reaction rates, and enhanced overall system efficiency. Techno economic assessments from the scale-up version should also be performed to evaluate the feasibility of applying this technology in wastewater treatment facilities.